POLITECNICO DI MILANO
DEPARTMENT OF ENERGY
DOCTORAL PROGRAMME IN ENERGY AND NUCLEAR SCIENCE AND TECHNOLOGY

Multi-dimensional CFD Simulation of Internal Nozzle Flows in High Pressure Fuel Injectors

Doctoral Dissertation of:
Filippo Giussani

Supervisor:
Prof. Federico Piscaglia

Co-supervisor:
Dr. Jerome Hèlie

Tutor:
Prof. Angelo Onorati

The Chair of the Doctoral Program:
Prof. Vincenzo Dossena

2020 – XXXI Cycle STEN

to my family

Acknowledgements

First of all, I would like to acknowledge my supervisors for having supported me during these four challenging years, and for having given me the possibility to attend this PhD. Probably, if I had the chance to go back in time, I would not do this again, but one never knows how tough something can be until you try it. Many times, I thought about giving up, but then I have never done it, and for this I have to acknowledge my parents and my brother for having supported and beared me in good and bad days; also my friends supported me a lot during this though part of my life. Probably, the fact I have so many good friends prevented me from taking wrong decision in these years. Finally, I have to thank Raffaele, who has supported me mentally every day, and who will actually bear me in good and bad luck for the time to come. Last but not the least, I want to thank COVID-19; it is such a pleasure to complete this journey having another challenge on my side. Thanks also to ANL and TGCC for having provided me the computational resources without wich I would have not been able at all to carry on with my research.

Abstract

The present work focuses on the modelization of in-nozzle flow and primary break-up of high pressure fuel injector for Gasoline Direct Injection (GDI) engines. Experimental high-speed camera visualizations on transparent glass-nozzle replica of gasoline fuel injectors, have been used in combination with a novel in-house developed high-fidelity LES-VOF multiphase solver in OpenFOAM, to study the evolution of vortex flow and cavitation in GDI injection, as well as the extent primary jet atomization. The development of a single-fluid solver supporting phase-change and able to capture the evolution of three fluids, two of which are miscible into the sharp interface capturing Volume of Fluid (VOF) approximation, is presented. The transport of each phase-fraction is solved independently by a flux-corrected transport method to ensure the boundedness of the void fractions over the domain. The closure of the system of equations is achieved by a cavitation model that handles the phase change between the liquid and the fuel vapor, and it also accounts for the interaction with the non-condensable gases. Verification of the solver has been performed on two numerical benchmarks: a two-dimensional bubble rising in a liquid column and a cavitating/condensing liquid column. Afterwards, a first validation of the solver has been performed using a test case at low injection pressure ($2.2\,bar$): numerical predictions from large-eddy simulations have been compared against experimental results available from literature for that operative pressure condition; in particular, validation against high-speed camera visualizations and Laser Doppler Velocimetry (LDV) measurements of cavitating in-nozzle flows in a fuel injector is reported. Finally, the solver has been validated on two configurations of a glass nozzle injector, provided by Continental Automotive SAS. They have been analyzed under a working pressure condition of $100\,bar$. Due to high pressure condition and reduced size of the nozzle orifice, only high-speed camera visualizations were available as experimental measurements. The simulated domain has been reconstructed from X-ray Computed Tomography (XCT) performed on the real nozzle replica. Both experiments and simulations capture the formation of unsteady vapor structures inside the nozzle volume. The first type, which is referred to as "shear-cavitation", is found at the core of the recirculations zone and originates at the sharp corners at the nozzle entrance. This is also called geometry-induced cavitation. The second type, which is referred to as "string-cavitation", is found at the core of high vorticity area along nozzle axis. It is shown that the numerical solver provides an accurate capture of the interface among the different phases within the nozzle hole and a very detailed description of the vortex generation in the injector nozzle; strings appear within the time scales that are relevant for a typical gasoline injection event and, for the specific case and operating condition studied, their generation seems mostly related to the flow pattern of the upstream region of

the nozzle. Vorticity and surface dynamics have been then used to identify the main factors for the formation of the surface instabilities, that lead to the so called “primary atomization”. Predictions of the primary atomization of jets on real nozzle geometries have been finally validated against the experimental measurements of the spray angle.

Keywords 3-phase VOF, internal nozzle flow simulation, cavitation, high pressure injection, primary breakup, high-speed camera visualizations, LibPoliMi/DAER

Riassunto

Il presente lavoro si concentra sulla modellizzazione di iniettori per motori ad iniezione diretta di benzina, operanti ad alta pressione: flusso di combustibile, all'interno degli ugelli, e rottura primaria del getto sono studiati nella seguente modellizzazione 3D. Visualizzazioni sperimentali, ottenute con videocamere ad alta velocitá, su diverse geometrie di iniettori con ugelli trasparenti, sono state usate in combinazione con un nuovo solutore multifase basato su approaccio LES-VOF. Quest'ultimo e' stato sviluppato all'interno di OpenFOAM con lo scopo di studiare l'evoluzione del flusso vorticoso e cavitante, cosí come la conseguente rottura primaria del getto di combustibile. Lo sviluppo del solutore multifase, basato su "modello ad un fluido", capace di catturare separatamente l'evoluzione di combustibile liquido, combustibile vapore e aria, e che possa descrivere correttamente il cambiamento di fase del combustibile, é quindi descritto. Il trasporto di ogni frazione volumetrica é risolto quindi separatamente attraverso un metodo basato su correzione dei flussi, per assicurare che il criterio di limitatezza sia verificato su tutto il dominio. La chiusura del sistema di equazioni é ottenuta tramite un modello di cavitazione che gestisce il cambiamento di fase tra combustibile liquido e vapore, tenendo in considerazione l'interazione con l'aria (gas non condensabili). La verifica del solutore é stata realizzata attraverso due test numerici di riferimento: la risalita di una bolla 2D in una colonna di liquido, e una colonna 1D parzialmente cavitante. Succesivamente, una prima validazione del solutore é stata eseguita usando un caso di iniezione di acqua in aria a bassa pressione ($2.2\,bar$): i risultati numerici della simulazione LES-VOF sono stati comparati con le misure sperimentali disponibili da letteratura per quella condizione operativa; in particolare, é riportata la validazione dei risultati numerici con immagini sperimentali, ottenute con videocamera ad alta velocitá, e con misure di velocitá, ottenute tramite anemometria laser doppler. In fine, il solutore é stato validato su due configurazioni di iniettore, con ugello trasparente, realizzate appositamente da Continental automotive. Le due geometrie sono state analizzate sotto condizioni operative di $100\,bar$. A causa delle elevate condizioni di pressione e delle dimensioni ridotte degli ugelli, le uniche misure sperimentali disponibili per la validazione dei risultati numerici sono state le immagini ottenute con videocamere ad alta velocitá. Il dominio simulato é stato ricostruito a partire dalla micro-tomografia computazionale a raggi x, applicata alle due geometrie di iniettore e alle sue diverse repliche. Sia gli esperimenti che le simulazioni hanno evidenziato la formazione di strutture di vapore instazionarie in seno al fluido, nel volume dell'ugello. Il primo tipo di struttura, chiamata "cavitazione da sforzo di taglio", si trova nella zona di distacco e nella zona di ricircolo che ne deriva, e si origina dagli spigoli acuti all'ingresso dell'ugello. Questo tipo di struttura é anche chiamata cavitazione indotta da geometria. Il secondo tipo di strut-

tura, chiamata “cavitazione a stringa”, si trova al centro di una zona ad alta vorticitá lungo l’asse dell’ugello. É mostrato come il solutore sia in grado di garantire un accurata cattura dell’interfaccia tra le varie fasi, e una descrizione dettagliata della generazione di vorticitá all’interno dell’ugello; le stringhe appaiono con una frequenza rilevante che é tipica degli iniettori a benzina e, per i casi specifici e le condizioni operative studiate, la loro generazione sembra per di piú collegata agli schemi di flusso nella regione a monte dell’ugello. Vorticitá e dinamica della superifice del getto sono state poi utilizzate per identificare i principali fattori responsabili della formazione delle instabilitá all’interfaccia, che conducono alla cosiddetta ”rottura primaria” del getto. A completare l’analisi, i risultati numerici dell’atomizzazione primaria delle due configurazioni, sono stati validati con le misure sperimentali dell’angolo del getto tramite le immagine ottenute con la videocamera ad alta velocitá.

Parole Chiave VOF 3 fasi, simulazione di flussi in ugelli, cavitazione, iniezione ad alta pressione, atomizzazione primaria, visualizzazioni con videocamere ad alta velocita’, LibPoliMi/DAER

Contents

List of Figures

List of Tables

Nomenclature

Abbreviations and Acronyms

H_2O	water
Re_l	liquid reynolds number
AMR	Automatic Mesh Refinement
AVOF	Algebraic Volume Of Fluid
BC	Boundary Condition
BFS	Backward Facing Step
BoB	Best of the Best
C	Bergwerk Cavitation Number
Ca	cavitation number
CFD	Computational Fluid Dynamics
CFL	Courant Lewis Friedrich condition
CIP	Constrained Interpolation Profile
CLS	Conservative Level Set
CLSVOF	Coupled Level Set-Volume Of Fluid
CR1	Curvature Radius 1
CR2	Curvature Radius 2
CSF	Continuum Surface Force
CSM	Cavitation Susceptibility MEter
CSM	Cavitation Susceptibility Meter
CSS	Continuum Surface Stress
CV	Control Volume
DI	Direct Injection
EDM	Electrical Discharge Machining
Eo	Eotvos Number
FCT	Flux Corrected Transport
FreeLIFE	Free-Surface Library of Finite Element
FT	Front Tracking
FV	Finite Volume
FVM	Finite Volume Method
GDI	Gasoline Direct Injection
GFM	Ghost Fluid Method
GVOF	Geometric Volume Of Fluid
HEM	Homogeneus Equlibrium Model
HFM	Homogeneous Frozen Model
HRM	Homogeneous Relaxation Model
IC	Initial Condition
JWP	Jet Wise Penetration
K	Nurick Cavitation NUmber
LDV	Laser Doppler Velocimetry
LES	Large Eddy Simulation
LHS	Left Hand Side
LS	Level Set
LSA	Left Spray Angle

MAC Marker And Cell

MFR Mass Flow Rate

MooNMD Mathematics and object oriented Numerics in MagDeburg

MULES Multi Dimensional Limier with Explicit Solution

n-Heptane normal Hepthane

NC Non Condensable

Oh Ohnesorge number

PDE Partial Differential Equation

PF Phase Field

PISO Pressure Implicit with Splitting of Operator

PIV Particle Image Velocimetry

PLIC Piecewise Linear Interface Calculation

RANS Reynolds Averaged Navier Stokes

Re Reynolds Number

RHS Right Hand Side

ROC Rate Of Convergence

RP Rayleigh-Plesset

RSA Right Spray Angle

SCT Sub-grid Curvature Tensor

SGS Sub Grid Scale

SGSD Sub Grid Surface Dynamics

SIMPLE Semi-Implicit Method for Pressure Linked Equations

SMD Saueter Mean Diameter

SMT Sub-grid Mass Transfer

SOI Start Of Injection

STL STereoLitography

TKE Turbulent Kinetic Energy

TP2D Transport Phenomena in 2D

TVD Total variation Diminishing

URANS Unsteady Reynolds Averaged Navier Stokes

VCO Valve Covered Orifice

VOF Volume Of Fluid

WALE Wall Adapting Local Eddy viscosity

We liquid weber number

WoW Worst of the Worst

XCT X-ray Computed Tomography

Subscripts

α void fraction

α-corr alpha equations corrector

α-sub alpha equation sub cycles

$^\circ$ degree

$\mathbf{i}$ x-direction unit vector

$\mathbf{j}$ y-direction unit vector

$\mathbf{k}$ z-direction unit vector

l_1 norm l_1

l_2 norm l_2

l_∞ norm l_∞

sat saturation

amb ambient

atm atmospheric

b bubble

corr corrector

eff effective

eq equivalent

f face

geom geometry

i i-th phase

in inlet

inj injection

j j-th face of a discrete surface

l liquid

liq liquid

nc non-condensable

nonortho-corr non-orthogonal corrector

out outlet

outer-corr outer corrector

p value of the variable in the cell center

rad radial

rms root mean square

s space

sat saturation

th theoretical

tot total

v vapor

vap vapor

x x component of a vector

y y component of a vector

z z component of a vector

Greek Symbols

α_i Void Fraction For the i-th phase

α_l

α_v

α_{nc}

β current time step, total time advancement ratio

$\left(\frac{D\alpha_v}{Dt}\right)^+$ condensation part of the source term

$\left(\frac{D\alpha_v}{Dt}\right)^+$ cavitation part of the source term

δ Dirac function

κ interface curvature

λ flux limiter for MULES

μ Mixture dynamic viscosity

ω vorticity

$\phi(\mathbf{x}, t)$ generic space-time dependent variable

ϕ_N value of the variable in the neighboring cells

ϕ_p value of a variable defined at the cell center

ψ limiter

ρ Mixture density

ρ_l liquid density

ρ_v vapor density

ρ_{nc} non-condensable density

Σ flame surface density interface density

σ mixture surface tension

σ_{lnc} liquid/vapor surface tension

σ_{lv} liquid/non-condensable surface tension

θ azimuthal angle for the glass nozzle injector views representation

τ deviatoric stress tensor

S_α phase-change source term

Latin Symbols

$\dot{m}$ Mass Flow Rate

$\dot{V}$ pressure equation source term

$\hat{\mathbf{n}}$ unit normal vector to the liquid interface

$\hat{\mathbf{n}}_{ij}$ volume average interface normal

$\hat{p}$ modified pressure

$\mathbf{g}$ gravitational acceleration

$\mathbf{H}(z, y, z)$ Heaviside function

$\mathbf{H}_p$ extra-diagonal term of a matrix

$\mathbf{n}$ unit normal vector to a cell face

$\mathbf{n}$ flow field unit normal vector

$\mathbf{S}_f$ cell surface area vector

$\mathbf{U}$	Velocity
$\mathbf{U}_c$	compression velocity
$\mathbf{U}_{c_{lnc}}$	liquid/non-condensable compression velocity
$\mathbf{U}_{c_{lv}}$	liquid/vapor compression velocity
$\mathbf{u}_c$	mean rising velocity
$\mathbf{u}_{lv}$	liquid/vapor mean interface velocity
$\mathbf{u}_{vnc}$	vapor/non-condensable mean interface velocity
$\mathbf{x}$	position vector
$\mathbf{x}_c$	bubble center of mass
$\mathbf{x}_s$	position vector referred to $\hat{\mathbf{n}}$
A	area
A_p	diagonal term of a matrix
C	degree of circularity
C_a	Area Coefficient
C_d	Discharge Coefficient
C_e	TKE coefficient
C_t	non-axial kinetic energy coefficient
C_v	Velocity Coefficient
C_α	compression coefficient
D_{32}	Sauter Mean Diameter
E_k	Non-axial kinetic energy
E_{global}	global mass relative error
e_{l_1}	relative error of the l_1 norm
e_{l_2}	relative error of the l_2 norm
e_{l_∞}	relative error of the l_∞ norm
$E_{marching}$	time evolution of the relative mass error
f_σ	surface tension forces
H_{lv}	liquid/vapor mean surface height
H_{vnc}	vapor/non-dondensable mean surface height
K_{geom}	Conicity factor
L	characteristic length scale
M_i	mass of the i-th phase
n_0	bubble concentration per unit volume of pure liquid
N_b	Number of Spherical Bubble
N_x	x-direction discretization
p	static pressure
p_∞	far-field pressure
q_t	temporal evolution of quantity q
$q_{t,ref}$	temporal evolution of a reference quantity q
R	radius of spherical bubble
$r_{b,0}$	Initial bubble radius
S_u	momentum Equation Source terms
T	temperature
t	time
U_g	characteristic bubble velocity
V	cell volume
V_i	cell volume occupied by the i-th phase
V_l	cell volume occupied by the liquid
V_v	cell volume occupied by the vapor
V_{nc}	cell volume occupied by the non-condensable
${B_{l_p}}^n$	liquid fraction equation variable
${B_{v_p}}^n$	vapor fraction equation variable
C	Color Function
D	nozzle diameter
f	generic marker function
H	Glass nozzle BFS height
h	inverse of refinement in x direction
k	grid refinement level
N	number of samples
off H	Glass nozzle BFS width

Q	Volumetric Flow Rate
W	generic weight used for space average

Superscripts

n	value of the variable at the time n
$n+1$	value of the variable at the time $n+1$
*	predicted variable
+	denoting condensation source term
-	denoting cavitation source term
k	k-th face considered in the space average over a surface

CHAPTER 1

Introduction

1.1 Injection Process in GDI engines: internal Nozzle flow and Primary Breakup

In the last decade, the application of Direct Injection (DI) in Gasoline Engines has rapidly increased due to an enforcement on pollutant emissions limits. An improved combustion efficiency can be achieved acting upstream or downstream to the combustion process. While the latter strategy is almost delegated to the after-treatment of exhausted gases, the former is focused on the quality of the fuel itself and on how the fuel is injected in the combustion chamber. In particular, fuel injection has a pivotal role in achieving the aforementioned goals. Therefore, the improvement of injector design is of paramount importance. Thus, both a better comprehension on how an injector geometry characterizes the spray quality and fuel air mixing and the investigation of flow structures, occurring within the nozzle orifice, can help during the design process of an injector. In this context, Computational Fluid Dynamics (CFD) is widely used by injector manufacturers during the design process of the injectors. Proper CFD-tool must be developed to fill the lack of non-intrusive experimental measurements within the nozzle orifice and in the proximity of the nozzle outlet, in the primary break-up region. This first break-up of the liquid is called “primary break-up” and results in large ligaments and droplets that form the dense spray near the nozzle, while the subsequent break-up process of already existing droplets into smaller ones is called “secondary break-up” and is due to aerodynamic forces caused by the relative velocity between droplets and surrounding gas [18]. These regions are shown In Fig. 1.1.

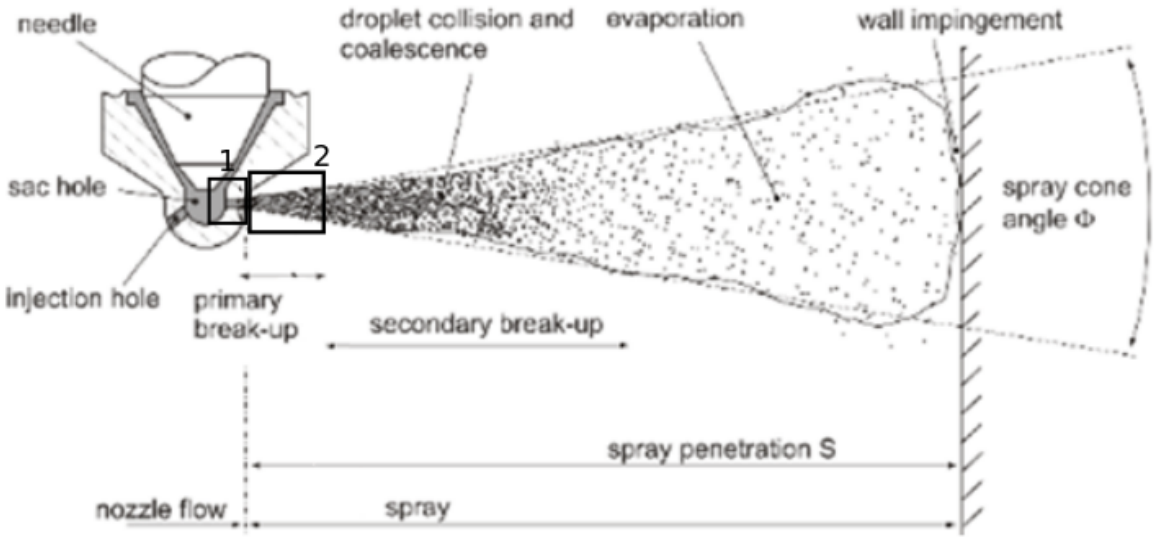

Figure 1.1: *Different stages of spray breakup. (1) in-nozzle flow;(2) Primary breakup. [18]*

In literature, just a few works on Particle Image Velocimetry (PIV) and Laser Doppler Velocimetry (LDV) applied to internal nozzle flow and primary breakup are available [6, 7, 40, 199, 200, 227]. The operative pressure condition of GDI injector and the small sizes of the nozzles (approximately $150 - 200\,\mu m$) make difficult to perform in a reliable way any kind of velocity measurement. For these reasons, when an optical access to the nozzles is feasible, mainly qualitative experimental measurements are performed using high-speed video cameras [43, 103, 172, 173], where only shadowgraph pictures of the internal nozzle flow and of the spray are obtained.

The main phenomena influencing the primary break-up mechanisms, generated inside the nozzle orifices, can be identified into two source: cavitation and turbulence, which are the subjects of the present work.

Secondary break-up mechanism, such as flash boiling and evaporation will not be treated and are out of the scope of the present research work.

1.1.1 Internal nozzle flow and cavitation-induced primary breakup

Pressure drops undergone by the nozzle orifice have the effect of producing bubbles of the same fluid (homogeneous nucleation) or of dissolved gases or very small solid particles (heterogeneous nucleation). This phenomenon, known as cavitation, occurs when the pressure falls down the saturation pressure of the fluid (at constant temperature) and leads to fuel acceleration in the nozzle. This process is shown in Fig. 1.2. It must be underlined that cavitation and flash boiling occur both with an abrupt pressure drop, however, they are characterized by different final states due to a different duration of the thermal effect (different time scales of thermal effect). In cavitation, the bubbles produced (in the $p < p_{sat}$ regions) can suddenly collapse or implode as the pressure recovers. Cavitation has a great potential to damage components during the bubble collapse: this can create shock waves impacting against surfaces damaging them. In nozzles, the cavitation bubbles can implode when leaving the nozzle because of the high ambient pressure inside the cylinder, or inside the nozzle itself, depending on the pressure boundary condition.

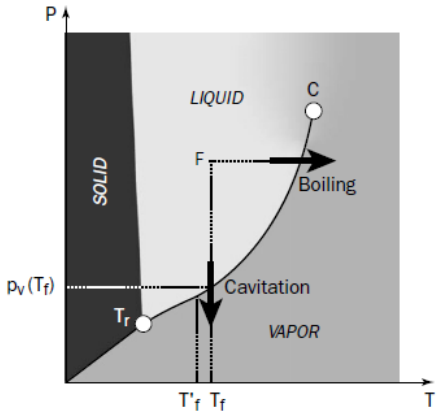

Figure 1.2: *Differences among boiling and cavitation. [68]*

On the contrary, when a liquid, initially in a sub-cooled state, is rapidly depressurized to a pressure sufficiently below the saturated vapor pressure, it can no longer exist in the liquid state, and a rapid boiling process called flash-boiling is initiated. A portion of the fuel then evaporates instantaneously and cools the rest of the liquid down. This sudden evaporation results in a significant increase of spray volume and a faster spray break-up. In case of gasoline injection, flash-boiling is much easier to obtain, than diesel injection, due to the lower boiling curve. Especially if gasoline is injected in the intake manifold, where the static pressure can fall below the saturated vapor pressure of some hydrocarbon fuel components. Such a condition will result in an unintended flash-boiling. This causes significant changes in the fuel spray distribution and the fuel- air mixing [18]. In case of vapor bubble growth due to flash-boiling, the latent heat of vaporization, which is transferred from the liquid to the bubble surface, must be included. In practical cases, flash boiling is often modeled using the same cavitation models but keeping into account the thermal effect.

In Fig. 1.2, boiling mechanism is shown as well. It' s clearly evident that boiling is due only to the thermal effect at constant pressure, while in cavitation the thermal effects are almost negligible. The path in the phase diagram (Fig. 1.2) is practically isothermal. However, in some cases, the heat transfer needed for the vaporization is such that phase change occurs at a temperature lower than the ambient liquid temperature. This temperature difference is called thermal delay in cavitation. It is greater when the ambient temperature is closer to the critical temperature of the fluid. This phenomenon may become important when pumping cryogenic liquids in rocket engines [68]. In [186] the authors combined the inertial and thermal effect into a ratio which allowed for an estimate of their relative importance. When the ratio is large is claimed that inertial effects dominate, and when the ratio is small, thermal effects dominate. In their work is stated that for a high-speed injection of water at $100\,MPa$ the critical time is found to be $13\,\mu s$. This is roughly the time required for a bubble to entirely pass out of the nozzle. However, according to the estimates of bubble growth used for this analysis, the bubble radius would be $3\,mm$, which is much larger than the radius of the nozzle. This physically impossible result, suggests that the bubbles never attain the size where heat transfer limits bubble growth. Consequently, the inter-phase heat transfer is neglected and models are focused on the inertial effects in most cases. For this reason, isothermal conditions are usually adopted for primary jet atomization under cavitating condition. Only in larger nozzles with hotter fluid the thermal effects could become important [186].

Cavitation could play a pivotal role in achieving finer atomization of spray to favor an improved fuel economy and reduced emission levels during combustion [132,238]; however, it may also cause a significant reduction in the stability of the spray [196] and to a potential damage of the injector components, leading to reduced reliability of the injector. In injector nozzles, after a surface spot is initially surrounded by a cavitating flow region, it tends to erode at an accelerated pace: cavitation pits increase the turbulence of the flow and create crevices that act as nucleation sites for new cavitation bubbles, thus leading to an avalanche effect. From high speed camera visualizations on transparent glass nozzles, two different forms of cavitation have been distinguished [72, 192] and they are known as "geometry-induced" and "vortex" (or string) cavitation respectively.

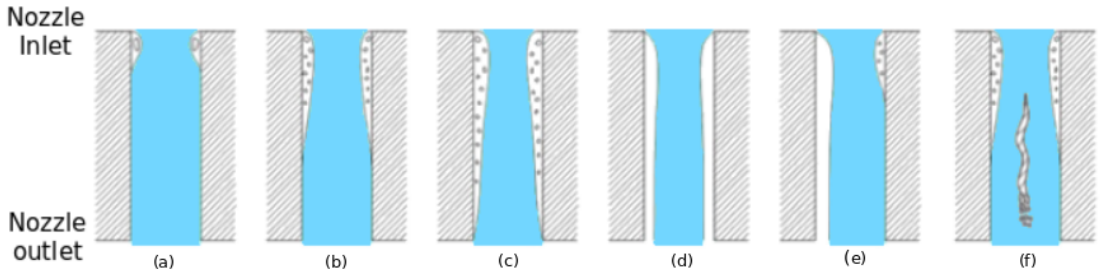

Figure 1.3: *Different cavitation regimes and types of cavitation occurring inside the nozzle of an injector [47]:(a) cavitation inception; (b) cavitation growth; (c) super cavitation; (d) hydraulic flip; (e) asymmetric hydraulic flip ; (f) string cavitation.*

Geometry-induced cavitation (Fig. 1.3-(a)-(b)-(c)) is initiated at sharp corners where the pressure falls below the saturation value [39, 95, 189] because of a sudden flow detachment and the accompanying recirculation region. Considering the same injector geometry, the more the injection pressure increases, the more the region of cavitation grows and extends to the outlet to form supercavitation (Fig. 1.3-(c)): the surface of jet flow becomes more turbulent due to the growth of the cavitation region, and the spray angle also becomes larger [200,201]. In this regime the liquid jet atomization is enhanced [201]. A further increment of the injection pressure leads to the so called "Hydraulic flip" (see Fig. 1.3-(d)): the air surrounding the nozzle outlet is sucked into the nozzle orifice to fill the cavitation area, which makes the cavitation disappear immediately and gets it replaced by a thin layer of gas attached to the wall [47]. This is not beneficial for the atomization and can badly affect the fuel-injection performance; a decrease of the spray cone angle is usually observed in this situation [47]. However, if the internal structure of the nozzle is not smooth and completely symmetrical, as usually occurs in a real nozzle due to the uncertainty and roughness produced after the manufacturing process, maintaining stable the hydraulic flip is difficult. Thus, the phenomenon of local reattachment will occur periodically (Fig.1.3-(e)).

String (or vortex) cavitation (Fig. 1.3-(f)), conversely, develops by the evolution of the vorticity which allows the formation of geometry-scale vortices and is significantly influenced by the walls and the interaction with other vortices [43]; additionally, low pressure regions in the centers of the vortices in the nozzle can generate a phase-change or entrap and stabilize bubbles that were entrained in their proximity, similarly to what is observed in hydromachines [105, 179]. Vortex cavitation in the injector nozzles was first observed by Kim [106] and since then it has been described in further studies performed in enlarged nozzle replicas and was termed also as "string cavitation" [10,93]. The main differences between

vortex cavitation in propellers and turbines and those in fuel injectors arise from the geometric configuration of the nozzle and the operating conditions of the flow. The nozzle flows, develops in very confined volumes, that may allow formation of large-scale vortices relative to the nozzle geometry, where each cavitating vortex may interfere with other vortices and where the influence of the walls can be significant. Also, huge pressure drops in fuel injectors are encountered within very short distances (few hundreds of micrometers) while the lifetime of the formed vortical structure is usually only a fraction of the injection period. Cavitation strings are usually formed during fuel injection in areas where large-scale vortical structures develop: this happens when local pressure level is lower than the vapor pressure of the fuel. In a typical nozzle geometry, cavitation vortices are located between the separation point on the needle surface and the separation point at the hole inlet corner, and where there is sharp flow turning inside the sac volume of the injector. Unlike geometrical cavitation, string cavitation is present in any nozzle geometry: with sac-type and Valve Covered Orifice-type (VCO) nozzles, with either cylindrical or tapered holes, whose inlet can be either sharp or rounded. This has raised questions about the existence of vaporized liquid in the said region; more recent studies [10, 38] suggest that string cavitation represents a transport process of vapor carried by the vortex flow rather than a phase-change process. Formation of string cavitation would originate from pre-existing (shear) cavitation sites, forming a continuous vapor column that extends into the flow region between adjacent holes. This can explain the presence of vapor where the pressure is quite high, for instance in the sac volume between holes.

Cavitation strings in injectors for diesel engines have been studied experimentally [73, 171, 172] and numerically [73, 153, 172]. Experiments has been performed on fully transparent nozzle replicas [103, 171] as well. In [73], enlarged replicas of VCO injectors incorporating tapered converging holes were simulated; a similar study has been published in [153], where the solver handled the presence of multiple phases using the homogeneous equilibrium model, to calculate the compressibility of the liquid/vapor mixture. Furthermore, different injection strategies and nozzle geometries were also tested. In [172], the formation of vortices of string cavitation, has been visualized in the flow upstream to the injector hole inlet of an automotive-sized optical diesel fuel injector nozzle, operating at pressures up to 2000 bar. The aim of the work was to understand the role of relative position and hole-to-hole interaction on the observed string cavitation vortices. In this case, the same solver as in [153] was used and turbulence was modeled using the RANS approach. Simulations were performed on a static 2.5 million cell grid where steady and transient fuel injections were simulated. While there has been a considerable number of investigation on high pressure diesel injection, the underlying physics of confined vortex cavitation still remains unclear and several aspects related to the onset of vortex cavitation are not yet fully understood. There are relatively few investigations on geometries whose features are similar to the real injectors used for Gasoline Direct Injection (GDI). Attempts to model bubble collapse in the vortex core for GDI injection has been reported in [33]. In GDI, vortex cavitation is particularly important because of the volatile components in gasoline, whose saturation pressure and are higher than in diesel. Compared to diesel injectors, gasoline injectors are characterized by a shorter nozzle length so that the turbulent flow cannot fully develop in the nozzle. Additionally, GDI engines have a lower in-cylinder pressure at SOI (Start of Injection) compared to diesel engines: the density jump is always very large. Flow, shear and vortex cavitation are thus key parameters affecting the flow characteristics of GDI injection. These factors pose serious challenges in investigating the flow characteristics of high pressure GDI injections, both numerically and experimentally. Moreover, being cavitation a multiscale phenomena, ranging from a few nanometers to few microns (bubbles grow from nuclei), realistic conclusions cannot be drawn from bigger representative geometries (a scale-up approach is not possible) [154].

Reliable understanding of the flow characteristics in high pressure nozzles thus requires the use of transparent replicas of real-world injectors. While it is possible to produce complex, fully transparent shapes for diesel nozzles [43, 103, 172, 173], experimental visualizations on actual real-sized nozzles under high-pressure conditions for gasoline injection is fraught with difficulties. There are few recent publications discussing experimental investigation of nozzles using transparent nozzles replicas of real-world injectors. Reid et. al [172] report an experimental set-up in which a rectangular transparent insert is integrated with a metal nozzle. Andriotis et. al [10] reported studies on injector configurations for marine diesel engine applications (the large dimensions of injectors for marine engine applications makes construction of replicas easier). Standard Shadowgraphy (illumination from above) on an internal nozzle flow of an asymmetric prototype glass nozzle has been performed [70].

Hence, cavitation modeling in high-pressure injection, and jet break-up, involves the simulation of multiphase (in the context of this paper it refers to liquid and gas) and multicomponent (several instances of the same phase) flows and poses great challenges. These challenges are due to the presence of the interfaces between phases and large or discontinuous properties variations across interfaces between phases and/or components.

"multiphase flow" is the term used to identify a system characterized by the simultaneous flow of a component or several components with two or more thermodynamic phases: they can be either liquid, gas or solid. The choice of the model to describe these complex systems depends on the topology of the flow. In literature, three main topology have been identified and referred to as:

- Separated flow (wave deformation): consists of two or more continuous streams of fluids separated by interfaces. These can be indeformable free surfaces and deformable interfaces. This is the typical topology of the free surface flow in ambient (e.g rivers, see etc.) that can undergo small or high deformations at the interface depending on the Re and Froude (Fr) numbers. This topology can refers also to the bubble rising in a liquid column, whose deformation depends on the Re and the Eo numbers. The approach used to describe this topology can make use of the one-fluid models such as Interface Tracking Method or Interface Capturing Method and their variants (See. Fig. 1.4).

- Dispersed flow: leaden flows of sprays, thus well defined particles distributed in a connected volume of continuous phase. This is the typical topology of solid particles transported within a carrier fluid (liquid or gas) or also the case of liquid droplets in a gaseous phase. The latter is the typical case of a fuel injection, especially for the description of the secondary break-up mechanism. Several approaches can be used to describe these kind of topology. Many of them, referred to as "trajectory model", are based on the kinetic theory, where the spray is described as a number density function that satisfies the Williams Boltzman Equation (WBE) [231]. A widely used approach to solve WBE is the Lagrangian-Monte-Carlo (LMC) method [25]. In this approach, the liquid is tracked with a Lagrangian description and the gas is solved in an Eulerian framework. Several works make use of this approach since a lot of physical processes such as evaporation and flash boiling can be implemented. Another approach to solve WBE is using the "two-fluid" approach as the Euler-Euler (EE) formalism, where both phases are treated as a *continuum*. Nevertheless, the direct resolution of WBE is not feasible since the total variable to solve are $(position, velocity, size, temperature)^N_{parcels}$ where $N_{parcels}$ is the number of stochastic particles (often called parcels) used during the injection, according to the MFR.

- Hybrid topology: stays in between the wave deformation and dispersed topology. They are formed when the interface between liquid and gas becomes deformed and droplets

are generated. For example, the breakup of a liquid jet through a nozzle into an ambient environment. In this case, it is not straightforward to define a dispersed phase and a continuous one: close to the nozzle outlet can be considered as separated flow; The deformation of the jet and the regime depend on Re_l and We_l; after few nozzle diameters, the liquid phase is dispersed and Lagrangian approaches should be used. Eulerian Lagrangian Spray Atomization (ELSA) tries to combine these two topology using the single-fluid model [220], [119]. In ELSA notation two velocities are still appearing cause the gas velocity can be recovered thanks to the extension of ELSA to the Quasi-Multiphase Euler flow [9] , [19]. Generally, can be grouped under the ELSA family models, all the models that try to take into account and to model two main terms that drive atomization process for non-fully resolved case: the subgrid turbulent liquid flux and the unresolved liquid-gas interface [11].

Even if ELSA have shown a big reliability in spray modeling [11], since it is able to describe either first and secondary break-up, it does not take into account phase-change phenomena.

Therefore, depending on the topology of the multiphase flow under analysis and depending on the computational method used for the simulation of a continuum media, the multiphase model is chosen. Within the Finite Volume Method (FVM) framework, two models are commonly used for the simulation of the multiphase and multicomponent of separeted flows: the multi-fluid and the single-fluid model (see Fig 1.4). In the multi-fluid, each phase and/or component is considered to fill a distinct volume and the interfaces between the phases and/or components are captured explicitly. This approach is a generalization of two-fluid approach [176]; typical applications [56, 79, 217] include the prediction of the motion of large bubbles in a liquid, the motion of liquid after a dam break, the prediction of jet break-up, and the capture of any liquid-gas interface. The mutual interaction at the interface can be described as an interfacial momentum transfer and, when interfacial mass and energy transfer are involved, they also need to be included in the equation sets. In order to model the transfer of mass for cavitation with a minimum set of equations for closure, an equation of state to correlate density and speed of sound with pressure and temperature is required: no additional transport equations are used for the vapor phase, whose void fraction is determined by the mixture composition. Similarly to barotropic models, the density is only a function of pressure. In the single-fluid, introduced for the first time by Kataoka [104], the phases and/or components are spatially averaged to lead to a homogeneous mixture; relative velocity among the phases is neglected, which implies the absence of closure for the transfer of mass, momentum and energy at the interfaces, while thermal equilibrium among the different phases is usually assumed.

Single fluid model is mainly grouped in two sub-groups, respectively named interface tracking approach and interface capturing approach. The interface-tracking techniques are based on topological changing mesh which tracks the interface whereas it undergoes deformations or a rigid motion in space-time domain. Because they do not require mesh update, the interface-capturing techniques are more flexible than the previous techniques. However, for comparable levels of spatial discretization, interface-capturing methods yield less accurate representation of the interface. These methods can be used as practical alternatives in carrying out the simulations when compromising the accuracy of the interfaces becomes less of a concern than facing major difficulties in updating the mesh to track such interfaces [211].

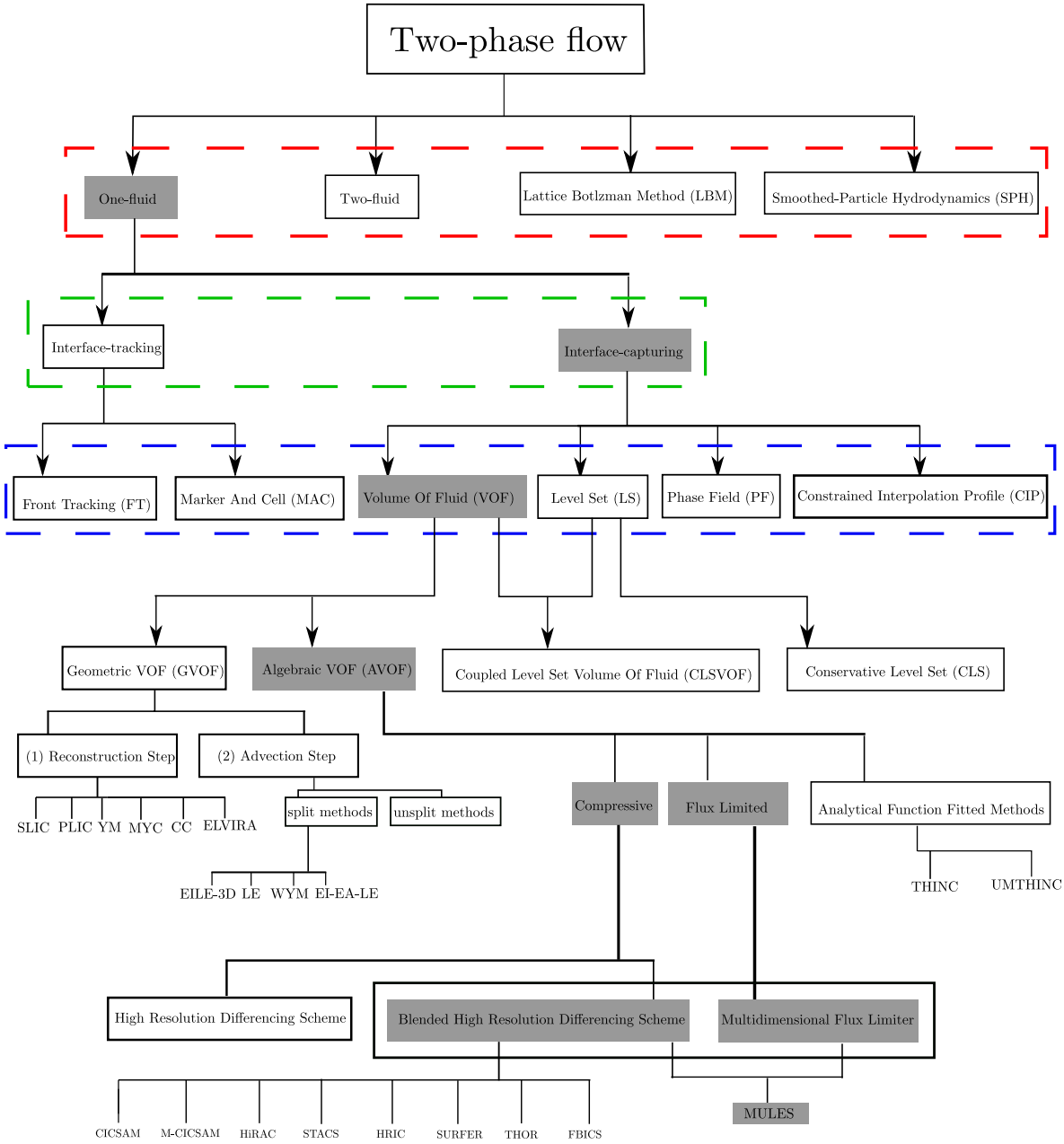

Figure 1.4: *Model review for two-phase flows. Models are grouped within the red dashed rectangle. Approaches are grouped within the green dashed rectangle. Classes are grouped within the the blue dashed rectangle [140]. Gray rectangle background identifies the model/approach/classes used in the present work.*

The interface-capturing techniques, developed primarily for free-surface and two-phase interface flows, are formulated typically over non-moving meshes, using an advection equation in addition to the flow equations. The advection equation governs the evolution of an interface function that marks the location of the interface:

$$\frac{\partial H}{\partial t} + \mathbf{U} \cdot \nabla H = 0 \tag{1.1}$$

which is only valid under the assumption of incompressible mixture ($\nabla \cdot \mathbf{U} = 0$). This does

not happen when phase change occurs. H is the Heaviside function defined as:

$$H(x,y,z) = \begin{cases} 0, & \text{if phase 2} \\ 1, & \text{if phase 1} \end{cases}$$

Which represents the hypothetical sharp interface among a couple of phases. However, numerically, H is replaced with its approximation, called marker function f. For a generic marker function f, the advection equation reads:

$$\frac{\partial f}{\partial t} + \mathbf{U} \cdot \nabla f = 0 \tag{1.2}$$

The interface is captured within the resolution of the finite volume mesh covering the area where the interface is located. According to the marker function used, the method is namely differently. In the Volume of Fluid (VOF) [86] the marker function used is the color function defined as :

$$C = \frac{1}{\Delta V} \int H(x,y,z) dV \tag{1.3}$$

which is also commonly called volume fraction, from which the model takes the name. $C = 0$ or $C = 1$ far from the interface and $0 \leq C \leq 1$ in the cells intersected by the interface, as shown in Fig. 1.5.

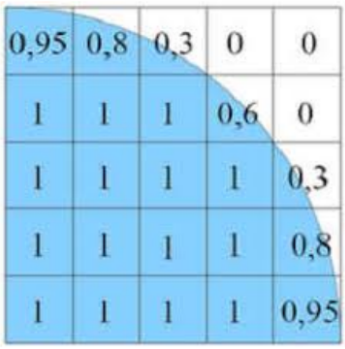

Figure 1.5: *Sketch of the VOF model:* $C = 0$ *or* $C = 1$ *far from the interface and* $0 \leq C \leq 1$ *in the cells intersected by the interface.*

The Level Set (LS) [190], uses as marker function a *level-set function* $\phi(\mathbf{x}, t)$, which is constructed as a distance function from the interface:

$$\phi(\mathbf{x}, t) = \begin{cases} +d, & \text{if phase 2} \\ -d, & \text{if phase 1} \end{cases}$$

where d represents the normal distance to the interface at time t. The level-set equation is derived using the fact that the level-set function should be constant along particle paths. In other words,

$$\frac{D\phi(\mathbf{x}(t), t)}{Dt} = 0 \tag{1.4}$$

Several other methods have been proposed to simulate multiphase flows, using the "one-fluid" formulation: The Coupled Level Set-Volume of Fluid (CLSVOF) [136,207,224], combines LS and VOF to reconstruct the interface; The value of VOF in the interface cells gives the volume on each side of the interface while the gradient of the LS field at the interface

gives the normal direction to the interface. These pieces of information, together with a Piecewise-Linear Interface Calculation (PLIC) [184, 237] approximation of the interface, are sufficient to enable the calculation of the position of the interface [53].

In the Constrained Interpolated Profile (CIP) [208,209,234,235], the advection equation of the marker function (Eq. 1.2) is supplemented by equations for the derivatives of f, obtained by differentiating Eq. 1.2. Generally the equation for the derivative will be the same as Eq. 1.2, except that the right-hand side is not zero. However, the derivatives are first advected in the same way as f, and a correction for the effect of the nonzero right-hand side then added. To do the advection, a cubic polynomial is fitted to f and its derivatives and the solution profile obtained is translated by $\mathbf{U}\Delta t$ (in one dimension) to give the new nodal values of f and its derivatives. Even though a fully multidimensional version of the method has been developed and works well, the original method generally shows slight oscillations near a sharp interface but these can be reduced by the use of rational polynomials (the RCIP method) [2].

Another method, called phase-field method (PF) [31, 41, 71], is based on modifying the governing equations by incorporating some of the physical effects that are believed to govern the structure of a thin interface. Although the smoothed region between the different fluids is described in a thermodynamically consistent way, in actual implementation the thickness of the transition is much larger than it is in real systems and it is not clear whether keeping the correct thermodynamics in an artificially thick interface has any advantages over methods that model the behavior of the transition zone in other ways. The phase function, which identifies the different fluids, is updated by nonlinear advection-diffusion known as the Cahn-Hilliard equation. The diffusion terms smear an interface that is becoming thin due to straining, but an anti-diffusive part prevents the interface from becoming too thick if the interface is being compressed. The Navier-Stokes equations are also modified by adding a term that results in surface tension in the interface zone. The key to the modification is the introduction of a properly selected free-energy function, ensuring that the thickness of the interface remains of the same order as the grid spacing [2] .

However, the VOF is widely used since it guarantees reliable results and it is easy to implement, especially if phase change is involved in the phenomena under investigation. Additionally, VOF is often used in the algebraic version, rather than in the geometric one: geometric reconstruction in VOF represents a daunting task, especially if extended to 3D multiphase flow with phase change. Geometric-VOF in OpenFOAM has been recently developed under the name of `isoAdvector` [178]. However it does not support the modeling of cavitation. In the algebraic VOF, the interface capture is delegated to the numerical schemes applied to the advection equation as the "compressive schemes"and the Flux Correct Transport (FCT) method [243], or a blending of these method. One of these "blended method" is the Multi-dimensional Universal Limiter with Explicit Solution (MULES) available in OpenFOAM [225, 229].

The number of phase fraction equations solved in the VOF can vary depending on the number of fluid interfaces to capture. Fluid properties, such as density and viscosity, sharply vary across the interface of the different phases; finally, the rate of the transfer of mass is controlled by a source term. This phase-change source term can be built in several ways, but mainly three approaches are found to be used for this purpose:

- Bubble Models, which are built starting from simplifications of Rayleigh-Plesset (RP) equation for the bubble dynamics [129,162–164]; Several models such as Zwart-Behlarmi [245], Singhal [194], Schnerr-Sauer [182,241,242] Kunz [111] and Merkle [138], comes out from different applications of RP equation. Some of them, as Kunz and Merkle, has been developed mainly with the purpose of modeling cavitation in hydrofoil, while e.g.

Schnerr-Sauer has been conceived for modeling cavitation in the injectors.

- Homogeneous Equilibrium Model (HEM), based on the chemical equilibrium assumption among phases, makes use of a barotropic equation of state to compute the vapor void fraction. The HEM model is appropriate for bubbly flows, where interphase momentum exchange is fast and large enough to prevent slip between the vapor and the liquid [186]. Barotropic equations of state are widely used for complex simulations because they are simple to implement and numerically stable. On the other hand, one of the main limitations using a barotropic equation of state is in the underestimation of the vorticity change, because it does not account for the misalignment between the gradient of pressure and the gradient of density $(\nabla\rho \times \nabla p)/\rho^2$ [8], unless a non-linear correlation between pressure and density is used [141]. This contribution, called baroclinity, is important either in compressible fluids and in incompressible and inhomogeneous fluids and it is identified by the interface in a VOF method. Another challenge, when cavitation is modeled using barotropic models, can be found in the definition of an appropriate equation of state for the mixture, which includes air in addition to liquid and vapor. Capture the interface between coexisting miscible phases (fuel vapor and non-condensable gases in this work) in injector nozzles may be important in presence of swirl cavitation and hydraulic flip regime [81, 197], when a severe detachment of flow pockets [197, 198] transported away from the hole allows non-condensable gases to flow back into the nozzle. This happens both in simplified, straight, central hole injectors [200] and in particular in non-axial or asymmetric nozzles, in which large pressure fluctuations are observed.

- Homogeneous Relaxation Model (HRM) [24, 54, 145, 181], represents the phase transition by means of one empirical equation, which estimates the time scale of the phase change. The time scale evaluates the temporal extent of the deviation of the local condition from thermal equilibrium. In practical cases it is used to model both cavitation and flash-boiling [146]. HRM lies in between the two extremes of thermodynamic two-phase models represented by the homogeneous equilibrium model (HEM) and the homogeneous frozen model (HFM) [54]; In the case of HEM, the two phases are assumed to be mixed homogeneously with the heat transfer occurring spontaneously. In a real-world scenario of two-phase flows, such as bubbly flows, instantaneous heat transfer is not feasible. The other extreme, HFM, assumes zero heat transfer i.e. an infinitely long heat transfer time scale. HRM captures the in-between practical two-phase flow scenarios [181].

Several attempts have been made to combine the potentiality of the VOF with the simplicity of mixture model. In [142] the cavitating fluid mixture (liquid and vapor) is considered as primary phase while the non-condensable gas is the secondary phase; in this case, only one interface is captured by solving the phase-fraction equation for the non-condensable (NC) gas and the void fraction of the cavitating fluid mixture is equal to $(1 - \alpha_{nc})$; the volume fraction of the fuel vapor in the cavitating fluid mixture is estimated from the mixture composition, where the densities of the different components are computed through non-linear equations of state. In [223], a mass transfer model published in [183] was extended to an eight-equation two fluid-model to include non-condensable gases. Other methods to describe a three-phase flow while considering non-condensable gases are the use of the homogeneous mixture model combined with a barotropic two-fluid cavitation model [151], or the coupling of a two-fluid approach with VOF [61]. In the latter case, a two-fluid approach is used to describe the interaction between liquid and vapor in the nozzle, while VOF is used to model the jet formation. All the mentioned models have in common the aspect that they capture a single

interface between the non-condensable gases and a multi-component mixture [141, 169]. Recently, attempts to extend VOF in order to include air in transport and in cavitation models, have been done [239], [34] where each phase is considered as a compressible fluid but the cavitation model used [111, 182] has been previously developed under incompressible formulation. Conversely, in [240] each phase is considered incompressible and isothermal but the change of density is addressed at the interface and keeps in consideration the presence of the air inside cavitation model. A multi-fluid quasi-VOF model with the transport of three phases has been proposed also in [127], considering different velocities among phases and thus momentum transfer rate among interfaces. Although several authors have developed different methodologies to describe cavitation and the jet formation, any simple benchmark has not been found in literature in order to provide any further information about the mass conservation guaranteed by the cavitation model, either using the Rayleigh-Plesset equation [129, 163] or using a barotropic equation of state coupled with vapor quality. Some tests have been performed using a shock tube or Rayleigh bubble collapse test case [58, 63, 110, 118], which deal with surface capture regardless of mass conservation when the phase change occurs.

1.1.2 Internal nozzle flow and turbulence induced primary break-up

Turbulence-induced primary break-up is regarded as one of the most important break-up mechanisms of high-pressure sprays. The modeling of the small-scale interactions between phases and components has a significant impact on macroscopic flow properties, this is why LES turbulence modeling is often required. Large turbulent scales are resolved, while smaller scales are modeled. This separation of scales is explicitly or implicitly [89, 109] obtained by filtering out the small flow scales that cannot be properly represented by the mesh [1]; their effect must be modeled on the filtered field by means of the so called subgrid-scale (SGS) model. Although the multiphase nature of the problem, the use of LES models is also very popular in multiphase single-fluid VOF simulations [21, 42, 74, 92, 100, 130]. It is worth mentioning that several numerical studies have been led with Unsteady Reynolds Averaged Naviers Stokes (URANS) equations but this approximation can significantly underestimate the formation and the extent of cavitation due to an overestimated turbulent viscosity in the cavitating zones [46, 90, 91, 128, 170]. A comparative study between URANS and LES models [110] shows that URANS models fail to predict the incipient cavitation when the inlet flow pressure is not far from the pressure at the nozzle outlet, while LES is able to better capture the cavitation onset thanks to a better characterization of the different flow scales. A possible solution to overcome the limitations of URANS when applied to cavitation modeling consists in reducing the eddy-viscosity predicted by the turbulence model [170]; this approach looks promising, but its validity does not seem general; LES looks therefore to be the best approach for the problem discussed, despite of its high computational cost.

Combined with an accurate interface advection technique, LES offers the advantage that many physical processes can be resolved to a large extent which is in contrast to modeling the whole range of turbulent length and time scales in RANS [107]. Generally, the formalism of LES uses a filter defined as a product of a convolution. In order to have properties like commutation with derivation, it is necessary for the convolution Kernel to be independent of time and space [180]. However, when applying this filter on flow with discontinuities, such as shock waves, flames or interfaces, the jump relative to the discontinuity contributes to the sub-grid fluctuations [215]. Notwithstanding, typical sgs-scale models are founded on the assumptions that the subgrid fluctuations comes from turbulence only. Therefore, existing LES models does not take into account the sgs fluctuations contribution of the aforementioned discontinuity [215]. Contrary to the single-phase flow, multiphase flow LES is still in early development stage and the research community has not yet converged to a standard set of

equations [107]. These different sets of equations come from:

- the different multiphase model used to describe the topology of the system under investigation;
- the different approaches of the aforementioned sub-model;
- the different filter used to achieve the final filtered set of equations;

LES for "separated flows" (leaden flows and sprays) has been widely investigated and developed in the last two decades [26, 37, 48, 50, 60, 64, 113, 131, 137, 139, 147, 203, 236]. The formulation of LES applied to two-fluid model (Euler-Euler) was named Large-Eddy & Structure Simulation (LESS) in the work of Lakehal [115]. The original formulation is given in his previous work [48], and in the work of Sirignano [195] where he considered the heat transfer and chemical reactions as well. In the framework of the "separated flows", LES for indeformable free surfaces has been investigated in [35, 191]. On the other hand, LES of deformable interfaces has been initially studied by several authors [112, 215]. In particular in [114] the author named this kind of approach Large Eddy & Interface Simulation (LEIS), and outlined the main difference with LESS in [115]. This Kind of formulation was used in several studies: in [117] for spilling waves flow, in [123] for simulating steam injection in water pool, in [116] to simulate a turbulent channel flow laden with resolved bubbles clustered near the wall. The progress in hardware technology helped LEIS to gain popularity for the jet-atomization simulation [20, 44, 59, 83, 99, 144, 161]. LEIS is indeed capable of predicting primary breakup without necessarily introducing additional sub-grid scale models, which could be required for secondary breakup mechanisms [115]. While, full DNS of liquid jet primary and secondary breakup indeed requires massive mesh resolutions [193]. Recently, Lakehal [115] has proposed a new approach namely All Regime Multiphase flow model (ARM), with the purpose of describing wider range of complex multi-scale, multi-fluid flow problem. The fact that LEIS is consider to be able to predict accurately the primary breakup is in part true only when the smallest length scales associated to the interface deformation are bigger than the cut-off width of the filter (mesh size) [215]. This occurs only if the interface is enough tight and thus perfectly resolved. Under this condition single-phase LES model is used and specific jump conditions are not required (no additional sub-grid terms at the interface). However, when the smallest length scale associated to interface deformation is smaller than cut-off with of the filter (mesh size), the effect of the smallest coherent turbulent structures becomes important. Therefore, it must be defined the under-resolved interface and the jump conditions to take into account the subgrid transfers that originate from the turbulence and the interface coupling in the interfacial region [215]. This approach has been named Interface and Subgrid Scales (ISS) by the author and can be grouped under the LEIS approach. The authors proposes a two-step up-scaling methodology. Firstly, a common LES filter is applied to the set of equations. Only large scales of both turbulence and interfaces are represented. Specific sub-models take into account the effect of the subgrid fluctuations on the filtered velocity and on the filtered interface. At this level, interfaces are viewed as a continuous transition zones. They have a finite non-zero thickness [215]. However, at this "continuous" vision of the interface corresponds a level of description where the coupling between the two phases is difficult to capture numerically. Two numerical issues arise at this description level: the first one consists in avoiding numerical diffusion of the profile in order to keep constant the size of the transition zone. The second one is about the computational cost necessary to capture these profiles. Since filtered quantities evolve strongly within the transition zone, the mesh size required to capture these strong variations would be much smaller than the filter size [215]. This outcome is in contradiction with the LES approach.

Thus, a second up-scaling step is required and can be referred to as finding the sharp-interface limit of a diffuse interface model [215]. The approach used in the aforementioned work was based on the surface-excess theory [62], through the method of the matched asymptotic expansions.

All the approached here mentioned can be also gathered in three main group depending on the filter used [107]: the common LES filter, used in the first up-scaling of Toutant [215] and also shown in the work of Labourasse [112]. The Favre-filtering proposed as a valid alternative to the common filter, in the work of Labourasse [112] but also shown in the work of Liovic et al. [126]. This is the filter used in the LEIS formulation. In the end, the phase averaging or filtering, again shown in the work of Labourasse [112] and [115] (LESS), mainly used for particle laden flows. Comparing these works, it is evident that using different filters also different closures for the jump conditions at the interface are required [107].

Notwithstanding this, in the work of Anez [11] is reported that either averaging and filtering will smooth the liquid volume fraction profile and let undetermined the actual position of the interface. This happens always when an interface capturing method is used. In some cases the problem is solved forcing a sharp transition between liquid and gas at the interface, which is in contradiction with the averaging/filtering procedure; in other cases the problem is solved using a smooth transition. In both cases the interface position is lost. However, numerous successful works in the literature ignore these problems and used averaged/filtered approaches while keeping a sharp transition between phase [11]. For this, if only the dense region of primary break-up is considered, the interface capturing method used (in the present work the AVOF based on MULES) is enough to describe the problem if the mesh resolution is high. In fact, as suggested in [11], the turbulent liquid flux coming from the filtering of the equation is only used when ELSA is active (when the AVOF fails in the diluted spray region, far from nozzle outlet). Therefore, in the context of this work, the turbulent liquid flux will be neglected.

Like in most industrial applications, the combined effect of cavitation and turbulent flow lead to the formation of large-scale vortical structures, involving complex interactions among vortex structure and phase-change phenomena [14]. This interaction has been investigated in several works dealing with hydrofoils [15,101,210] or in Venturi-type sections [17,204,205]. The geometries investigated in both cases have allowed for further measurement: The structure of the two-phase flow inside the cavity was investigated in [204, 205]. In this work the authors succeeded in measuring local void fraction and the velocities inside the cavities. The 3D cavitation shedding-dynamic and cavitation-vortex interaction has been deeply investigated numerically in a particular hydrofoil shape [101]. On the other hand, nozzle scales ranges from some mm to few μm depending on the application. A detailed characterization of such large-scale vortical structures and interaction with phase-change phenomena, in a real injector geometry, is a difficult task, because they are highly transient and strongly affected by the nozzle geometry and the operating conditions of the injector. In addition, optical techniques, used to visualize the cavitating structures within the nozzle orifices and sac volume, are particularly sensitive to high density variation zones [135].

1.2 Objective, approach and structure of the thesis

The objective of this study is to present the development of a single-fluid isothermal VoF solver, belonging to the variable-density incompressible flow category. The solver is able to capture the evolution of three phases (liquid fuel, fuel vapor and non-condensable gases), two of which are miscible; phase change (fuel cavitation/condensation) is modeled through the Rayleigh-Plesset equation [77].

Two different test cases are proposed for the solver verification: a) a modified version of the test case presented in [94, 108] to explore the accuracy of the solver in capturing three interfaces without phase change; b) a novel one-dimensional test case, that consists of a 1D column half filled with liquid, where non-condensable gas (air) stays above the liquid. The hydrostatic pressure field resulting from the weight force of each fluid in quiescent state produces a pressure gradient Δp at the interface, letting the onset of cavitation in the liquid. Later on, condensation of the vapor is enforced to reach the initial state. The relative mass conservation error is monitored, together with other relevant quantities, to prove the conservativeness of the solver. Then, the solver has been initially validated on a three-dimensional internal-nozzle flow of a low pressure ($0.22\,MPa$) water-injection, whose experimental results are available in the literature at one operating point [199]. Finally, the solver has been tested and validated on two different configurations of transparent glass-nozzle replica of a real gasoline injector, that has been *ad-hoc* built by Continental Automotive Powertrain [5]. The replicas has been realized using a novel rapid prototyping technique recently demonstrated using laser-etched manufacturing in [5]. Validated simulation results are used to investigate the physical mechanism that drives the nozzle disturbances, that is naturally excited by air-liquid interaction, inner-nozzle turbulence, shear and string cavitation. In the latter test, the operative pressure was of $100\,bar$, and the fluid used was n-Heptane. These choices allow to have similar breakup and in-nozzle structure typical of a GDI injector. The discretization of the governing equations used in this study is based on the finite-volume approach as implemented in OpenFOAM [212]. Mass and momentum are solved using the pressure-implicit split-operator (PISO) algorithm [96]. The cavitation and the condensation term have been included in a semi-implicit formulation of the phase-fraction equations, where a flux corrected transport technique [230] is used to preserve boundedness of the solution; cavitation modeling follows the theory by Schnerr and Sauer [182] with the extensions proposed by Yuan [241]. The implemented three-phase solver is able to capture the interface of three phases, namely the liquid, the condensable gas (vapor) and the non-condensable gas (air). Turbulence is modeled using LES: large turbulent scales are resolved, while smaller scales are modeled [1, 121, 166].

This work is organized as follow: the theory of the three phase solver with phase change and the turbulence modeling is discussed in the Chapter 2. The verification of the solver is presented with the modified rising bubble test case [94] and the new one-dimensional liquid-column benchmark in chapter 3. In the same chapter, a first validation on a low pressure water injection test from literature is presented as well. Afterwards, the simulation setup for the glass nozzle injectors is presented in chapter 4. Finally, the internal nozzle flow and the primary breakup of the two glass nozzle configurations are shown respectively in chapter 5 and chapter 6. Main conclusions are summarized in Chapter 7.

CHAPTER 2

Numerical Modelling

2.1 Phase-fraction equations in the VOF solver

The cavitating fluid, the vapor and the non-condensable gas in the three-phase flow are represented in a single-fluid approximation as a mixture of phases, in which the phase-fraction distribution includes a sharp yet resolved transition between the phases.

An algebraic-type VoF method belonging to the family of the interface-capturing methods [87], is used to capture the interface; more specifically, the interface is visualized by the contour of a scalar function, that is assumed to be the iso-value (set to 0.5 in this work) of the void fraction of the phase considered. Each phase i has a partial volume V_i, that is a fraction of the volume V of the cell element ($V_i \subseteq V$) and it is defined by its local volume fraction $\alpha_i \in$ [0;1]:

$$\alpha_i = \frac{V_i}{V} \tag{2.1}$$

with:

$$\sum_{i=1}^{3} \alpha_i = 1 \tag{2.2}$$

a "mixture" density:

$$\rho = \sum_i \alpha_i \rho_i \tag{2.3}$$

and a "mixture" viscosity:

$$\mu = \sum_i \alpha_i \mu_i \tag{2.4}$$

It is important to note that the mixture density in the solver varies with pressure, through the phase transport equations. The effect of the heat transfer on the temperature, that should be

accounted by solving the energy equation, is not considered in the present work. Each phase has been considered incompressible. These hypothesis will be discussed in chapter 5. The complete system of equations for three-phase flow with phase change are the phase-fraction equations, that are written as:

$$\begin{cases} \dfrac{\partial \alpha_l}{\partial t} + \nabla \cdot (\mathbf{U}\alpha_l) = -\dfrac{S_\alpha}{\rho_l} \\ \dfrac{\partial \alpha_v}{\partial t} + \nabla \cdot (\mathbf{U}\alpha_v) = \dfrac{S_\alpha}{\rho_v} \\ \dfrac{\partial \alpha_{nc}}{\partial t} + \nabla \cdot (\mathbf{U}\alpha_{nc}) = 0 \end{cases} \tag{2.5}$$

In the system of equations (2.5), S_α is a source term to model the phase-change (cavitation or condensation) at the liquid interface through the cavitation model and couples the effects of the cavitation with the evolution of the interface directly:

$$S_\alpha = \frac{\rho_v \rho_l}{\rho + \alpha_{nc}(\rho_l - \rho_{nc})} \frac{D\alpha_v}{Dt} \tag{2.6}$$

In Eq. (2.6) the subscripts *l* and *v* are adopted for liquid and vapor (that are involved in the phase change) respectively, while the subscript *nc* is adopted for non-condensable gases. It is important to note that the closure of the system of equations (2.5) in presence of a cavitation/condensation source term S_α, requires to explicitly resolve the transport of a third phase fraction (non-condensable phase), in order to include a cavitation model and to couple the equations with the compatibility condition (2.2); in this way, the system is closed and implicitly bounded, thanks to (2.2). In absence of source terms, 3-phase VOF solvers usually calculate the void fraction of non-condensable gases directly from Eq. (2.2), that is sufficient for closure only in that case. These aspects are discussed in detail in App. A and App. B, where the derivation of the full system of equations is shown and the formulation of the source terms for the phase change is also described.

Counter-gradient transport in VOF

In the FV framework, numerical diffusion, which is very high in the transport term in second-order spatial discretization, "smears" the sharp liquid-gas interface. In OpenFOAM, the strategy commonly followed in multiphase VOF solvers to model the transport of the void fraction consists in adding a convection term which compresses the interface and preserves boundedness: this is similar to what is done for the treatment of the scalar-flux second-moment closure, used for the "counter-gradient" transport in some complex combustion models describing the dynamic of turbulent flames [188]. In the VOF treatment, a common closure used for counter-gradient transport has the form:

$$\nabla \cdot [\mathbf{U}_c \, \alpha \, (1 - \alpha)] \tag{2.7}$$

where $\mathbf{U}_c$ is the compression velocity at the interface between the phases, which is a consequence of the different densities and the term $\alpha(1-\alpha)$ ensures boundedness [230]. In the VOF solver used, the compression velocity is modeled as:

$$\mathbf{U}_c = c_\alpha |\mathbf{U}| \hat{\mathbf{n}}_{ij} \tag{2.8}$$

The employed formulation of the compression velocity is:

$$\mathbf{U}_c = \min \left[c_\alpha |\mathbf{U}|, \max(|\mathbf{U}|) \right] \hat{\mathbf{n}}_{ij} \tag{2.9}$$

The discretized form of Eq. (2.7) is a flux (counter-gradient term, Eq. 2.61) computed at the cell faces using a Total Variation Diminishing (TVD) scheme. In this work, the TVD scheme used is called `interfaceCompression` scheme [230], in which the limiter ψ to compute the flux is defined as:

$$\psi(\phi_P, \phi_N) = min\left\{ max\left[1 - max\left(\sqrt{1 - 4 \cdot \phi_P \cdot (1 - \phi_p)}, \sqrt{1 - 4 \cdot \phi_N \cdot (1 - \phi_N)} \right), 0 \right], 1 \right\} \tag{2.10}$$

where ψ is bounded between 0 and 1; ϕ_P is the value of the variable, defined at the cell center, where the limiter is applied; ϕ_N is the value of the same variable in the neighboring cells.

The compression rate should be set in order to ensure interface sharpness. Higher values of the compression rate might introduce numerical instability or slow convergence. The term C_α in Eq. (2.9) is the compression coefficient and it is set to unity in this work. The compression coefficient C_α is a binary coefficient which switches interface sharpening on ($C_\alpha \geq 1$) or off (C_α=0). With C_α set to 0 for a given phase pair, there is no imposed interface compression resulting in phase dispersion. If C_α is set to 1, sharp interface capturing is applied and VOF-style phase fraction capturing occurs, forcing interface resolution on the mesh. If a compression term is not applied, the interface will be very diffuse. In most applications, it is suggested a c_α of the order of unity [230]. A complete discussion about the interface compression method and the compression coefficient can be found in [225].

To ensure that the compression term does not bias the solution, it should only introduce flow of α, normal to the interface, in the direction of the volume average interface normal $\hat{\mathbf{n}}_{ij}$. For a three-phase solver it has been computed as net gradient of the phase $i - th$ at the interface [212]:

$$\hat{\mathbf{n}}_{ij} = \frac{\alpha_j \nabla \alpha_i - \alpha_i \nabla \alpha_j}{||\alpha_j \nabla \alpha_i - \alpha_i \nabla \alpha_j||} \tag{2.11}$$

In the convention adopted (see Fig. 2.1), $\hat{\mathbf{n}}_{ij}$ always points towards the lighter fluid. A

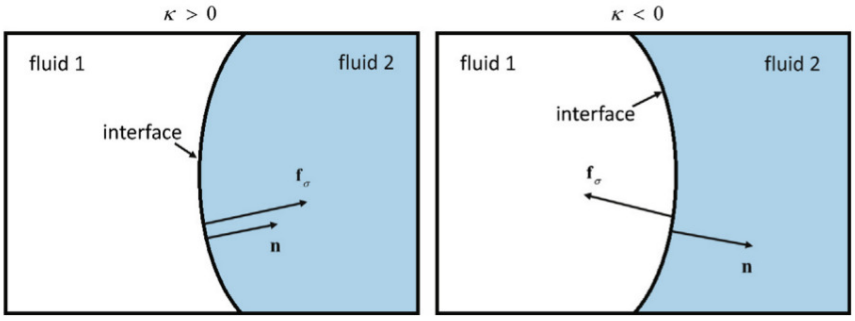

Figure 2.1: *Schematic of the interface between two fluids.* $\mathbf{f}_\sigma$ *is the surface force per unit inter-facial area ;* $\hat{\mathbf{n}}$ *and* κ *are namely the interface normal and the interface curvature. According to the sign convention adopted,* $\mathbf{f}_\sigma$ *is always oriented towards the concave interface and* $\hat{\mathbf{n}}$ *always points towards lighter couple of fluids [16].*

common practice is to use the compression term only where surface sharpness wants to be preserved: in the proposed formulation, the convection-based term is used only to compress the interface between the immiscible (liquid fuel) and the miscible phases (fuel vapor and non-condensable gases). The phase-fraction equations for the three phase VOF take the form:

$$\begin{cases} \dfrac{\partial \alpha_l}{\partial t} + \nabla \cdot (\alpha_l \mathbf{U}) + \underbrace{\nabla \cdot (\alpha_l \alpha_v \mathbf{U}_{c_{lv}}) + \nabla \cdot (\alpha_l \alpha_{nc} \mathbf{U}_{c_{lg}})}_{\text{compression term, liquid-vapor + liquid-gas}} = -\dfrac{\rho_v}{\rho + \alpha_{nc}(\rho_l - \rho_{nc})} \dfrac{D\alpha_v}{Dt} \\ \dfrac{\partial \alpha_v}{\partial t} + \nabla \cdot (\alpha_v \mathbf{U}) + \underbrace{\nabla \cdot (\alpha_l \alpha_v \mathbf{U}_{c_{lv}})}_{\text{compression term, liquid-vapor}} = \dfrac{\rho_l}{\rho + \alpha_{nc}(\rho_l - \rho_{nc})} \dfrac{D\alpha_v}{Dt} \\ \dfrac{\partial \alpha_{nc}}{\partial t} + \nabla \cdot (\alpha_{nc} \mathbf{U}) + \underbrace{\nabla \cdot (\alpha_l \alpha_{nc} \mathbf{U}_{c_{lg}})}_{\text{compression term, liquid-noncondensable gas}} = 0 \end{cases} \tag{2.12}$$

In Eqs. 2.12, no additional terms to model interface compression between miscible phases are used; numerical diffusion is assumed to be sufficient to model the small diffusion of mass at the interface when convection is dominant (i.e. with large values of Reynolds and low Schmidt numbers). Different modeling approaches for sub grid-scale computation of the mass transfer are only proposed for low-Re and high Schmidt number flows [28,67,228]. The term $\frac{D\alpha_v}{Dt}$ in Eqs. (2.12) includes the effects of the phase change (cavitation/condensation) and it is therefore linked to the cavitation/condensation model.

2.2 Mass conservation in the VOF solver

During cavitation and condensation, liquid and vapor phase are both affected by a strong variation of density. The latter influences significantly the numerics of the segregated solver. Therefore, to ensure the stability of the solver under the aforementioned condition, the continuity equation is used in its non-conservative form as suggested in [202] and which it has already been used [182, 187, 240]:

$$\nabla \cdot \mathbf{U} = -\frac{1}{\rho} \frac{D\rho}{Dt} \tag{2.13}$$

The advantage of using volume fluxes rather than mass fluxes (conservative form) consists of having continuous volume fluxes at the interface, thus favoring the solution of pressure correction equation. With phase change and three phases, Eq. (2.13) can be rewritten as:

$$\nabla \cdot \mathbf{U} = \frac{\rho_l - \rho_v}{\rho + \alpha_{nc}(\rho_l - \rho_{nc})} \frac{D\alpha_v}{Dt} \tag{2.14}$$

The derivation of the RHS of Eq. (2.14) is reported in App. A.

2.3 Momentum conservation in the VOF solver

The momentum equation reads:

$$\frac{\partial (\rho \mathbf{U})}{\partial t} + \nabla \cdot (\rho \mathbf{U} \otimes \mathbf{U}) = -\nabla \hat{p} + \nabla \cdot \boldsymbol{\tau} + \mathbf{f}_\sigma + S_U - \mathbf{g} \cdot \mathbf{x} \nabla \rho \tag{2.15}$$

where $\hat{p}$ is a modified pressure, that is calculated by removing the hydrostatic part from the static pressure p, $\boldsymbol{\tau}$ is deviatoric the stress tensor, S_U includes the source terms, $\mathbf{f}_\sigma$ is the surface force per unit inter-facial area calculated at the fluid interface in the control volume, $\mathbf{g}$ is the gravitational acceleration. The term $-\mathbf{g} \cdot \mathbf{x} \nabla \rho$ in the RHS of Eq. (2.15) is a consequence of the removal of the modified pressure $\hat{p}$ from the static pressure:

$$\hat{p} = p - \rho \mathbf{g} \cdot \mathbf{x} \tag{2.16}$$

which yields:

$$\nabla \hat{p} = \nabla p - \nabla(\rho \mathbf{g} \cdot \mathbf{x}) = \nabla p - \rho \mathbf{g} \nabla \mathbf{x} - \mathbf{g} \cdot \mathbf{x} \nabla \rho \tag{2.17}$$

so:

$$-\nabla p + \rho \mathbf{g} \nabla \mathbf{x} = -\nabla \hat{p} - \mathbf{g} \cdot \mathbf{x} \nabla \rho \tag{2.18}$$

The use of $\hat{p}$ in the momentum equation favors a more stable solution of the density jumps at the sharp interface and simplifies the implementation and setup of the boundary conditions on pressure. In Eq. (2.15), $\mathbf{f}_\sigma$ is defined as:

$$\mathbf{f}_\sigma = \sigma \, \kappa \, \hat{\mathbf{n}} \, \delta \left(\mathbf{x} - \mathbf{x_s} \right) \tag{2.19}$$

where σ is the fluid surface tension coefficient in [N/m], $\hat{\mathbf{n}}$ is the unit vector normal to the liquid interface, whose center is located in $\mathbf{x}_s$, δ is the Dirac function to ensure that the force is applied only at the liquid interface, κ is the interface curvature $[m^{-1}]$, which is defined as:

$$\kappa \equiv -\nabla \cdot (\hat{\mathbf{n}} \cdot \mathbf{S}_f) \tag{2.20}$$

Where $\mathbf{S_f}$ is the cell faces surface area vector defined as the scalar product between the cell faces normal and the cell face area. In Eq. (2.19), $\mathbf{f}_\sigma$ is always oriented towards the concave interface (Fig. 2.1). It is important to note that the interface curvature in Eq. (2.19) and (2.20) used is the one of the interface of the phase with highest density (liquid in this case):

$$\hat{\mathbf{n}} = \frac{\nabla \alpha_l}{\| \nabla \alpha_l \|} \tag{2.21}$$

The surface tension coefficient σ appearing in Eq. (2.19), has been written as an average of the surface tensions weighted with the phase-fractions computed in the control volume:

$$\sigma = \frac{\alpha_v \sigma_{lv} + \alpha_{nc} \sigma_{lnc}}{\alpha_v + \alpha_{nc}} \tag{2.22}$$

where σ_{lv} is the surface tension between the liquid fuel and fuel vapor, while σ_{lnc} is the surface tension between liquid fuel and non-condensable gases. Similarly to viscosity and density, the surface tension coefficient σ for the mixture is computed as a weighted-average, where the weighting factors are the void fractions; the concept of miscible phases implies that their surface tension coefficient is zero, so σ does not include the surface tension between fuel vapor and non-condensable gases. Finally, to compute the surface tension force, the term $\hat{\mathbf{n}} \, \delta \left(\mathbf{x} - \mathbf{x}_s \right)$ in Eq. (2.23) must be also modeled. The Continuous Surface Force (CSF) approximation [29] is therefore used, yielding to:

$$\mathbf{f}_{\sigma_i} = \sigma \kappa \nabla \alpha_i \tag{2.23}$$

It must be remarked that CSF is the simplest model commonly used in VOF solvers. Despite its popularity, it has been proven (in surface tension dominated/driven flow) that it does not guarantee momentum conservation [167], leading to the onset of physically unrealistic velocities at the interface. These parasitic currents can be relevant when the flow is highly dominated by surface tension forces. For that reason, several different formulations as the Continuum-Surface-Stress (CSS) approximation [78] and the Ghost fluid Method

(GFM) [65] have been proposed. The former is based on the integral formulation rather than on the volumetric one, and gives more advantages such as inclusion of the tangential stresses due to a variable surface tension (i.e Marangoni Effect). However, since it was only applied within high-order (spline-based) front-tracking interface description framework [4,168], CSF is rather preferred for its simplicity, especially if surface tension is not dominant. On the contrary, the GFM is a technique used to handle sharp transitions and in the case of capillary forces, it explicitly introduces the singular pressure jump condition into the discretization equations. Each phase is then artificially extended across the interface, producing ghost cells which contain properties of the extrapolated phase used for the discretization scheme, removing the tendency for the adjacent inter-facial cells to diffuse due to the sharp transition. This method has been also extended by several authors [52, 150, 206] but always based on LS and CLSVOF since they can compute in a more accurate way the interface curvature [88].

2.4 Cavitation modeling

Cavitation may consist either of small bubbles (bubbly-flow cavitation) or may contain large pockets of vapor (cloud cavitation) [30]; with a sharp interface-capturing method, the bubble must be larger than the cell to be accurately resolved, otherwise a sub-model is needed.

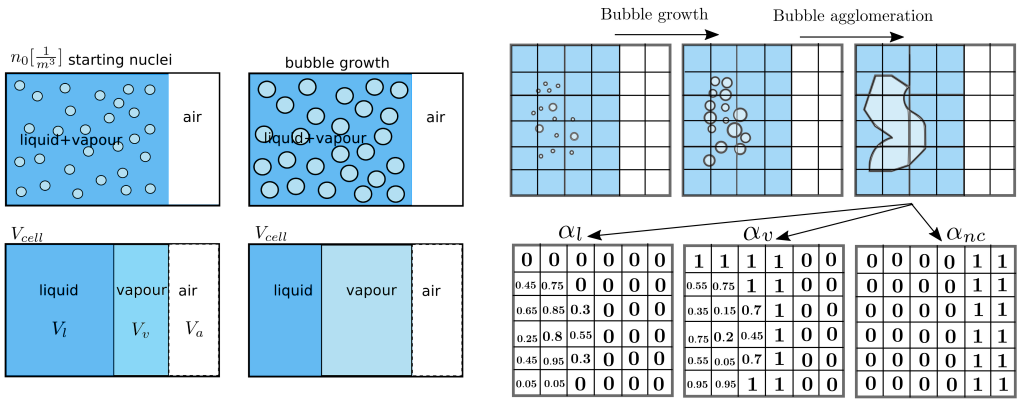

(a) *Single cell sketch of dispersed VOF-RP* **(b)** *Simplified sketch of dispersed VOF-RP*

Figure 2.2: *Simplified representation of the current VOF-RP coupled model with dispersed/diluted and blob/aggregated vapor regimes.*

The aim of the model is to propose a smooth transition between two regimes: when the thermodynamic state of the liquid corresponds to a phase change, bubbles will grow around nucleons according to Rayleigh-Plesset dynamic and is acting through the cavitation source term (bubble dispersed/diluted regime). Later on, when the thermodynamic state corresponds to an intense, maintained, localized phase change, the individual bubbles will collapse into a larger spot that can be resolved on the discretized domain (blob/agglomerated regime). The dynamic of this large vapor blob, including its interface dynamic (tension forces and compactness) can be captured thanks to the interface capturing VOF.

In the approach followed in this work, a sub-model for cavitation is always used to provide an expression for the term $\frac{D\alpha_v}{Dt}$. This is required to close the system of governing equations (2.12), (2.14) and (2.15).

The rates of fuel vaporization and condensation are determined by a simplification of the Rayleigh-Plesset equation which assumes spherical bubbles of radius R subject to uniform pressure variations. Spherical bubbles are then represented by a fraction of the vapor phase

in the computational cell; from [187] and considering that liquid, vapor and non-condensable gases may coexist in a control volume, it follows:

$$V_v = N_b \frac{4}{3}\pi R^3 = n_0 V_l \frac{4}{3}\pi R^3 \tag{2.24}$$

where V_v and V_l are respectively the volume of the vapor and the liquid in the computational cell of volume V, N_b is the number of spherical bubbles of radius R in the computational cell and n_0 is defined as the bubble concentration per unit volume of pure liquid. The use of relations of Eq. (2.24) requires an a-priori knowledge of the nuclei concentration n_0 and an estimation of their initial radius R. Some measurements of cavitation nuclei were carried out a few decades ago on water using Cavitation Susceptibility Meter (CSM) and Holographic measurement [49]; even though the holographic measurements have proven to be more accurate than CSM, both techniques cannot detect bubbles at the sub-micrometer scale and they may omit many additional nuclei. In addition, the growth of the smallest bubbles is affected by the surface tension, that is not considered [162] to have a simple correlation describing the bubble growth. A proper estimation of the surface tension would require a numerical approach to determine the bubble growth rate, but it would require a significant increase of the computational cost [162]. Nucleation can be originated either by homogeneous and by heterogeneous nuclei as well (air dissolved in the liquid, particles, etc) [30, 226]. For the sake of simplicity, only homogeneous nuclei have been considered in the present model; as a consequence, it is not straightforward to set the value of this parameter for the case of high-pressure injection, since measurements of nuclei are not available in literature. For fuel injection, it is usually accepted that the number of nuclei, due to impurities, are large enough that they should not influence the results of the model. Dissolved gas could also contribute [194], but as a first step, in the present study they are not considered as nucleon precursors. The complete expression for the rate of fuel vaporization, derived in App. B, is:

$$\frac{D\alpha_v}{Dt} = \begin{cases} \dfrac{3\alpha_v \frac{DR}{Dt}}{R + R^4 \frac{4}{3}\pi n_0 \left[\frac{\rho+\alpha_{nc}(\rho_v-\rho_{nc})}{\rho+\alpha_{nc}(\rho_l-\rho_{nc})}\right]} = -\dfrac{3\alpha_v max(p-p_{sat},0)\sqrt{\frac{2}{3}\frac{1}{\rho_l|p-p_{sat}|}}}{R + R^4 \frac{4}{3}\pi n_0 \left[\frac{\rho+\alpha_{nc}(\rho_v-\rho_{nc})}{\rho+\alpha_{nc}(\rho_l-\rho_{nc})}\right]} = \alpha_v \left(\frac{D\alpha_v}{Dt}\right)^+ & if\ p > p_{sat} \\ \dfrac{\alpha_l 4\pi n_0 R^2 \frac{DR}{Dt}}{1 + R^3 \frac{4}{3}\pi n_0 \left[\frac{\rho+\alpha_{nc}(\rho_v-\rho_{nc})}{\rho+\alpha_{nc}(\rho_l-\rho_{nc})}\right]} = -\dfrac{\alpha_l 4\pi n_0 R^2 min(p-p_{sat},0)\sqrt{\frac{2}{3}\frac{1}{\rho_l|p-p_{sat}|}}}{1 + R^3 \frac{4}{3}\pi n_0 \left[\frac{\rho+\alpha_{nc}(\rho_v-\rho_{nc})}{\rho+\alpha_{nc}(\rho_l-\rho_{nc})}\right]} = \alpha_l \left(\frac{D\alpha_v}{Dt}\right)^- & if\ p < p_{sat} \end{cases} \tag{2.25}$$

which can be rewritten as a net contribution between cavitation and the condensation:

$$\frac{D\alpha_v}{Dt} = \left(\frac{D\alpha_v}{Dt}\right)^+ \alpha_v + \left(\frac{D\alpha_v}{Dt}\right)^- \alpha_l \tag{2.26}$$

In the transport equation for the liquid phase α_l in the system (2.12) $\frac{D\alpha_v}{Dt}$ is replaced by rewriting Eq. (2.26) in the form:

$$\begin{aligned}\frac{D\alpha_v}{Dt} =& \left(\frac{D\alpha_v}{Dt}\right)^{+}\alpha_v + \left(\frac{D\alpha_v}{Dt}\right)^{-}\alpha_l \\ =& \left(\frac{D\alpha_v}{Dt}\right)^{+}(1-\alpha_{nc}-\alpha_l) + \left(\frac{D\alpha_v}{Dt}\right)^{-}\alpha_l \\ =& \left[\left(\frac{D\alpha_v}{Dt}\right)^{-} - \left(\frac{D\alpha_v}{Dt}\right)^{+}\right]\alpha_l + \left(\frac{D\alpha_v}{Dt}\right)^{+}(1-\alpha_{nc})\end{aligned} \tag{2.27}$$

while in the transport equation of the vapor phase α_v, still in the system (2.12), Eq. (2.26) is manipulated to write $\frac{D\alpha_v}{Dt}$ in the form:

$$\begin{aligned}\frac{D\alpha_v}{Dt} =& \left(\frac{D\alpha_v}{Dt}\right)^{+}\alpha_v + \left(\frac{D\alpha_v}{Dt}\right)^{-}\alpha_l \\ =& \left(\frac{D\alpha_v}{Dt}\right)^{+}\alpha_v + \left(\frac{D\alpha_v}{Dt}\right)^{-}(1-\alpha_v-\alpha_{nc}) \\ =& \left[\left(\frac{D\alpha_v}{Dt}\right)^{+} - \left(\frac{D\alpha_v}{Dt}\right)^{-}\right]\alpha_v + \left(\frac{D\alpha_v}{Dt}\right)^{-}(1-\alpha_{nc})\end{aligned} \tag{2.28}$$

Both in Eq. (2.27) and (2.28), the first term in the square brackets is the coefficient of a part of the equation that will be implicitly solved, while the remaining part is explicitly solved. As it will be explained in the further sections, solving the source term in a semi-implicit fashion favors improved numerical stability and boundedness. The final form of the system describing the transport of the three phase fractions reads:

$$\begin{cases} \frac{\partial \alpha_l}{\partial t} + \nabla\cdot(\alpha_l\mathbf{U}) + \underbrace{\nabla\cdot(\alpha_l\alpha_v\mathbf{U}_{c_{lv}}) + \nabla\cdot(\alpha_l\alpha_{nc}\mathbf{U}_{c_{lnc}})}_{\text{compression term, liquid-vapor + liquid-gas}} = -\frac{\rho_v}{\rho+\alpha_{nc}(\rho_l-\rho_{nc})}\left\{\left[\left(\frac{D\alpha_v}{Dt}\right)^{-} - \left(\frac{D\alpha_v}{Dt}\right)^{+}\right]\alpha_l + \left(\frac{D\alpha_v}{Dt}\right)^{+}(1-\alpha_{nc})\right\} \\ \frac{\partial \alpha_v}{\partial t} + \nabla\cdot(\alpha_v\mathbf{U}) + \underbrace{\nabla\cdot(\alpha_l\alpha_v\mathbf{U}_{c_{lv}})}_{\text{compression term, liquid-vapor}} = \frac{\rho_l}{\rho+\alpha_{nc}(\rho_l-\rho_{nc})}\left\{\left[\left(\frac{D\alpha_v}{Dt}\right)^{+} - \left(\frac{D\alpha_v}{Dt}\right)^{-}\right]\alpha_v + \left(\frac{D\alpha_v}{Dt}\right)^{-}(1-\alpha_{nc})\right\} \\ \frac{\partial \alpha_{nc}}{\partial t} + \nabla\cdot(\alpha_{nc}\mathbf{U}) + \underbrace{\nabla\cdot(\alpha_l\alpha_{nc}\mathbf{U}_{c_{lnc}})}_{\text{compression term, liquid-noncondensable gas}} = 0 \end{cases} \tag{2.29}$$

2.5 Turbulence modeling

The LES governing equations for the aforementioned multiphase topology and AVOF approach used are obtained by filtering the continuity equation 2.13, the momentum equation (Eq. 2.15) and the void fractions equations (Eq. 2.29), using the filtering kernel $G(\mathbf{x},\mathbf{x}'')$. For an arbitrary variable ϕ is adopted:

$$\overline{\phi(\mathbf{x},t)} = \int_\Omega \phi(\mathbf{x}'',t)G(\mathbf{x},\mathbf{x}'')d\mathbf{x}'' \tag{2.30}$$

The approach starts selecting a filtering function and the cut-off width in order to resolve all the eddies with a length scale greater than the chosen cut-off width. The cut-off is intended as an indicative measure of the size of the eddies resolved. When discretization is applied in FVM, it is useless to select a cutoff width smaller than grid size. The most common selection

is to take the cut-toff width to be of the same order as the grid size, for instance, the cubic root of the grid cell volume:

$$\Delta = \sqrt[3]{\Delta_x \Delta_y \Delta_z} \tag{2.31}$$

Using the above filter definitions, the sub-grid part (non-resolved) ϕ'' is expressed as:

$$\phi''(\mathbf{x}, t) = \phi(\mathbf{x}, t) - \overline{\phi(\mathbf{x}, t)} \tag{2.32}$$

Hence, the filtered continuity equation reads:

$$-\frac{1}{\overline{\rho}} \frac{D\overline{\rho}}{Dt} = \nabla \cdot \overline{\mathbf{U}} + \nabla \cdot \tau_{\rho u} \tag{2.33}$$

where $\overline{\rho} = \rho_l \overline{\alpha_l} + \rho_v \overline{\alpha_v} + \rho_{nc} \overline{\alpha_{nc}}$ is the filtered mixture density, while $\tau_{\rho u}$ denotes the unresolved interface mass-flux at the phase interface. The filter is then applied to the momentum equation (Eq. 2.15). The complete form of the filtered momentum equation reads:

$$\frac{\partial(\overline{\rho}\overline{\mathbf{U}} + \tau_{\rho u})}{\partial t} + \nabla \cdot (\overline{\rho}\overline{\mathbf{U}} \otimes \overline{\mathbf{U}} + \tau_{sgs}) = -\nabla \overline{\rho} + \nabla \cdot \left(\overline{\mu}\left[\nabla \overline{\mathbf{U}} + (\nabla \overline{\mathbf{U}})^T - \tfrac{2}{3}(\nabla \cdot \overline{\mathbf{U}})\mathbf{I}\right] + \tau_\mu\right) + \sigma \delta_s \widehat{\mathbf{n}} \nabla_s \cdot \widehat{\mathbf{n}} + \tau_{f_\sigma} - \mathbf{g} \cdot \mathbf{x} \nabla \bar{\rho} \tag{2.34}$$

The filtering of momentum equation under the single-fluid model leads to some additional terms: in addition to the classical single-phase LES subgrid stress tensor τ_{sgs}, now $\tau_{\rho u}$, τ_μ and τ_{f_σ} appear. *a-priori* analysis of these terms and their possible modeling are available in several works [112,115,125,213]. $\tau_{\rho u}$ is the same term appearing in Eq. 2.33 . In the research community this term is still under investigation and models are not available yet. Thus, it is commonly neglected. τ_μ comes from the non-linearity of the deviatoric stress tensor. Being the mixture viscosity computed as:

$$\mu = \sum_{i=1}^{3} \alpha_i \mu_i \tag{2.35}$$

It follows that when LES filters is applied:

$$\overline{\mu} = \mu - \mu'' \tag{2.36}$$

the variation of mixture density and mixture cinematic-viscosity must be considered at the interface, resulting in an additional subgrid term τ_μ. In [115] is stated to be a term traditionally neglected, without rigorous arguments, also in variable-density compressible flows. Also in [11] it is pointed out the presence of this term but it is stated to be still under investigation. For this reason τ_μ is commonly neglected as well. The term τ_{f_σ} denotes the Sub-grid Curvature Tensor (SCT) and appears in Eq. 2.34 as the result of non-linearity of curvature κ (or the normal vector $\hat{\mathbf{n}}$). Published works on two-phase interfacial flows (without phase-change) [112, 215, 221] proved that in specific flow configurations [221], known as "separation of phase", those sub-grid terms cannot be neglected. At least three possible closure terms have been published to model the Sub-grid Curvature Tensor: the Sub-Grid Surface Dynamics (SGSD) model [84], the Sub-grid curvature model [126] and the ADM-τ [12, 13]. It must be remarked that the "separation of phase" test [221], used for the sub-grid interface analysis, is dominated by the surface tension forces effects. According to authors' research, no published works studied the contribution of the sub-grid interface with high speed flows including phase-change: such a study would therefore represent a big step towards an improved mathematical description of the formulation of LES single-fluid VOF solvers with phase-change.

On the contrary, τ_{sgs} requires modeling for the equation to be closed. In the present work SGS tensor is modeled as:

$$\tau_{sgs_{ij}} = \frac{1}{3}\tau_{sgs_{kk}}\delta_{ij} - \mu_t\left(\frac{\partial\overline{U_i}}{\partial x_j} + \frac{\partial\overline{U_j}}{\partial x_i}\right) \tag{2.37}$$

Where δ_{ij} is the Kronecker delta, and μ_t is the SGS turbulent eddy viscosity computed with the Wall Adapting Local Eddy (WALE) model [148]. It has the advantage of reproducing the laminar-turbulent transition and the wall asymptotic y^3 behavior ($\mu_t = O(y^3)$), that are significant for the revealing of the turbulence-cavitation interactions in wall bounded flows [180].

$$\mu_t = \overline{\rho}L_s^2\frac{(\mathbf{S}_{ij}^d\mathbf{S}_{ij}^d)^{3/2}}{(\overline{\mathbf{S}}_{ij}\overline{\mathbf{S}}_{ij})^{5/2} + (\mathbf{S}_{ij}^d\mathbf{S}_{ij}^d)^{5/4}} \tag{2.38}$$

Where $\overline{\mathbf{S}}_{ij}$ is the filtered rate-of-strain tensor, and $\mathbf{S}_{ij}^d$ and L_s^2 are defined respectively as follows:

$$\mathbf{S}_{ij}^d = \frac{1}{2}(\overline{g}_{ij}^2 + \overline{g}_{ji}^2) - \frac{1}{3}\delta_{ij}\overline{g}_{kk}^2 \tag{2.39}$$

with $\overline{g}_{ji} = \frac{\partial\overline{U_i}}{\partial x_j}$, and

$$L_s = min[\kappa d, C_w(\Delta V)^{1/3}] \tag{2.40}$$

L_s is the subgrid scale mixing length, κ is the von Karman constant, d is the wall distance of the cell center, ΔV is the cell volume, and C_w is the WALE constant. Then, applying the same filter on the Eqs. 2.29, they now read:

$$\begin{cases} \dfrac{\partial\overline{\alpha_l}}{\partial t} + \nabla\cdot(\overline{\mathbf{U}}\overline{\alpha_l}) + \nabla\cdot\tau_{\alpha_l} + \nabla\cdot(\overline{\alpha_l}\,\overline{\alpha_v}\mathbf{U}_{c_{lv}}) + \nabla\cdot(\overline{\alpha_l}\,\overline{\alpha_{nc}}\mathbf{U}_{c_{lnc}}) = -\dfrac{\overline{S_\alpha}}{\rho_l} \\ \dfrac{\partial\overline{\alpha_v}}{\partial t} + \nabla\cdot(\overline{\mathbf{U}}\overline{\alpha_v}) + \nabla\cdot\tau_{\alpha_v} + \nabla\cdot(\overline{\alpha_l}\,\overline{\alpha_v}\mathbf{U}_{c_{lv}}) = \dfrac{\overline{S_\alpha}}{\rho_v} \\ \dfrac{\partial\overline{\alpha_{nc}}}{\partial t} + \nabla\cdot(\overline{\mathbf{U}}\overline{\alpha_{nc}}) + \nabla\cdot\tau_{\alpha_{nc}} + \nabla\cdot(\overline{\alpha_l}\,\overline{\alpha_{nc}}\mathbf{U}_{c_{lnc}}) = 0 \end{cases} \tag{2.41}$$

In Eqs. 2.41, no additional terms to model interface compression between miscible phases are used; numerical diffusion is assumed to be sufficient to model the small diffusion of mass at the interface when convection is dominant (i.e. with large values of Reynolds and low Schmidt numbers). Different modeling approaches for sub grid-scale computation of the mass transfer are only proposed for low-Re and high Schmidt number flows [28, 67, 228]. Depending on the kind of the filter applied, additional terms may arise or not from the second term of LHS [107]. Using the common LES filter:

$$\nabla\cdot(\overline{\mathbf{U}\alpha_i}) = \nabla\cdot(\overline{\mathbf{U}}\overline{\alpha_i}) + \nabla\cdot\tau_{\alpha_i} \tag{2.42}$$

τ_{α_i} are the so called *turbulent phase flux* [11], also know as Subgrid Mass Transfer (SMT) terms, that represent the transport of the i-th fraction induced by the velocity fluctuations. In [214, 221] it is reported that in some cases, especially for dispersed flow (like the "separation of phase" test case), it may have the same order of magnitude of the filtered resolved advection term. In [11] the authors try to propose model for the unclosed terms issued from the averaging/filtering process but also to propose an Interface Resolve Quality (IRQ) sensor to evaluate when it is necessary to consider these models. However, these work [11] is related to two phase flow without phase-change phenomena, and in particular it focuses on the

magnitude and relevance of these terms in the atomization problem, far from the nozzle tip (dilute region).

As mentioned above, in the dense spray region the AVOF approach employed is enough to describe the interface among liquid and air, and thus τ_{α_l} and $\tau_{\alpha_{nc}}$ could be neglected.

Concerning the vapor phase-fraction α_v, this is hardly subject to high-frequency fluctuation according to the definition of Eq. (B.5), because the pressure fluctuations only acts directly on the time-derivative of the bubble radius R [42]. Since cavitation is modeled by several micro-bubbles, their status is little sensitive to pressure pulsation rather than to the mean pressure distribution; for this reason, the sub-grid scale related to the SMT (*turbulent phase fluxes*) should be negligible with respect to the filtered vapor volume fraction field in the cavitation regions, where the mean pressure is relatively uniform. Moreover, in the regions with sharp pressure gradient, the vapor volume fraction is itself small enough to allow SMT to be neglected.

Finally, when the filter is applied to the phase-change source term S_α, it produces some additional subgrid terms:

$$\overline{S_\alpha} = \tau_{S_\alpha} + \left(\frac{\rho_v \rho_l}{\overline{\rho} + \overline{\alpha_{nc}}(\rho_l - \rho_{nc})} \frac{D\overline{\alpha_v}}{Dt} \right) \tag{2.43}$$

The first one is denoted by τ_{S_α} and it comes from the non-linearity of S_α, while the second one is denoted by $\frac{D\overline{\alpha_v}}{Dt}$. Looking at the definition of $\frac{D\alpha_v}{Dt}$ in Eq. 2.25, it is clear that this term is strongly non-linear. For this reason, when the filter is applied to Eq. 2.25, two additional sub-grid terms appears: τ_{cond} is due to the non-linearity of condensation term, while τ_{cav} is due to the non-linearity of cavitation term. In the end, the final form of filtered void fractions equations (Eq. 2.41) reads:

$$\begin{cases} \frac{\partial \overline{\alpha_l}}{\partial t} + \nabla \cdot (\overline{\mathbf{U}}\overline{\alpha_l}) + \nabla \cdot (\overline{\alpha_l}\,\overline{\alpha_v}\mathbf{U}_{c_{lv}}) + \nabla \cdot (\overline{\alpha_l}\,\overline{\alpha_{nc}}\mathbf{U}_{c_{lnc}}) = -\frac{\tau_{S_\alpha}}{\rho_l} - \frac{\tau_{cav}}{\rho_l} - \frac{\tau_{cond}}{\rho_l} - \frac{\rho_v}{\overline{\rho} + \overline{\alpha_{nc}}(\rho_l - \rho_{nc})} \left\{ \left[\left(\frac{\overline{D\alpha_v}}{Dt} \right)^- - \left(\frac{\overline{D\alpha_v}}{Dt} \right)^+ \right] \overline{\alpha_l} + \left(\frac{\overline{D\alpha_v}}{Dt} \right)^+ (1 - \overline{\alpha_{nc}}) \right\} \\ \frac{\partial \overline{\alpha_v}}{\partial t} + \nabla \cdot (\overline{\mathbf{U}}\overline{\alpha_v}) + \nabla \cdot (\overline{\alpha_l}\,\overline{\alpha_v}\mathbf{U}_{c_{lv}}) = \frac{\tau_{S_\alpha}}{\rho_v} + \frac{\tau_{cav}}{\rho_v} + \frac{\tau_{cond}}{\rho_v} + \frac{\rho_l}{\overline{\rho} + \overline{\alpha_{nc}}(\rho_l - \rho_{nc})} \left\{ \left[\left(\frac{\overline{D\alpha_v}}{Dt} \right)^+ - \left(\frac{\overline{D\alpha_v}}{Dt} \right)^- \right] \overline{\alpha_v} + \left(\frac{\overline{D\alpha_v}}{Dt} \right)^- (1 - \overline{\alpha_{nc}}) \right\} \\ \frac{\partial \overline{\alpha_{nc}}}{\partial t} + \nabla \cdot (\overline{\mathbf{U}}\overline{\alpha_{nc}}) + \nabla \cdot (\overline{\alpha_l}\,\overline{\alpha_{nc}}\mathbf{U}_{c_{lnc}}) = 0 \end{cases} \tag{2.44}$$

where $\left(\overline{\frac{D\alpha_v}{Dt}} \right)^+$ and $\left(\overline{\frac{D\alpha_v}{Dt}} \right)^-$ are computed using the product of filtered variables. However, τ_{S_α} and especially τ_{cond} and τ_{cav}, are extremely non-linear and it is hard to know *a-priori* their magnitude. From authors' knowledge there are not work in the present literature about an *a-priori* test with DNS to know if they are negligible or not and how to model them whether they were not negligible.

It is worth to remind that in the Finite Volume (FV) approach, both the computational grid and the discretization of the operators implicitly act as a top-hat filter to the equations [51]. Since most of the CFD solvers in the FV framework are usually limited to second order accuracy [120], the SCT and the SMT term coming from filtering of the equations would be probably biased by the discretization schemes and by the grid [134, 159], even when explicit filtering is applied.

2.6 Pressure-Velocity coupling

Eq. 2.13 and Eq. 2.15 are solved by the segregated pressure correction method, which will be outlined in this section. OpenFOAM relies on co-located grid arrangements. In order to use the segregated pressure correction method, avoiding checkerboards pressure fields, the so called Rhie-Chow momentum interpolation method is used [177]. This interpolation is based

on formulating a discretized momentum equation for the face, so that the computation of the driving pressure force involves the pressure value at the nodes adjacent to the face in question and, therefore at the node itself. Starting from the discretized momentum Equation, without any source term, and where pressure gradient is separated from the source:

$$\mathbf{U}_p^{n+1} = \frac{\sum_{nb} A_{nb}\mathbf{U}_{nb}^n + b_p}{(A_p)_p} - \left(\frac{\nabla \hat{p}_p^{n+1}}{(A_p)_p}\right) \tag{2.45}$$

where A_p is the diagonal of the matrix, representing the coefficient of the variable to solve $(\mathbf{U}_p^{n+1})$. The term $\sum_{nb} A_{nb}\mathbf{U}_{nb}^n$, which is called $\mathbf{H}_p$ denotes the extra-diagonal term coming from neighbor nodes (nb) during the discretization on a generic cell center p, while b_p denotes the known part of the linear system, which come from discretization procedure as well, depending on the scheme used. In the end, Eq. 2.45 reads:

$$\mathbf{U}_p^{n+1} = \frac{\mathbf{H}_p}{(A_p)_p} - \left(\frac{\nabla \hat{p}_p^{n+1}}{(A_p)_p}\right) \tag{2.46}$$

However velocity found does not satisfied the continuity and its value stands in cell center which would yield to checkerboard pressure field. The first issue is resolved introducing a pressure equation whose solution allow to find a new velocity field which can fulfill continuity. The second issue is resolved using the so called Rhie-Chow interpolation which consist in mimicking the interpolation on cell center for velocity fluxes:

$$\mathbf{U}^{n+1} = \frac{\mathbf{H}_p}{A_P} - \frac{1}{A_P}(\mathbf{f}_\sigma - \mathbf{g}\cdot\mathbf{x}\nabla\rho\cdot\hat{\mathbf{n}})|\mathbf{S_f}| - \frac{1}{A_P}\left(\nabla \hat{p}_p^{n+1}\right) \tag{2.47}$$

Then pressure equation is built recalling the non conservative form of continuity of Eq. 2.14:

$$\nabla\cdot\mathbf{U}_f^{n+1} = \frac{\frac{D\alpha_v}{Dt}(\rho_l - \rho_v)}{\rho + \alpha_{nc}(\rho_l - \rho_{nc})} \tag{2.48}$$

thus applying divergence to relation 2.47, the pressure equation reads:

$$\nabla\cdot\left(\frac{\mathbf{H}}{A_p}\right)^n - \nabla\cdot\frac{1}{A_P}\left[(\mathbf{f}_\sigma - \mathbf{g}\cdot\mathbf{x}\nabla\rho\cdot\hat{\mathbf{n}})|\mathbf{S_f}|\right]^n - \frac{1}{A_P}\nabla^2\hat{p}_P^{n+1} = \frac{\frac{D\alpha_v}{Dt}(\rho_l - \rho_v)}{\rho + \alpha_{nc}(\rho_l - \rho_{nc})} \tag{2.49}$$

However,pressure equation developed has not as variable to be solved p but the modified pressure $\hat{p} = p - \rho\mathbf{g}\cdot\mathbf{x}$. In addition, the source term on RHS of Eq. 2.49 is based on $\frac{D\alpha_v}{Dt}$, whose value depends on the difference between p and p_{sat} as shown in Eq. B.11. The fully-explicit treatment of the source term would lead to the numerical instability during the solution of the correspondent linear system built for the pressure equation. This issue is handled linearizing the source term. $p - p_{sat}$ is therefore rewritten as:

$$p - p_{sat} = p - \rho\mathbf{g}\cdot\mathbf{x} - p_{Sat} + \rho\mathbf{g}\cdot\mathbf{x} = \hat{p} - p_{Sat} + \rho\mathbf{g}\cdot\mathbf{x} \tag{2.50}$$

Thus, Eq. B.11 will be rearranged to be suitable as source term for Eq. 2.49. If we call $\dot{V}_p$ the term on RHS of Eq. 2.49:

$$\dot{V}_p = \begin{cases} \frac{(\rho_l-\rho_v)}{\rho+\alpha_{nc}(\rho_l-\rho_{nc})}\frac{3\alpha_v\frac{DR}{Dt}}{R+R^4\frac{4}{3}\pi n_0\left[\frac{\rho+\alpha_{nc}(\rho_v-\rho_{nc})}{\rho+\alpha_{nc}(\rho_l-\rho_{nc})}\right]} = -\frac{(\rho_l-\rho_v)}{\rho+\alpha_{nc}(\rho_l-\rho_{nc})}\frac{3\alpha_v(\hat{p}-p_{sat}+\rho\mathbf{g}\cdot\mathbf{x})pos(p-p_{sat})\sqrt{\frac{2}{3}\frac{1}{\rho_l|p-p_{sat}|}}}{R+R^4\frac{4}{3}\pi n_0\left[\frac{\rho+\alpha_{nc}(\rho_v-\rho_{nc})}{\rho+\alpha_{nc}(\rho_l-\rho_{nc})}\right]} = (\hat{p}-p_{sat}+\rho\mathbf{g}\cdot\mathbf{x})\dot{V}^+ & if\ p > p_{sat} \\ \frac{(\rho_l-\rho_v)}{\rho+\alpha_{nc}(\rho_l-\rho_{nc})}\frac{\alpha_l 4\pi n_0 R^2\frac{DR}{Dt}}{1+R^3\frac{4}{3}\pi n_0\left[\frac{\rho+\alpha_{nc}(\rho_v-\rho_{nc})}{\rho+\alpha_{nc}(\rho_l-\rho_{nc})}\right]} = -\frac{(\rho_l-\rho_v)}{\rho+\alpha_{nc}(\rho_l-\rho_{nc})}\frac{\alpha_l 4\pi n_0 R^2(\hat{p}-p_{sat}+\rho\mathbf{g}\cdot\mathbf{x})neg(p-p_{sat})\sqrt{\frac{2}{3}\frac{1}{\rho_l|p-p_{sat}|}}}{1+R^3\frac{4}{3}\pi n_0\left[\frac{\rho+\alpha_{nc}(\rho_v-\rho_{nc})}{\rho+\alpha_{nc}(\rho_l-\rho_{nc})}\right]} = -(\hat{p}-p_{sat}+\rho\mathbf{g}\cdot\mathbf{x})\dot{V}^- & if\ p < p_{sat} \end{cases} \tag{2.51}$$

The final form of source term in pressure equation reads:

$$\dot{V}_p = -(\dot{V}^- - \dot{V}^+)^n \hat{p}^{n+1} + (p_{sat} - \rho \mathbf{g} \cdot \mathbf{x})^n (\dot{V}^- - \dot{V}^+)^n \tag{2.52}$$

2.7 Discretized form of the phase-fraction equations

The solver has been developed in order to model high-speed injection and primary atomization. This a very challenging task for interface tracking and capturing methods. In this regard, the most important factor that must be considered is the mutual effect of turbulence and cavitation. Breakup and cavitation processes are dominated by surface instabilities, which are affected by turbulence, by the boundary conditions and by the numerics. Turbulence in the liquid, and to a lesser extent in the gas phase, strongly influences the predictions in the injection breakup; the fact that surface structures being resolved are of a similar space and time-scale to small, but not the smallest, turbulent structures suggests that this interaction cannot be realistically represented by traditional RANS modeling and that LES turbulence is the most appropriate approach. The use of LES imposes tight constraints on the numerics in the case setup: high resolution schemes and accurate numerics are required for differentiation, in order to preserve the energy associated with the resolved turbulent structures and to avoid a numerical error working as artificial dissipation [134]. On the other hand, high-order methods applied to high-speed flows in complex geometries may lead to instabilities; for this reason, special care must be taken in the discretization of the convection of momentum and of the temporal derivatives. In particular, the numerical fluctuation created by the VOF approach, possibly coming from the compression and mostly from the cavitation/condensation source terms, are preserved by second-order time-differencing schemes; as a result, a wrong accumulation of energy may be found and, in turn, the simulation is destabilized. The stencil of the discretization for the phase-fraction equations of system (2.29) makes use of a first-order time differencing scheme, as it happens when first order hyperbolic PDE are used [122]:

$$\begin{cases} \frac{(\alpha_l^{n+1} - \alpha_l^n)_p}{\Delta t} V_p + \sum_f F_f^n = B_{l_p}^n \left[\left(\frac{D\alpha_v}{Dt} \right)^- - \left(\frac{D\alpha_v}{Dt} \right)^+ \right]_p^n \alpha_{l_p}^{n+1} V_p + B_{l_p}^n \left[\left(\frac{D\alpha_v}{Dt} \right)^+ \right]_p^n (1 - \alpha_{nc})_p^n V_p \\ \frac{(\alpha_v^{n+1} - \alpha_v^n)_p}{\Delta t} V_p + \sum_f F_f^n = B_{v_p}^n \left[\left(\frac{D\alpha_v}{Dt} \right)^+ - \left(\frac{D\alpha_v}{Dt} \right)^- \right]_p^n \alpha_{v_p}^{n+1} V_p + B_{v_p}^n \left[\left(\frac{D\alpha_v}{Dt} \right)^- \right]_p^n (1 - \alpha_{nc})_p^n V_p \\ \frac{(\alpha_{nc}^{n+1} - \alpha_{nc}^n)_p}{\Delta t} V_p + \sum_f F_f^n = 0 \end{cases} \tag{2.53}$$

where the subscript P in the equations indicates that quantities are defined at the center of the Control Volume (CV); $\sum_f F_{i,f}$ is the sum of the convective fluxes for the $i-th$ phase (see Sec. 2.8) and:

$$B_{l_p}^n = \left[-\frac{\rho_v}{\rho + \alpha_{nc}(\rho_l - \rho_{nc})} \right]_p^n \tag{2.54}$$

$$B_{v_p}^n = \left[\frac{\rho_l}{\rho + \alpha_{nc}(\rho_l - \rho_{nc})} \right]_p^n \tag{2.55}$$

System of equations (2.53) is then solved explicitly as follows:

$$\begin{cases} \alpha_{l_p}^{n+1} = \dfrac{\alpha_{l_p}^n - \sum_f F_{i,f}^n \frac{\Delta t}{V_p} + B_{l_p}^n \left[\left(\frac{D\alpha_v}{Dt} \right)^+ \right]_p^n (1-\alpha_{nc})_p^n \Delta t}{1 - B_{l_p}^n \Delta t \left[\left(\frac{D\alpha_v}{Dt} \right)^- - \left(\frac{D\alpha_v}{Dt} \right)^+ \right]_p^n} \\ \alpha_{v_p}^{n+1} = \dfrac{\alpha_{v_p}^n - \sum_f F_{i,f}^n \frac{\Delta t}{V_p} + B_{v_p}^n \left[\left(\frac{D\alpha_v}{Dt} \right)^- \right]_p^n (1-\alpha_{nc})_p^n \Delta t}{1 - B_{v_p}^n \Delta t \left[\left(\frac{D\alpha_v}{Dt} \right)^+ - \left(\frac{D\alpha_v}{Dt} \right)^- \right]_p^n} \\ \alpha_{nc_p}^{n+1} = \alpha_{nc_p}^n - \dfrac{\Delta t}{V_p} \sum_f F_{i,f}^n \end{cases} \tag{2.56}$$

TVD [80] is applied in the calculation of $\alpha_{l_p}^{n+1}$ and $\alpha_{v_p}^{n+1}$, to ensure a stable solution and boundedness of the phase fraction with large density ratios. In this way, the oscillations in the solution near discontinuities in the phase-fraction equations (represented by the interface of the VOF) are smoothed and monotonicity is preserved. Phase transition leads to large values of the fluxes: this is particularly apparent in the calculation of the transport equation for the liquid phase. It has a direct effect on the stability of the solver and may put constraints in the time-step advancement. Similar considerations may be drawn for the transport equation of the vapor phase, but in this case the contribution on the fluxes deriving from the phase transition (condensation) is not so large as for the liquid and a bounded solution can be achieved. To stabilize the solution of the transport equation for the liquid fraction in (2.29), the term $\alpha_l \nabla \cdot \mathbf{U}$ is added and subtracted on its RHS. The equation is then written as:

$$\begin{aligned} \frac{\partial \alpha_l}{\partial t} + \nabla \cdot (\mathbf{U}\alpha_l) + \nabla \cdot (\mathbf{U}_{c_{lv}} \alpha_l \alpha_v) + \nabla \cdot (\mathbf{U}_{c_{la}} \alpha_l \alpha_{nc}) &= -\frac{\rho_v}{\rho + \alpha_{nc}(\rho_l - \rho_{nc})} \frac{D\alpha_v}{Dt} - \alpha_l \nabla \cdot \mathbf{U} + \alpha_l \nabla \cdot \mathbf{U} = \\ &= -\frac{\rho_v}{\rho + \alpha_{nc}(\rho_l - \rho_{nc})} \frac{D\alpha_v}{Dt} - \alpha_l \frac{\frac{D\alpha_v}{Dt}(\rho_l - \rho_v)}{\rho + \alpha_{nc}(\rho_l - \rho_{nc})} + \alpha_l \nabla \cdot \mathbf{U} = \\ &= \frac{D\alpha_v}{Dt} \frac{\rho_l \rho_v}{\rho + \alpha_{nc}(\rho_l - \rho_{nc})} \left[-\frac{1}{\alpha_l} + \alpha_l \left(\frac{1}{\rho_l} - \frac{1}{\rho_v} \right) \right] + \alpha_l \nabla \cdot \mathbf{U} = \\ &= \frac{D\alpha_v}{Dt} \frac{\rho_l \rho_v}{\rho + \alpha_{nc}(\rho_l - \rho_{nc})} A_l + \alpha_l \nabla \cdot \mathbf{U} \end{aligned} \tag{2.57}$$

The discretized form of Eq. (2.57) reads:

$$\frac{(\alpha_l^{n+1} - \alpha_l^n)_p}{\Delta t} V_p + \sum_f F_f^n = B_{l_p}^n \left[\left(\frac{D\alpha_v}{Dt} \right)^- - \left(\frac{D\alpha_v}{Dt} \right)^+ \right]_p^n \alpha_{l_p}^{n+1} V_p + B_{l_p}^n \left[\left(\frac{D\alpha_v}{Dt} \right)^+ \right]_p^n (1-\alpha_{nc})_p^n V_p + \alpha_{l_p}^n \sum_f \mathbf{U}_f^n \cdot \mathbf{S}_f \tag{2.58}$$

where

$$B_{l_p}^n = \left[\frac{\rho_l \rho_v}{\rho + \alpha_{nc}(\rho_l - \rho_{nc})} A_l \right]_p^n \tag{2.59}$$

The final expression to calculate the liquid fraction α_l^{n+1} in (2.29) is:

$$\alpha_{l_p}^{n+1} = \frac{\alpha_{l_p}^n(1+\sum_f \mathbf{U}_f^n \cdot \mathbf{S}_f \frac{\Delta t}{V_p}) - \sum_f F_f^n \frac{\Delta t}{V_p} + B_{l_p}^n \left[\left(\frac{D\alpha_v}{Dt}\right)^+\right]_p^n (1-\alpha_{nc})_p^n \Delta t}{1 - B_{l_p}^n \Delta t \left[\left(\frac{D\alpha_v}{Dt}\right)^- - \left(\frac{D\alpha_v}{Dt}\right)^+\right]_p^n} \tag{2.60}$$

Multiple calculations of the system of equations (2.56), with updated values of the phase fractions, are performed to favor a bounded and more accurate solution. This procedure is repeated iteratively until the global conservation of the void fractions is reached. It is important to note that, similarly to what is done in the calculation of the specie transport, the last phase (non-condensable gases in this cases) is usually solved as the complement to reach the unity. In the case of cavitating flows, as discussed in the previous paragraph, the solution of the phase fraction equations is required for closure; this means that, after the iterative procedure just described to calculate independently α_l, α_v and α_{nc} is completed, the (small) residual error must be added to the non-condensable phase fraction before the pressure-velocity coupling is calculated.

2.8 Discretization of the convective fluxes in the phase fraction equations (MULES)

The implemented system of phase-fraction equations for the three-phase VOF, Eq. (2.12), have been discretized following the MULES, to ensure boundedness and consistency even in presence of flow cavitation and condensation. The method to solve the phase fraction equations is fundamentally explicit and introduces a strict Courant number limit with a direct impact on time step advancement; time step sub-cycling, commonly used to enlarge time-steps in VOF solvers, is applied here to ensure consistency and boundedness of the solution with strong cavitation/condensation. One of the critical issues with the VOF method used is the discretization of the advective term in Eq. (2.60), that includes either the convective fluxes and the counter-gradient term (compressive fluxes):

$$\sum_f F_{i,f}^n = \sum_f \underbrace{\alpha_{i_f}^n \mathbf{U}_f \cdot \mathbf{S}_f}_{\text{convective fluxes}} + \sum_f \underbrace{\alpha_{i_f}^n \sum_{j \neq i} \alpha_{j_f}^n \mathbf{U}_{C_{ij_f}} \cdot \mathbf{S}_f}_{\text{counter-gradient transport}} = \sum_f F_{\alpha_f}^n + \sum_f F_{C_f}^n \tag{2.61}$$

Numerical diffusivity of first order schemes might smear the interface; on the other hand, higher order schemes are unstable and may cause numerical oscillations. It is therefore needed to derive advection schemes able to keep the interface sharp and to produce monotonic profiles of the color function. In the modified system of phase fraction equations (2.56), the Flux Correct Transport (FCT) technique has been applied: flux limiters are computed by an iterative procedure which allows the use of high-order schemes preserving boundedness, mass conservation and sharp interface capturing. The theory originally formulated in [27] was further extended to multi-dimensional problems in [243]. The method involves several stages of calculation: first, the discretization of the advective term $F_{\alpha_f}^n$ is provided by a higher $F_{f,i}^H$ and a lower order $F_{f,i}^L$ (obtained applying a monotonic and a diffusive advective scheme) flux approximation; Then, an anti-diffusive flux (F_A) is defined to attempt and reduce the numerical diffusion resulting from the lower order scheme. An estimate of the anti-diffusive fluxes F^A for the $i-th$ phase equation is given by:

$$F_{f,i}^{A} = F_{f,i}^{H} - F_{f,i}^{L} \tag{2.62}$$

Anti-diffusive fluxes $F_{f,i}^{A}$ are limited to $F_{f,i}^{C}$ by a flux-limiting technique [243] based on the calculation of a TVD limiter λ to prevent undershoots and overshoots in the phase fraction in the control volume:

$$F_{f,i}^{C} = \lambda \, F_{f,i}^{A} \quad \text{with} \quad \lambda \in [0,1] \tag{2.63}$$

being $\lambda = f(F_{\alpha_f}^{n})$ a function of the void fractions.

2.9 Solution algorithm

The code resolves the governing equations by the FVM; a cell-centered formulation with co-located arrangement is used for the sequential solution of the governing equations on a polyhedral mesh. The segregated solution of the governing equations (mass and momentum) is achieved by a pressure-velocity coupling algorithm. The turbulent viscosity μ_t is modeled using the wall-adapting local eddy-viscosity model (WALE) [148], which has been proved to be suitable for wall-bounded flows and single-fluid approach [43].

The steps needed to find actual pressure field and velocity field are shown in the flow diagram 2.9, in which also the solution of void fraction equations is illustrated. Numerical solution is achieved by means of Transient Simple (Semi Implicit Method for Pressure Linked Equation) algorithm [66] which is an enhanced version of the PISO (pressure implicit with Splitting of Operator) algorithm developed by Issa [97]. It improves significantly the temporal convergence and time step limits in multiphysics problems in which not only the pressure-velocity coupling plays a big role but also other phenomena such as multiphase flows, combustion, fluid-structure interaction do. The structure of transient-SIMPLE algorithm allows to improve temporal convergence when analyzing the multiphysiscs flows by iterating for each time step the strong coupling between extra physics and the pressure-velocity fields and viceversa. Multiphase flow with cavitation falls inside this group of multiphysics which has a strong coupling between phase fraction equations and the $p - U$ coupling.

Transient simple algorithm with explicit solution of void fractions equations

0. Set initial and boundary conditions for the fields, $\mathbf{U}$, $\hat{p}$, α_l, α_v, α_{nc}
1. Set time step, if time step is variable in accordance to the CFL criteria
2. Initialize the mixture: compute viscosity μ and density ρ with an explicit limiting of void fractions $0 \leq \alpha_i \leq 1$
3. Perform Outer loop $N_{outer-corr}$ times
   - 3.1 Perform α-sub cycle $N_{\alpha-sub}$ times (explicit sub time stepping)
     - 3.1.1 update/define interface-compressive fluxes ϕ_c
     - 3.1.2 Perform α correction $N_{\alpha-corr}$ times
       - 3.1.2.1 Update/define ϕ_{α_i}
       - 3.1.2.2 Solve Eqs. 2.53 for α_i explicitly with MULES
       - 3.1.2.3 Bound α_i locally (at the interface) and globally (whole domain)
       - 3.1.2.4 Update/define mass flux $\rho\phi$ of the $N_{\alpha-corr}^{th}$ cycle
     - 3.1.3 Compute $\rho_f\phi$ of the $N_{\alpha-sub}^{th}$ cycle

3.1.4 Compute new density

3.2 Update mass flux $\rho_f\phi = \sum_{i=1}^{N-\alpha-sub} \frac{\delta t^i}{\Delta t}(\rho_f\phi)^i$ with $\delta t^i = \Delta t / N_{\alpha-sub}$

3.3 Construct discretized momentum equation

3.4 If momentum predictor is activated, solved momentum equation with old pressure field

3.5 Perform PISO loop N_{corr} times

3.5.1 Assemble A_p and $\mathbf{H}_p$ to compute $\mathbf{U}^{n+1} = \frac{\mathbf{H}_p}{A_p}$

3.5.2 Compute flux predictor ϕ^* (Eq. 2.47) with $\mathbf{U}$ from previous time step

3.5.3 Construct pressure Equation (Eq. 2.49) and solve it $N_{nonortho-corr}$ times (non orthogonal corrector loop)

3.5.3.1 Bound $\hat{p}$ to avoid negative values generated during cavitation

3.5.3.2 Correct fluxes with the fluxes coming from the solved pressure equation $\phi = \phi^* - (A_p^{-1})_f \mathbf{S_f} \cdot \nabla_f^{\perp} \hat{p}^{n+1}$

3.5.4 Update cell-centered velocity field $\mathbf{U}$ with assembled momentum coefficient

3.5.5 Update boundary condition

3.5.6 Check PISO convergence

3.6 Compute $p = \hat{p} + \rho \mathbf{g} \cdot \mathbf{x}$

3.7 Correct turbulent viscosity

4 Check convergence

5 Update $\mathbf{U}$, $\hat{p}$, α_i of the $N_{outer-corr}^{th}$ cycle

6 Advance in time

CHAPTER 3

Multiphase Modelling Verification and Validation

Simulations have been performed on three different cases, in order to test the numerical properties of the newly implemented solver (in the following referred as `interPhaseChangeMixingFoam`) in terms of ability to: a) capture the interfaces, while maintaining them sharp; b) preserve the conservativeness and the boundedness of the solution of the phase-fraction equations with phase-change. Finally, the robustness of the solver and its application to the description of real flow physics is tested on a large parallel simulation of an injector geometry. Validation test cases that will be discussed in the further sections are:

1) the evolution of a two-dimensional bubble rising in a liquid column [94], to test the ability of the solver to properly capture the interface between fluids of different densities;

2) the study of the evolution of a free-surface in a partially cavitating/condensing liquid column, to verify the conservativeness and boundedness while phase-fraction equations are solved with phase-change;

3) a cavitating flow evolving inside an injector nozzle [23, 199].

3.1 Verification of multiphase VoF

3.1.1 Bubble Rising In A Liquid Column

The two-dimensional bubble rising in a liquid column [94] has been proposed as a validation test-case to study the ability of the multiphase solvers to capture the interfaces. The first test case studied consists of a two-dimensional rising bubble problem, where a gas bubble immersed in a chamber filled with liquid moves until it breaks up. The case setup, the boundary conditions and the physical properties of the fluid are described in Fig. 3.1. Forces acting on the bubble are surface tension and gravity. The domain has an aspect ratio width/height=0.5; no-slip boundary conditions on the velocity are set at the upper and lower boundaries, while free-slip is applied at the right and left bounds; gravity $\mathbf{g}$ is oriented towards the negative y direction. At time $t = 0$ s, the bubble center is located at $(x, y) = (0.5, 0.5)$ and the bub-

ble radius is $r_{b,0} = 0.25$ m. This test-case has been already used by the authors in [156] to validate a 2-phase VOF solver and it is now used again with some necessary modifications in the case setup: as shown in Fig. 3.1, the evolution of the bubble in the surrounding liquid (identified by the void fraction α_1) is now captured by the transport of two identical phases ($\alpha_2 = \alpha_3$). In this test, phase change is disabled. It is expected that the solution of the three-phase solver tends to the solution of the two-phase solver of [156]. This is not trivial in the VOF framework, since global conservation of the phase fractions is more difficult as the number of phases increases and in a single-fluid solver it is strictly linked to the calculation of the fluid properties (see Eq. 2.3 and 2.4).

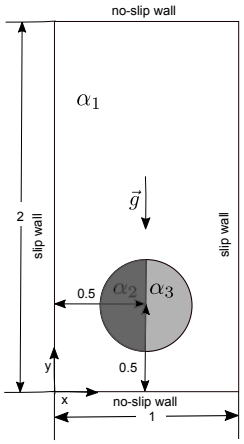

Parameter	Value	Unit
ρ_1	1000	$\mathrm{kg/m^3}$
$\rho_2 = \rho_3$	1	$\mathrm{kg/m^3}$
μ_1	10	$\mathrm{kg\,m^{-1}s^{-1}}$
$\mu_2 = \mu_3$	0.1	$\mathrm{kg\,m^{-1}s^{-1}}$
g	-0.98	$\mathrm{m/s^2}$
σ	1.96	$\mathrm{N/m}$
Re	35	–
Eo	125	–

Figure 3.1: *Bubble rising in a liquid column: case setup, boundary and initial conditions. Four different grid resolutions are tested: a) 40x80 cells; b) 80x160 cells; c) 160x320 cells; d) 320x640 cells (reference solution).*

The physical properties of interest of the fluid, listed in Fig. 3.1, are:

- the Eötvös number Eo, defined as the ratio between the buoyancy force and surface tension:

$$\mathrm{Eo} = \frac{\rho_1 U_g^2 L}{\sigma} \tag{3.1}$$

- the Reynolds number Re of the liquid, defined as:

$$\mathrm{Re} = \frac{\rho_1 U_g L}{\mu_1} \tag{3.2}$$

where $L = 2\,r_{b,0}$ is the characteristic length scale and $U_g = \sqrt{2 g r_{b,0}}$ is the characteristic rising velocity. At high values of Eo, the bubble shape will be something in between the shape observed for the skirted and the dimpled ellipsoidal-cap regimes, implying that a breakup is likely to occur [45]. Simulations at high values of Eo are challenging for interface capturing algorithms and can yield to different predictions of the evolution and of the formation of newly created droplets. Following the work of [94], the evolution of the bubble has been investigated for a total time $T = L/U_g$ and a fixed time step with $\Delta t = 1/(2N_x)$ s has been used for time marching. In the surrounding region of the bubble initial conditions for the void fractions are $\alpha_2 = \alpha_3 = 0$ and $\alpha_1 = 1$; in the bubble region, $\alpha_1 = 0$, $\alpha_2 = 1$ and $\alpha_3 = 0$ (left half) and $\alpha_2 = 0$ and $\alpha_3 = 1$ (right half) are set. This leads to a stair-cased shaped interface, so a preliminary simulation without gravity (g $= 0$) is needed to obtain a smooth

initial bubble shape. The results from the zero-gravity precursor simulation are then used as the initial condition for the actual simulation.

Quantitative validation of the described code extensions, based on geometrical metrics proposed in [94], is now presented. For a fair comparison with [94], the grid used is Cartesian with a resolution $N_x \times 2N_x$ cells, being N_x 40, 80, 160 and 320 respectively (four grids were tested in total). The monitored quantities from the simulations were:

a) *bubble center of mass*:

$$\mathbf{x}_c = \frac{\iint_A (\alpha_2 + \alpha_3)\mathbf{x}_c \, \mathrm{d}x\mathrm{d}y}{\iint_A (\alpha_2 + \alpha_3) \, \mathrm{d}x\mathrm{d}y} \tag{3.3}$$

b) *degree of circularity* for a two-dimensional domain [222], being bubble Area defined as $A_b = \pi r_{eq}^2$:

$$\begin{aligned} C =& \frac{\text{perimeter of equivalent circle}}{\text{actual perimeter of the bubble}} = \frac{2\pi r_{eq}}{\iint_A (\nabla\alpha_2 + \nabla\alpha_3) dxdy} \\ =& \frac{2\pi\sqrt{\frac{A_b}{\pi}}}{\iint_A (\nabla\alpha_2 + \nabla\alpha_3) dxdy} = \frac{2\pi\sqrt{\frac{A_b}{\pi}}}{\iint_A (\nabla\alpha_2 + \nabla\alpha_3) dxdy} \end{aligned} \tag{3.4}$$

where r_{eq} is the equivalent radius, defined as:

$$r_{eq} = \sqrt{\frac{A_b}{\pi}} = \sqrt{\frac{\iint_A (\alpha_2 + \alpha_3) dxdy}{\pi}} \tag{3.5}$$

The C parameter is equal to unity for a perfectly circular bubble and lower than unity for other cases;

c) *mean rising velocity*:

$$\mathbf{u}_c = \frac{\iint_A (\alpha_2 + \alpha_3)\mathbf{U} \, \mathrm{d}x\mathrm{d}y}{\iint_A (\alpha_2 + \alpha_3) \, \mathrm{d}x\mathrm{d}y} \tag{3.6}$$

Results in this section are organized as follows: using the procedure of [94], simulations on the four grids (40x80, 80x160, 160x320 and 320x640 cells respectively) are presented, to monitor the grid-dependency of the results. In a second step, the solution from the finest grid is taken as reference solution and it is compared with CFD simulations from three incompressible interfacial flow codes, namely: a) TP2D [152, 218] and FreeLIFE [155], that are based on the level-set approach applied on a static grid; b) MooNMD [102] where the interface is tracked in a Lagrangian manner and inner mesh points are then projected onto the interface by solving a linear elasticity problem. The evolution in time of the quantities described above is studied on four grids of different resolution: results are reported in Fig. 3.2 and in Tab. 3.1, while in Fig. 3.3 and 3.4 the graphical evolution of the bubble with different grids is reported. Bubble circularity (Fig. 3.2-b) shows a monotonic diminishing tendency, that does not seem very influenced by the mesh resolution, until the beginning of the bubble break-up. Conversely, mean bubble rising velocity (Fig. 3.2-c) does not present a monotonic tendency and this can be justified by the local deformation of the bubble, that is increasing in time. Two local maxima are clearly visible: while the bubble is rising, its velocity reaches a first maximum $\mathbf{u}_{c_{max,1}}$, whose position looks independent by the mesh resolution used; this allows to assume that all the grids have sufficient resolution to describe the main features of

the bubble before break-up. The second maximum is instead occurring when the tail in the bottom region of the bubble becomes relevant; in this case, the mesh resolution influences the predictions, since the bubble tail and its ligaments are differently described from coarser to finer grid resolution. Thinner predicted tails favor a larger velocity in the second local peak and its shifting to later times. As the break-up of the tail occurs, the mean rising velocity decreases again. Finally, the evolution of the bubble centroid, Eq. (3.3), is mostly independent by mesh resolution until the size of the tails becomes relevant and influences the position of the bubble mass in the domain.

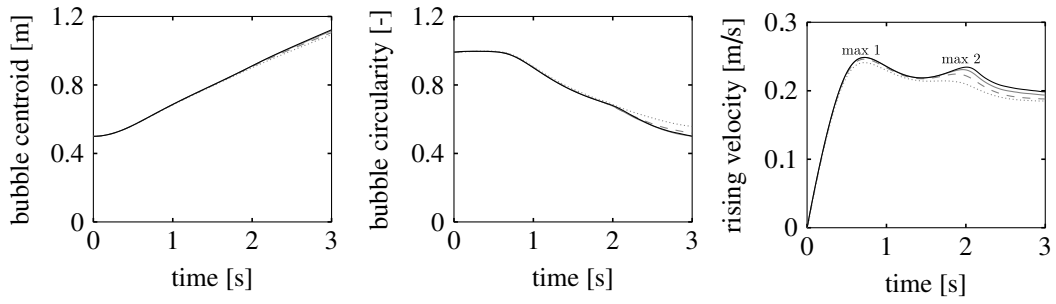

(a) *bubble centroid* **(b)** *bubble circularity* **(c)** *rising velocity*

Figure 3.2: *Two-dimensional bubble rising in a liquid column, validation test case. Evolution in time of: (a) bubble centroid location C; (b) bubble circularity $C \in [0; 1]$ and (c) bubble rising velocity $\mathbf{u}_c$; circularity is equal to unity if the bubble shape is a perfect circle. Test have been performed by* `interPhaseChangeMixingFoam` *using four different grids: .... 40x80 cells; – – – 80x160 cells; — 160x320 cells; — 320x640 cells.*

Table 3.1: *Minimum circularity, maximum rising velocities and final position of center of mass and their corresponding time occurrence for* `interPhaseChangeMixingFoam`*. $\mathbf{u}_{c_{max,1}}$ and $\mathbf{u}_{c_{max,2}}$ denote the first and the second local peak of the bubble rising velocity, see Fig. 3.2-c.*

grid	40x80	80x160	160x320	320x640
C_{min}	0.5579	0.5186	0.5002	0.50072
$t(C_{min})$	3.0	3.0	3.0	3.0
$\mathbf{u}_{c_{max,1}}$	0.2409	0.2461	0.2487	0.2488
$t(\mathbf{u}_{c_{max,1}})$	0.725	0.725	0.725	0.7234
$\mathbf{u}_{c_{max,2}}$	0.2144	0.2244	0.2309	0.2345
$t(\mathbf{u}_{c_{max,2}})$	1.725	1.88125	1.959375	2.009375
$\mathbf{x}_c(t_{final})$	1.094	1.1058	1.1164	1.1223

The evolution of the bubble shape is monitored at different times; the bubble interface is obtained by an iso-contour plot of the liquid void fraction using $\alpha_l = 0.5$ as threshold value. In Fig. 3.3, the temporal evolution of the bubble using four different meshes is reported to justify previous considerations. From 0 s to 1.8 s the capture of the bubble surface is almost independent by the mesh resolutions used. As soon as the onset of breakup occurs, the grid starts producing different deformations of the elongated filaments (2.2 s) leading to completely different flow configurations, as evidenced in Fig. 3.4. While coarse grids (40x80 and 80x160) do not capture any breakup, this starts to appear with the 160x320 mesh and it is reproduced with good detail by the finest mesh.

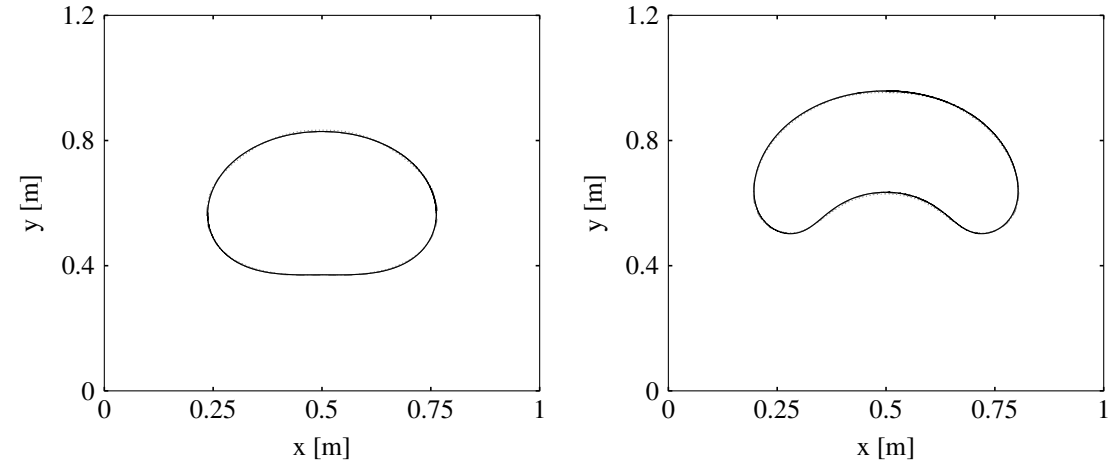

(a) *t = 0.6 s*

(b) *t = 1.2 s*

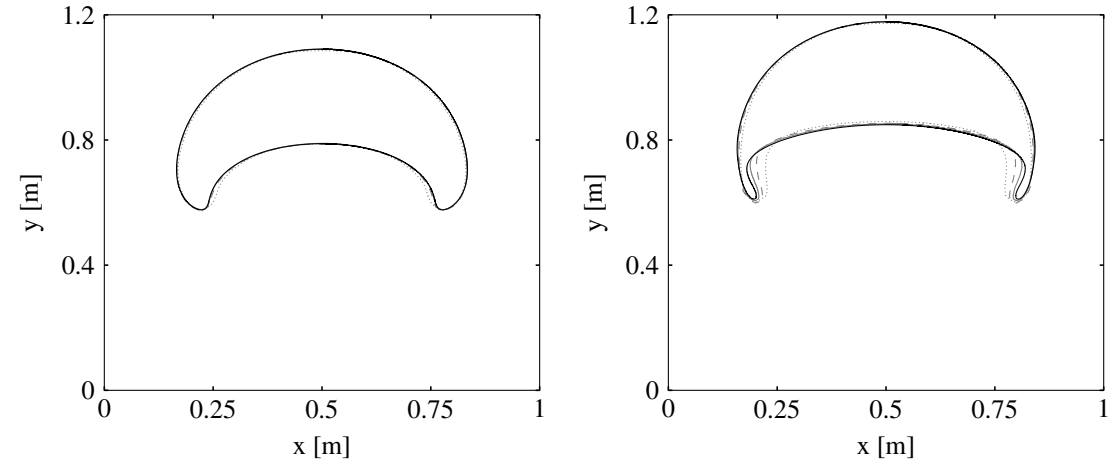

(c) *t = 1.8 s*

(d) *t = 2.2 s*

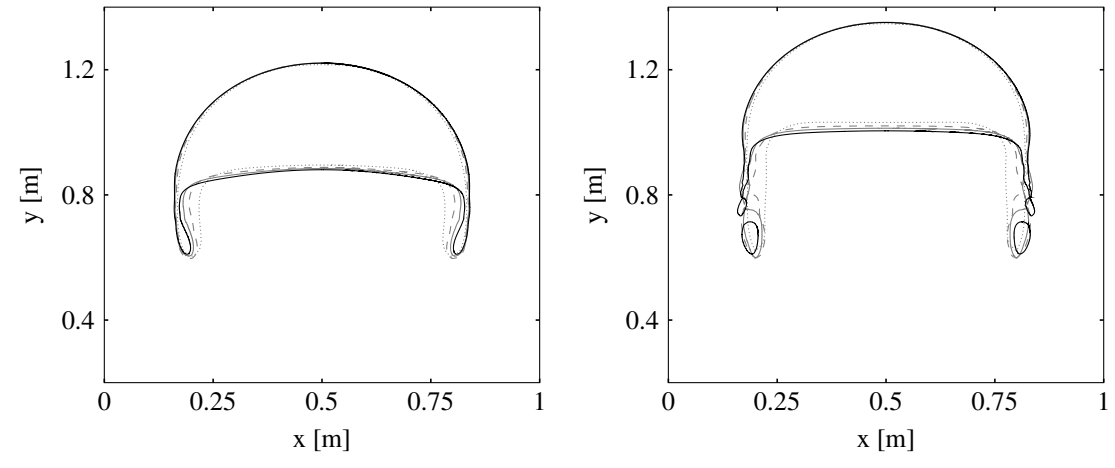

(e) *t = 2.4 s*

(f) *t = 3 s*

Figure 3.3: *Bubble evolution from 0.6 to 3 s calculated by* `interPhaseChangeMixingFoam` *on four different grids: .... 40x80 cells; – – – 80x160 cells; — 160x320 cells; — 320x640 cells*

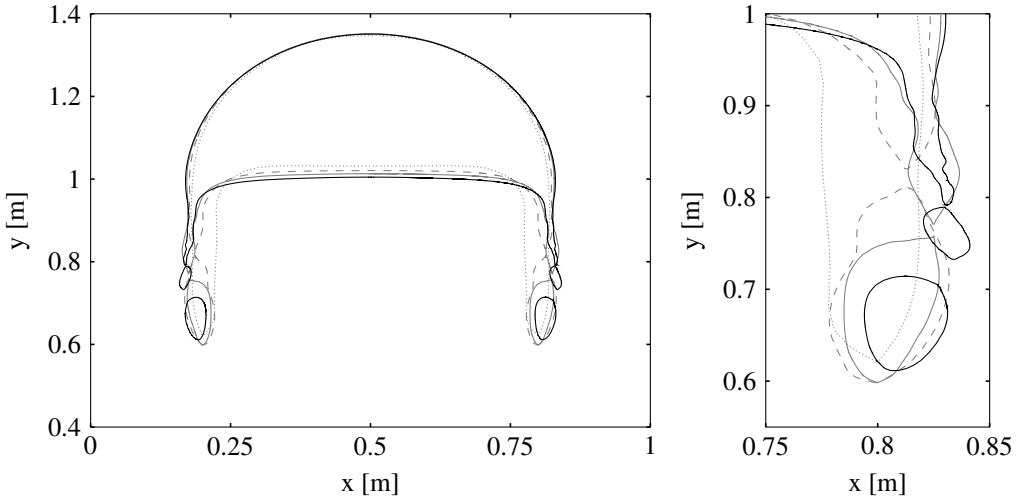

Figure 3.4: *Bubble breakup at time t=3 s. Comparison of* `interPhaseChangeMixingFoam` *behavior using four different discretizations: .... 40x80 cells; – – – 80x160 cells; — 160x320 cells; — 320x640 cells*

Similarly to [94], relative error of the norm of the temporal evolution of the bubble center of mass $\mathbf{x}_c$, of the bubble circularity C and of the mean rising velocity $\mathbf{u}_c$ are calculated using a suitable reference solution, represented by the finest grid:

$$e_{l_1} = \frac{\sum_{t=1}^{N} |q_{t,ref} - q_t|}{\sum_{t=1}^{N} |q_{t,ref}|} \tag{3.7}$$

$$e_{l_2} = \left(\frac{\sum_{t=1}^{N} |q_{t,ref} - q_t|^2}{\sum_{t=1}^{N} |q_{t,ref}|^2} \right)^{1/2} \tag{3.8}$$

$$e_{l_\infty} = \frac{max_t |q_{t,ref} - q_t|}{max_t |q_{t,ref}|} \tag{3.9}$$

where q_t is the temporal evolution of quantity q, and N the number of samples in time of q. Standard linear interpolation has been used in order to account for different sampling rates between $q_{t,ref}$ and q_t, that are calculated on different grids. For each relative error norm, the Rate Of Convergence (ROC) of q is:

$$ROC \approx \frac{log_{10}(||e^{k+1}||/|e^k|)}{log_{10}(h^{k+1}/h^k)} \tag{3.10}$$

where k denotes the grid refinement level and $h = 1/\Delta x$. Since the finest grid (320x640 cells) has been used as reference solution, the computed ROC will not indicate how well a method converges to the exact solution, but how it converges to an approximate solution. In Tab. 3.2 the relative error norms and the rates of convergence are reported: more than a linear convergence order is achieved in the l_1, l_2 and l_∞ norms as the resolution of the grid increases. While the order of convergence for the bubble centroid and for mean rising velocity increases with the grid resolution, the same tendency is not noticed in l_1 and l_2 norms of the bubble circularity: this is probably due to the fact that the two coarser grids do not exhibit break-up of ligaments. The order of convergence of the l_∞ norm of the bubble circularity increases with the mesh resolution, because its definition is based on the highest absolute deviation between the coarsest and finest mesh: in other words, moments in time characterized by the

highest deviations (e.g. bubble break-up) are converging faster with respect to the moments where the bubble is only deformed and where the mesh resolution does not play a significant role.

Table 3.2: *Relative error norms and rates of convergence for different grid resolutions. Results for the grid 320x640 is taken as reference.*

	grid	e_{l_1} %	ROC_1	e_{l_2} %	ROC_2	$\|\|e\|\|_{l_\infty}$ %	ROC_∞
	40x80	5.31	-	0.66	-	10.87	-
$\mathbf{x}_c$	80x160	2.85	0.8988	0.4	0.7384	6.3	0.7865
	160x320	1.01	1.4986	0.17	1.2568	2.67	1.2430
	40x80	2.16	-	0.09	-	5.74	-
C	80x160	0.57	1.9271	0.02	1.940	1.79	1.6779
	160x320	0.2	1.5213	0.008	1.5179	0.55	1.7119
	40x80	1.15	-	0.043	-	2.54	-
$\mathbf{u}_c$	80x160	0.54	1.1010	0.02	0.9669	1.47	0.7868
	160x320	0.14	1.9202	0.007	1.6625	0.52	1.4966

Finally, a second investigation has been carried out to compare the results from the implemented solver against the original benchmark [94]. The time t=3 s (Fig. 3.6) is chosen for the comparison, being the most representative of the bubble breakup. From Fig. 3.6 it is apparent that the upper part of the bubble is well described by the different solvers, that make use of different methods to capture the interface. Differences can be noticed in the tails produced in the bottom part of the bubble, where each solver differently describes the breakup process, by describing different filament lengths.

However, when analyzing monitoring quantities among different solvers, using the same mesh resolution, it is possible to determine if their trends are well reproduced among different approaches.

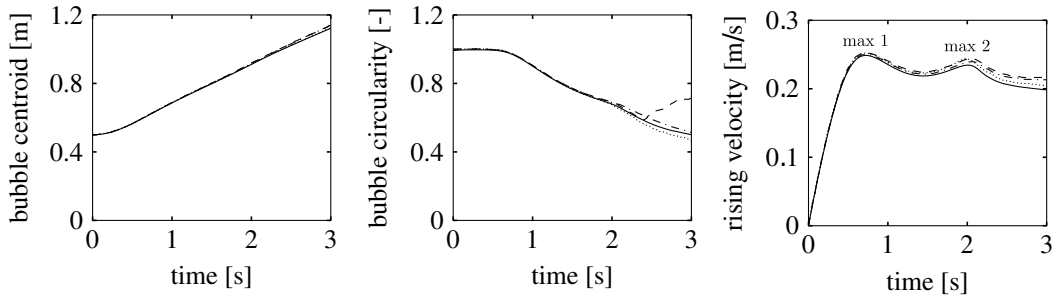

(a) *bubble centroid* **(b)** *bubble circularity* **(c)** *rising velocity*

Figure 3.5: *Two-dimensional rising bubble problem, validation test case. Evolution in time of: (a) bubble centroid location C; (b) bubble circularity $C \in [0; 1]$ and (c) bubble rising velocity $\mathbf{u}_c$; circularity is equal to unity if the bubble shape is a perfect circle. Legend:* — `interPhaseChangeMixingFoam`, — — — *TP2D code,* — · — *FreeLIFE code,* · · · *MooNMD [94].*

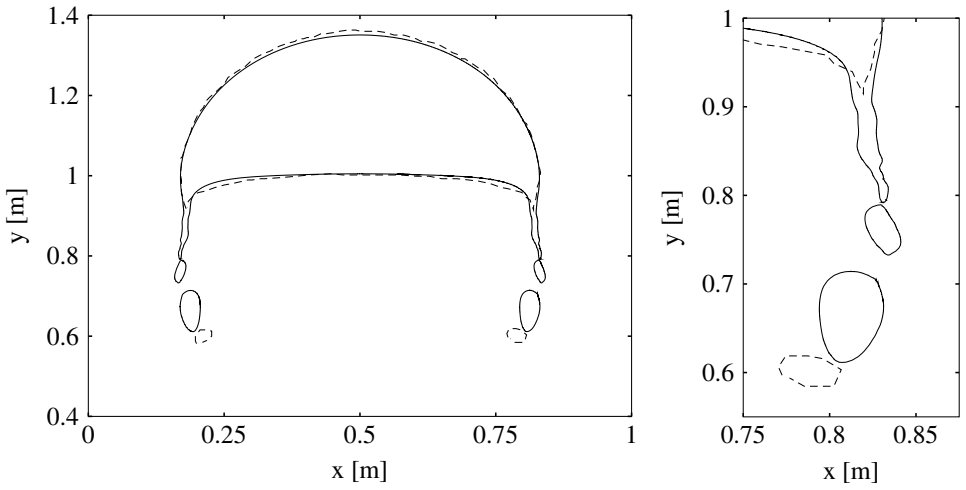

(a) *TP2D*

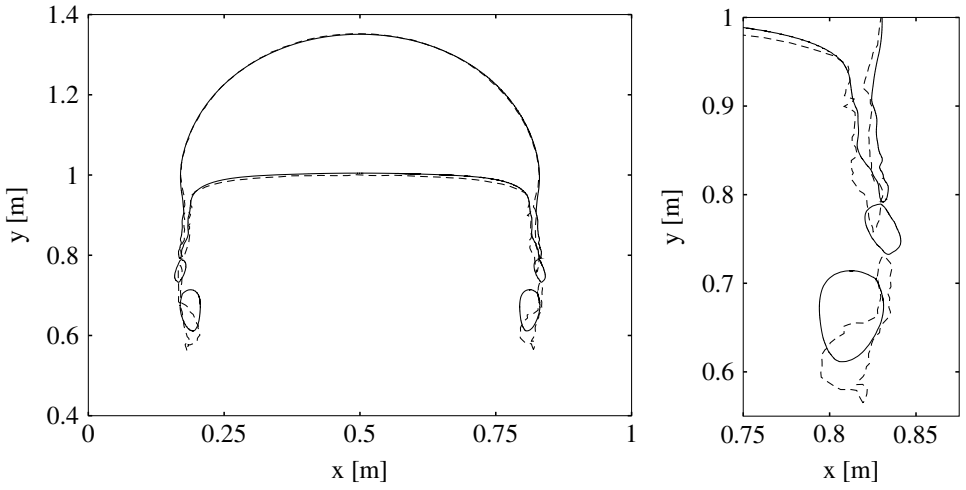

(b) *FreeLife*

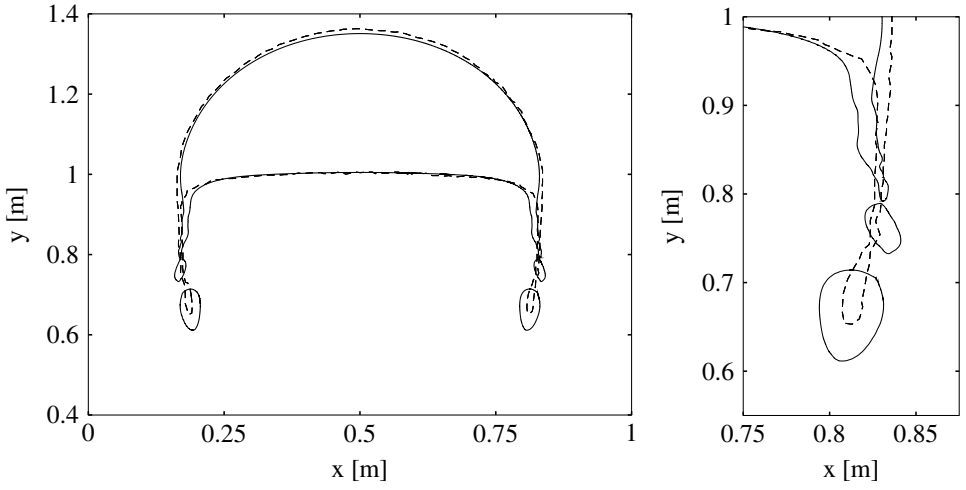

(c) *MooNMD*

Figure 3.6: *Bubble breakup at time t=3 s; comparison between* — `interPhaseChangeMixingFoam` *and* — — —*: (a) TP2D, (b) FreeLife, (c) MooNMD.*

Table 3.3: *Comparison of: a) minimum bubble circularity b) maximum rising velocity c) position of the center of mass for the different codes compared. The grid resolution used for the tests was 320x640 cells. Subscripts 1 and 2 denote the first and the second local maximum respectively.*

	`interPhaseChangeMixingFoam`	TP2D	FreeLife	MoonNMD
C_{min}	0.50072	0.5943	0.4647	0.5144
$t(C_{min})$	3.0	2.3439	3.0	3.0
$\mathbf{u}_{c_{max,1}}$	0.2488	0.2538	0.2514	0.2502
$t(\mathbf{u}_{c_{max,1}})$	0.7234	0.7340	0.7281	0.7317
$\mathbf{u}_{c_{max,2}}$	0.2345	0.2467	0.2440	0.2393
$t(\mathbf{u}_{c_{max,2}})$	2.009375	2.0553	1.9844	2.0600
$\mathbf{x}_c(t_{final})$	1.1223	1.1387	1.1249	1.1376

3.2 Verification of multiphase VoF with phase change

3.2.1 Evolution of the free-surface in a partially cavitating/condensating liquid column

In the bubble rising problem, no phase-change is involved. At the time this work is published [77], no simple numerical test cases are proposed to check if boundedness and conservativeness is ensured while phase-change occurs in a solver using a VOF method to capture the interface. Mass conservation is easier to achieve with the HEM, the HRM [24, 54, 145] and the Bubble Model, but it is critical for VOF methods where phase-change is implemented in the phase-fraction equations. Comparisons between the Bubble Model and the HRM for an injector test case [232] are reported in [32], where it is shown similar behavior in the prediction of the cavitation onset and similar limits in the description of condensation effects. With multiphase flows, the common way to validate models is through visual comparison of the flow evolution: this is still possible when cloud and wake cavitation occur in proximity of the blades, because pockets of vapor are located in a large and well defined region near the trailing edge. On the other hand, visualization of bubbly flows inside a nozzle is very hard, because of its micrometric size and of the short lifetime of the vapor bubbles (the order of magnitude is $1\,\mu s$). Besides, in both types of cavitating flows it is hard to split the errors coming from the solution of the momentum equation and those coming from the resolution of the phase-fraction equations.

In this work, a simple benchmark configuration is proposed to check boundedness and conservativeness of the VOF solver. The test-case consists of a one-dimensional column, opened at its top, whose dimension is L in y-direction; half of the volume of the column is filled by 95% of liquid and 5% of fuel vapor, while the remaining half of the volume is filled by non-condensable gases (Fig. 3.7). The system is initially at rest; The pressure distribution over the vertical y-axis is hydrostatic. In a first stage of the test, which duration of 0.1 s, the condensation term is disabled and the saturation pressure of the liquid is set to $p_{sat} = 100300\,Pa$; as a consequence, in the regions where the hydrostatic pressure is lower than the saturation pressure, the liquid cavitates, and non-condensable gases are pushed out of the outlet boundary. The final state of the system at t=0.1 s is then used as initial condition for a second stage of the test (from t=0.1 s to t=0.2 s), where the vapor is forced to condensate, by setting the saturation pressure of the fluid to $p_{sat} = 99700\,Pa$. The different values of the saturation pressure have been chosen to reproduce similar pressure gradients in the liquid and in the vapor and thus to have similar magnitude of the source terms (with different signs) during cavitation and condensation. In the simulations, no-slip boundary conditions are applied at the lower boundary, free-slip is imposed on the side walls while a Neumann condition is applied at the upper boundary. Tests on two different one-dimensional

grid domains have been performed; discretization along the y-axis was respectively made of 1x640 cells (this grid will be referred in the following as grid A) and 1x1280 cells (grid B). Monitored benchmark quantities are the position of the interface, its sharpness and its velocity, together with the overall mass conservation and the instantaneous mass balance between the liquid fuel and the fuel vapor. The same test-case has been simulated in two dimensions; additional information about the setup together with the analysis of the results are included in App. C.

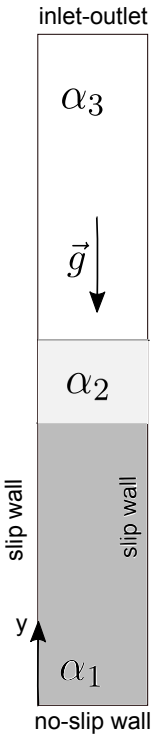

Initial Condition		
Parameter	cavitation case	condensation case
α_1	$\alpha_1(t_0)$=1, y $\in [0, 0.95)$	$\alpha_1(t_0)$= $\alpha_1(t_f)_{cav.}$
α_2	$\alpha_2(t_0)$=1, y $\in [0.95, 1)$	$\alpha_2(t_0)$= $\alpha_2(t_f)_{cav.}$
α_3	$\alpha_3(t_0)$=1, y $\in [1, 2]$	$\alpha_3(t_0)$= $\alpha_3(t_f)_{cav.}$
p	hydrostatic pressure	hydrostatic pressure
U	0 ms^{-1}	0 ms^{-1}
p_{sat}	100300 Pa	99700 Pa

Fluid Properties		
Parameter	Value	Unit
ρ_1	1000	$\mathrm{kg\,m}^{-3}$
$\rho_2 = \rho_3$	1	$\mathrm{kg\,m}^{-3}$
μ_1	10	$\mathrm{kg\,(ms)}^{-1}$
$\mu_2 = \mu_3$	0.1	$\mathrm{kg\,(ms)}^{-1}$
$\mathbf{g}$	-0.98	$\mathrm{m\,s}^{-2}$
$\sigma_{12} = \sigma_{13}$	1.96	$\mathrm{N\,m}^{-1}$

Figure 3.7: *Computational domain, boundary and initial conditions, fluids properties of the cavitation/condensation test case.*

The final purpose of the proposed benchmark is to establish a reference solution to quantify the conservation error of the solver and it can be interesting for comparison of the performance of different methodologies to model phase-change. The following quantities have been used:

1) evolution of the *mass of each phase*:

$$M_i = \int \alpha_i \rho_i dy \tag{3.11}$$

2) *liquid/vapor and vapor/air mean surface height*:

$$H_{lv} = \frac{\int \mathbf{y_c} \alpha_l (1-\alpha_l) dy}{\int \alpha_l (1-\alpha_l) dy} \qquad H_{va} = \frac{\int \mathbf{y_c} \alpha_{nc} (1-\alpha_{nc}) dy}{\int \alpha_{nc} (1-\alpha_{nc}) dy} \tag{3.12}$$

Where y_c represents the y component of cell centers

3) *liquid/vapor and vapor/non-condensable gas (air) mean interface velocity*:

$$\mathbf{u}_{lv} = \frac{\int \mathbf{U} \alpha_l (1-\alpha_l) dy}{\int \alpha_l (1-\alpha_l) dy} \qquad \mathbf{u}_{va} = \frac{\int \mathbf{U} \alpha_{nc} (1-\alpha_{nc}) dy}{\int \alpha_{nc} (1-\alpha_{nc}) dy} \tag{3.13}$$

As in the computation of height, the surface region is identified by the coexistence of the pair of phases.

4) time evolution of the *relative mass error*, to verify if mass is conserved during phase-change:

$$E_{marching} = \frac{|(M_l(t+1) - M_l(t)) - (M_v(t+1) - M_v(t))|}{M_l(t_0)} \tag{3.14}$$

This is a sufficient condition for global mass balance to be verified.

5) *global mass relative error*:

$$E_{global} = \frac{|(M_l(t_f) - M_l(t_0)) - (M_v(t_f) - M_v(t_0))|}{M_l(t_0)} \tag{3.15}$$

where subscripts 0 and f denote respectively the start and the end of the simulation.

A variable time-step is used in the simulation, to preserve a maximum Courant number $CFL_{max} = 0.1$. Second-order differencing schemes have been applied both for temporal and spatial derivatives.

3.2.2 Cavitation test: results

Starting from an hydrostatic distribution of pressure in the domain, the liquid starts cavitating (Fig. 3.8b). Being the vapor lighter than liquid, it moves towards the upper part of the domain and pushes the non-condensable gas (air) outside. In Fig. 3.8a the mass of air in the domain decreases, while the amount of vapor increases (Fig. 3.8c).

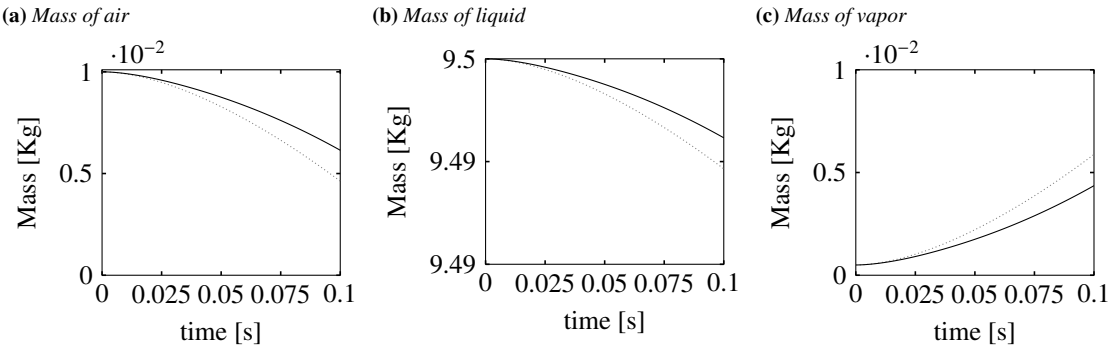

Figure 3.8: *One-dimensional cavitation problem, validation test case. Evolution in time of: (a) air mass (b) liquid mass; (c) vapor mass. Tests were carried out on two different grids: .... grid A (640 cells); — grid B (1280 cells).*

At the end of the simulation the surface height Δy of the vapor/air interface is larger if compared to that of the liquid/vapor, as shown in Fig. 3.9. Being the ratio $\rho_l/\rho_v \simeq 10^3$, the volume of the vapor from the cavitation is larger than the liquid volume.

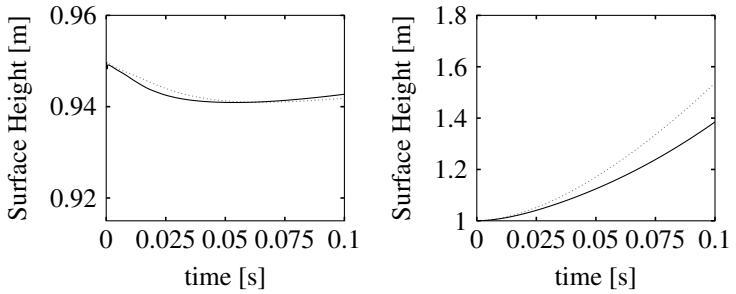

(a) *liquid/vapor height* **(b)** *vapor/air height*

Figure 3.9: *One-dimensional cavitation problem, validation test case. Evolution in time of the surface heights: (a) liquid/vapor (b) air/vapor on two different grids: .... grid A (640 cells); — grid B (1280 cells).*

The evolution of the two surfaces fronts is shown in Fig. 3.10. In both cases, the interface between the fuel vapor and the non-condensable gas (air) is sharp, because the vapor and the non-condensable gas (air) in the calculation have the same physical properties;

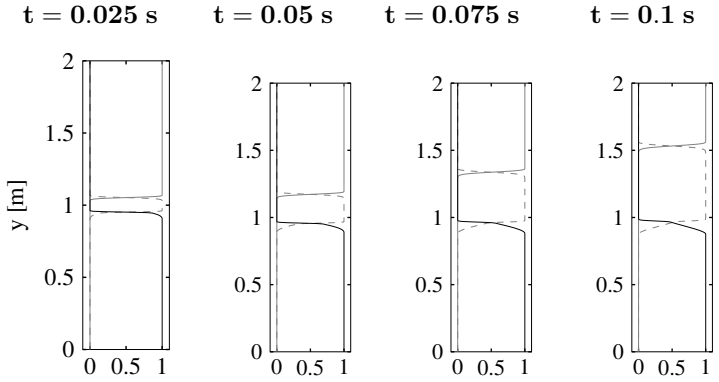

Grid A

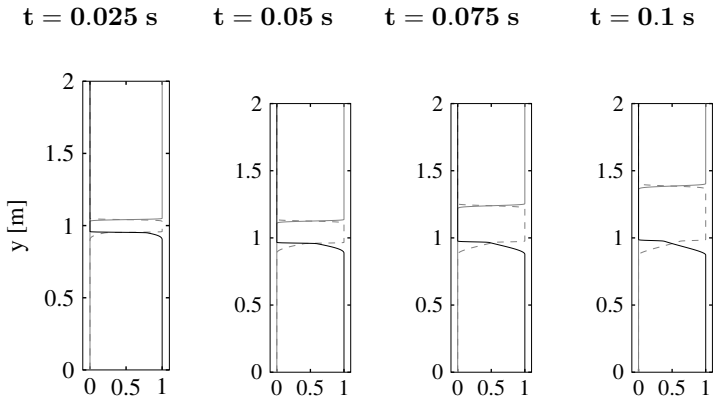

Grid B

Figure 3.10: *One-dimensional cavitation problem. Evolution of the void fractions from 0.025 to 0.1 s. Top) grid A, 1x640 cells; bottom) grid B, 1x1280 cells. Legend: α_l —, α_{nc} —, α_v – – –.*

this particular condition avoids any instability at the interface that would produce mixing of the fluids and then lead to a diffusion of the interface. Conversely, the liquid/vapor interface is stretched towards the opposite direction: vapor moves towards the upper part of the column, while liquid tends to stay at the bottom of the domain because of its higher density.

The liquid/vapor and the air/vapor interface velocities calculated by Eq. (3.13), are reported in Fig. 3.11a. The mass of each phase-fraction has then been monitored to compute the time step continuity error and the global conservation error for each phase.

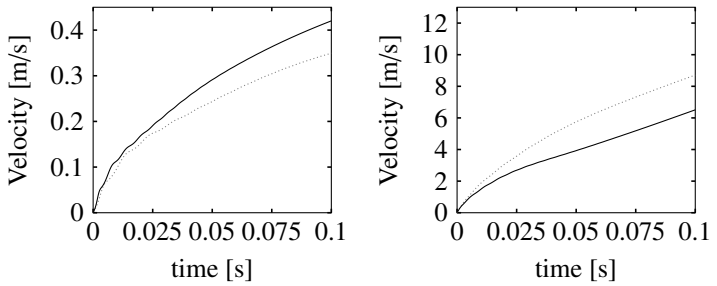

(a) *liquid/vapor* **(b)** *vapor/air*

Figure 3.11: *One-dimensional cavitation problem, validation test case. Evolution in time of the mean interface velocity (Eq. 3.13): (a) liquid/vapor; (b) vapor/non-condensable gas for two different grids: .... 640 cells;* **—** *1280 cells.*

The evolution of the time step continuity error is shown in Fig. 3.12 on the left. Both for the coarse (grid A) and the fine mesh (grid B), the error is very small. At the beginning of the simulation and in the early time steps (until time=0.02 s), it shows an increase that is dependent on the initial conditions, but it is then stabilized to a small value. As expected, the continuity error is larger for the coarsest grid than the finest grid, but it is still very small and therefore acceptable. In Fig. 3.12 the evolution of volume-weighted average void fractions:

$$\overline{\alpha}_i = \sum_{j=1}^{n_c} \frac{\alpha_{i_j} V_j}{V} \tag{3.16}$$

and the global conservation of the volume-weighted void fractions

$$\overline{\alpha} = \sum_{i=1}^{3} \overline{\alpha}_i \tag{3.17}$$

are shown. In Eq. (3.16) and (3.17), n_c is the number of computational cells, while V is the total volume of the mesh:

$$V = \sum_{j=1}^{n_c} V_j \tag{3.18}$$

As apparent from Fig. 13, the boundedness and conservativeness of the solution of the void fractions is satisfied. Also, the global mass error (Tab. 3.4) proves that mass is properly conserved during the simulation with very limited error peaks.

Table 3.4: *Relative error on the global mass conservation for the cavitation test case.*

No. cells	640	1280
$E_{global}\%$	0.11301	0.0811

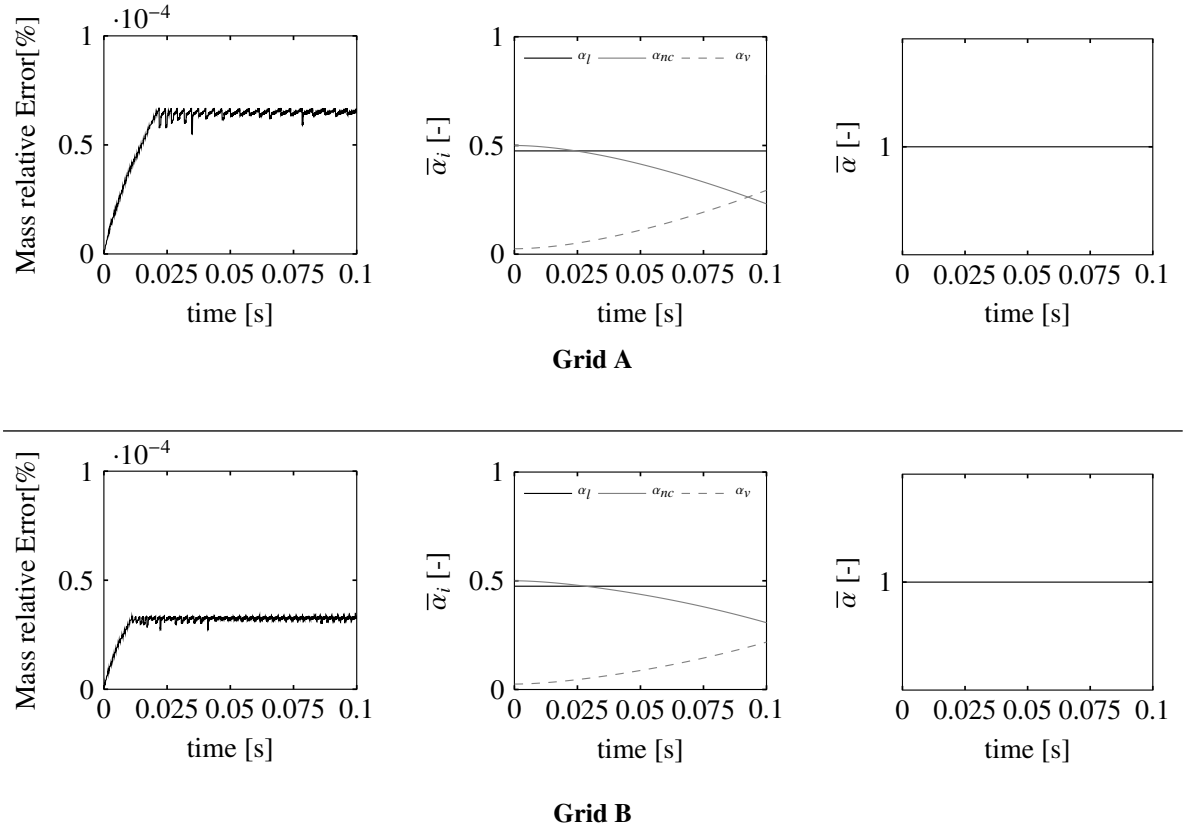

Figure 3.12: *One-dimensional cavitation test case, evolution in time of: left) mass relative error; center) volume-weighted void fractions; right) sum of the volume-weighted void fractions. Grid A: 1x640 cells. Grid B: 1x1280 cells.*

3.2.3 Condensation test: results

The distribution of the phase-fractions derived from the calculation of the liquid column problem with cavitation is then used as the initial condition for the condensation problem. In Fig .3.13a it is shown that as soon as the condensation is artificially triggered (by changing the threshold value of the liquid saturation pressure), the phase fractions of liquid and the vapor start changing: condensation induces negative velocity fluxes at the liquid/vapor interface, and the vapor changes direction of its motion, causing a suction of non-condensable gas (air) from the upper boundary.

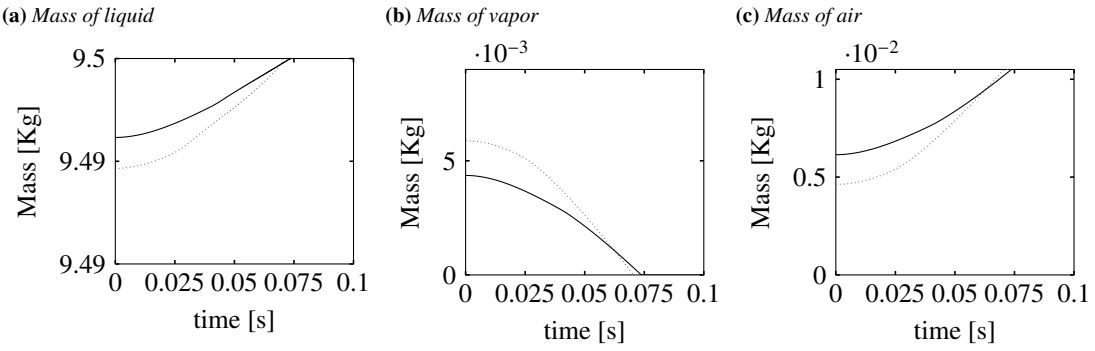

Figure 3.13: *One-dimensional condensation problem, validation test case. Evolution in time of: (a) liquid mass; (b) vapor mass and (c) air mass for two different grids: .... grid A; — grid B.*

At t= 0.075 s, the condensation is completed; this is confirmed either by the constant value of the surface height (Fig. 3.14) and by the evolution of the surface (Fig. 3.15). With condensation, the vapor/air interface is still quite sharp, despite fluctuations at the vapor/liquid interface are visible in Fig. 3.15 ($t = 0.05\ s$); their nature is purely numerical and their existence can be justified by analyzing the implicit and the explicit part of the source term in the discretized form of the void fraction equations, Eq. (2.56):

- when air impacts the liquid surface, the implicit part of the source term in the second equation of (2.56) reads:

$$B_v^n \left[\left(\frac{D\alpha_v}{Dt}^+ \right) - \left(\frac{D\alpha_v}{Dt}^- \right) \right]_p \tag{3.19}$$

  during condensation, $(\frac{D\alpha_v}{Dt}^-) = 0$ while $(\frac{D\alpha_v}{Dt}^+) > 0$; from Eq. (2.25), it follows:

$$\frac{D\alpha_v}{Dt}^+ = f(p - p_{sat}) \tag{3.20}$$

  if fluctuations in pressure appears, then an error peak in Fig. 3.17 is observed;

- the explicit part of the source term in the first equation of (2.56) is:

$$B_l^n \left(\frac{D\alpha_v}{Dt}^+ \right)_p^n (1 - \alpha_{nc})_p^n \tag{3.21}$$

  during condensation, $(\frac{D\alpha_v}{Dt}^+) > 0$, $p > p_{sat}$. By Eq. (3.20) and (3.21), pressure results linked to the evolution of the void fractions.

As shown in Fig. 3.17, non-conservation of mass is negligible but it is always present: this is a consequence of adding the source terms S_α for phase-change in the projection method as volume fluxes.

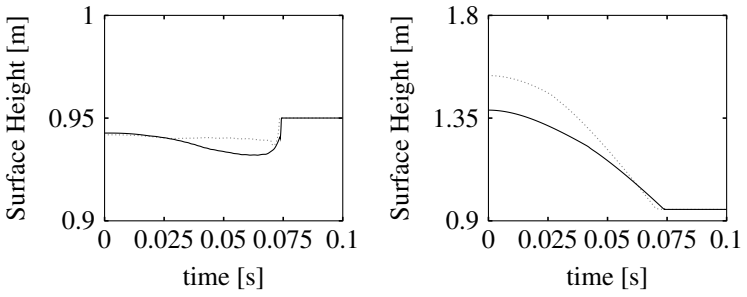

(a) *liquid/vapor height* **(b)** *vapor/air height*

Figure 3.14: *One-dimensional condensation problem, validation test case. Evolution in time of the surface heights: (a) liquid/vapor; (b) air/vapor on two different grids: .... grid A; — grid B*

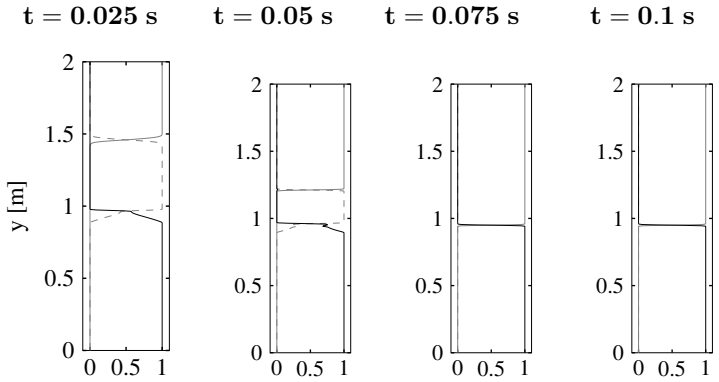

Grid A

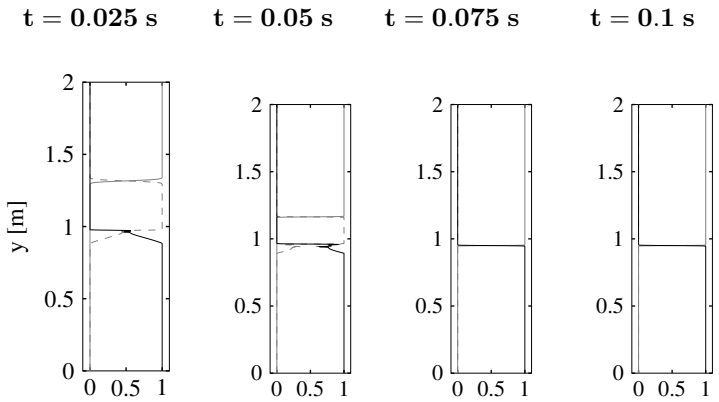

Grid B

Figure 3.15: *One-dimensional condensation problem. Evolution of the void fractions from 0.025 to 0.1 s. Top) grid A, 1x640 cells; bottom) grid B, 1x1280 cells. Legend: α_l —, α_{nc} —, α_v – – –.*

With condensation, the liquid/vapor and vapor/non-condensable gas (air) mean interface velocity (Eq. 3.13) becomes negative in the y direction and reaches the zero velocity condition in a steep way (see Fig. 3.16).

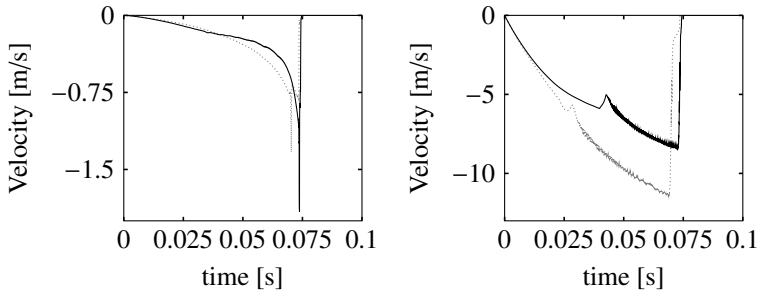

(a) *liquid/vapor* **(b)** *vapor/non-condensable gas*

Figure 3.16: *One-dimensional condensation problem, validation test case. Evolution in time of the mean interface velocity, Eq. (3.13): (a) liquid/vapor; (b) vapor/non-condensable gas for two different grids: .... 640 cells; — 1280 cells.*

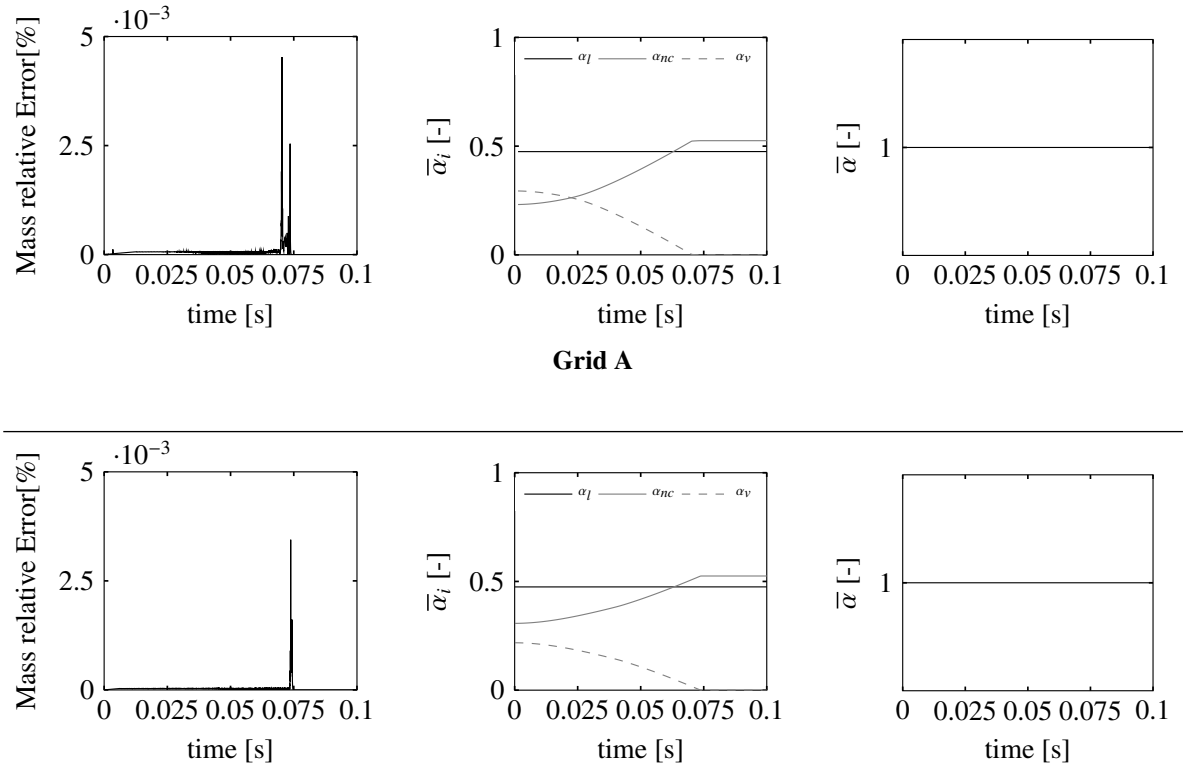

Figure 3.17: *One-dimensional condensation test case, evolution in time of: left) mass relative error; center) volume-weighted void fractions; right) sum of the volume-weighted void fractions. Grid A: 1x640 cells. Grid B: 1x1280 cells.*

Mean interface velocity in Fig. 3.16 is estimated by Eq. (3.13). In Fig. 3.16-b, minor fluctuations in the vapor/non-condensable gas mean interface velocity appear. This is a consequence of the numerical algorithm adopted for the iterative solution of Eq. (2.12), because the residual error at the last iteration is added to α_{nc}. The fluctuations in the solution of α_{nc} have a very minor impact on mass conservation (see Fig. 3.17, t<0.07 s). In Fig. 3.17, a peak in the error of the mass conservation is centered around t=0.075 s. From the analysis of the variation of volume-weighted void fractions in time, this peak occurs when the vapor fully

condenses ($\alpha_v \rightarrow$0) and the number of phases that switches from three to two. As shown in the same figure, the magnitude of the error peaks is very limited (about $4 \cdot 10^{-3}\%$) and the mass relative error follows the same trend that has been noticed in the cavitation problem: after a time of about 0.02 s, during which the error grows because of the initialization, the error stabilizes to a value of the order of $10^{-4}\%$. Also for condensation, it is then demonstrated that mass conservation is satisfied with a good level of accuracy. Boundedness and conservativeness of the solution of the void fractions (Eq. 3.16 and 3.17) in the domain is satisfied also here. Moreover, Fig.3.17 shows also that conservation of the void fraction with phase-change is preserved very well during the simulation: the global mass error (Tab. 3.5) is very limited with both the grids.

Table 3.5: *Relative (percentage) error on global mass conservation for condensation test case*

No. cells	640	1280
$E_{global}\%$	0.1126	0.0707

3.3 Validation Test: Simulation of Internal Nozzle Flows

The final problem used for the validation is based on the experiments from [199] and [23], that consist of water injection in an air reservoir. The thermodynamic conditions of the fluids are listed in Tab. 3.6.

Table 3.6: *Thermodynamic properties for* $\mathrm{H_2O_{(liq)}}$, $\mathrm{H_2O_{(vap)}}$, *and non-condensable gas (air) at T=20^o C.*

Parameter	Fluid			Unit
	$\mathrm{H_2O_{(liq)}}$	$\mathrm{H_2O_{(vap)}}$	air	
density	998	0.73853	1.19	$\mathrm{Kg/m^3}$
dynamic viscosity	$1.2 \cdot 10^{-3}$	$1.227 \cdot 10^{-5}$	$1.725 \cdot 10^{-5}$	$\mathrm{Kg/(ms)}$
surface tension	0.07			$\mathrm{N/m}$
saturation pressure	2300			Pa

The transparent injector presents an asymmetric nozzle with a squared-shaped cross-section. A sketch of the nozzle geometry and position of the Laser Doppler Velocimetry (LDV) beams is reported in Fig. 3.18, while a detailed description of the experimental apparatus is documented in [199] and [200].

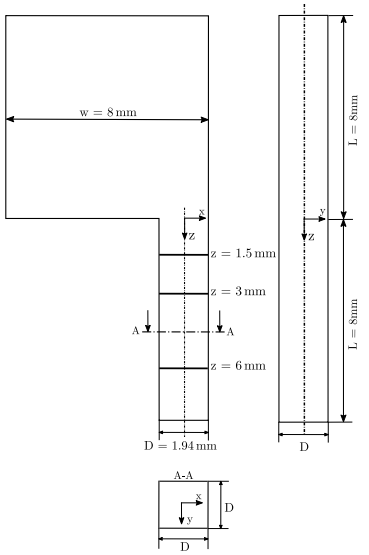

Figure 3.18: *Sketch of injector geometry and locations of LDV measurements.*

In the present work, the operating condition with an inlet pressure of $0.22\ \mathrm{MPa}$ was simulated and a validation with LDV measurements available from the literature is shown. Input parameters for the simulation are listed in Tab. 4.4; the cavitation number (Ca), the liquid Reynolds number (Re_l), the Weber number (We) and Ohnesorge number (Oh) are defined as follows:

$$Ca = \frac{p_{amb} - p_{sat}}{0.5\rho_l U_l^2} \tag{3.22}$$

$$Re_l = \frac{p_l U_l D}{\mu_l} \tag{3.23}$$

$$We = \frac{\rho_l U_l^2 D}{\sigma} \tag{3.24}$$

$$Oh = \frac{\sqrt{We}}{Re} \tag{3.25}$$

where p_{amb} is the ambient pressure, p_{sat} is the saturation pressure of the liquid, ρ_l the density of the liquid water and U_l is the mean liquid velocity computed from Measured volumetric flow rate and nozzle cross-section area.

Table 3.7: *Experimental operation condition for 0.22* MPa *operative point*

Parameter	Value	Unit
p_{inlet}	0.22	MPa
p_{amb}	0.1	MPa
Meas. Volumetric Flow Rate Q	$4.8 \cdot 10^{-5}$	m^3/s
Mean liquid Velocity U_l	12.8	m/s
Re	20577	-
Ca	1.2	-
We	4496.3	-
Oh	$3.26 \cdot 10^{-3}$	-

According to [174], being $\rho_l/\rho_{air} \sim 10^3$, the regime of the jet flow is in between second

wind-induced breakup and the atomization regime; the jet is therefore wavy, as it has also been observed in [199]. The cavitation number suggests the existence of a developing cavitation regime as well, where a vapor cloud forms without reaching the spray domain. The grid used for the simulations is reported in Fig. 3.19; in order to limit the overall number of grid cells by ensuring a proper resolution for a LES simulation, several refinement regions were selected and a wide use of cell gradings was adopted.

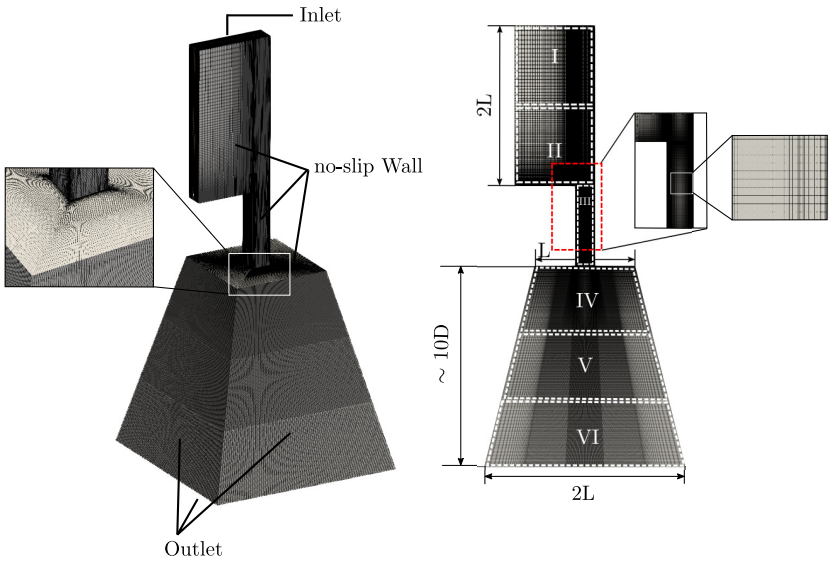

Figure 3.19: *Injector geometry: domain discretization and refinement regions.*

Overall information about mesh resolution, cell size and aspect ratio for each region is listed in Tab. 3.8.

Table 3.8: *Grid resolution and refinement levels for each mesh region.*

Mesh region	Mesh size [μm]			No. Cells
	x Ratio	y Ratio	z Ratio	
I	6.5/344	6.5/59.8	264/490	286120
II	6.5/344	6.5/59.8	26.5/264	1020377
III	6.5/59.8	6.5/59.8	26.5/106	1149840
Nozzle Refinement block	3.25/29.9	3.25/29.9	13.25/53	9005544
IV	7.5/443	7.5/443	27.8/58.3	5138880
V	54.6/531	54.6/531	58.3/85.1	2560000
VI	74.1/620	74.1/620	85.1/117	2016000
Domain				$\sim 2.1 \cdot 10^6$

In Fig. 3.19, the spray domain includes twelve refinement regions, four in the radial direction and three in the axial direction. Atmospheric pressure condition is applied on the lateral and bottom surfaces of the spray domain; no-slip wall boundary conditions on velocity are set at the walls. Both the fluids are assumed to be incompressible and isothermal; the numerical models and parameters are listed in Tab. 3.9.

Table 3.9: *Numerical setup and models parameter*

Numerical setup	
Bubble number density	$10^{15}\,\mathrm{m}^{-3}$
Bubble Nuclei Diameter	$1.5\,\mu\mathrm{m}$
Turbulence Model	LES-WALE [148]
CFL_{max}	0.25
Outer corrector	7
void fraction corrector	2
Precursor part	$4\,\mathrm{ms}$
Averaging part	$9\,\mathrm{ms}$

The averaging procedure on the benchmarked quantities to be compared with LDV measurements and analysis of spray pattern is calculated after $4\,\mathrm{m}s$ and it lasts $9\,\mathrm{m}s$. The numerical setup is the same as discussed in Sec. 2.7 and Sec. 3.1.1. Non-dimensional parameters calculated from the simulation results are in line with the values reported in Tab. 4.4. In Fig. 3.20, a comparison between simulation and experiments is shown; cavitation starts at the left corner, where a recirculation zone makes pressure drops below P_{sat}; this is classified as geometry induced cavitation.

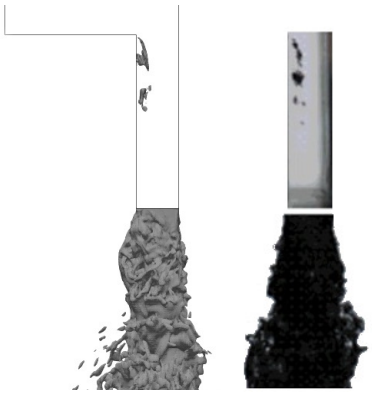

Figure 3.20: *Internal nozzle flow test case [199]. Left)* `interPhaseChangeMixingFoam`*; right) visualizations from experiments.*

The cloud of vapor does not reach the outlet of the nozzle but condensates at about $5\,\mathrm{mm}$ from the nozzle inlet. This developing cavitation regime is justified by the small inlet pressure of the experiment and by the high L/D ratio ($L/D \sim 4$); besides, it favors the detachment of fluid at the corner and the formation of a recirculation zone, where a consistent amount of turbulence is produced. In-nozzle turbulence is responsible of the primary breakup of the liquid jet at the nozzle tip, where the aerodynamic forces start triggering surface instabilities. In the specific operating point studied, vapor bubbles are not acting as promoters for the primary breakup since they collapse before reaching the spray domain; this usually happens at higher pressures at the inlet [61, 110, 199]. Comparisons with experimental profiles of average and rms values of the stream-wise velocity at three different positions inside nozzle from [199] are reported in Fig 3.21. Probes were located in the channel center plane ($x = 0\,\mathrm{mm}, y = 0\,\mathrm{mm}$) at different positions along the nozzle axis: $z = 1.5\,\mathrm{mm}$, $z = 3\,\mathrm{mm}$ and $z = 6\,\mathrm{mm}$ downstream of the nozzle entrance. In Fig 3.21, black filled circles are the experimental sampled points, while time-averaged CFD results are plotted as continuous black solid lines.

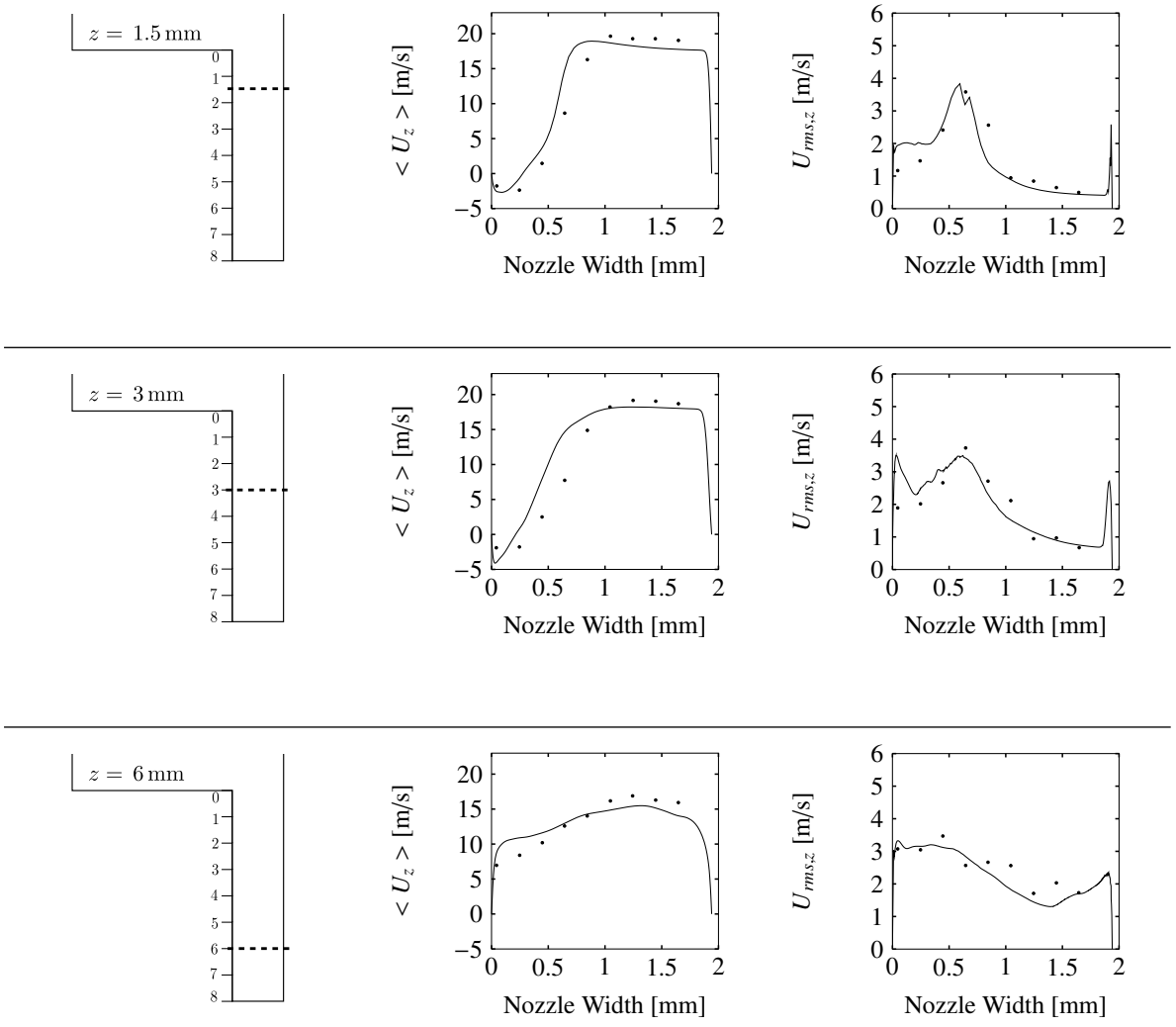

Figure 3.21: *Mean streamwise in-nozzle flow velocity and RMS turbulent velocity at different positions:* $z = 1.55\,\mathrm{mm}$ *(top),* $z = 3\,\mathrm{mm}$ *(middle),* $z = 6\,\mathrm{mm}$ *(bottom);* • *experiments [199]* — `interPhaseChangeMixingFoam`.

The agreement between experiments and predicted average velocity, also when both liquid and vapor are present, looks satisfying. This situation corresponds to negative velocity values ($z = 1.5\,\mathrm{mm}$, $z = 3\,\mathrm{mm}$) in the recirculation zone, where a certain amount of vapor is generated due to the pressure drop of the fluid at the nozzle entrance. At $z = 6\,\mathrm{mm}$, the vapor cloud has already collapsed and the stream-wise velocity assumes only positive values. Also rms values of the velocity are captured fairly well. The small over-prediction of the fluctuating velocity at the left-hand corner of the channel, when vapor and liquid are present at the same time, shows that the amount of predicted turbulent kinetic energy is too large in that region: this could be due to a slightly overestimation of vapor production along the shear layer which causes enhancement of the velocity gradients and thus of the turbulence production, as it has already been noticed in [110].

CHAPTER 4

Simulation Setup of glass nozzle injectors

In the following section are presented the two glass nozzle geometries chosen for the validation of the solver. The chapter is divided in three main sections:

- **The experimental setup**. The reason behind the choice of these geometries is outlined. Then, the experimental apparatus is described and particular attention is given to the geometrical features of each geometry.

- **The Numerical Setup**. The procedure used for the manipulation of the geometry, from CAD to mesh, is shown at first. Afterwards, the mesh is described and fluid properties, general hypothesis behind the simulation of multiphase flow and operative condition are presented. Finally, the simulation setup such as information about sampling planes, boundary/initial condition and numerical schemes and algorithm are listed.

- **The tool used for the analysis** are finally described.

4.1 Experimental Setup

The solver has been further validated on two glass-nozzle configurations. These two configurations have been chosen among ten glass-nozzle injectors which can be easily mounted on the same feeding system. Configurations ID-3 and ID-10 have been chosen because they have shown opposite behavior in terms of Jet Wise Penetration (JWP). They respectively represent the Worst of the Worst (WoW) and the Best of the Best (BoB) in terms of JWP. This is illustrated in Fig. 4.1 for the mentioned 10 configurations. The curves have been obtained averaging 20 experimental realizations. As a rule of thumb, it was decided to discard from the averaging procedure the realizations who have exhibited tip wetting (e.g for leakage of the fluid from the o-ring). This was necessary for preventing from the tip wetting affecting the average.

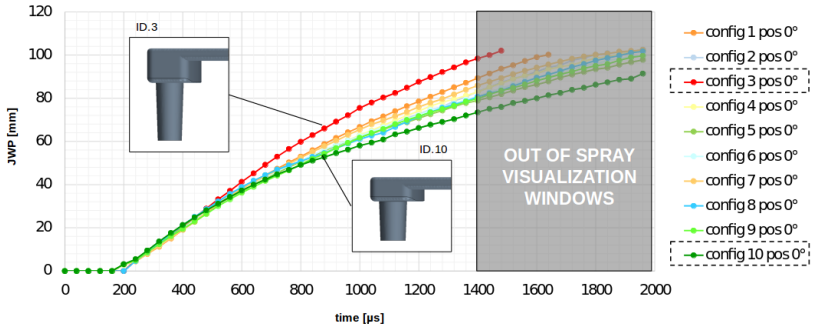

Figure 4.1: *JWP from 20 repetitions experiments. Realizations with tip wetting are discarded.*

These real-size/real-pressure glass nozzle injectors, *ad-hoc* built by Continental, have been studied to contribute to the nozzle design and cavitation control for GDI injectors [5]. The geometrical features of the prototype have been thought to reproduce a single-hole injector, representing a $60\,^\circ$ sector of a real multi-hole injector, as reported in Fig. 4.2 . This includes the needle, the sac geometry, the hole geometry and the external nozzle shape. The injector prototype has been built in quartz glass (fused silica) by a laser-etched manufacturing process [5]. A surface roughness of $1 - 3\,\mu m$ is obtained. This corresponds to the order of magnitude of micro-EDM (Electrical Discharge Machining) process that is typically used for manufacturing process of real injectors. A sample is shown in Fig. 4.3a. The fully transparent nozzle has been demonstrated to be compatible with rapid prototyping approach with complex geometrical changes. It can withstand pressure up to $350\,bar$ and it is compatible with any working fluid. The sector angle is slightly enlarged to respect the $60°$ flow, even if the side wall presence and the single hole presence are obviously a modification if compared to real injectors. These samples have been validated in simple central single-hole test cases and tested with convergent, straight and divergent holes [5]. The nozzle is connected to an actuated valve, placed on the upper position of the quartz part, that is connected to the needle. Experimental tests of liquid-into-air injection have been carried out at a needle lift of $79\,\mu m$, that is fully representative of a fully opened nozzle; n-Heptane was chosen as working fluid, despite both the numerical solver and the test bench are able to work with real fuels. Then, the injector geometry has been measured by a multisensor coordinate measuring machine based on a X-ray computed tomography (see Fig. 4.3b and Fig. 4.3c), as a check of the quality of the manufacturing process and to ensure correspondence between simulated and experimental geometry. The XCT is a V Tome XS 240 kV from General Electric.

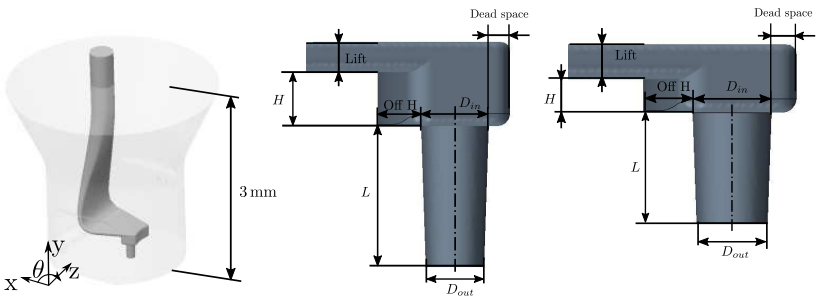

Figure 4.2: *Geometry of the feeding system (left), the nozzle geometries studied, named as configuration ID-3 (middle), ID-10 (right).*

The nano-focus, 180 kV x-ray tubes at $18\,W$ (maximum power) has been used together with a tungsten-synthetic diamond target. It is worth mentioning that high resolution XCT cannot properly capture sharp edges; this may be a serious limit when dealing with injectors, because the sharpness of the edges strongly influences the development of cavitation at nozzle entrance. To correct this bias, measurements at the microscope were therefore used to quantify the hole edge rounding and to verify the average wall roughness (that were both found to be smaller than 1 μm). Hence, a manual correction of the geometrical STL file has been performed to recover the sharp edges. XCT measurements are shown in Fig. 4.3 and the design values confirmed by XCT are presented in Tab. 4.1.

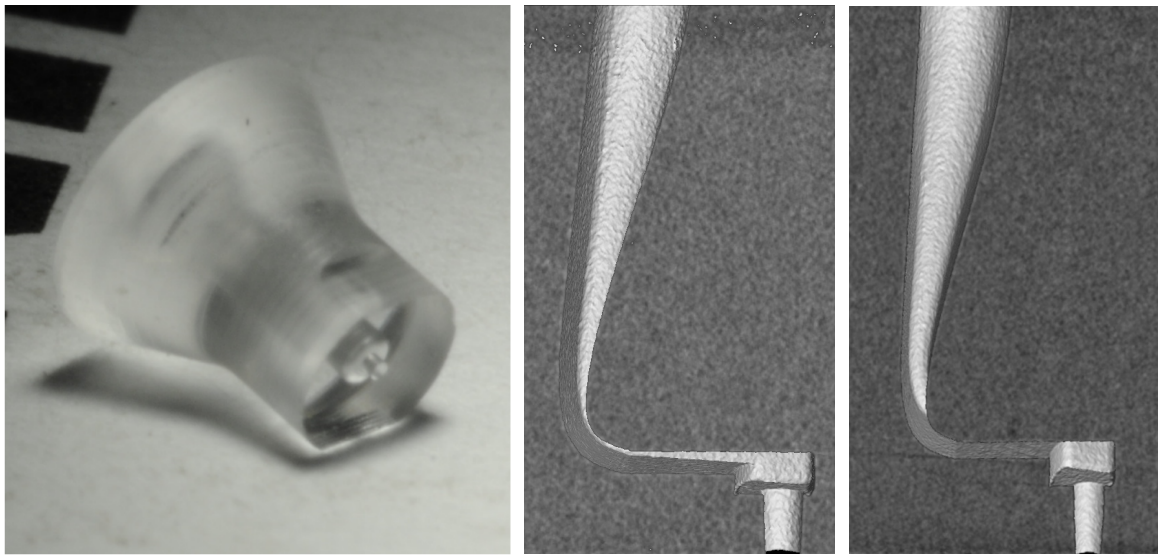

(a) (b) (c)

Figure 4.3: *Transparent glass nozzle replica sample: a) external view; b) XCT visualization of glass nozzle side of config-3; c) XCT visualization of glass nozzle side of config-10*

Experiments were carried out for an injection pressure of $100\,bar$. The liquid n-Heptane was injected in a reservoir with air at ambient conditions. Experimental shadowgraphies have been taken using a long-range microscope; a white steady light in the background of the area of interest was achieved by the use of a half-inch flexible fiber optic light guide in combination with a powerful LED illuminator. Image acquisition was done at $100\,kHz$ with an exposure time of 2 μs by a Phantom V1210 high-speed video camera.

Table 4.1: *Geometrical features of the glass nozzles from XCT measurements.*

Quantity	Dimension config-10 [μm]	Dimension config-3 [μm]
curvature radius 1 (CR1)	140	131
curvature radius 2 (CR2)	237	220
nozzle length (L)	241	351
sac height (H)	78.5	136
inlet diameter (D_{in})	165	166
outlet diameter (D_{out})	148	147
lift	79	80.04
off h	78.5	102
dead space length	44.9	38
$K_{geom} = (\frac{D_{in}-D_{out}}{D_{out}} \cdot 100)$	10.52	12.92

4.2 Numerical Setup

4.2.1 Discretization

Fig. 4.4 shows the process followed for the geometry reconstruction proposed in the present work: from the nominal CAD project the transparent glass nozzle replica has been built up. XCT and microscope measurements have been used to reconstruct an estimate of the real surface in stereolitography format (STL).

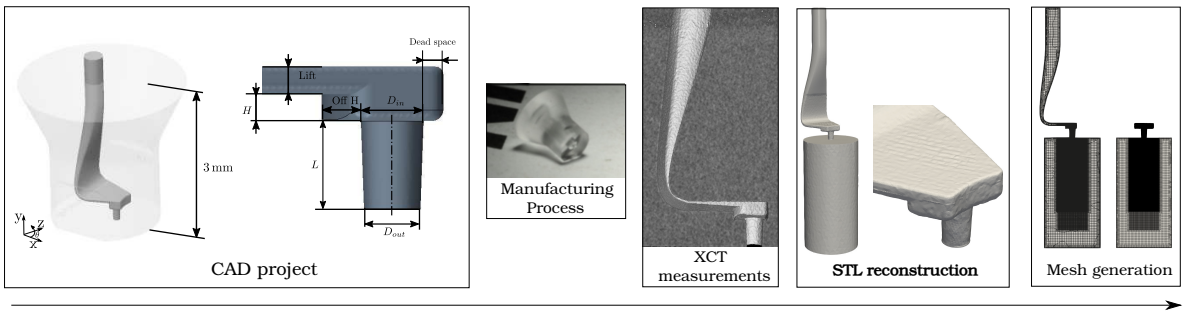

Figure 4.4: *Sketch of the process from CAD project to mesh generation*

Being LES calculations computationally very expensive, it is important to check that the input geometry for the solver does not differ from the actual injector before the simulation actually runs. In this sense, the comparison between the nominal and the real geometry allowed to verify this aspect and also to quantify the quality and the reliability of the manufacturing process. Thus, the reconstructed geometry was finally compared to the nominal geometry and it was used to generate the computational mesh after the sharpness of the edges has been manually recovered. In Fig. 4.5 are shown the details of the meshes generated from the STL file reconstructed from XCT and microscope visualizations. The grid features 70 million of (polyhedral) cells, that allow different refinement levels in the different regions of the injector geometry, as show in Fig. 4.5.

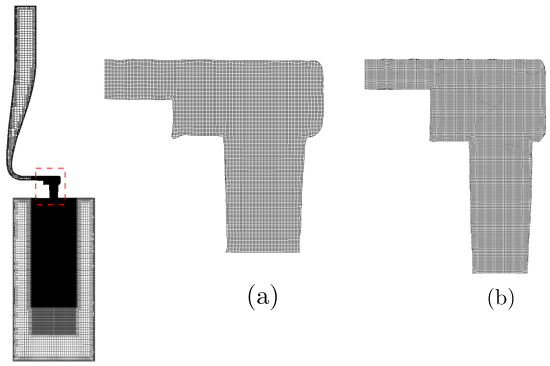

Figure 4.5: *Discretization adopted for the simulation for the two configurations. On the left is shown the ambient domain refinement, on the right the discretization used in the nozzle. (a) config. ID-10, (b) config. ID-3*

The nozzle region is followed by an open cylindrical reservoir (a portion of the ambient volume where injection takes place) with different cell refinement levels. In particular, the

grid is fine in the region where the cavitation and the atomization occurs and it is much coarser elsewhere:

- the finest refinement region having average cell size of $1\ \mu\mathrm{m}$ covers the sac, the nozzle and part of the reservoir, where primary atomization takes place;
- a region with average cell size of $8\ \mu\mathrm{m}$ is used in between the fine and the coarse regions of the grid and it is located in the reservoir, near the outlet of the domain.
- the coarse cell region features an average cell size of $40\ \mu\mathrm{m}$ and it is used where the flow is fully liquid (injector inlet) and in the buffer regions.

In the work of Fuster et al. [69], several numerical results of primary breakup using an Adaptive Mesh Refinement (AMR) technique show a fairly good agreement with experimental data. The multiphase solver that will be used in this work is able to support dynamically load-balanced Adaptive Mesh Refinement (AMR), but the authors' choice was to use a static polyhedral grid because:

1. As for any topological change, AMR has a negative impact on the accuracy in the calculation of the temporal derivatives (see a brief discussion in Appendix A of [233]);
2. In the LES simulations presented in this work, the initial grid must have a large number of cells: AMR has a non-negligible impact on the simulation time, because it requires the mesh connectivity to be updated anytime AMR is triggered;
3. The operation of the LES filtering is changing with the dynamic topological change of the mesh due to the AMR;
4. AMR causes load unbalance among the processors; dynamic load balancing with AMR is supported by the solver used, this procedure implies additional computational load.

In other words, for the large cases simulated in this work, the advantages of AMR might be not so apparent.

Experiments have been carried out at Continental Automotive SAS in the site of Toulouse, where the experimental apparatus is located. The aim of the experiments was to provide a detailed visualization of the in-nozzle flow and of the extent primary jet breakup. Tests have been carried out using high speed camera for two different view angles, $\theta_1 = 0^\circ$ (front view) and $\theta_2 = 90^\circ$) (lateral view), being θ the azimuthal angle as shown on the left picture of Fig. 4.2;. n-Heptane was chosen as representative of a real fuel; thermophysical properties of n-Heptane are listed in Tab. 4.2.

Table 4.2: *Thermodynamic properties for* $\mathrm{n-Heptane_{(liq)}}$, $\mathrm{n-Heptane_{(vap)}}$ *at T=25^o C, and non-condensable gas (air) at T=15^o C.*

Parameter	Fluid			Unit
	$\mathrm{n-Heptane_{(liq)}}$	$\mathrm{n-Heptane_{(vap)}}$	air	
density	684	4.25	1.225	$\mathrm{Kg/m^3}$
dynamic viscosity	$4.0835e^{-4}$	$7.0125e^{-6}$	$1.7885e^{-5}$	$\mathrm{Kg/(ms)}$

The saturation pressure and the surface tension coefficient are reported in Tab. 4.3. The fuel supply is obtained using a low-pressure electrical pump, a heat exchanger (to cool down), a high pressure pump (CPT), a common rail to damp oscillation, a fuel supply line with a pressure sensor (Kistler) to the injector-valve followed by the tested transparent nozzle. The outlet condition is ambient. In the present work inlet fuel pressure has been set to 100 bar.

Even though the solver has been conceived for isothermal condition, the Tab. 4.2 reports the fluid properties computed at two different temperatures. In experiments usually n-Heptane and air have a different temperature: n-Heptane is usually warmer, 25^oC, while air in the injection chamber stays at 15^oC. Under isothermal approximation, the sensible heat exchange that would have been occurred during fuel-air mixing has been therefore neglected.

Table 4.3: *Thermodynamic properties for* $\mathrm{n-Heptane}$*, at T=25° C.*

Parameter	Value	Unit
surface tension	0.019517	$\mathrm{N/m}$
saturation pressure	7000	Pa

Contrary to the previous test case used for validation, which has involved water at pressure of $2\,bar$, here the injection pressure is 50 times higher, and vapor phase could be subject to compressibility effect. As shown in Fig. 4.6, at pressure for which cavitation is reached (at constant temperature), the liquid phase exhibits a very high speed of sound, which makes the hypothesis of incompressibility valuable. On the other hand, at $0.07\,bar$ the vapor has a speed of sound of $161\,m/s$ which is of the same order of magnitude of the maximum velocity reached in the nozzle (See Fig. 5.29a).

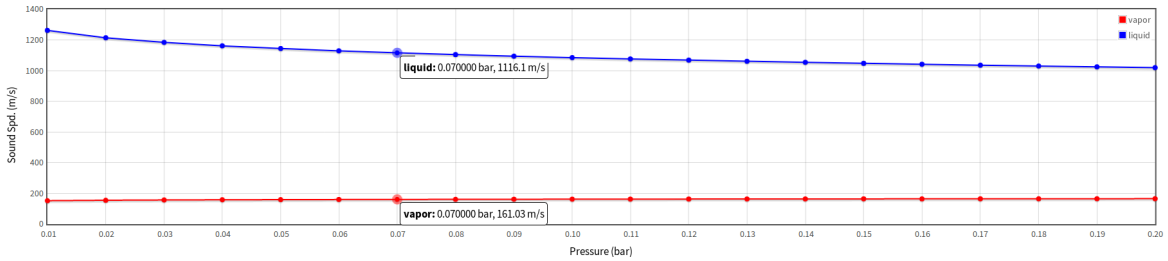

Figure 4.6: *Speed of sound of n-Heptane vapor (in red) and liquid (in blue) at 300K, for a pressure region close to the onset of cavitation*

However, under one fluid model approximation, the solver does not resolve for vapor velocity but rather for a mixture velocity. The mixture velocity resolved is much more affected by the phase that occupies the most of the nozzle. Moreover, the time scales of cavitation/condensation (which are represented by the inverse of source term in the void fraction equations) are 3-4 order of magnitude higher than the time scales of an acoustic wave propagating in the vapor produced in the nozzle. It means that before one can see the compressibility effect of the vapor, the vapor has already disappeared.

Input parameters for the simulation are listed in Tab. 4.4; the cavitation number K according to Nurick [149] and the cavitation number C according to Bergwerk [22], the liquid Reynolds number (Re_l), the liquid Weber number (We) and Ohnesorge number (Oh) are

defined as follows:

$$K = \frac{p_{inj} - p_{sat}}{p_{inj} - p_{back}} \tag{4.1}$$

$$C = \frac{p_{inj} - p_{back}}{p_{back} - p_{sat}} \tag{4.2}$$

$$Re_l = \frac{\rho_l U_l D}{\mu_l} \tag{4.3}$$

$$We = \frac{\rho_l U_l^2 D}{\sigma} \tag{4.4}$$

$$Oh = \frac{\sqrt{We}}{Re} \tag{4.5}$$

$$\tag{4.6}$$

where p_{inj} is the upstream fuel pressure, p_{back} is the downstream chamber pressure, p_{sat} is the saturation pressure of the liquid, ρ_l the density of the liquid n-Heptane and U_l is the mean liquid velocity defined as:

$$\mathbf{U}_l = \frac{< \dot{m} >}{\rho_l A_{N_6}} \tag{4.7}$$

where A_{N_6} is the cross-sectional area of the N_6 plane, ρ_l is the density of the liquid n-Heptane and $< \dot{m} >$ is the time-averaged Mass Flow Rate (MFR) from experiments.

Table 4.4: *Experimental operation condition for 100* bar *operative point for ID-3 and ID-10*

Parameter	ID-10 Values	ID-3 Values	Unit
p_{inlet}	10	10	MPa
p_{amb}	0.1	0.1	MPa
Mean liquid Velocity U_l	155.07	149.43	m/s
Re at plane N_6	36110	35104	-
Re at plane S_1	14499		-
K	1.0095	1.0095	-
C	104.9422	104.9422	-
We	110049	104712	-
Oh	0.009187	0.009218	-

The two configurations fall in the *atomization regime* region as shown in Fig. 4.7.

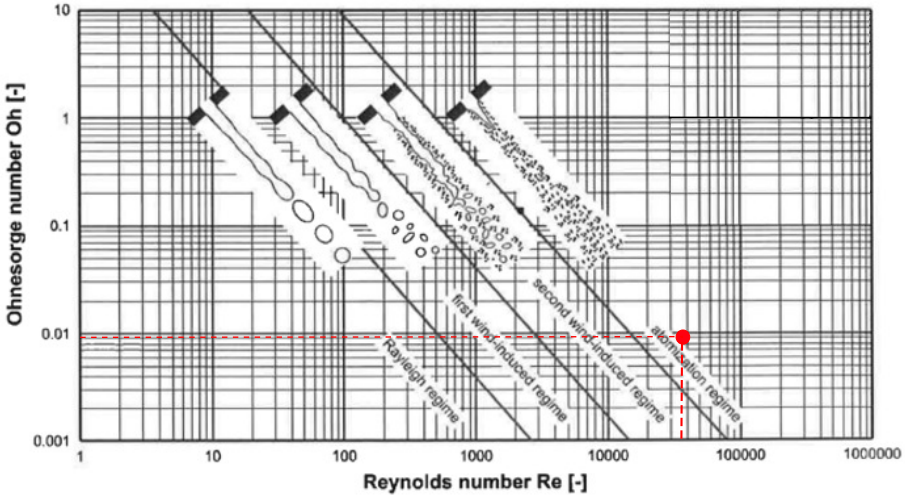

Figure 4.7: *Diagram [Re]-[Oh] of Atomization regimes [174]. Red circle denotes the zone of atomization regimes of ID-3 and ID-10*

4.2.2 Simulation setup

For what concern the internal nozzle flows, average and rms values are computed on several different sections:

- three planes in the sac (see Fig. 4.8a). S_1 before the step, S_2 and S_3 after the step and perpendicular to the nozzle axis;
- six cross-planes, perpendicular to the nozzle axis (see Fig. 4.8b);
- two cutting planes, parallel to the nozzle axis (see Fig. 4.8c). D_1 and D_2 correspond respectively to $\theta_1 = 0°$ and $\theta_2 = 90°$;

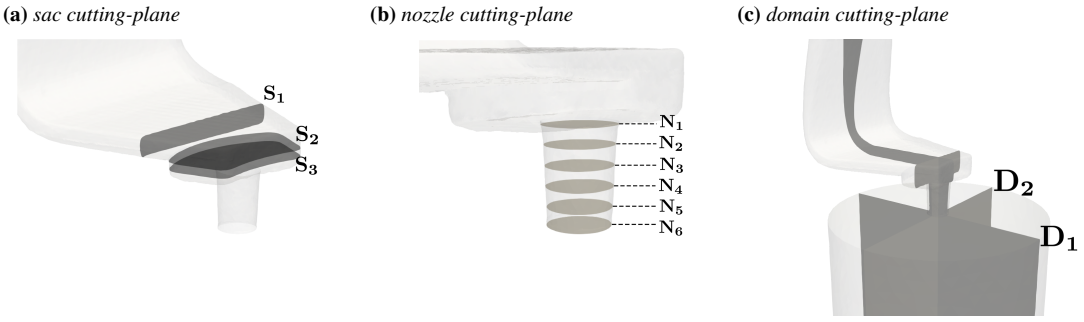

Figure 4.8: *Planes used for the visualization of the resolved quantities*

For the primary break-up, visualization of average fields are reported on D_1 and D_1 (See Fig. 4.8) as well and on some additional section perpendicular to the nozzle axis. These are called A_1, A_2, A_3, A_5 and are shown in Fig. 4.9a. Each plane is spaced $0.25\,mm$; the first plane (A_1) is $0.25\,mm$ far from the nozzle outlet and the last plane (A_5) is $1\,mm$ far from the nozzle outlet.

Then, time average of spatial weight-averaged quantities (such as axial velocity, non axial velocity, void fractions, vorticity, pressure, density) are computed on the planes in the finer

region ($2\,mm$), as shown in Fig. 4.9. In Fig. 4.9b, each plane is spaced $0.1\,mm$. The first plane is located at $0.1\,mm$ from the nozzle outlet and the last plane used is placed at $1.9\,mm$ from the nozzle outlet. A total of 19 planes have been used.

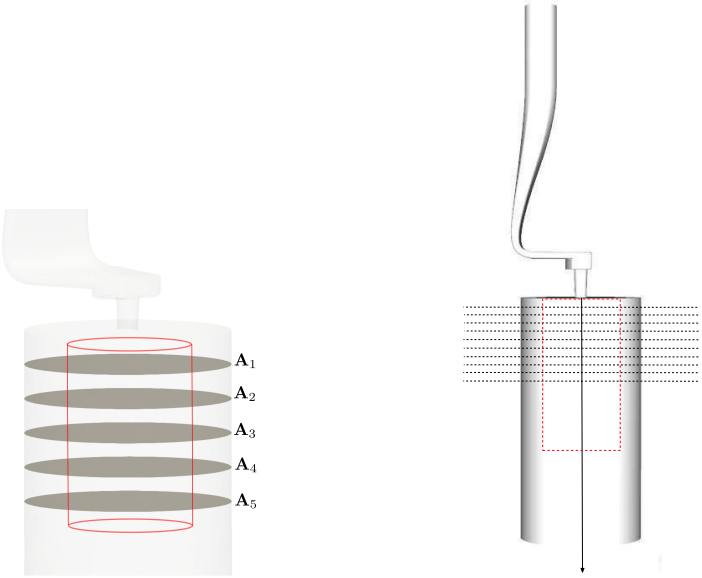

(a) *field ambient cutting plane*

(b) *trend ambient cutting-plane*

Figure 4.9: *Planes used for the visualization of the resolved quantities and spray analysis in the ambient domain. The region used for the space average on the planes stays within the red-dashed rectangle.*

4.2.3 Boundary and Initial conditions

Initialization of a multiphase injection poses great issues on the numerical convergence in the very early instants of the simulation. The simulation is performed starting from a quiescent state ($\mathbf{U} = 0$ everywhere in the domain). $\hat{p}$ is set to atmospheric pressure, which corresponds to the value of the ambient region where atomization process occurs. The injector, the upstream feeding region and the sac are set full of liquid ($\alpha_l = 1$), while the ambient domain is set full of non-condensable gases ($\alpha_{nc} = 1$). The boundary conditions are listed in Tab. 4.5.

patch	inlet	outlet	walls
U	`pressureInletOutletVelocity`	`pressureInletOutletVelocity`	`noSlip`
$\hat{p}$	`uniformTotalPressure`	`totalPressure`	`fixedFluxPressure`
p	`calculated`	`calculated`	`calculated`
nut	`zeroGradient`	`zeroGradient`	`zeroGradient`
α_l	`uniform 1`	`inletOutlet` (inlet value 0, value 0)	`zeroGradient`
α_v	`uniform 0`	`inletOutlet`(inletValue 0, value 0)	`zeroGradient`
α_{nc}	`uniform 0`	`inletOutlet` (inletValue 1, value 1)	`zeroGradient`

Table 4.5: *Boundary conditions for the simulation of configurations ID3 and ID10.*

Similarly to Riemann's problems, the simulation of a multiphase flow deals with the description of a discontinuity (here the the interface among phases); therefore, the total pressure condition can be set both on inlet and outlet. However, to favor the numerical convergence, the inlet pressure is not imposed as a step function of 100 bar but rather as a ramp from P_{atm} to $P_{inlet} = 100\ bar$. This condition has been provided by the `uniformTotalPressure`

BC. Additionally, a source term on the momentum equation is used to limit the velocity in the early stages of the injection: some cells can reach non-physical values of velocity who may lead to numerical instabilities and often to an impairment of the simulation. As soon as injection progresses, and pressure at the inlet reaches the nominal pressure, vapor is generated through the phase-change model embedded in the void-fraction equations.

4.2.4 Numerical Schemes and Algorithms

The numerical setup is the same as discussed in Sec. 2.7, Sec. 3.1.1 and Sec. 3.3.

4.3 Tools used for the analysis

4.3.1 Time Averaging process

Since LES approach is used for the current work, it is possible to distinguish two different parts of the simulation:

1. *Initialization*. The case is set up using a ramp of pressure at the inlet, till it reaches the value of 100 bar. This is necessary to avoid numerical instability during the early stage of the injection. Once the nominal value of pressure is reached, the simulation is made run until the Mass Flow Rate (MFR) at the nozzle outlet is stabilized. In the present work, MFR stabilized at $112\,\mu s$; from that time, temporal statistics started being calculated.

2. *Averaging*. Temporal running average has been calculated after the statistical convergence was reached. In general, for a time-space dependent variable $\phi(\mathbf{x}, t)$, it states:

$$< \phi(\mathbf{x}, t) >^{n+1} = (1 - \beta) < \phi(\mathbf{x}, t) >^{n} + \beta\phi(\mathbf{x}, t)^{n} \tag{4.8}$$

with $\beta = \Delta t^n / \Delta t_{tot}$, where the Δt^n is the time step advancement fixed by the CFL and Δt_{tot} is the time window in which the averaging is performed:

$$\Delta t_{tot} = \sum_{j=0}^{f} (t_{j+1} - t_j) \tag{4.9}$$

where t_0 is the value of time which denotes the beginning of average part, and t_f is the end time of the simulation. The same procedure is used for the computation of the running variance:

$$(\phi(\mathbf{x}, t)^2_{rms})^{n+1} = (1 - \beta)(\phi(\mathbf{x}, t)^2_{rms})^{n} + \beta(\phi(\mathbf{x}, t)^{n})^2 - (< \phi(\mathbf{x}, t) >^{n})^2 \tag{4.10}$$

4.3.2 Space Averaging process

In the nozzle and near the nozzle tip, it is more interesting to analyze on planes some particular quantities of interest using different weights. In general the space average of time-space dependent variable $\phi(\mathbf{x}, t)$ reads:

$$< \phi(\mathbf{x}, t) >_s = \frac{\sum_{j=1}^{k} \phi(\mathbf{x}, t)_j \cdot W_j}{\sum_{j=1}^{k} W_j} \tag{4.11}$$

Where $j = 1, ..., k$ is the j-th face of the plane of k-faces on which spatial average is computed. W_j denotes the weight used for the average. Defining $\mathbf{S_f}_j = \mathbf{n_f}_j |\mathbf{S_f}_j|$ the surface area vector and $\mathbf{n_f}_j$ the face unity normal vector, W assumes several formulation depending on the quantity used.

1. Mass flow rate weighting.

$$W(\mathbf{x},t)_j = \rho(\mathbf{x},t)_j|\overline{\mathbf{U}(\mathbf{x},t)}_j \cdot \mathbf{S}_{\mathbf{f}j}| \tag{4.12}$$

2. Area average

$$W_j = |\mathbf{S}_{\mathbf{f}j}| \tag{4.13}$$

3. Normal area average:

$$W_j = \mathbf{S}_{\mathbf{f}j} \tag{4.14}$$

For other quantities simple integral is used:

$$\phi(\mathbf{x},t)_s = \int_S \phi(\mathbf{x},t) \cdot d\mathbf{S} = \sum_{j=1}^{k} \phi(\mathbf{x},t)_j \cdot \mathbf{S}_{\mathbf{f}j} \tag{4.15}$$

Both Eq. 4.11 and Eq. 4.15 can be computed at each temporal advancement of simulation. Therefore, average and variance are then computed using their values from t_0 to t_f.

4.3.3 Mean flow direction reference frame

In complex geometries, as injectors, the mean flow direction is barely oriented as the nozzle axis direction. Time to time, the flow direction along nozzle axis changes by the unsteady effects such as cavitation, fluid vena detachment at the nozzle inlet, and vortex structures along the nozzle. Therefore, flow field direction is both function of space and time. The unity normal flow field direction $\mathbf{n}_U$ is computed from the local velocity field as:

$$\mathbf{n}_U(\mathbf{x},t) = \frac{\overline{\mathbf{U}(\mathbf{x},t)}}{||\overline{\mathbf{U}(\mathbf{x},t)}||} \tag{4.16}$$

Thus, over a discrete plane, $\mathbf{n}_U$ can be defined for each j-th face of the plane in every instant of time. In general, it is of major importance understand how the average flow direction will evolve in the nozzle. This information provides a better comprehension of the jet deviation in the primary breakup and which is the redistribution of the main flow among axial mean flow direction and non-axial mean flow direction. Using Global Reference Frame (GRF) (y-axis oriented as the nozzle axis) to analize axial flow and non-axial flow would bias the values of these quantities. For this purpose, for each sample plane used in the nozzle (N_1,N_2,N_3,N_4,N_5,N_6), it will be defined a space average flow reference frame using Eq. 4.11:

$$< \mathbf{n}_U(\mathbf{x},t) >_s = \frac{\sum_{j=1}^{k} \mathbf{n}_U(\mathbf{x},t)_j \cdot |\mathbf{S}_{\mathbf{f}j}|}{\sum_{j=1}^{k} |\mathbf{S}_{\mathbf{f}j}|} \tag{4.17}$$

Then, the time average of the mean flow direction is computed in the useful time-window. This is denoted with $<< \mathbf{n}_U >_s>$. The velocity field of the GRF on the planes is projected on the new Local Reference Frame (LRF) for each plane. It reads:

$$proj_{<<\mathbf{n}_U>_s>}\overline{\mathbf{U}}_j = \frac{<< \mathbf{n}_U >_s> \cdot \overline{\mathbf{U}}_j}{|| << \mathbf{n}_U >_s> || \, ||\overline{\mathbf{U}}_j||} << \mathbf{n}_U >_s> \tag{4.18}$$

Example of the possible differences existing between $\mathbf{n}_U$ (LRF) and y-direction (GRF) are shown in Fig. 4.10.

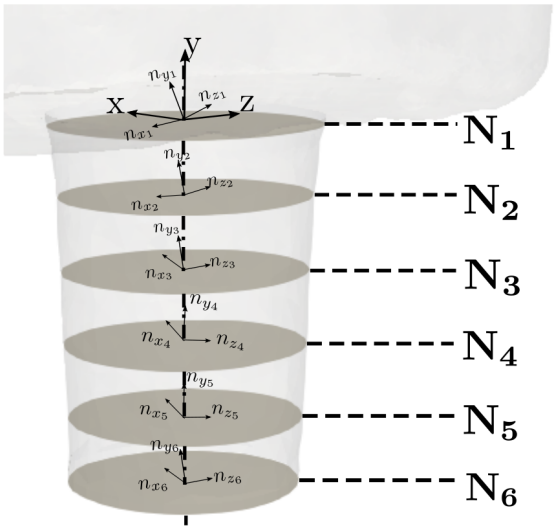

Figure 4.10: *Global Reference Frame and Local Reference Frame in the nozzle, on* N_1,N_2,N_3,N_4,N_5,N_6 *planes*

For a generic plane i and a generic face j belonging to plane i, axial velocity and non-axial velocity are respectively computed in the j-th face of the plane as:

$$\mathbf{U}_{axial_i} = (proj_{<<\mathbf{n}_U>_s>_i} \overline{\mathbf{U}}_{j_i}) \cdot [0, n_{y_i}, 0] \tag{4.19}$$

and

$$\mathbf{U}_{non-axial_i} = \sqrt{((proj_{<<\mathbf{n}_U>_s>_i} \overline{\mathbf{U}}_{j_i}) \cdot [0, 0, n_{z_i}])^2 + ((proj_{<<\mathbf{n}_U>_s>_i} \overline{\mathbf{U}}_{j_i}) \cdot [0, 0, n_{z_i}])^2} \tag{4.20}$$

4.3.4 Streamlines

Streamlines denotes a family of curves instantaneously tangent to the velocity field in each point of the domain. These show the direction in which a massless fluid element will travel at any point in time (mass cannot cross streamlines). In the present work the streamlines are computed from the average velocity components. If reported on a 2D plane they are computed from the average velocity components belonging to the plane on which are shown. These support the reader in the identification of the average vortical structures. Alternatively, they denote the projection of the 3D average streamlines on a plane. For sake of clarity, 3D average streamlines have been reported as well.

4.3.5 Side, direct, reverse flows

In an injector, knowing which part of the nozzle is more fed by the fuel than another zone can help to determine which are the zones subjected to the highest fluid vena detachment, which ones to the highest recirculation, and which are the main geometrical parameters influencing the inlet flow field the most. A sketch of the flow field expected to occur in the sac is shown in Fig. 4.11.

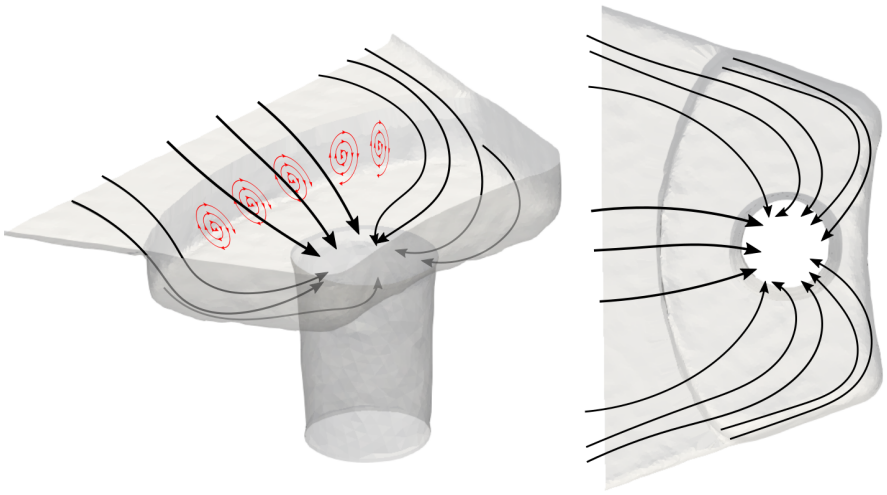

Figure 4.11: *Sketch of the flow field feeding the injector.*

For this purpose, three velocity field respectively namely side flow, direct flow and reverse flow have been computed on the nozzle entrance (plane N_1). They are computed comparing the magnitude of the velocity component belonging to the inlet plane (in the present work $\overline{U_x}$ and $\overline{U_z}$) on the GRF:

- areas where $|\overline{U_z}| > |\overline{U_x}|$ denote side flow;
- areas where $|\overline{U_x}| > |\overline{U_z}|$ and $\overline{U_x} > 0$ denote the converse flow;
- areas where $|\overline{U_x}| > |\overline{U_z}|$ and $\overline{U_x} < 0$ denote the reverse flow;

CHAPTER 5

Simulation of Internal Nozzle Flows

In the following section the numerical results of the internal nozzle flow for the config. ID-10 and the config. ID-3 are reported. As mentioned in the previous chapter, they respectively represent the WoW and BoB in terms of JWP. However, before presenting the primary breakup, the work focuses on the flow field within the sac and the nozzle. The purpose of the present analysis is both to understand which are the geometrical factors leading to shear cavitation and vortex cavitation, and also how the geometrical differences, among the two configurations, leverage when the aforementioned phenomena occur. The first section of the chapter (Sec .5.1) shows the numerical results and it is structured as follows:

- In sec. 5.1.1 is reported a general analysis on the average flow field performed in the sac and in the nozzle volumes to outline the differences and the similarities existing between the two configurations. The average velocity field and $\overline{\mathbf{U}}_{rms}$ are firstly shown upstream of the nozzle inlet on planes S_1, S_2 and S_3, to show the effect of the feeding system (bend-shape, BFS, etc).
- In sec. 5.1.2, an analysis of how the fuel is spread over the nozzle inlet is proposed to show which zones are subjected to the highest fluid vena detachment, which ones to the highest recirculation, and those geometrical parameters mostly influencing the inlet flow field. For these reasons, side, direct and reverse flows are computed using the definition proposed in Sec. 4.3.5. Afterwards, average velocity field and $\overline{\mathbf{U}}_{rms}$ are shown on planes D_1 and D_2. where the 2D average streamlines support the reader in the identification of the average vortical structures. For sake of clarity, also 3D average streamlines have been reported.
- In sec. 5.1.3, average pressure field and $\overline{p}_{rms}$ are also reported to clearly identify the regions with the highest probability to have a cavitating zone. Average pressure along the nozzle is reported as well and compared for the two configurations.
- In sec. 5.1.4, the pieces of information coming from each configuration are then compared to identify a relation among geometry and internal nozzle flow. For this purpose,

discharge, velocity and area coefficients are computed in the average time-window as well. Afterwards, average velocity magnitude, static pressure, liquid volume fraction and nozzle-streamwise vorticity are shown on planes N_1, N_2, N_3, N_4, N_5, N_6. These fields give an indication of the area occupied by the liquid and the vapor, the acceleration induced by the reduction of available area, the nature of the recirculation zone at the nozzle entrance, and the link between the vortical structures and the phase change phenomena. The 2D average streamlines are reported on the same planes; their role is essential for the identification of main counter rotating vortical structures and of secondary vortices along the nozzle axis. Coupled with the nozzle-streamwise vorticity they give an indication of their intensity, how they radially expand and their direction of rotation. Spatial average over each plane is also used to show the average trend of the axial-velocity, non-axial velocity, vorticity magnitude, liquid area along the nozzle. These trends are compared for the two configurations and main results are outlined.

- In the end, the non-axial kinetic energy and turbulent kinetic energy are investigated at the nozzle outlet and then, their effect has been linked to the nozzle geometry (see Sec. 5.1.5). The main goal is to identify the most important in-nozzle parameters for a preliminary jet-flow description.

The second section of the chapter (sec. 5.2) shows a qualitative validation with the instantaneous shadowgraphies from high velocity camera to prove the reliability of the solver in describing the cavitating structures occurring in the real glass nozzle injector. Finally, in sec. 5.3 the main conclusions are reported.

5.1 Results

5.1.1 General analysis of the average flow field

On the cross-section S_1 of config. ID-10 (Fig. 5.1a), the mean velocity is about $56.64\,m/s$, as reported in Tab. 5.1. In the central part of the section, the flow is influenced by downstream direction: a main overflow is present, close to the bottom wall. On the contrary, a highly fluctuating area is present on the opposite upper wall (see Fig. 5.1b). This is due to a detachment zone in the upper part of the wall, which is clearly visible in Fig. 5.8c and also identified by two small recirculation vortices in Fig. 5.5c.

Conversely, on the cross-section S_1 of config. ID-3 (Fig. 5.2a), the mean velocity is about $43.048\,m/s$, as reported in Tab. 5.1. Similarly to config. ID-10, a main overflow is present, close to the bottom wall, while a highly fluctuating area is present on the opposite upper wall (see Fig. 5.2b). Respect to config. ID-10 (Fig. 5.1a), the overflow peak is more concentrated in the bottom left side of the Fig. 5.2a: the flow structure coming from the upstream feeding system of config. ID-10 seems to be more symmetric than ID-3. In the same way, fluctuations of velocity field comply to this flow symmetry in ID-10. On the contrary, in ID-3 higher fluctuations come from the left side of upstream feeding system, while lower values are visible on the right side (Fig. 5.2b).

This is probably due to the different values of "lift" and "H", featuring the two configurations, producing a different detachment zone. The final effect is a different local pressure drop at the BFS.

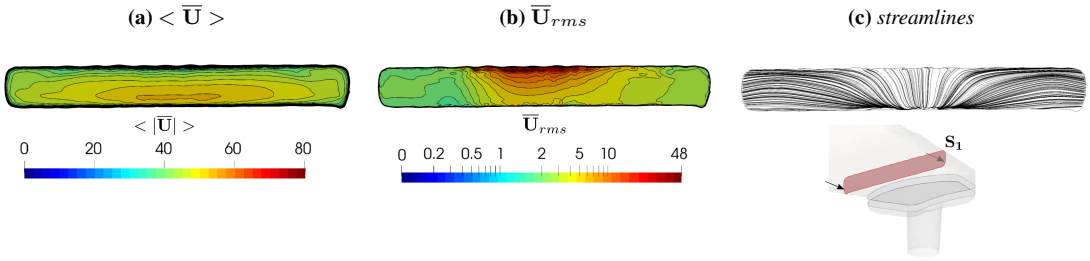

Figure 5.1: *flow analysis on plane* $\mathbf{S_1}$ *for config. ID-10*

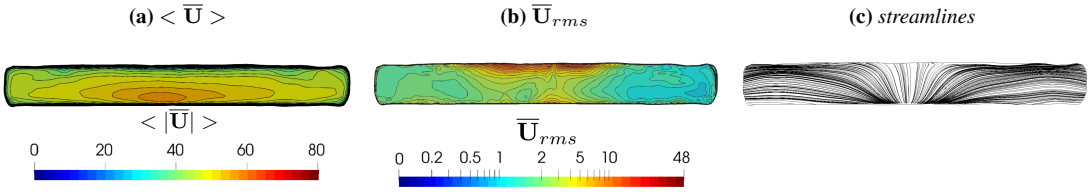

Figure 5.2: *flow analysis on plane* $\mathbf{S_1}$ *for config. ID-3*

The 2D streamlines (Fig. 5.1 and Fig. 5.2) do not give any additional information about the flow. The asymmetry of the average velocity profile on S_1 is also provided by the real geometry: small defaults of surfaces and small asymmetry in the lateral edges are promoter of this flow asymmetry.

Both differences of the average velocity and asymmetry have consequences on vortical structures developing on plane S_2 and then on plane S_3. Being ID-10 characterized by a higher average velocity, good symmetry and a higher side fluctuation on S_1, the effects of separation on S_2 (Fig. 5.1c) becomes higher than ID-3 (Fig. 5.2c), where the two side vortices are absent. The intensity of this separation can be seen as:

- presence of side vortices from 2D streamlines together with their dimensions and their number.
- different width of a lateral low velocity area. In ID-10, Fig. 5.1a, this area is almost doubled than separation zone in ID-3 Fig. 5.2a);
- higher velocity fluctuations on the side. It is clearly shown in Fig. 5.1b that ID-10 has higher fluctuations in that region, where ID-3 does not (see Fig. 5.2b).

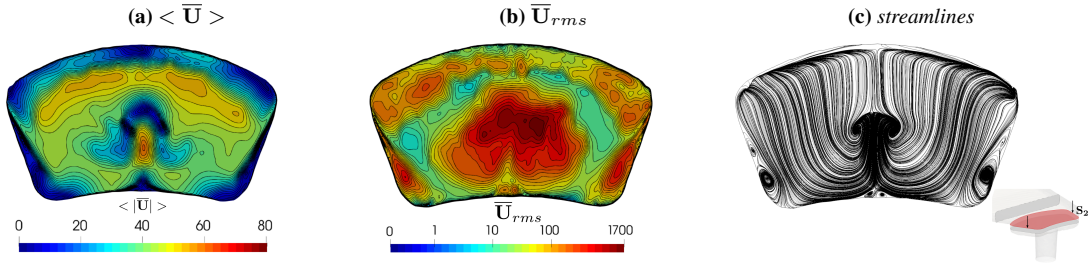

Figure 5.3: *flow analysis on plane* $\mathbf{S_2}$ *for config. ID-10*

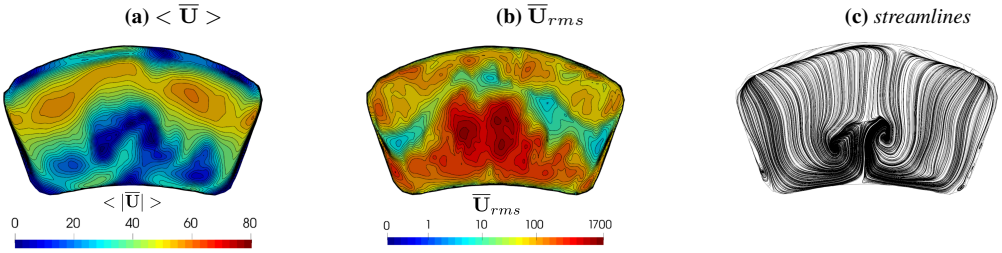

Figure 5.4: *flow analysis on plane* $\mathbf{S_2}$ *for config. ID-3*

Again, higher symmetry is confirmed in ID-10, where both side vortices and central counter rotating vortices exhibit the same structures (Fig. 5.3c) and almost the same velocity profile on both sides (Fig. 5.3a). The same outcomes cannot be applied to ID-3: the central counter rotating vortices are asymmetric (Fig. 5.4a). The right zone is characterized by a bigger vortex, further from the bottom side, while the left zone shows a smaller vortex shrunker to the bottom side (Fig. 5.4c). This behavior is coherent with the different velocity fluctuations seen among right side and left side on plane S_1.

About the flow separation due to the BFS, the low velocity area on the upper part of S_2 is wider for the config. ID-10 (see 5.3a). The separation zone of BFS in ID-10 increases on S_3 and velocity profile is still almost symmetric (Fig. 5.5a). The velocity peak is centered on the hole. Fluctuations are confined to the upper left and right sides, and in the center of the hole (see Fig. 5.5b). These are linked with the side vortices and central counter rotating vortices (Fig. 5.5c). Differently, in ID-3 the asymmetry of the average velocity profile is way more worsened: a global velocity maximum cannot be identified. Two peaks are visible in the upper part of the nozzle hole: the left peak is higher and wider than the right peak as shown in Fig. 5.6a. However, highest fluctuations are visible in the center/bottom part close to the hole (Fig. 5.6b), where two counter rotating vortices are located (see Fig. 5.6c). Now, two side vortices are visible, together with additional vortices in the upper part, close to the BFS. The latters are occurring due to the presence of a bigger step. In fact, these are not visible at all in ID-10 (Fig. 5.5c). A different values o $\overline{\mathbf{U}}_{rms}$ on S_3, among ID-10 and ID-3 close to the BFS, is a testifier of the role of bigger "H" value.

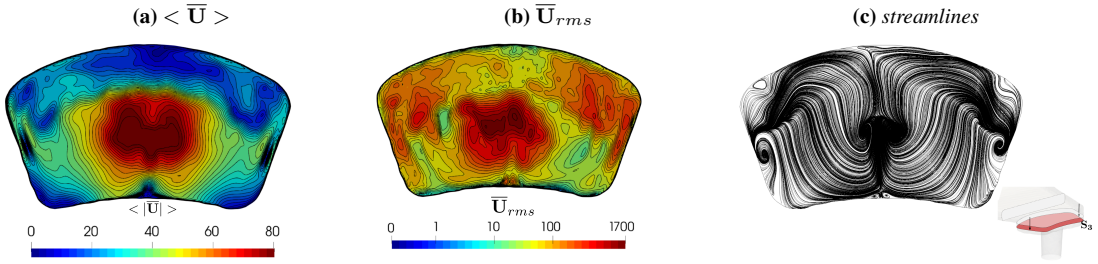

Figure 5.5: *flow analysis on plane* $\mathbf{S_3}$ *for config. ID-10*

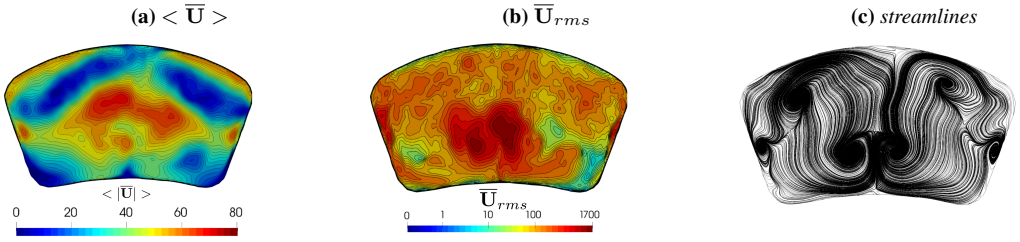

Figure 5.6: *flow analysis on plane* $\mathbf{S_3}$ *for config. ID-3*

Higher average velocity on S_2 and S_3 are visible for the config. ID-10 (see Tab. 5.1), denoting a better organized motion in the sac and less recirculation produced by the BFS.

Table 5.1: *area-weighted average of* $< \mathbf{U} >$ *for plane* S_1, S_2 *and* S_3

	Plane S_1		Plane S_2		Plane S_3	
Config.	ID-10	ID-3	ID-10	ID-3	ID-10	ID-3
$< \overline{\mathbf{U}} > [m/s]$	56.64	43.05	27.53	15.34	19.29	15.45

5.1.2 Study of direct, side and reverse flow

Fig. 5.7 shows the areas respectively associated with side, direct and reverse flows on the nozzle entrance (plane N_1) for config. ID-10 (Fig. 5.7a) and config. ID-3 (Fig. 5.7b). Each area denotes a different flow condition, whose definition is given in Sec. 4.3.5.

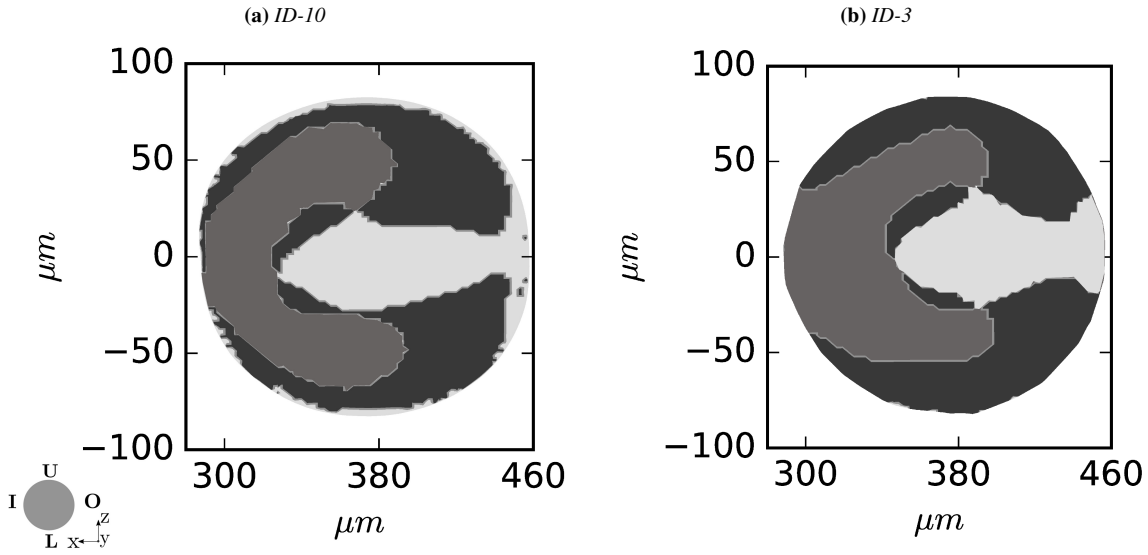

Figure 5.7: *Flow analysis on plane* N_1 *for the two configurations: (Black) average side flow; (dark-gray) average direct flow; (light-gray) average reverse flow.*

Quantitative values of area magnitude, average MFR and average velocity for each condition are reported in Tab. 5.2.

Table 5.2: *Average area, MFR and velocity for side, direct and reverse flow on plane N_1 for config. ID-10 and ID-3*

	side flow		direct flow		reverse flow	
Config.	ID-10	ID-3	ID-10	ID-3	ID-10	ID-3
Area $[mm^2]$	0.01	0.00968	0.00734	0.007779	0.005423	0.004271
MFR $[g/s]$	0.682	0.6555	0.59041	0.6023	0.3137	0.3033
$< \overline{\mathbf{U}} > m/s$	100.36	99.47	118.53	113.32	84.81	103.95

It is clearly evident from Tab. 5.2 that side flow area is 50% higher than reverse flow and 30% higher than direct flow in ID-10. The latter acts on a smaller area than side flow and presents a higher velocity. Therefore, direct flow cannot be considered as the promoter of the secondary flow. It depends mostly by the effect of the side flow which leads to the generation of a twin counter-rotating cells enrollment. This vortex formation is highly sensible to some geometry's parameters such as the lift of the needle and the sac-volume design. In this simplified geometry the first relevant parameter is represented by the following ratio:

$$\frac{lift + H}{offH} \tag{5.1}$$

here called BFS ratio for sake of simplicity. These parameters have already been shown in Fig. 4.2 and are responsible for the different size of the dead zones area related to the direct flow. The second parameter is represented by the "dead space" (see Fig. 4.2), which is responsible for the dead zones areas related to the reverse flow. A remarkable change of these parameters would significantly modify the magnitude of the primary and the secondary flow.

In ID-3 the side flow area is till 50% bigger than reverse flow, while is only 20% bigger than direct flow. Side flow is the main promoter in the creation of the secondary flow. For the config. ID-3, the ratio of Eq. 5.1 is equal to 2.12 while for config. ID-10 is equal to 2.

The small difference of the mentioned ratio (see Eq. 5.1), among the two configurations, does not provide any remarkable effects on the MFR associated to direct and reverse flows.

Config. ID-3, which is characterized by higher ratio, shows lower side MFR and higher direct MFR, while ID-10 shows higher side MFR and lower direct MFR. The second parameter, which influences the reverse flow, is the dead space: the higher is the dead space, the higher will be the direct MFR. In fact config. ID-10, which has a dead space of 6.9 μm longer than config. ID-3 is characterized by a reverse MFR of $0.01\ g/s$ more than config. ID-10.

Hence, in both configurations, sac volume is characterized by a direct and a reverse flow. The direct flow is coming from the upstream area without changing direction, directly entrapped in the hole after a short bend turn. It covers only a quarter of the surface S_1. Notwithstanding the highest velocity in this centered area, direct flow is higher as seen Fig. 5.3a. It also drives the complete section depth (in the z direction): flow is detaching from the roof almost at the hole entrance x-position (see Fig. 5.8a). The reverse flow exhibits a more complex rotation, enrolling inside the complete domain volume from the two remaining opposite left and right sides of the entrance S_1. This rotation is described by the 2D streamlines on the plane S_2 (Fig. 5.3c): the fluid by-passes the central zone, where the hole is located, turns around, following the sac side, and then turns back to the hole entrance.

In particular for the config. ID-3, as soon as the direct flow encounters the step, velocity drastically decreases. From plane S_1 to S_2 the average velocity is about 65% smaller. The bigger recirculation zone produces a redistribution of the flow on the side and reverse zones as can be noticed from higher value of velocity in Fig 5.4a and Fig. 5.6a. Comparing the 2D streamlines of config. ID-10 (Fig. 5.5c) and of config. ID-3 (Fig. 5.6c) it is clear that the

recirculation undergone by the fluid, far from the hole and close to the limiting external wall, is now more complex. The two central counter-rotating vortices are always present, as the smaller lateral vortices; two new vortices have appeared in ID-3 due to the larger BFS and they will influence the direct flow.

Separation zones of the direct flow are visible in Fig. 5.8a and Fig. 5.10a. On plane D_1 it is evident that the feeding side (left side of the nozzle) presents more detachment which is favored also by the separation at the BFS. The height of the step is not large enough to produce a significant recirculation zone. This is also confirmed by the medium level of $\overline{\mathbf{U}}_{rms}$ (see Fig. 5.8b) in that zone (simulation of geometries with larger step has shown they can lead to cavitation in that region). On the dead zone side (right side of the nozzle in the D_1 plane), the probability to have separation and consequent shear cavitation, is smaller.

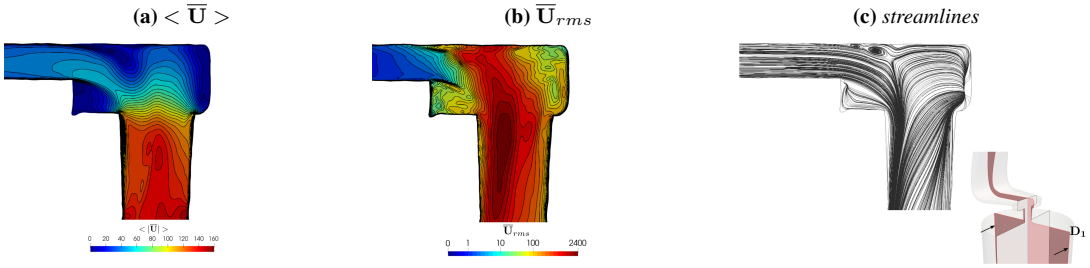

Figure 5.8: *flow analysis on plane* $\mathbf{D_1}$ *for config. ID-10*

Similarly to ID-10, in config. ID-3, looking at D_1, it is evident that the feeding side (left side of the nozzle) presents more detachment (Fig. 5.9a), which is favored also by the separation at the BFS. In this configuration, being the height of the BFS larger than the BFS height of config. ID-10, a significant recirculation zone is produced. The level of $\overline{\mathbf{U}}_{rms}$ visible in Fig. 5.9b is higher if compared to Fig. 5.8b. However, recirculation intensity is still not enough to provoke a remarkable pressure drop; consequently, cavitation does not occur at the BFS. On the dead zone (right side of the nozzle in the D_1 plane), the probability to have separation is almost the same. However, the dead zone is still very short and reverse MFR is the lowest. Therefore, just a few amount of vapor is produced in that zone, as it will be shown later on.

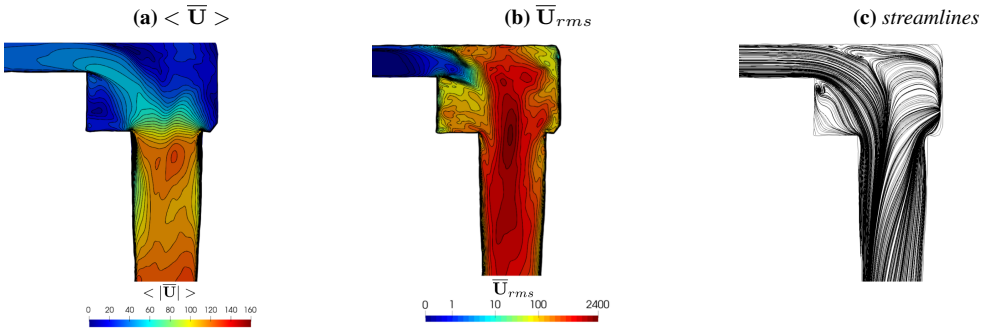

Figure 5.9: *flow analysis on plane* $\mathbf{D_1}$ *for config. ID-3*

On the contrary, on plane D_2, for the config ID-10 separation has the same intensity on both sides (see Fig. 5.10a), and it originates from side flow. Although feeding system has a preferential direction, looking at the planes S_2 (Fig. 5.3a) and S_3 (5.5a) we can see how the main flow is spread on the sides of the sac. As a result, part of the flow by-passes the central part, and two big vortices are created in the center of the plane. On plane D_2, especially in Fig. 5.10c, one vortex per side in the lowest corner is visible. These are the same vortical structures found on plane S_2 and S_3 perpendicular to D_2. The fact that structures are visible on perpendicular planes to S_2 and S_3 denotes the 3D nature of such structures.

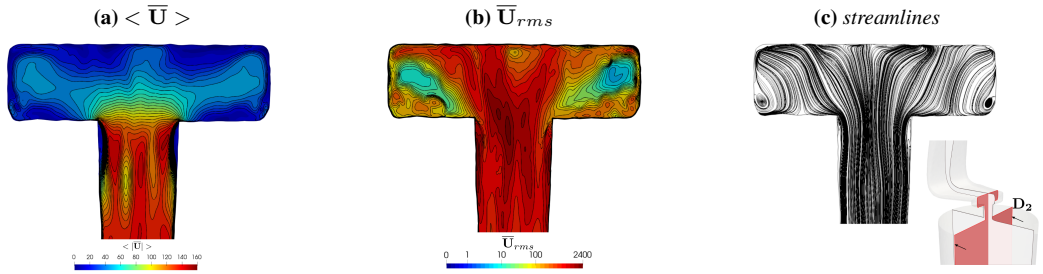

Figure 5.10: *flow analysis on plane* $\mathbf{D_2}$ *for config. ID-10*

Conversely, for the config ID-3 the separation has the higher intensity on the right side as shown in Fig. 5.11a. If compared to ID-10, the separation zone is shorter along nozzle axis, and occupies also a wider portion of nozzle sections from N_1 to N_3. On the plane D_2, especially looking at Fig. 5.11c, one vortex per side in the lowest corner is barely visible. Most of the 3D vortical structures are not occupying D_2 section but a zone closer to the BFS (as seen in Fig. 5.6c).

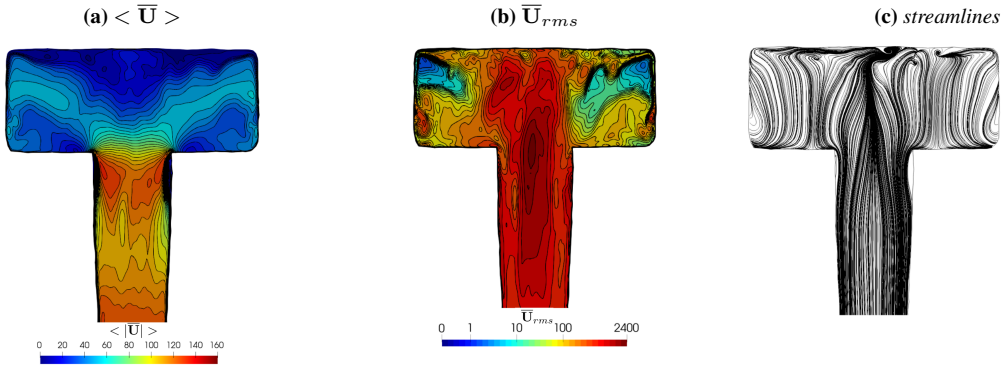

Figure 5.11: *flow analysis on plane* $\mathbf{D_2}$ *for config. ID-3*

As a matter of fact, Fig. 5.12a and Fig. 5.12b confirm the presence of these sac-side vortices, showing that they are reorganized in the so called side-reverse flow producing two main 3D vortical structures whose center-line is mainly identified by the nozzle axis. Fig. 5.12a shows that they are not perpendicular to the top-wall part of the geometry but they are canted and only after they enter the nozzle, they align with it. This behavior is due to the 3D particular shape of the sac volume.

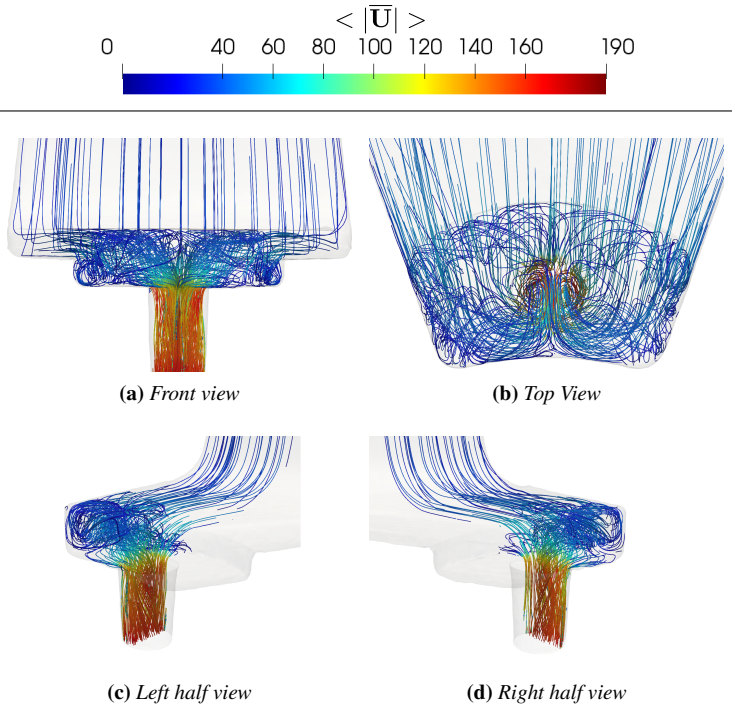

(a) *Front view* **(b)** *Top View*

(c) *Left half view* **(d)** *Right half view*

Figure 5.12: *3D representation of the average streamlines for config. ID-10*

Differently, Fig. 5.12c and Fig. 5.12d show, on the inner side of the nozzle, straight streamlines completely bypassing the step and the most of the flow coming from the side: the left and the right counter-rotating vortices produce an overall swirl motion within the nozzle which is the main contributor of the pressure drop and consequent cavitation.

The presence of these sac-side vortices and their reorganization in the so called side-reverse flow is confirmed also in ID-3, as shown in Fig. 5.13a and Fig. 5.13b. From Fig. 5.13a it is visible that they are not perpendicular to the top-wall part of the geometry but they are canted and only after they enter the nozzle, they align with it. This behavior is mainly due to the 3D particular shape of the sac volume.

To the contrary, Fig. 5.13c and Fig. 5.13d show, on the inner side of the nozzle, straight streamlines completely bypassing the step and the most of the flow coming from the side: as for ID-10 the left and the right counter-rotating vortices produce an overall swirl motion within the nozzle which is the main contributor of pressure drops and consequent cavitation. However, conversely to ID-10, in Fig. 5.13c and Fig. 5.13d it is shown a less intense swirl motion for ID-3. This outcome will be discussed later looking at average fields on the perpendicular planes to the nozzle axis. In general, the side flow is more intense in config. ID-10 and the longer the nozzle and the lift are, the straighter the streamlines will be. Notwithstanding this, mostly the same flow features have been noticed among the two configurations.

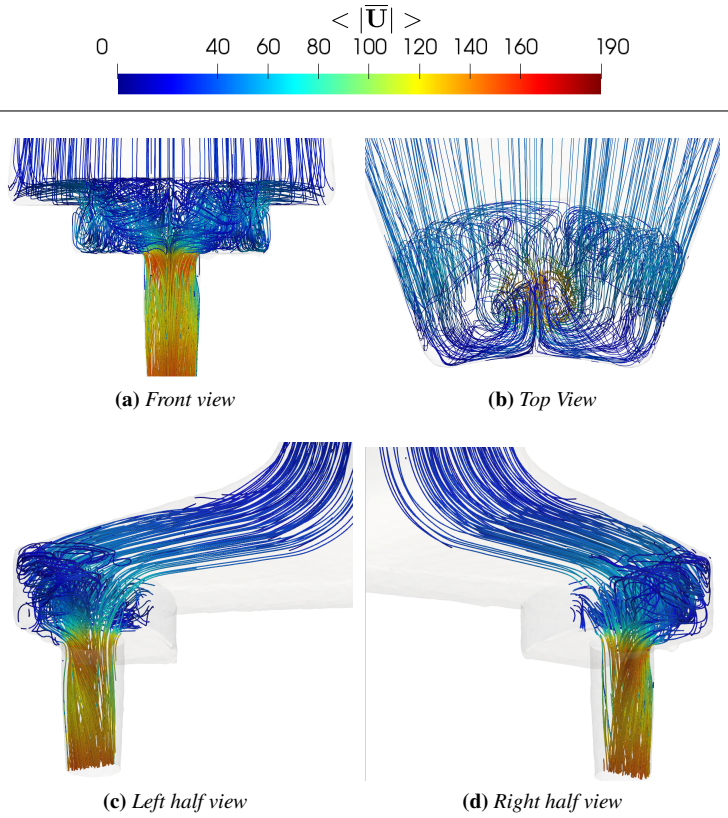

(a) *Front view* **(b)** *Top View*

(c) *Left half view* **(d)** *Right half view*

Figure 5.13: *3D representation of the average (pseudo-steady) frozen streamlines for config. ID-3*

5.1.3 Pressure field

In both configurations, plane S_1 and S_2 are characterized by the same average pressure (see Tab. 5.3). Conversely, in config. ID-3, the average pressure on S_3 is $2\,bar$ smaller than config. ID-10. This additional pressure drop is due to the higher value of "H" and "Off H": the bigger the recirculation area is, the bigger the pressure drop and the recirculation zone will be.

Table 5.3: *area-weighted average of* $< \overline{p} >$ *for plane* S_1, S_2 *and* S_3

	Plane S_1		Plane S_2		Plane S_3	
Config.	ID-10	ID-3	ID-10	ID-3	ID-10	ID-3
$< \overline{p} > \ [bar]$	91.31	91.16	87.53	87.18	85.69	83.27

Average pressure field and pressure fluctuations are here reported on planes S_2,S_3, D_1 and D_2. As expected, the lowest pressure values are located in the vortex core. As seen from 3D streamlines, as soon as the fluid reaches the nozzle inlet, the vortical structures becomes perpendicular to N_1 and their intensity increases, which means the vortex is progressively accelerating. As a consequence from plane S_2 (see Fig. 5.14a) to plane S_3, (see Fig. 5.16a) pressure in the vortex core decreases. High pressure fluctuations are visible in Fig. 5.14b and Fig. 5.16b since the center of the hole is the zone of the sac characterized by the highest perturbations.

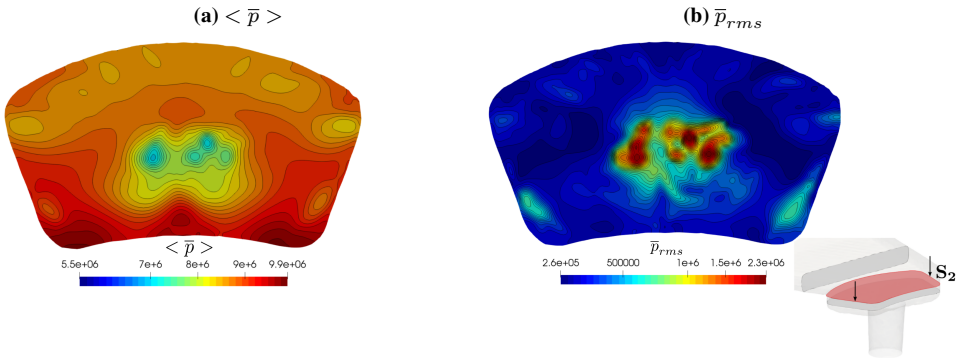

Figure 5.14: *average pressure field (a) and pressure RMS (b) on plane* $\mathbf{S_2}$ *for config ID-10*

However, in ID-3 (Fig. 5.15b and Fig. 5.17b) these fluctuations are not as high as the ones found in config. ID-10 (Fig. 5.14b and Fig. 5.16b). This is a clear indication of less cavitating geometry.

In addition, the top region of Fig. 5.15a and Fig. 5.17a show the zone of BFS: the higher values of “H” and “lift" have clearly increased the pressure drops in this zone if compared to config. ID-10 (see Fig. 5.14a and Fig. 5.16a).

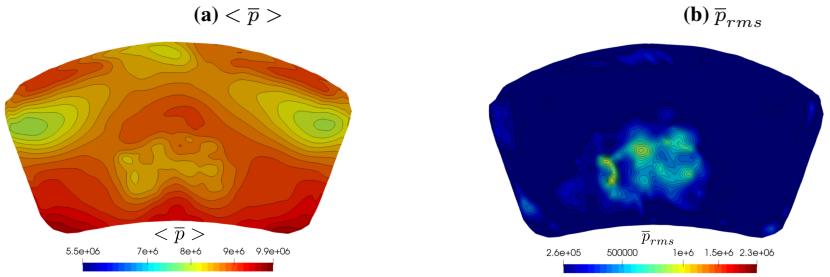

Figure 5.15: *average pressure field (a) and pressure RMS (b) on plane* $\mathbf{S_2}$ *for config. ID-3*

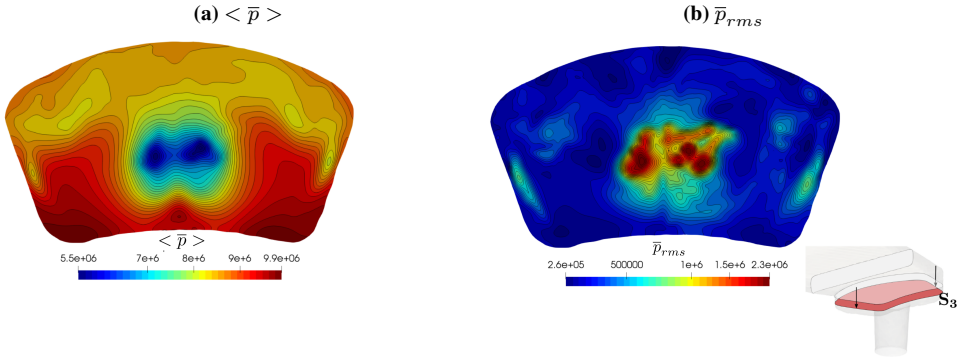

Figure 5.16: *average pressure field (a) and pressure RMS (b) on plane* $\mathbf{S_3}$ *for config. ID-10*

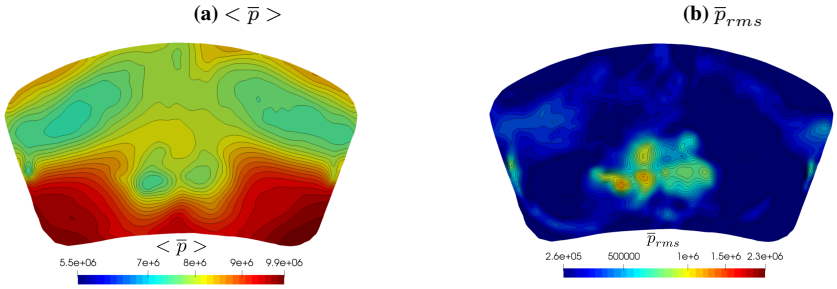

Figure 5.17: *average pressure field (a) and pressure RMS (b) on plane* $\mathbf{S_3}$ *for config. ID-3*

These high perturbations are also visible in Fig. 5.18b and Fig. 5.20b and are represented as vertical strings. The higher the fluctuations are, the higher the probability to have an event in time where pressure falls below the saturation pressure will be. Therefore, these zones can represent the possible spots where string cavitation could occur. Averagely, cavitating string are not visible in Fig. 5.18a, nor in Fig. 5.20a. Cavitation mainly originates from the corners (detachment at nozzle entrance) and from the two main core vortices developed along the nozzle as shown in Fig. 5.20a.

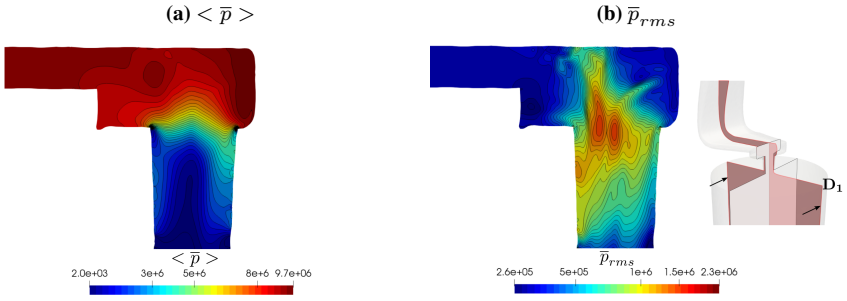

Figure 5.18: *average pressure field (a) and pressure RMS (b) on plane* $\mathbf{D_1}$ *for config. ID-10*

Pressure fluctuations are also visible in Fig. 5.19b and Fig. 5.21b and are represented as vertical strings. However, these strings are shorter than those visible in the config. ID-10 in Fig. 5.18b and Fig. 5.20b, meaning that there will be less probability to cavitate in that region. Cavitation mainly originates from the corners (detachment at nozzle entrance) and from the two main core vortex developed along the nozzle as shown in Fig. 5.21a, but generally, the phenomenon is less intense if compared to what has been outlined in the config. ID-10.

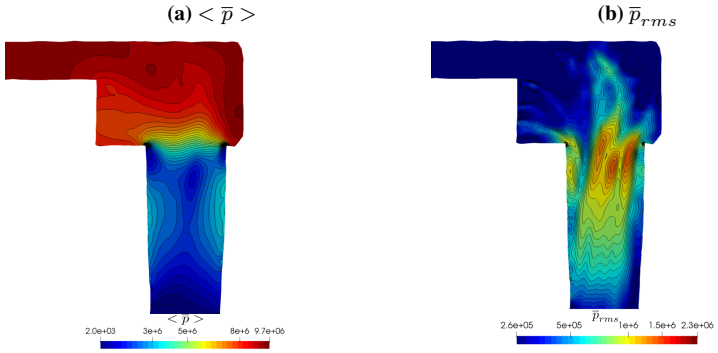

Figure 5.19: *average pressure field (a) and pressure RMS (b) on plane* $\mathbf{D_1}$ *for config. ID-3*

The three high pressure fluctuation zones, shown in Fig. 5.20b as three separated strings, denote the region where pressure deviates the most from the average condition. Since vortices are not stable within the sac but they periodically grow and disrupt, those zones represent possible spot in the sac where string cavitation is likely to occur.

In ID-3, three high pressure fluctuation zones are noticeable in Fig. 5.19b, while two central spots are visible in Fig. 5.21a. These are less stretched along nozzle axis, conversely to what has been observed for the config. ID-10 (Fig. 5.20b).

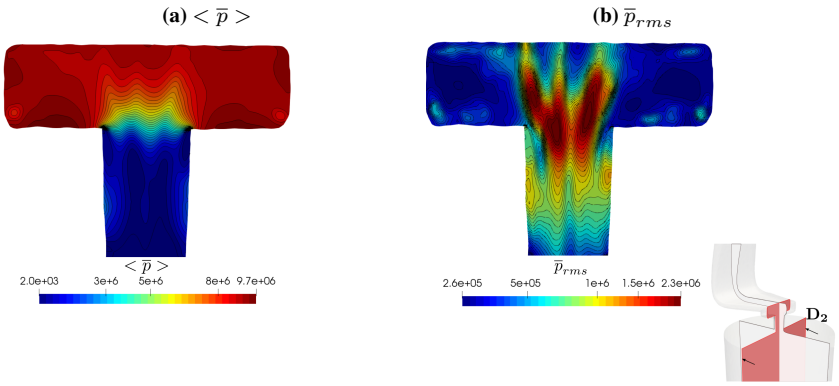

Figure 5.20: *average pressure field (a) and pressure RMS (b) on plane* $\mathbf{D_2}$ *for config. ID-10*

Different pressure condition in the nozzle are due to some specific geometrical features; L/D and conicity factor K_g play a pivotal role. As shown in Fig. 5.22, for both the configurations, the average pressure is almost the same at N_1. From N_1 to N_2 it is almost the half, due to the high detachment region around the rounded edges of the nozzle. For both configurations, the highest detached zone is the one interested by the side flow. Between plane N_1 and plane N_2 a recirculation zone is produced and pressure consequently falls below p_{sat} value. This determines the pressure drop visible among the two planes.

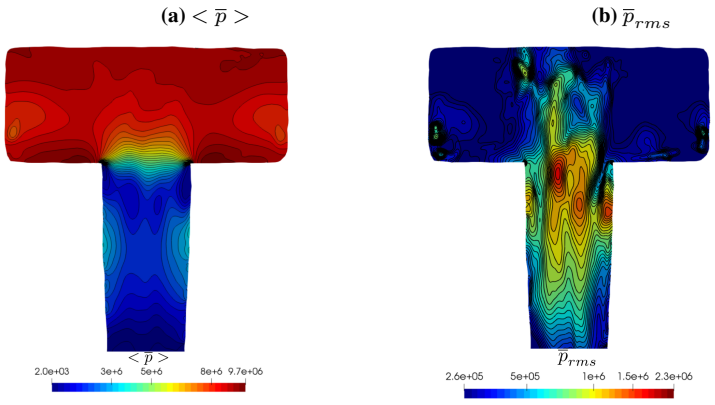

Figure 5.21: *average pressure field (a) and pressure RMS (b) on plane* $\mathbf{D_2}$ *for config. ID-3*

In ID-3, the average pressure is characterized by a different trend after plane N_2. Instead of a stable average pressure value, now from plane N_2 to plane N_4, the pressure recovers almost 85% of nozzle inlet average pressure reaching a local maximum at plane N_3. This behavior is to be addressed to higher conicity factor of this configuration. In general, having a higher average pressure in this nozzle area (middle region) is again a clear factor of lesser vapor generation. High pressure areas are visible in the lateral zone of the nozzle in Fig. 5.19a and Fig. 5.21a.

From plane N_2 to plane N_4 pressure keeps almost stable in ID-10. In the end, from plane N_4 to plane N_6 a sudden expansion occurs: fluid must fulfill the constrain of ambient pressure in the ambient domain. This expansion produces additional vapor and its production can continue outside the nozzle region (See. chapter 6).

Conversely, in ID-3, once the local maximum has been reached on N_3, pressure decrease of $5\,bar$ at N_4 and then it drops drastically. Notwithstanding, the average pressure values on planes N_4 and N_5 are always higher than the average pressure found in the config. ID-10.

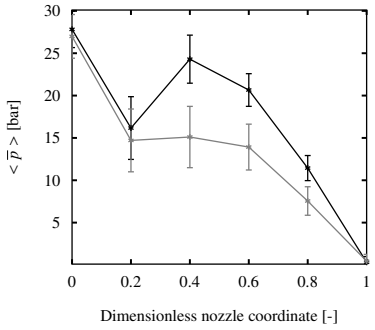

Figure 5.22: *Time average of the normal area-weighted average of pressure along nozzle axis: — ID-10, — ID-3. Dimensionless nozzle coordinate corresponds to plane* N_1*,* N_2*,* N_3*,* N_4*,* N_5 *and* N_6*.*

5.1.4 Flow analysis along the Nozzle

In Fig. 5.23 and Fig. 5.25 respectively show the signals of discharge coefficient (C_d), the velocity coefficient (C_v) and the area coefficient (C_a) at nozzle outlet (plane N_6) for ID-10 and ID-3.

The same criteria has been applied to void fractions signal at nozzle outlet, whose results are shown in Fig. 5.24 and Fig. 5.26. In ID-10 The 91% of the fluid at the outlet is liquid n-Heptane, about 9% is n-Heptane vapor and almost 0.01% is occupied by non-condensable gases, while in ID-3 The 97% of the fluid at the outlet is liquid n-Heptane, about 2.99% is n-Heptane vapor and almost 0.01% is occupied by non-condensable gases. It is evident from these values that ID-10 promotes a bigger generation of vapor.

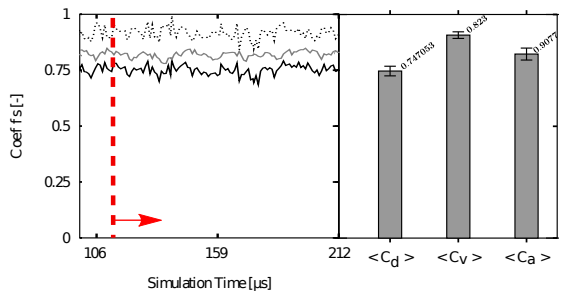

Figure 5.23: *Computed Cd,Cv and Ca at nozzle outlet with histogram representing the average values and standard deviation for config. ID-10.*

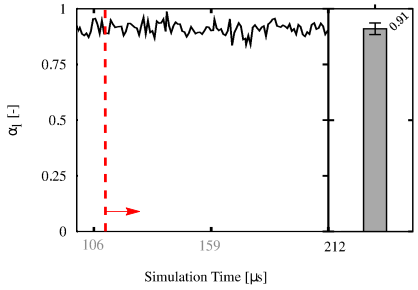

Figure 5.24: *Liquid void fraction at nozzle outlet with histogram representing the average liquid void fractions and standard deviation for config. ID-10.*

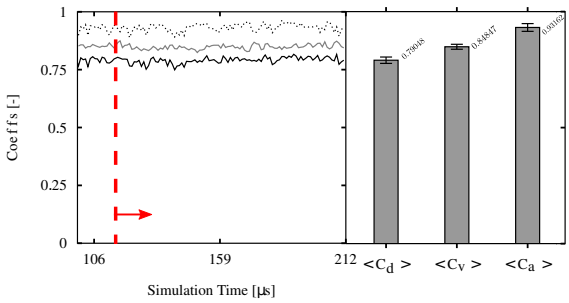

Figure 5.25: *Computed Cd,Cv and Ca at nozzle outlet with histogram representing the average values and standard deviation for config. ID-3.*

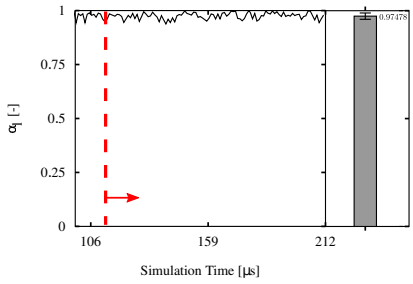

Figure 5.26: *Liquid void fraction at nozzle outlet with histogram representing the average liquid void fraction and standard deviation for config. ID-3.*

From $15\,\mu s$ to about $112\,\mu s$ the signal denotes the development of the flow field within the nozzle. Starting from $112\,\mu s$, (denoted by the red dashed line) time average and standard deviation are performed run-time. The latters are represented by the column on the right side of Fig. 5.23. The actual mass flow rate is useful to determine the discharge coefficient C_d of the injector, computed as follows:

$$C_d = \frac{< \dot{m} >}{\dot{m}_{th}} = \frac{A_{eff} U_{eff} \rho_l}{A_{th} U_{th} \rho_l} = C_a C_v \tag{5.2}$$

where $< \dot{m} >$ denotes the average mass flow rate from numerical simulation and $\dot{m}_{th}$ denoting the theoretical mass flow rate obtained using as velocity Bernoulli's theoretical velocity:

$$U_{th} = \sqrt{\frac{2(p_{inj} - p_{back})}{\rho_l}} \tag{5.3}$$

A_{th} denotes the real geometric cross sectional area of plane N_6 and ρ_l the density of liquid n-Heptane. As shown in Eq. 5.2, C_d can be also thought as the product of two coefficient:

- C_v denotes the velocity coefficient, which compares the effective velocity with the theoretical one computed using Bernoulli's theorem (see Eq. 5.3), if all the pressure energy was transformed into kinetic energy without losses. U_{eff} is computed using the normal area average (see Eq. 4.11) as follows:

$$\frac{\sum_{j=1}^{k} < \overline{\mathbf{U}} >_j \cdot \mathbf{S_f}_j}{\sum_{j=1}^{k} |\mathbf{S_f}_j|} \tag{5.4}$$

  Where $j = 1, ..., k$ is the j-th face of the plane of k-faces on which spatial average is computed. $< \overline{\mathbf{U}} >_j$ denotes the time average velocity vector of the j-th face; $\mathbf{S_f}_j$ represents the surface area vector of the j-th face computed as $|\mathbf{S_f}_j| \cdot \hat{\mathbf{n}}_j$ where $\hat{\mathbf{n}}_j$ is the unity normal vector to the j-th face of the surface.

- C_a denotes the area coefficient, which characterizes the reduction of the effective area with respect to the real geometric one (from XCT). This reduction is mainly due to the existence of a non-uniform velocity profile inside the nozzle, the presence of cavitation zones and the existence of possible recirculation zones caused by the boundary layer separation. C_a is computed as the ratio of A_{eff} and A_{th} (the actual area of plane N_6). As mentioned above, A_{eff} must take into account the flow contraction due to non-uniform flow profile, recirculation zones and cavitation. Therefore, it is computed as follows:

$$A_{eff} = \sum_{j=1}^{k} |\mathbf{S_f}_j| \Big|_{[(<\overline{\mathbf{U}}>_j \cdot \hat{\mathbf{n}}_j)>0] \cap (<\overline{\alpha_l}>_j = 1)} \tag{5.5}$$

  where $(< \overline{\mathbf{U}} >_j \cdot \hat{\mathbf{n}}_j) > 0$ denotes the condition of zone with the mixture leaving the nozzle, while $< \overline{\alpha_l} >_j = 1$ denotes the condition of area occupied by the liquid only. This two condition must be fulfilled simultaneously.

Eventual changes in density, which are important as injection pressure increases or when cavitation occurs, are taken into account by the previous coefficients, since these changes affect the effective area and velocity. The oscillation in the C_a are in fact related mostly to α_l variation (Fig. 5.24), which is used for the density calculation. The presence of vapor at the outlet reduces the available area to inject liquid fuel and is also responsible for the mass flow rate oscillation.

For the config. ID-10 the values of the three coefficient computed from the numerical simulations are $C_d = 0.747053$, $C_a = 0.9077$, $C_v = 0.823$. Higher values are obtained for ID-3: $C_d = 0.79048$, $C_a = 0.93162$, $C_v = 0.84847$. In general, additional reduction in the discharge coefficient is mainly due to kinetic energy losses within the nozzle sac and at nozzle entrance (plane N_1). However, being config. ID-3 characterized by higher conicity factor and nozzle length than ID-10, a higher recovery of the initial kinetic energy of C_d and C_v is noticed.

As a matter of fact, the recirculation zone, identified between plane N_1 and N_3, reduces the available area. However, flow detachment does not reach the outlet (plane N_6) and a reduction of cross sectional area, due to nozzle convergent geometry and to flow recirculation, contribute to recover a part of initial kinetic energy. This recovery is shown in Fig. 5.29a: from plane N_3 to plane N_6 the velocity increment in ID-3 is bigger than the one obtained in the nozzle of ID-10.

The flow detachment and the area occupied by the liquid in each section are shown in Fig. 5.27b for ID-10: from plane N_1 to plane N_6 the average liquid fraction can be seen; planes N_1, N_2 and N_3 are characterized by shear cavitation. Triggered by the detachment of the side flow and by a lesser contribution of the direct flow, the shear cavitation occupies the maximum area on the second plane and starts vanishing at N_3, when fluid vena is reattaching to the nozzle wall. The recirculation zone, which is responsible for the onset of cavitation, is interested by secondary vortices near wall in the streamwise direction. This is visible in Fig. 5.27c. At plane N_2 the velocity magnitude, in the recirculation zone, is about $20\,m/s$. In the center of N_2 it reaches peaks of $160\,m/s$. Outer zone are characterized by values of $140\,m/s$.

- Plane N_1 is characterized by one anticlockwise vortex on the upper side and clockwise vortex on the lower side: these are generated by the side flow. In the zone identified by the direct flow, two vortices are developing but they are not visible from 2D streamlines on plane N_1 (see Fig. 5.27a). In the central zone of the plane, two big vortices are visible. In the lower side the vortex has a anticlockwise rotation, while in the upper side it has a clockwise one. In addition, the lower central vortex is bigger than the upper one: this asymmetry in the flow field is addressed to the real geometry used for the simulation.

- On the plane N_2 the side vortices are now visible in Fig. 5.27a. Central vortices have grown up occupying almost 50% of the hole, and they are still preserving the asymmetric pattern. On the inner part, the vortices triggered by detachment of direct flow are now visible. In the lower part, there is an anticlockwise vortex while in the upper part there is a clockwise one. It must be remarked that the detachment of side flow produces also vortices in the spanwise direction, the so called “hairpin vortices”.

In ID-10, from plane N_4 to N_6, secondary vortices related to the side flow disappear since the flow reattaches to the nozzle wall. The two big central vortices now are occupying that zone. The center of rotation has moved towards the inner side, leaving space to the vortices on the outer side. The latters come from the reverse flow and they grow progressively from the nozzle entrance to the nozzle outlet. They are initially one thing with the vortices of the side flow but they can progressively be distinguished from them. Besides, these vortices do not trigger any kind of cavitation, as it can be noticed in Fig. 5.27b.

In Fig. 5.28b, from plane N_1 to plane N_6, the average liquid fraction is shown for ID-3. In this configuration, only planes N_1 and N_2 are characterized by shear cavitation. Triggered by the detachment of the side flow and by a lesser contribution of the converse flow, the shear cavitation occupies the maximum area on the second plane. At plane N_3 the fluid vena is already attached and averagely shear cavitation disappeared. The recirculation zone, which is the main responsible for the onset of cavitation, is visible in Fig. 5.28c, where the velocity magnitude is about $20\,m/s$. The central area of plane N_2 does not show a large zone interested by high velocity as it happened in config. ID-10 (see Fig. 5.27c). The high velocity zone is almost halved, and in fact looking at space average on plane N_2 for the two configurations, this is higher for config. ID-10. The near nozzle wall region is still interested by secondary vortices in the streamwise direction (see Fig. 5.28d) but in plane N_2 these are almost disappeared:

- Plane N_1 is characterized by one clockwise vortex on the lower side and an anticlockwise vortex on the upper side. These are generated by the side flow and confined in the reverse flow region, while for the config. ID-10 they were more elongated and were occupying the whole central area of the nozzle (see Fig. 5.27a). These vortices are also visible in 5.28a. and present an asymmetry. A first look at Fig. 5.28d may mislead

to wrong conclusions: the lower vortex seems bigger if one just looks at the core, but actually the upper vortex is more stretched as shown in Fig. 5.28a.

- On plane N_2 the side vortices are almost disappeared. Central vortices have grown up and streamwise vorticity decreased. During this expansion they are still preserving the asymmetric pattern.

- None vortical structures are now visible in the reverse flow side from plane N_3 to N_4.

For ID-3, the higher conicity is playing a key factor: secondary vortices related to the side flow disappear after plane N_2. The two big central vortices move progressively to the central part of the nozzle and are mostly responsible for the cavitation in the nozzle, as shown in Fig. 5.28b.

In Fig. 5.29a, for each configuration, both axial velocity on GRF and LRF are reported. On plane N_1, the axial velocity is almost the same for ID-10 and ID-3. In the zone of flow detachment (from plane N_1 to plane N_3), the gap between the two curves progressively increases:

- In ID-10, as shear cavitation occurs, available area decreases of almost 2.5% at plane N_4 (see Fig. 5.29f). This contraction of cross-sectional area makes the flow accelerate in the axial direction: almost 45% of this acceleration occurs among N_1 and N_2 as shown in Fig. 5.29c. Another 5% of acceleration occurs in a linear way along the nozzle. This linear behavior is mainly due to a proportional increment of axial velocity and decrease of non-axial velocity.

- On the contrary, in ID-3, shear cavitation occurs at N_1, available area decreases of almost 2.5% at plane N_2 5.29e, but as soon as vena is reattached, the available area at plane N_4 becomes the same of N_1. Thus, the contraction of the cross-sectional area due to the flow detachment has a minor influence respect to the situation observed for config. ID-10. The axial acceleration here is mostly due to the higher conicity factor. Only 15% of this acceleration occurs among N_1 and N_2, as shown in Fig. 5.29c. An additional 10% of acceleration occurs in a linear way along the nozzle. This linear behavior is mainly due to a proportional increment of axial velocity and a decrease of non-axial velocity.

  A general consideration can be outlined for both configurations: since U_{non-ax} has decreased, (see Fig. 5.29b), the vortices in nozzle-direction have to become larger in order to conserve the angular momentum. This situation explains why cavitating vortices are expanding radially, especially from plane N_5 to N_6. As a consequence, the liquid area to cross-sectional area ration suddenly decreases of almost 2.5%.

The average values of streamwise vorticity on plane N_5 and N_6 (see Fig. 5.29d) confirm the decrease of $\mathbf{U}_{non-ax}$: although the pair of counter-rotating vortices is still present, the core value has decreased. However, it is possible to notice that in Fig. 5.29d, vorticity magnitude has increased from plane N_2 to plane N_5. This means vorticity has increased on spanwise and crosswise (normal) direction, becoming more and more dominant along the nozzle.

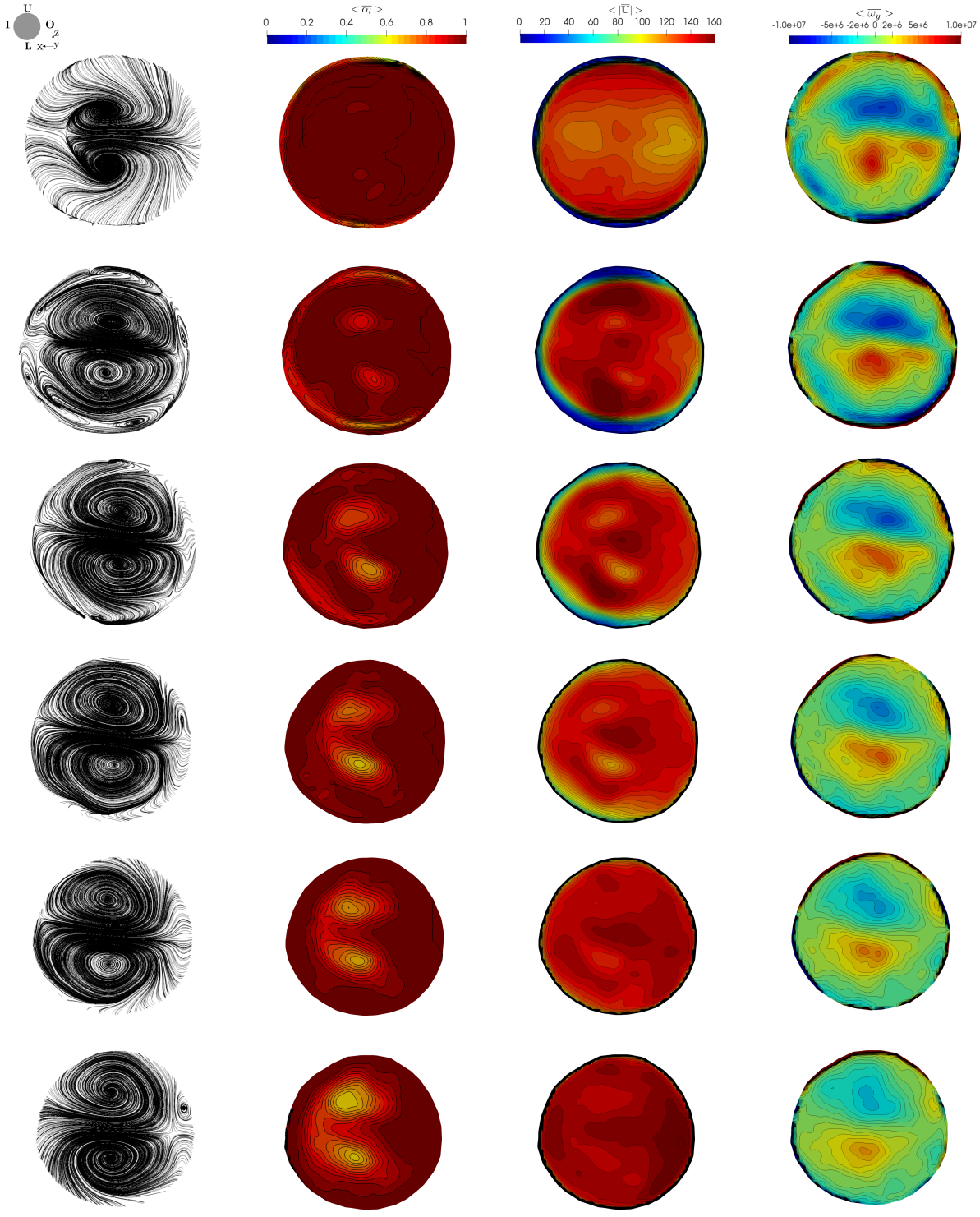

(a) *average streamlines* **(b)** $< \overline{\alpha_l} >$ **(c)** $< |\overline{\mathbf{U}}| >$ **(d)** $< \overline{\omega_y} >$

Figure 5.27: *Average quantities on nozzle cutting planes. From top to bottom* N_1, N_2, N_3, N_4, N_5, N_6 *for config. ID-10.*

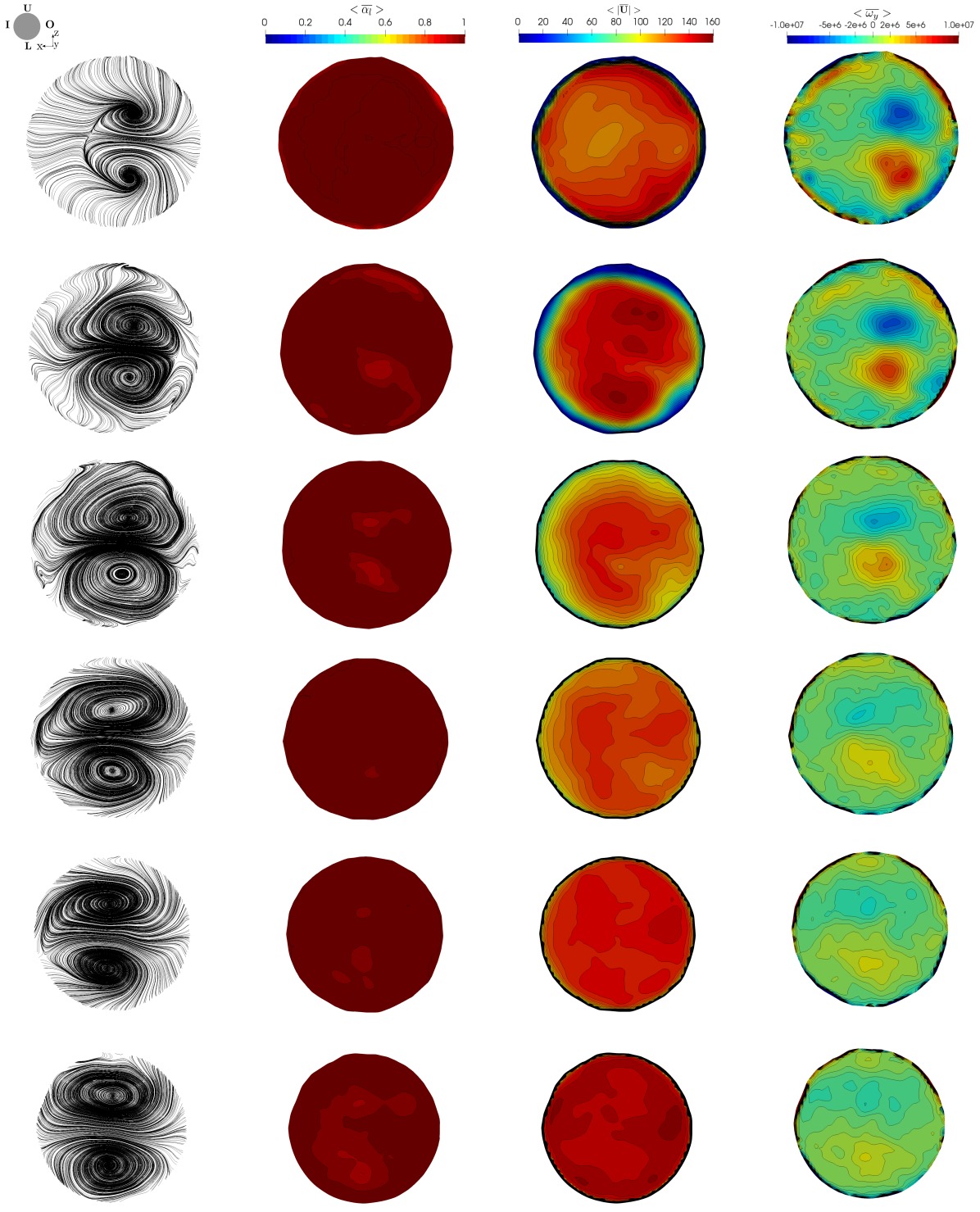

(a) *average streamlines* **(b)** $< \overline{\alpha_l} >$ **(c)** $< |\overline{\mathbf{U}}| >$ **(d)** $< \overline{\omega_y} >$

Figure 5.28: *Average quantities on nozzle cutting planes. From top to bottom* N_1, N_2, N_3, N_4, N_5, N_6 *for config. ID-3*

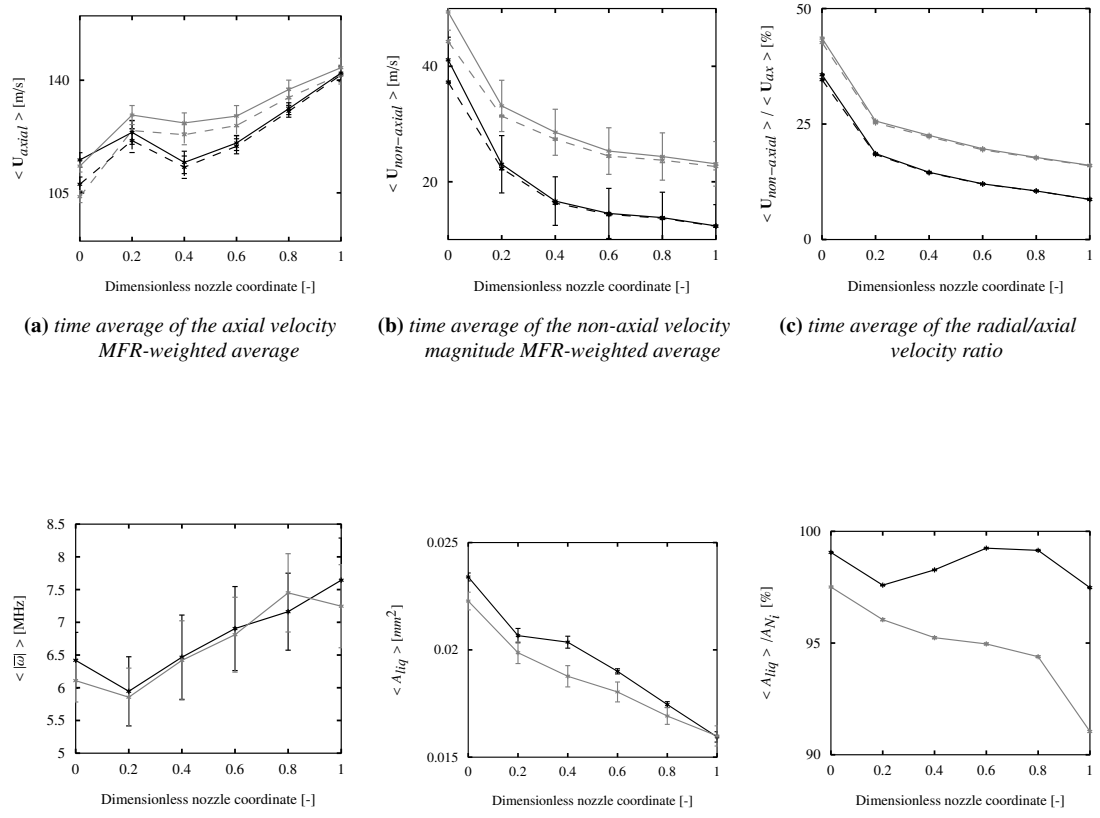

(a) *time average of the axial velocity MFR-weighted average*

(b) *time average of the non-axial velocity magnitude MFR-weighted average*

(c) *time average of the radial/axial velocity ratio*

(d) *time average of the vorticity magnitude MFR-weighted average*

(e) *time average of the liquid fraction area integral*

(f) *time average of the liquid area/cross sectional area ratio*

Figure 5.29: *Time Average of space averaged quantities along nozzle axis:— id-10, — id-3 on GRF, – – – id-10, – – – id-3 on LRF. Dimensionless nozzle coordinate corresponds to plane N_1, N_2, N_3, N_4, N_5 and N_6.*

5.1.5 Turbulence and non-axial flow

The level of the total Turbulent Kinetic Energy (TKE) at the nozzle outlet gives an indication of the efficiency in the atomization. It has been shown in several works that the higher the level of turbulence is, the higher the atomization will be. In some injectors this goal is achieved imposing a deflection of the flow inside the nozzle. In this work, the deflection is supposed to be operated by the turning bend in the upstream region and by the sac geometry (BFS). However, many studies [143], [85], [175] have illustrated that the level of turbulence is not the only key factor in controlling atomization efficiency. Another indicator of paramount importance is the non-axial flow produced by the aforementioned deflection. In the work of Dumouchel et al. [57] these indicators have been deeply analyzed and results have shown that the sum of turbulent kinetic energy and the non-axial kinetic energy (E_k) at the nozzle outlet represents the energy available for the atomization process. This must not be confused with the total available energy in the fluid. The time average of both total TKE and E_k are computed from the MFR-weighted average at the nozzle outlet. The weighted average is computed over the plane, for each time advancement, using the formulation of Eq. 4.11. For

E_k it reads:

$$< E_k(\mathbf{x},t) >_s = \frac{\sum_{j=1}^{n} E_k(\mathbf{x},t)_j \cdot W_j}{\sum_{j=1}^{n} W_j} \tag{5.6}$$

where $E_k(\mathbf{x},t)_j$ is defined as follow:

$$E_k(\mathbf{x},t)_j = \frac{1}{2}\rho(\mathbf{x},t)_j \sqrt{((proj_{<\mathbf{n}_U>_i}\mathbf{U}_{j_i}) \cdot [0,0,n_{z_i}])^2 + ((proj_{<\mathbf{n}_U>_i}\mathbf{U}_{j_i}) \cdot [0,0,n_{z_i}])^2} \tag{5.7}$$

according to LRF (see Sec. 4.3.3). Within the LES approach, a contribution of TKE comes from the resolved velocity field, another contribution comes from the sgs one:

$$TKE_{tot} = \overline{TKE} + TKE_{sgs} \tag{5.8}$$

The first term on RHS of Eq. 5.8 comes from the root-mean-square (RMS) of the resolved velocity fluctuations, thus it reads:

$$\overline{TKE} = \frac{1}{2}(< (\overline{u}')^2 > + < (\overline{v}')^2 > + < (\overline{w}')^2 >) \tag{5.9}$$

being $\overline{\mathbf{U}} = (\overline{u}, \overline{v}, \overline{w})$ the resolved velocity. The time average operator is denoted with $<>$ and the fluctuation in time of a field is denoted with $'$. The second term on the RHS Eq. 5.8 can be calculated using the turbulence model. Therefore, it reads:

$$TKE_{sgs} = (\frac{< \mu_t >}{C_k \Delta})^2 \tag{5.10}$$

Where Δ is the cut-toff width to be of the same order as the grid size, as defined in Eq. 2.31, C_k is a constant whose value is 0.094 and μ_t from WALE model (see Sec. 2.5 and Eq. 2.38). In the end, the weighted average reads:

$$< TKE_{tot}(\mathbf{x},t) >_s = \frac{\sum_{j=1}^{n} TKE_{tot}(\mathbf{x},t)_j \cdot W_j}{\sum_{j=1}^{n} W_j} \tag{5.11}$$

For both $< E_k >_s$ and $< TKE_{tot} >_s$ the weight used is MFR, therefore:

$$W(\mathbf{x},t)_j = \rho(\mathbf{x},t)_j |\mathbf{U}(\mathbf{x},t)_j \cdot \mathbf{S}_{\mathbf{f}_j}|. \tag{5.12}$$

Table 5.4: *Non-dimensional coefficient and nozzle geometry parameters for the two configurations*

Config.	$\overline{TKE}$	TKE_{sgs}	TKE_{sgs}/TKE_{tot}	Unit
10	662.1	7.31	0.01093	J/kg
3	603.2	20.76	0.03327	J/kg

A requirement for LES is that at least 80% of the turbulent kinetic energy should be resolved by the simulation [166]: in other words $TKE_{sgs}/TKE_{tot} < 0.02$. This requirement is fulfilled by config. ID-10, while ID-3 is out of 1.3% for this requirement, but it is still acceptable. The TKE_{tot} values found in the present work are about 100 times the level of turbulence found in [57]. This is mainly due to the high differences in the operative pressure condition; in the present work the pressure is 20 times higher ($100\,bar$ instead of $5\,bar$) than the one in the work of Dumouchel [57]. As it has been performed for the non-axial velocity, also E_k has been computed either on GRF and LRF.

To understand the influence of the nozzle geometry on the atomization, two non-dimensional coefficients have been built ([57]):

$$C_e = \sqrt{\frac{E_k}{\rho_l U_{th}^2}} \tag{5.13}$$

and

$$C_t = \sqrt{\frac{TKE_{tot}}{U_{th}^2}} \tag{5.14}$$

where U_{th} represents Bernoulli's velocity (see Eq. 5.3) and contains the difference between the injection pressure and the ambient pressure in the downstream chamber. Thus, these coefficients, as the discharge coefficient C_d, compare a characteristic velocity with Bernoulli's one. As mentioned in [57], if all the energy was converted into non-axial kinetic energy, C_e would be equal to 1, and $C_d = C_t = 0$. On the other hand, if all energy was converted in TKE, C_t would be equal to 1 and $C_d = C_e = 0$.

Table 5.5: *Non-dimensional coefficient and nozzle geometry parameters for the two configurations*

Config.	C_e	C_t	(lift+H)	off H	K
10	0.1713	0.1521	157.5	78.5	10.52
3	0.1326	0.1484	216.04	102	12.92

The values of C_e and C_t found, are in accordance with the trend found in [57] for the sensitivity on the cavity height: the higher the (lift+H) parameter, the smaller the non-dimensional coefficients. This decrease is also augmented in config. ID-3 by the higher value of "off H", which has the same effect of the eccentricity of the injector used in [57]. In general, for both the configurations, the non-axial flow will have a pivotal role on the atomization and additionally for the config. ID-10 the turbulence level would help. However, in the present work, the influence of pressure could not be analyzed since only one operative point has been simulated. Nevertheless, it is interesting to notice how the value of the non-dimensional coefficients found, are similar to those of a low pressure injection [57]. In fact, it was found that the trend of these parameters was more influenced by the geometry of the injector than by the Δp_i itself. However, without simulating these two injectors under several different pressure conditions, it is not possible to guarantee the same conclusions.

5.2 Comparison with Experiments

Shadowgraph pictures are realized using a light generator on one side and the camera on the other side, having the sample in between. Backlit imaging is based on ray deflection by interfaces. Assuming that interfaces are never perfectly flat and oriented perpendicularly to the incident rays, most of the rays crossing an interface are deviated with an angle bigger than the collection angle, whatever they are reflected or refracted through the interface. As a consequence, bubbles and vapor cavities appear dark in the image. On the contrary, liquid regions would appear bright, as (in absence of density gradient) they do not induce any ray deviation [135]. Two capturing views are realized by turning the sample around its axis: a front view ($\theta = 0°$), and a lateral view ($\theta = 90°$).

For the optical path, a long-range microscope (Navitar with home-made tubes from RD-vision) has been used. As light source, a half-inch flexible fiber optic light guide mated with a powerful LED illuminator (white steady light) has been employed.

Videos have been made with a high-speed video camera (Phantom V1210). The experimental images reported here were obtained using the fast camera with a sample rate of 100000 fps with an exposure time of $2\,\mu s$ for an interval of $15\,ms$. The resolution of the recorded area is 256 pixel x 256 pixel (16 bit gray scale). The camera has also been used at higher sample rate of 571428 fps, with an exposure time of $1,\mu s$. However, being the recorded area of these latter measurements of only 128 pixel x 16 pixel (16 bit gray scale), the visualization of the flow structures in the nozzle and the further analysis of a single image becomes more difficult than the higher resolution images at lower sample rate. Motion blur effect on the individual image has no relevance when time-averaging is finally performed. For the image processing an open-source java software (ImageJ-Fiji [185]) has been used.

Here it is only reported a qualitative comparison of numerical and experimental results on the front view ($\theta = 0°$) and on the lateral view ($\theta = 90°$) for the two configurations. This kind of analysis can give a qualitative index of reliability of the solver in describing the cavitating structures occurring inside the nozzle. In Fig. 5.30, Fig. 5.31, Fig. 5.32 and Fig. 5.33 a selection of instantaneous events from simulations and from experiments is proposed, where similarities have been manually tracked. These two views are helpful to distinguish the contribution of each type of cavitation and the multiphase flow topology of each zone.

configuration ID-10

Fig 5.30 are focused on the string cavitation, while, Fig. 5.31 is focused on the shear cavitation as string one is barely observed.

In Fig 5.30, especially in $\theta = 90°$ view, a pair of counter-rotating vortices is visible in the hole. In Fig. 5.30-(a), the cavitating vortices are not only occupying the nozzle region, as inf Fig. 5.30-(b) and Fig. 5.30-(c), but also half of the portion of the sac volume. This result confirms that the flow in the hole is highly interacting with the up-stream geometry (the U-bend upper volume) and the sac.

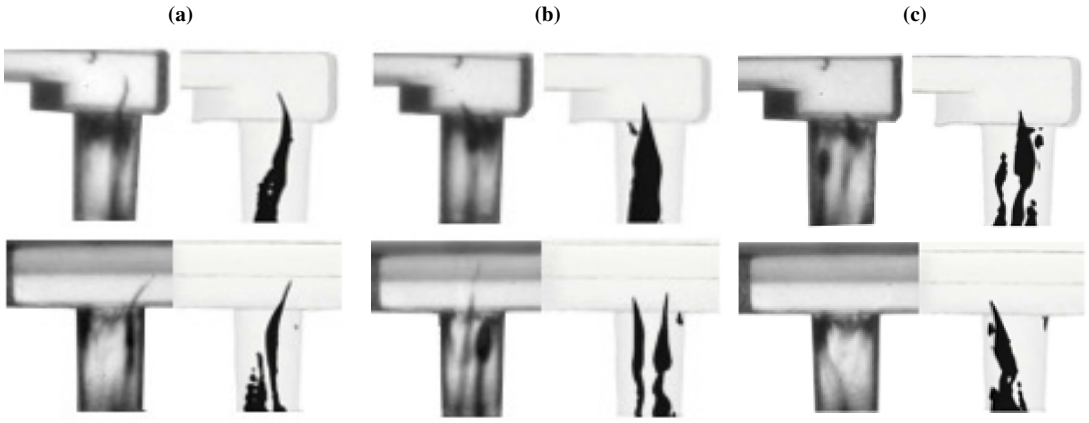

Figure 5.30: *From (a) to (c) qualitative comparison of detected string cavitation structures between experiments (left) and numerics (right): $\theta = 0°$ on the top and $\theta = 90°$on the bottom.*

In Fig. 5.31 the presence of the shear cavitation, despite the unsteadiness, is always covering only half part of the hole. Shear vortices are still visible but only inside the hole, close to the nozzle outlet where the shear cavitation has disappeared.

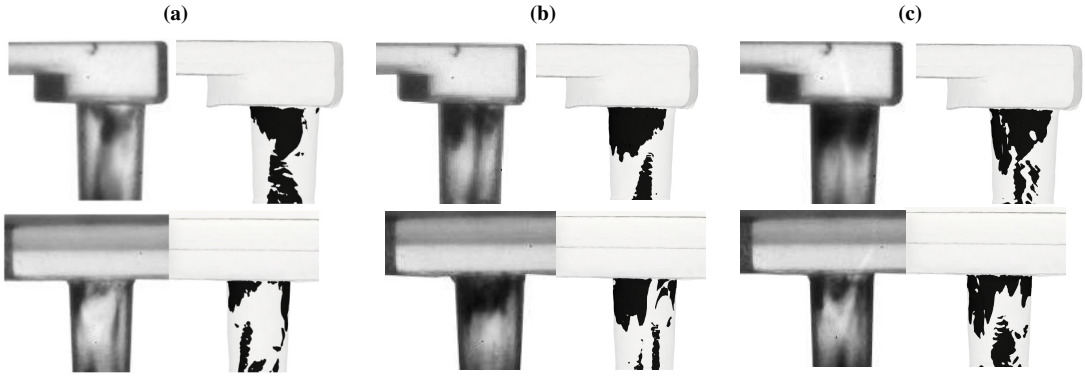

Figure 5.31: *From (a) to (c) qualitative comparison of detected shear cavitation structures between experiments (left) and numerics (right): $\theta = 0°$ on the top and $\theta = 90°$on the bottom.*

configuration ID-3

Fig 5.32 is focused on the string cavitation, while, Fig. 5.33 focuses on the shear cavitation as string cavitation is barely observed.

In Fig. 5.32 strings cavitation is less intense than string cavitation of config. ID-10. In particular, this is always accompanied by the shear cavitation which covers only a little portion of the nozzle inlet region. Strings are mostly occupying the nozzle region as evinced by experimental results as well.

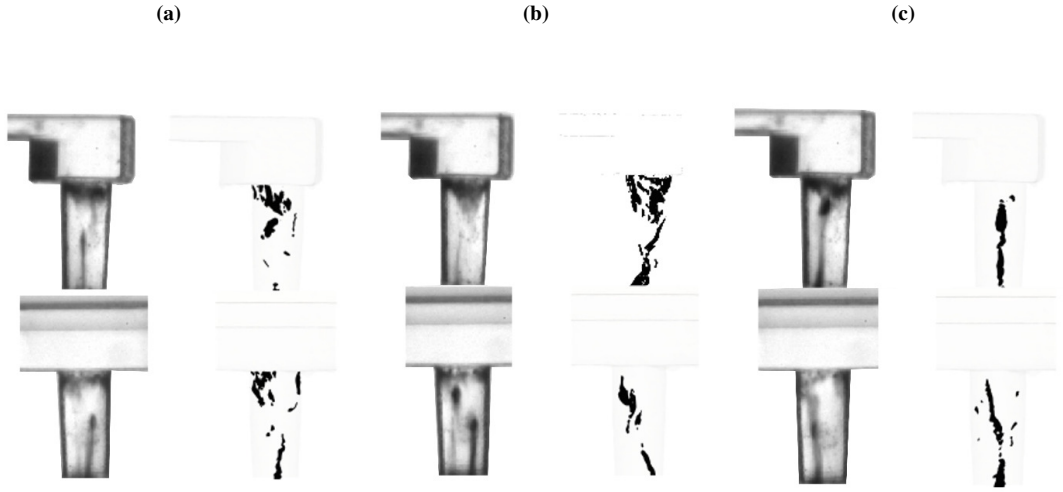

Figure 5.32: *From (a) to (c) qualitative comparison of detected string cavitation structures between experiments (left) and numerics (right): $\theta = 0°$ on the top and $\theta = 90°$on the bottom.*

Shear cavitation events are also shown in Fig. 5.33. From experimental pictures it is evident how the phenomenon interests only 20% of the nozzle volume and it is not as intense as the shear cavitation of config. ID-10. From numerical results it seems that sometimes the structures are coherent and sometimes they are absent.

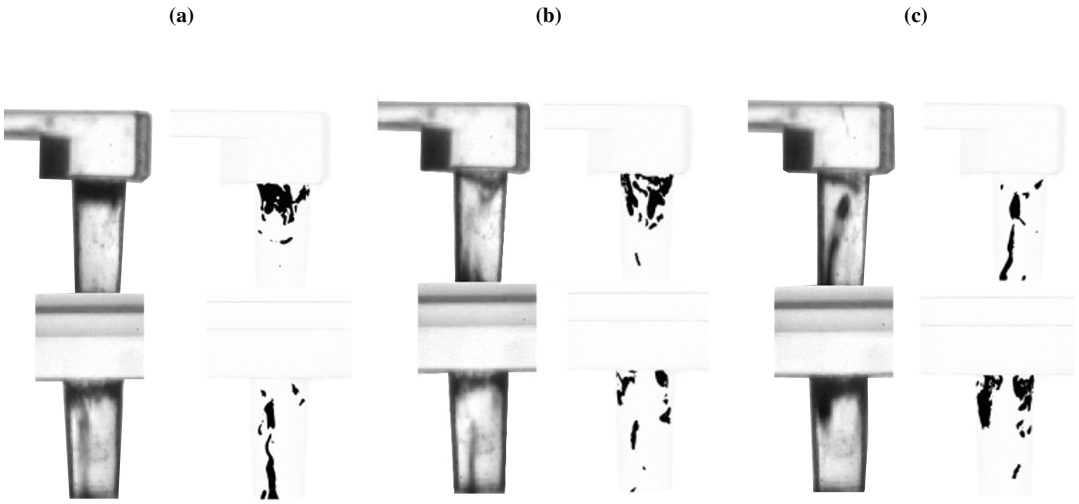

Figure 5.33: *From (a) to (c) qualitative comparison of detected shear cavitation structures between experiments (left) and numerics (right): $\theta = 0°$ on the top and $\theta = 90°$on the bottom.*

This said, the modifications brought to the sharp edges at the BFS and at the nozzle inlet, have a clear influence on how the fluid vena detaches from the corners and in the end on the order of magnitude of the recirculation, and therefore of the vapor production.

5.3 Conclusion

Differences in the behavior among config. ID-10 and ID-3 are significantly due to the geometry differences (e.g nozzle diameters, height, dead spaces) and to the inlet flow conditions developing from the small details in the sac. An example is given from the irregular shape of S_1. Already on this plane, it is clear the asymmetry brought about by these small details. At same inlet pressure condition, a different lift parameter is the responsible of a higher velocity in this section. Thus, ID-10 is characterized by a higher velocity of the flow. After this section, "sac height","off h" and "dead space" parameters determine how fuel will feed the nozzle. Although both the configurations have shown a similar behavior in terms of direct, side and reverse flow, it has been noticed that the higher the BFS ratio is (see Eq. 5.1), the higher the direct-MFR but the smaller the side-MFR will be. In particular this ratio has more influence on the side flow. It is also possible to conclude that the higher the ratio is, the smaller the counter rotating vortices produced at the nozzle inlet will be. Therefore, the BFS shape indirectly acts as a vortex generator. In particular it acts on the separation zone. In both cases, reverse flow has a minor importance than side and direct flow, which are almost the double. This means the dead space is not big enough to promote any kind of additional rotational flow at the nozzle inlet, and detachment as well. Additionally, the BFS provides a pressure drop among S_1 and N_1, reducing the available Δp to discharge fuel. This produces a different effect according to nozzle length and conicity:

- Config. ID-10, which is characterized by higher average pressure on N_1, has a shorter nozzle and lower conicity. If the outlet pressure is assumed almost the same, the acceleration induced on the flow for a higher Δp, will be higher itself. Bigger acceleration means more flow detachment at the inlet and thus more shear cavitation occurring at the nozzle inlet edges. Further contraction of cross section area is a promoter of the flow acceleration. However, the flow is not directed as the nozzle axis, mostly due to the bend

shape and the upstream BFS. Hence, in addition to an overall deviation of the flow, this will be highly characterized by two main counter rotating vortices, which occupy the center of the nozzle, while some additional small vortices are visible on the side. Due to the axial acceleration of the flow, the velocity component in the perpendicular plane (non-axial flow) becomes progressively smaller. The combined effect of expansion and vortex occurrence is of pivotal role for high string cavitation effect.

- Config. ID-3, which is characterized by lower average pressure on N_1, has a longer nozzle. This is also characterized by higher conicity. If the outlet pressure is assumed almost the same, the acceleration induced on the flow for a lower Δp with longer nozzle, will be way smaller. For this reason, both inlet detachment and shear cavitation are lower and also the string cavitation will result to be less intense.

Hence, the BFS plays a pivotal role in the sac flow determination: therefore, the choice of the nozzle dimensions, such as inlet and outlet diameters and length, can amplify or not the phenomena induced by the BFS. The opposite flow behavior of config. ID-10 and ID-3 is also proven by the different value of computed discharge coefficient. The geometry more characterized by higher cavitation occurrence, ID-10, shows a bigger oscillation in time of C_d and a smaller average value. Conversely, the one characterized by less intense cavitation,ID-3, shows smaller oscillation in time of C_d and higher average value. From the analysis of total turbulent kinetic energy and non-axial kinetic energy one can also evince that ID-10 is the configuration with the higher deflection of the jet and higher primary atomization. For both the cases the ratio TKE_{sgs}/TKE_{tot} at nozzle outlet has shown that LES simulation is providing accurate results.

For what concern the validation with the experimental measurements, it has been noticed, especially in config. ID-3, that even if the main cavitating structures along the nozzle are well captured, shear cavitation seems to be a bit underestimated. The nozzle-inlet flow conditions become highly influenced by the level of approximation in describing the shape of the edges. These results could be addressed to the accuracy of the micro XCT during the measurements of the geometries and also to their further adaptation for the mesh generation. Micro-XCT is not able to perfectly reproduce a curvature of the edges under sub-micrometer voxel resolution: the quality of the curvature of the edges obtained by the measurements is really poor in that sense. To overcome this lack of resolution, a kind of sharp edges have been recovered at the nozzle entrance and at the BFS. As a matter of fact, their shape, after this procedure, is not completely sharp because the surfaces are characterized by some smaller imperfections detectable with the micro-XCT. Thus, respect to the simulations performed on the nominal geometries [76], characterized by sharp edges and smooth surfaces, the simulations of the present work, based on the reshaped geometry, have shown to be characterized by lower shear cavitation.

CHAPTER 6

Primary Breakup

After a detailed analysis of the flow inside the sac and inside the nozzle, results for the primary break-up are finally presented in this chapter, which is structured as follows:

- The numerical results are reported in Sec. 6.1. In particular, the average values of the void fractions are reported onto two planes parallel to the nozzle axis, D_1 and D_2 (See Fig. 4.8). Then, time-average of spatial weight-averaged quantities (such as axial velocity, non axial velocity, void fractions, vorticity, pressure, density) are computed on perpendicular planes to nozzle axis (A_1, A_2, A_3). On these planes only the inner finer region ($2\,mm$) (see Fig. 4.9) has been considered for the average.
- A brief discussion on the interface resolution is reported in Sec. 6.2. Starting from the flame surface density concept used in the numerical combustion theory, it has been explained how the same concept has been used for the LES of multiphase flow. Therefore, interface density is introduced with some interface resolution sensors taken from literature. These are computed for three different instant of time for both D_1 and D_2 plane and for A_1.
- Afterwards, in Sec. 6.3, vorticity dynamic analysis has been used to outline the role of the structure of the vortices on the generation of surface's instabilities. Each term of vorticity equation has been computed for the same instant of time used in the interface resolution analysis.
- Finally, in Sec. 6.4 and Sec. 6.5 the validation for the primary breakup and the droplets size analysis are respectively reported. Main conclusions are summarized in Sec. 6.6.

6.1 Results

As shown in Fig. 6.1 and Fig. 6.2, for both the configurations, cavitation is not stable and it is not straightforward to define a precise cavitation regime. In general, as it has been outlined in the previous section, comparing the two configurations, one can notice that the

differences in the geometry, in particular “H”, “off H”, “nozzle length” and nozzle “outlet diameter”, influence significantly the cavitation within the nozzle orifice (see Sec. 5). The outcome of this different vapor production and collapse lead to a different spray angle width in the spanwise and crosswise direction. In particular, from the analysis on TKE_{tot} and E_k performed at nozzle outlet (see Sec. 5.1.5) it has been found that:

- the fuel jet in the proximity of the nozzle outlet will be wider in the spanwise and the crosswise direction but more deflected in the config. ID-10. The cause for this behavior must be addressed to the smaller BFS. As a consequence, ID-10 is characterized by higher cavitation, and higher vapor content at the nozzle outlet.
- The fuel jet in ID-3 will be narrower in the spanwise and the crosswise direction but more symmetric than ID-10: as a consequence, it is characterized by lower cavitation and vapor content at the nozzle outlet. This behavior is mostly addressed to the higher BFS.

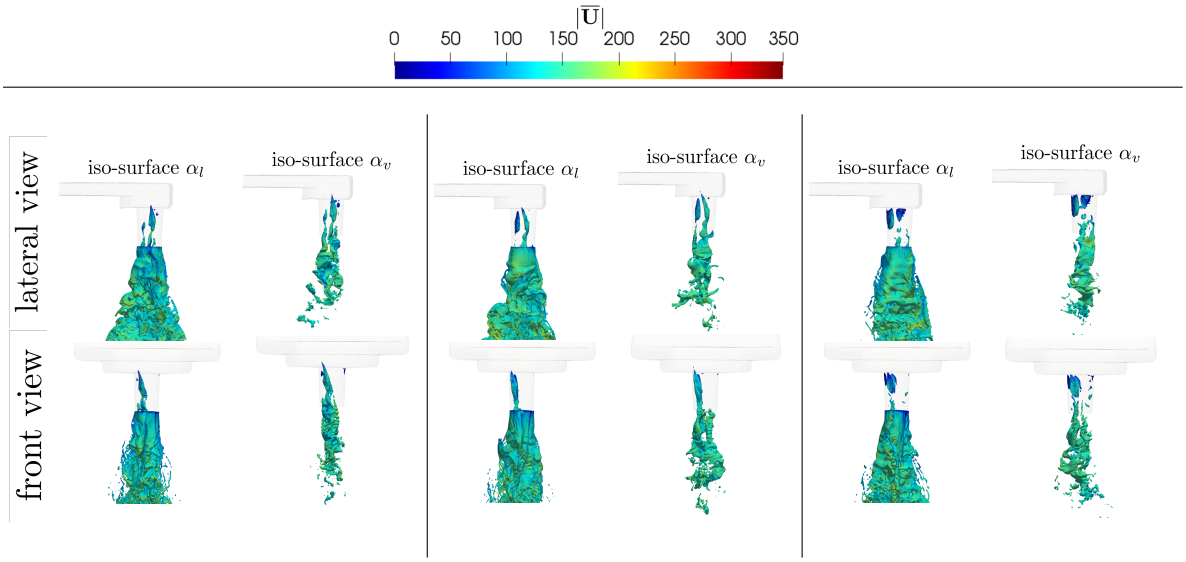

Figure 6.1: *Config. ID-10: evolution of the liquid jet and vapor generation from* 0.181 *to* $0.185\,ms$ *using iso-surfaces of* $\alpha_l = 0.35$ *and iso-surfaces of* $\alpha_v = 0.5$ *colored by velocity magnitude*

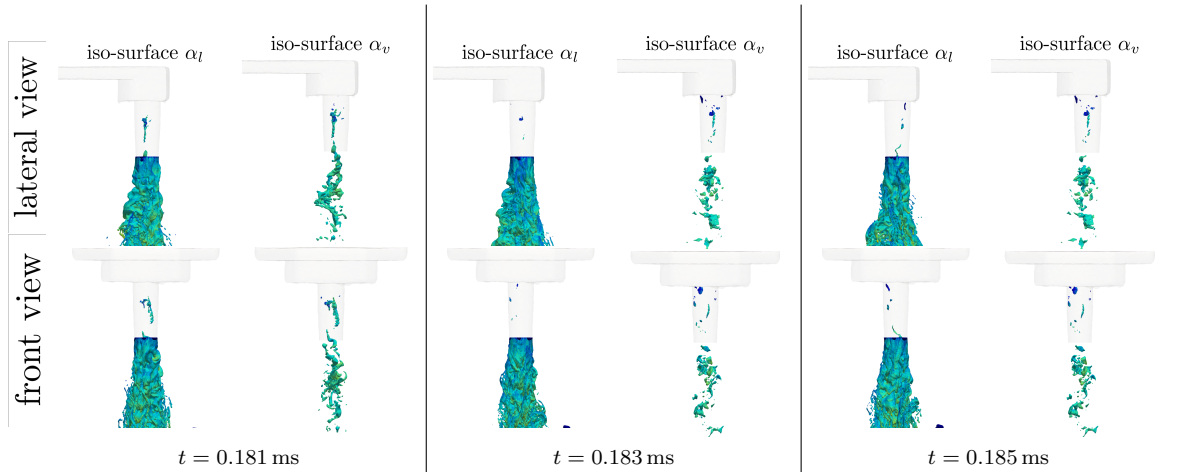

Figure 6.2: *config. ID-3: evolution of the liquid jet and vapor generation from* 0.181 *to* $0.185\,ms$ *using iso-surfaces of* $\alpha_l = 0.35$ *and iso-surfaces of* $\alpha_v = 0.5$ *colored by velocity magnitude*

Comparing vapor fraction iso-surfaces of Fig. 6.1 and Fig. 6.2, it is possible to notice the different expansion of the two vortices in the non-axial direction: ID-10 is characterized by a higher vapor content at the nozzle outlet and close to the nozzle tip. Conversely, ID-3 is characterized by lower vapor content close to the nozzle tip and this seems to be generated in a region whose diameter is almost the same of the nozzle outlet. This means that the two cavitating vortices are not as intense as the ones of ID-10: they do not show any abrupt expansion in the non-axial direction.

In Fig. 6.3 and Fig. 6.4 are respectively shown for ID-10 and ID-3, the evolution of the resolved liquid volume fraction on three different planes (A_1, A_2, A_3).

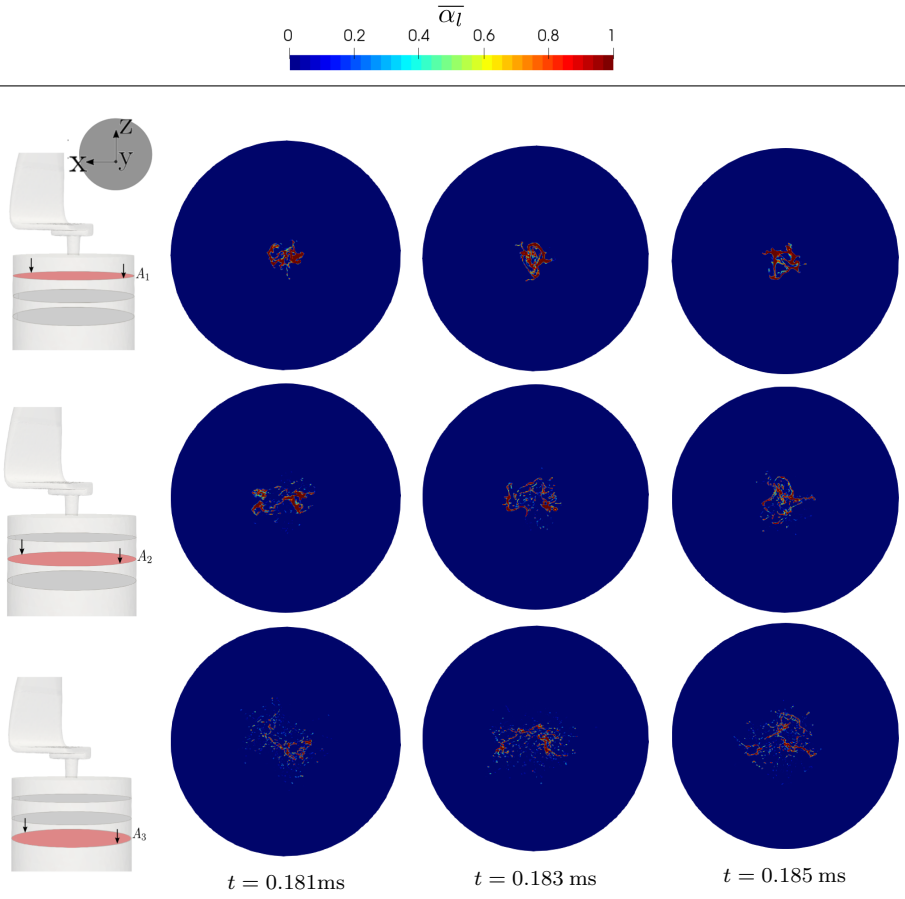

Figure 6.3: *config. ID-10: temporal evolution of resolved liquid fraction on A_1, A_2 and A_3.*

The different liquid distribution is already visible from plane A_1 ($0.25\,mm$ from nozzle outlet): ID-10 shows some thin ligaments in the outer part of the jet. The inner part is occupied by vapor. At each time, as shown in Fig. 6.3, two distinct zones are visible, which represent the two cavitating vortices reaching the ambient domain. They are not always characterized by the same diameter. As mentioned in Sec. 5, cavitation is intrinsically unsteady, thus, string cavitation intensity can vary time to time, leading to a different liquid distribution. Conversely, ID-3 shows a more compact liquid distribution. Ligaments are barely visible as the two distinct side: this outcome confirm a lower vapor content close to the nozzle tip as well. On plane A_2 ($0.5\,mm$ from nozzle outlet), the jet of ID-10 is occupying a zone which is almost the double of the one occupied by the jet of ID-3: the ligaments are spread over a wider zone due to the two vortices that have expanded in the non-axial direction. The inner

core is in fact not occupied by the liquid and the jet in ID-10 is assuming a particular shape which is similar to an hollow cone. The jet of ID-3 is still compact; some additional ligaments and droplets occurs in the outer region at the liquid/NC gases interface. This means that the primary break-up could be mainly induced by surface's instabilities. On plane A_3 ($0.75\,mm$ from nozzle outlet), vapor is almost all collapsed, and the central zone is then occupied by NC gases. This happens especially in ID-10, where very thin ligaments and droplets are spread over the plane in an asymmetric way: z-direction is the preferential direction over which liquid is spreading. Therefore, it is reasonable to expect a wider jet in the lateral view, and a narrower jet in the front view. The jet in ID-3 is still showing a central zone with a lot of liquid content. For this reason, air entrainment is not occurring as in the ID-10. Additionally, the jet seems to be more characterized by a symmetry in both x and z directions.

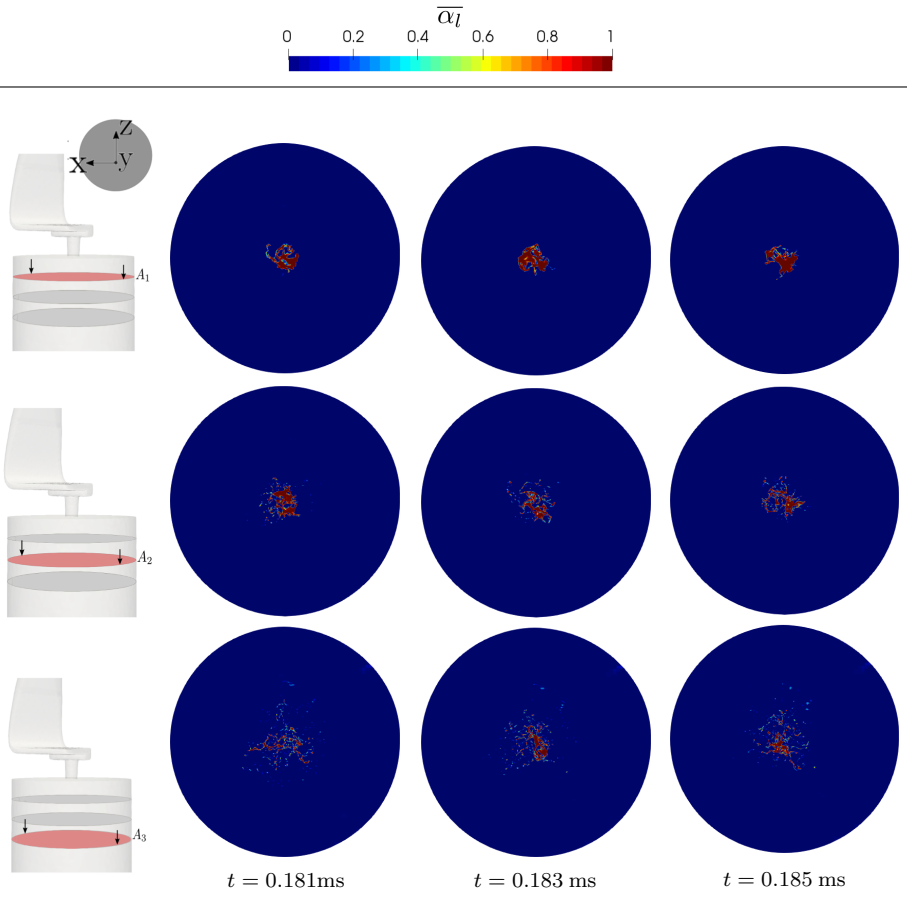

Figure 6.4: *config. ID-3: temporal evolution of resolved liquid fraction on A_1, A_2 and A_3.*

This qualitative outcome is in accordance with the JWP measurements of Fig. 4.1: the narrower the spray is, the higher the JWP will be. This behavior is verified looking into details at the time-average liquid fraction (Fig. 6.5a and Fig. 6.5d) and at time-average vapor fraction (Fig. 6.5c and Fig. 6.5f) on plane D_1 and D_2. This said, if we look into details at each configuration, we can see that:

- ID-10 averagely shows a wider jet in lateral view and a narrower jet in the front view. Although the flow field analysis within the sac has demonstrated that the flow is almost symmetric, the liquid volume fraction field shows asymmetry in both the views outside the nozzle. This asymmetry of the jet is due to the two cavitating vortices visible in Fig.

6.5c which are progressively expanding from the nozzle inlet to 0.2 mm after the nozzle tip. Shear cavitation is visible as well: this is almost due to the side flow in the sac. Hence, shear cavitation is mainly visible in the front view of Fig. 6.5c.

- ID-3 averagely shows narrower jet in both views (see Fig. 6.5d). Jet symmetry is almost preserved in both views. Two cavitating string are less visible in the front view of Fig. 6.5f. As mentioned in the Sec.5, the larger BFS has a negative effect on the vapor production in the nozzle. Shear cavitation is barely visible too. Consequently, the vapor content at the nozzle outlet is lower.

In general, from Fig. 6.5c and Fig. 6.5f, at $0.5\,mm$ from nozzle outlet, the average vapor content on A_2 is almost 0.000625.

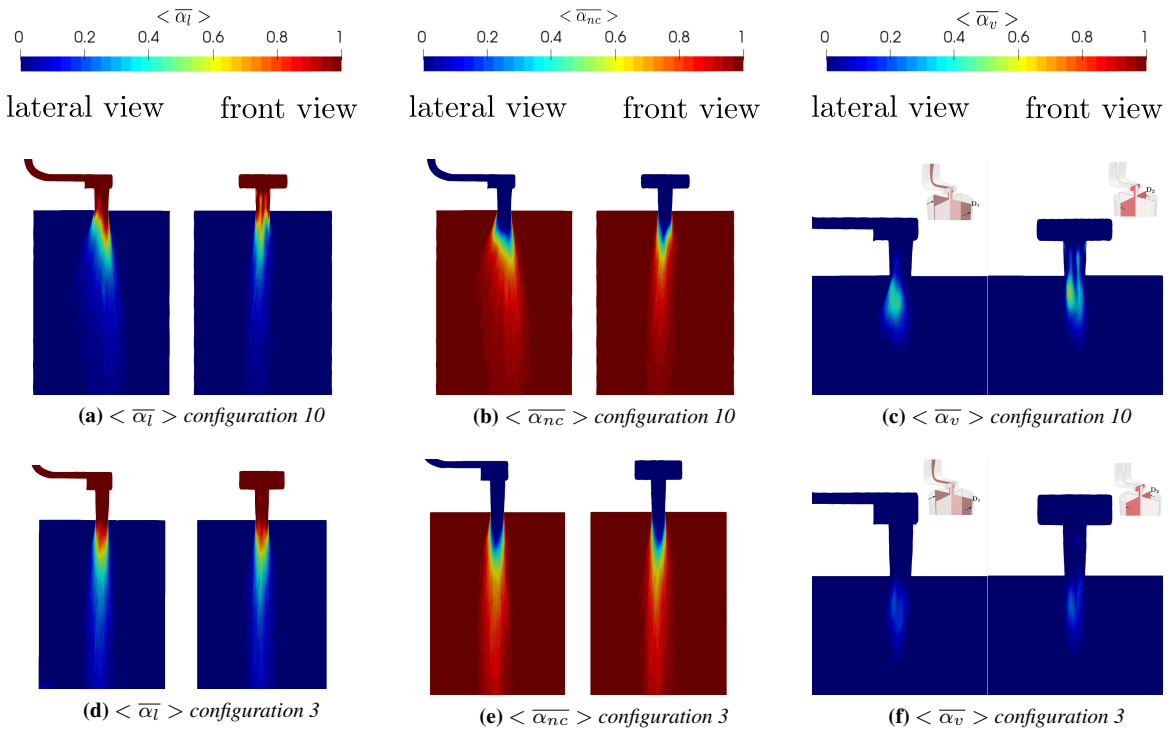

(a) $< \overline{\alpha_l} >$ *configuration 10* **(b)** $< \overline{\alpha_{nc}} >$ *configuration 10* **(c)** $< \overline{\alpha_v} >$ *configuration 10*

(d) $< \overline{\alpha_l} >$ *configuration 3* **(e)** $< \overline{\alpha_{nc}} >$ *configuration 3* **(f)** $< \overline{\alpha_v} >$ *configuration 3*

Figure 6.5: *Average liquid fraction (right pictures), average air fraction (middle pictures) and average vapor fraction (left pictures): config. ID-10 on the top row; config. ID-3 on the bottom row.*

As shown in Fig. 6.6b, the average vapor fraction coming from the nozzle is 50% higher in the config. ID-10. Notwithstanding this difference of vapor generation in the nozzle, which has been clearly addressed to the difference in the injector geometry, the trend followed by the two simulations is the same. From $0\,mm$ to $0.2\,mm$ vapor generation is still occurring: it reaches a peak and then condensation proceeds till $1\,mm$; distance at which the vapor is completely disappeared. This vapor is concentrated in the core of the jet and comes from an abrupt expansion of the vortices originating within the nozzle. This sudden expansion is visible in Fig. 6.6i: at $1\,mm$ from nozzle outlet, the average pressure is about $0.01\,bar$, which is three order of magnitude smaller than the pressure at the nozzle inlet (See Fig. 5.22). As soon as the jet moves far from the nozzle outlet, the pressure recovers to P_{atm}. For what concerns average liquid and average non-condensable, the discrepancies are due to how the lighter phase (NC) is acting on the surface of the jet leading to a different distribution of the liquid phase in the spanwise and crosswise directions.

From Fig. 6.1 and Fig. 6.2, it is already known that the jet of config. ID-10 is wider than the jet of config. ID-3. This, anyway, does not mean a bigger volume of liquid too, as the vapor trend (Fig. 6.6b), its average position within the jet, and the jet shape itself show. The more the vapor is generated in the core, the more the liquid must occupy the outer part of the jet with a consequent expansion of it. This is visible comparing the red zone (high probability in time to have liquid) of config. ID-10 (Fig. 6.5a) and config. ID-3 (Fig 6.5d). On plane D_1, in config. ID-10, the liquid is mostly occupying the outer part of the jet in a certain asymmetric way, while in config. ID-3 the liquid is mostly occupying the core of the jet. As soon as pressure recovers, the vapor collapses and an air entrainment occurs as shown in Fig. 6.5b and Fig. 6.5e

These two views explain why in config. ID-10, as soon as vapor disappears, the liquid fraction on the plane is lower than the quantity of liquid in the config. ID-3 (see Fig 6.6a).

On the other hand, the average non-condensable volume fraction will be higher in config. ID-10 (see Fig. 6.6c). This expansion of the jet is indirectly operated by the vapor but it is actually provided by the streamwise vortices expanding in the spanwise and crosswise direction. Till $0.4\,mm$ from nozzle tip, the average axial velocity is approximately $125\,m/s$ (see Fig 6.6d). From $0.4\,mm$ to $1\,mm$, region in which the vapor completely vanishes, the narrower jet of config. ID-3 owns a higher axial velocity. Conversely, the wider jet (config. ID-10) is characterized by an almost flat average axial velocity profile, which is kept stable till $2\,mm$. For the config. ID-3, after $1\,mm$, velocity tends to decrease almost linearly to reach the final value of $80\,m/s$, which is about half of the axial velocity at the nozzle outlet. As a first approximation, the jet of config. ID-10 has a hollow cone shape, which reduces the cross sectional area and thus reduces the overall drag on the liquid jet. On the contrary, being the jet of config. ID-3 narrower and concentrated around the nozzle axis (streamwise direction), the cross sectional area of the liquid is higher (the density of the mixture is higher as shown in Fig. 6.6h) and so is the overall drag. It follows that axial velocity tends to decrease.

The profile of the average non-axial velocity is shown in Fig. 6.6e. As for the axial velocity, from $0\,mm$ to $0.4\,mm$ the trend is the same, even if it is shifted of almost $5\,m/s$, which is a consequence of a smaller non-axial velocity coming from the nozzle (see Fig 5.29b). After $0.5\,mm$ from the nozzle tip, as already mentioned, the different amount of vapor generated has led to a different shape and width of the jet. For config. ID-10, this shape is similar to a hollow cone. This particular liquid structure has a smaller moment of inertia. For the conservation of angular momentum in the streamwise direction, if the moment of inertia decreases, the angular velocity must increase. Additionally, since the jet is expanding radially, for the angular momentum to be conserved, the radial velocity must increase. This effect is not visible for the config. ID-3 where the jet is much more compact and narrower. In general, as shown in Fig. 6.6f, the average non-axial velocity is always less than 20% for the config. ID-3 while for the config. ID-10 it is about the 20% nearby the nozzle tip and progressively reaches almost 30% during atomization. Conversely, to what happens inside the nozzle, axial and non-axial velocity difference among GRF and LRF is very small. The curves are almost overlapping, and their values are in accordance with their ones noticed on N_6 (see Fig. 5.29a and Fig. 5.29b): the curves progressively converge to the same value from N_1 to N_6. As a consequence, in the ambient domain the mean jet direction can be approximated very well by the nozzle axis direction. Increment of vorticity in the streamwise direction could be evinced also from Fig. 6.6g. However, a further analysis of vorticity dynamic along streamwise (y-axis), spanwise (z-axis) and crosswise (x-axis) direction is necessary to understand which are the phenomena that contribute the most to the break-up and which can be neglected. One can notice that even if non-axial velocity is higher for config. ID-10, the vorticity magnitude is lower than ID-3. This inversion must be addressed to the weight used in the space-average

on the planes. Being the weight a MFR weight, as defined in Eq. 4.12, the quantity is mainly conditioned by high velocity and in particular by high density regions. This difference in density can be clearly evinced by the Fig. 6.6h, where density profile of config. ID-10 stays below the density profile of config. ID-3.

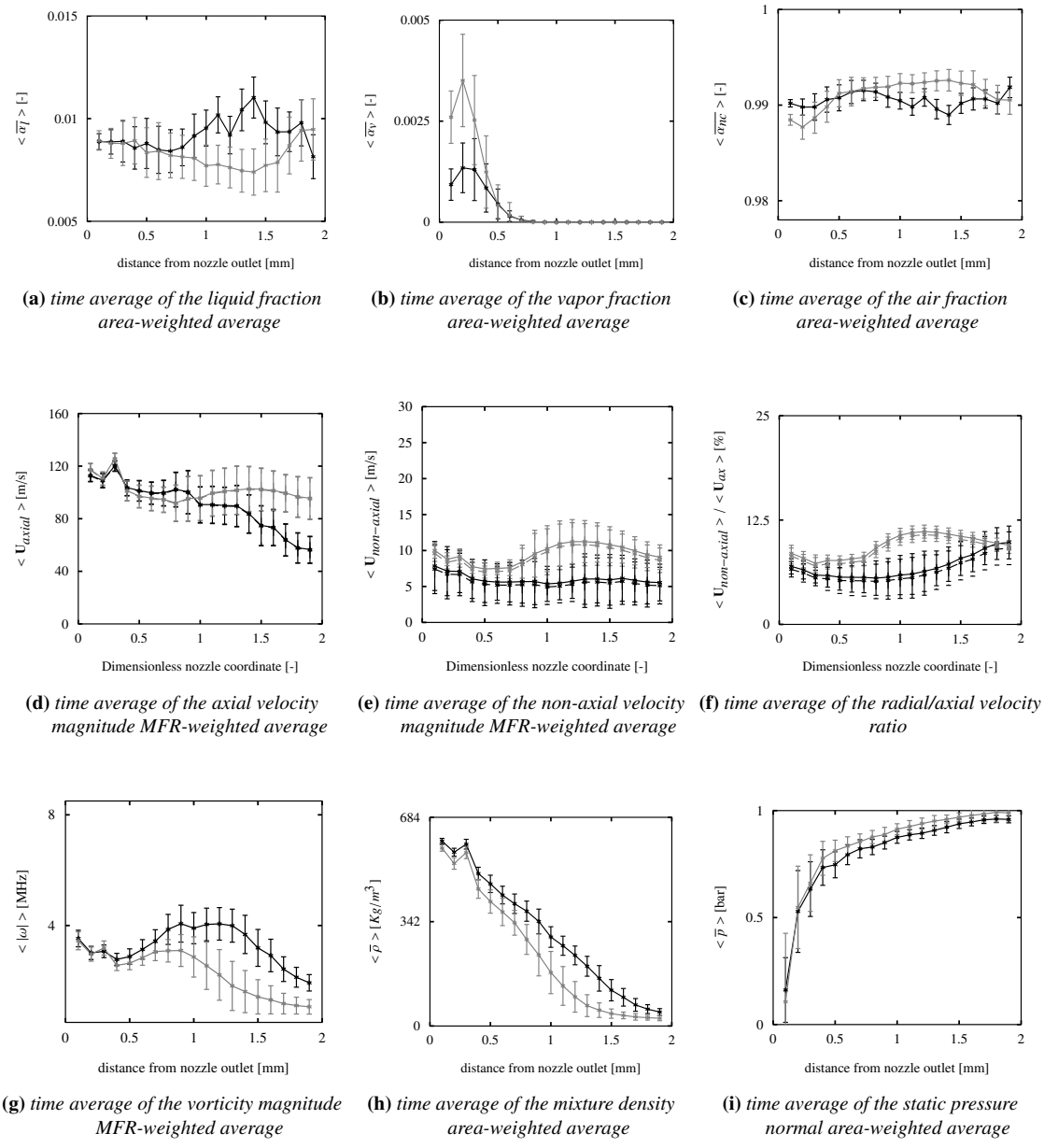

(a) *time average of the liquid fraction area-weighted average*

(b) *time average of the vapor fraction area-weighted average*

(c) *time average of the air fraction area-weighted average*

(d) *time average of the axial velocity magnitude MFR-weighted average*

(e) *time average of the non-axial velocity magnitude MFR-weighted average*

(f) *time average of the radial/axial velocity ratio*

(g) *time average of the vorticity magnitude MFR-weighted average*

(h) *time average of the mixture density area-weighted average*

(i) *time average of the static pressure normal area-weighted average*

Figure 6.6: *Time average quantity profiles along refined region of ambient domain: — id-10, — id-3 on GRF, – – – id-10, – – – id-3 on LRF . Each point denotes the time average of a space average quantity at a fixed distance from nozzle outlet.*

6.2 Interface Resolution

Description of interfaces in turbulent flows has gained popularity in the 80s and 90s in order to describe the turbulent mixing [165], turbulent premixed flames [36], [216] and turbulent diffusion flames [133]. [165]. These can be analyzed in terms of material surfaces, propagat-

ing surfaces and constant-property surfaces [165]. The concept of flame surface was firstly introduce by Marble et al. [133] to describe the turbulent diffusion flame. It simply specified the flame surface area per unit volume:

$$\Sigma(\mathbf{x}, t) = \frac{\delta A}{\delta V} \tag{6.1}$$

For an infinitely thin flame, the flame surface density can be estimated using the following relation [165]:

$$\Sigma = \Sigma(c*) = \overline{|\nabla c| \delta_d(c - c*)} = \left(\overline{|\nabla c| \Big|_{c=c*}}\right) P(c*) \tag{6.2}$$

where $0 < c < 1$ denotes the normalized progress variable, whose convective form reads:

$$\frac{\partial c}{\partial t} + \mathbf{U} \cdot \nabla c = \frac{1}{\rho}[\nabla \cdot (\rho \nabla c) + \dot{\omega}_c] \tag{6.3}$$

δ_d is the Dirac's delta, $\left(\overline{|\nabla c| \Big|_{c=c*}}\right)$ is the filter of the magnitude of the progress variable conditioned on the surface $c*$ and $P(c*)$ is the probability to find $c = c*$ in a given position. Therefore, starting from Eq. 6.3 it is possible to obtain a surface flame density equation [165], [216]:

$$\frac{\partial \Sigma}{\partial t} + \nabla \cdot (< \mathbf{U} >_{surf} \Sigma) =< \nabla \cdot \mathbf{U} - \mathbf{nn} : \nabla \mathbf{U} >_{surf} - \mathbf{n} \nabla \cdot (S_L \Sigma) \tag{6.4}$$

Where S_L is the relative velocity of the flame front on the iso-surface $c = c_0$, $\mathbf{U}$ is the local fluid velocity and $n = -\nabla c / |\nabla c|$ is the unit normal vector to the flame front (surface $c = c*$) and pointing towards fresh gases. $< \phi >_{surf}$ denotes the surface average of a generic variable ϕ, and it is defined as:

$$< \phi >_{surf} = \frac{\left(\overline{\phi |\nabla c| \Big|_{c=c*}}\right)}{\left(\overline{|\nabla c| \Big|_{c=c*}}\right)} \tag{6.5}$$

If the flame front has a thickness (not infinitely thin), Eq. 6.15 can be integrated over all possible values of c:

$$\int_0^1 \Sigma(c*) dc* = \int_0^1 \left(\overline{|\nabla c| \Big|_{c=c*}}\right) P(c*) dc* = \overline{|\nabla c|} \tag{6.6}$$

Therefore, replacing the surface average $< \phi >_{surf}$ with the generalized surface average:

$$\overline{< \phi >_{surf}} = \frac{1}{|\nabla c|} \int_0^1 < \phi >_{surf} \Sigma(c*) dc* \tag{6.7}$$

it possible to write an equation of propagation for $\overline{\Sigma}$, which reads:

$$\frac{\partial \overline{\Sigma}}{\partial t} + \nabla \cdot (\overline{< \mathbf{U} >_{surf}} \, \overline{\Sigma}) = \dot{\overline{\Sigma}} \tag{6.8}$$

Where terms composing $\dot{\overline{\Sigma}}$ need a closure to perform LES computation. Using a phenomenological approach, based on the existing modelization of the interfacial area concentration in

turbulent reacting mixing flow, an analogous interface density equation to Eq. 6.8 can be written [220], [219]. In fact, $\overline{< \mathbf{U} >_{surf}}$, that corresponds to the advection velocity of the interface density (filtered interface velocity [55]), cannot be used. This is defined, within the CV of the filter, using a Dirac's delta centered on the interface. Therefore, this velocity cannot be directly used in LES computation and it must be modeled. For The ELSA approach [220] [219], the authors suggested to rewrite Eq. 6.8, replacing $\overline{< \mathbf{U} >_{surf}}$ (velocity of the interface density), with the velocity of the i-th phase, in order to transport the interface density:

$$\frac{\partial \overline{\Sigma}}{\partial t} + \nabla \cdot (\overline{\Sigma}\,\overline{\mathbf{U}_i}) = \nabla \cdot (\overline{\Sigma}(\overline{\mathbf{U}_i} - \overline{< \mathbf{U} >_{surf}})) + \dot{\overline{\Sigma}} \tag{6.9}$$

The first term on the RHS of Eq. 6.9 denotes the dispersion of the interface by turbulence, while $\dot{\overline{\Sigma}}$ must take into account the physical phenomena responsible for interface destruction and production. For this reason, the latter term can be decomposed as the sum of three different sink/source terms:

$$\dot{\overline{\Sigma}} = \dot{\overline{\Sigma_{int}}} + \dot{\overline{\Sigma_{vap}}} + \dot{\overline{\Sigma_{mix}}} \tag{6.10}$$

When studying the jet atomization:

- $\dot{\overline{\Sigma_{int}}}$ denotes the production/destruction due to stretching, turbulence and liquid structures interactions. These phenomena coexist within the control volume, thus it is difficult to determine the relative importance among them.
- $\dot{\overline{\Sigma_{vap}}}$ denotes the production/destruction due to vaporization. This term is difficult to be modeled. In literature has been always neglected [3], [11].
- $\dot{\overline{\Sigma_{mix}}}$ denotes the production due to liquid/gas mixing. This term is not originally present in the formulation of flame surface density and it present some problems in its definition and initialization as well.

In the context of dense media, the dispersion of the interface by turbulence has been modeled as a standard diffusion term [220], [119], neglecting any contribution of the average slip velocity:

$$\overline{\Sigma}(\overline{\mathbf{U}_i} - \overline{< \mathbf{U} >_{surf}}) \approx D_\Sigma \nabla \overline{\Sigma} = \frac{\nu_t}{Sc_t} \nabla \overline{\Sigma} \tag{6.11}$$

In the original formulation of ELSA, $\dot{\overline{\Sigma_{mix}}}$ was not introduced. Afterwards, Vallet et. Al [220] and Lebas et al. [119] have proposed two different formulations. However, in both cases, this term does not have a strong effect on the whole calculation. An alternative has been proposed by Chesnel [3], and use also by Anez [11]. $\overline{\Sigma}$ can be decomposed in an average component $\overline{\Sigma}_{min}$ and a fluctuating component $\overline{\Sigma'}$:

$$\overline{\Sigma} = \overline{\Sigma}_{min} + \overline{\Sigma'} \tag{6.12}$$

$\overline{\Sigma}_{min}$ should represent the minimum surface that can be found in a control volume for a given liquid fraction. In the LES context it denotes the resolved interface density [3]. As a result, it is required to compute the evolution of $\overline{\Sigma'}$, built following Eq. 6.9:

$$\frac{\partial \overline{\Sigma'}}{\partial t} + \nabla \cdot (\overline{\Sigma'}\,\overline{\mathbf{U}_i}) = \nabla \cdot (\overline{\Sigma'}(\overline{\mathbf{U}_i} - \overline{< \mathbf{U} >_s})) + \dot{\overline{\Sigma_{int}}} \tag{6.13}$$

where $\dot{\overline{\Sigma_{mix}}}$ does not appear for the hypothesis made on $\overline{\Sigma}_{min}$. At this point, once $\dot{\overline{\Sigma_{int}}}$ is modeled, according to the work of Lebas et al. [119] and Duret et al. [59], Eq. 6.13 can be solved, and Σ is finally computed through Eq. 6.12 and Eq. 6.9.

However, $\overline{\Sigma}_{min}$ must be modeled as well: this has been proposed through two simple analytical studies on a cube and on a sphere [3] using LS approach. For the case of the sphere, the analytical solution has been compared with computation from DNS and generally:

$$\Sigma_{min} \approx \frac{2.4\sqrt{\overline{\Phi}(1-\overline{\Phi})}}{a} \tag{6.14}$$

This approximation represents in a good way the minimun interface density. In the work of Chesnel, Σ_{min} (Eq. 6.14) has been modeled using the level set function. Successively, in the work of Anez et al. [11], the same model has been proposed using the VOF-ELSA.

In the present work, the algebraic VOF can only describe accurately the dense part of the spray (close to the nozzle tip), and no additional term are used to take into account the sub-grid scales at the interfaces in the dilute region. However, $\overline{\Sigma}$ is useful to understand in which region of the domain, the AVOF is resolving interface correctly. Although, no transport equation of $\overline{\Sigma}$ is present, this can be estimated through the Eq. 6.6, using the resolved liquid volume fraction field:

$$\Sigma =< |\nabla \overline{\alpha_l}| > \tag{6.15}$$

This can help to estimate the small-scale characteristics such as droplet size distribution and mean droplet diameter. Since liquid shapes are not always spherical and a single diameter cannot account for all other ligaments or any complex shape of the interface, $\overline{\Sigma}$ is more general and can take into account any kind of interface.

In [11], resolved Σ is used also to compute Interface Resolved Quality (IRQ) sensors, to know when the models coming from the LES filtering (at the interface) must be considered or not: IRQ sensors are used in combination of a modification of C_α to switch to ICM to ELSA. For the present work, the IRQ sensors proposed in [11] can be used to give an estimate of how well the AVOF is resolving, and where it is actually resolving well.

- IRQ_Σ is given by the ratio of the minimum resolved interface area, Σ_{min} and the actual one, Σ:

  $$IRQ_\Sigma = \frac{\Sigma_{min}}{\Sigma} \tag{6.16}$$

  Thus, the higher the interface is wrinkled within a cell, the lower the IRQ_Σ is and sub-grid effects become relevant. In other words when the resolved Σ is bigger than the Σ_{min}, $IRQ_\Sigma < 1$ which means that sub-grid effects must be taken into account cause the grid is not enough fine to resolve the interface. On the contrary, values of $IRQ_\Sigma >> 1$ denote a good interface capturing.

  Σ_{min} is the minimum surface density that can be evaluated for a given value of resolved liquid volume fraction:

  $$\Sigma_{min} = \frac{2.4\sqrt{\overline{\alpha_l}(1-\overline{\alpha_l})}}{a} \tag{6.17}$$

  This parameter is inversely proportional to a parameter a which considers the length scale of the control volume. In the LES framework, this parameter is equal to the filter length scale. In the present work, $a = \Delta = \sqrt[3]{\Delta x \Delta y \Delta z}$.

- IRQ_κ, conversely, considers the interface curvature κ (See Eq. 2.20). The sensor reads:

  $$IRQ_\kappa = \frac{1}{\Delta\kappa} \tag{6.18}$$

  The smaller the interface curvature is, the better the resolution of the interface will be and the higher the sensor value will be too. In the present work IRQ_κ has not been computed but it has been reported for sake of clarity.

These sensors have been originally conceived for a two-phase flow without phase-change. However, in the present work the liquid belongs to two different interfaces: liquid/vapor and liquid/non-condensable gases, and thus Σ should be computed separately for the two interfaces. Using the resolved liquid volume fraction for the definition of the two sensors does not allow to know which is the interface better resolved. On the other hand, vapor production/destruction is based on a bubble model which allows only to describe bubbles bigger than mesh resolution, but it is impossible to know *a-priori* their dimensions. In any case, values of IRQ applied to the liquid/vapor interface would be probably biased by the phase-change approach and cavitation model used. For this reason, the IRQ_{sigma} has been computed using $\overline{\alpha_l}$, which is equal to consider the two aforementioned interfaces as a unique interface.

Fig. 6.7 shows the evolution from $t = 0.181\text{ms}$ to $t = 0.185$ ms for the resolved liquid volume fraction, the estimate of $\overline{\Sigma}$, and the $IRQ_{\overline{\Sigma}}$ for config. ID-10 on D_1 and D_2, while in Fig. 6.8 the fields are visualized on a plane perpendicular to the nozzle axis, which is $0.25\,\text{mm}$ far from the nozzle outlet.

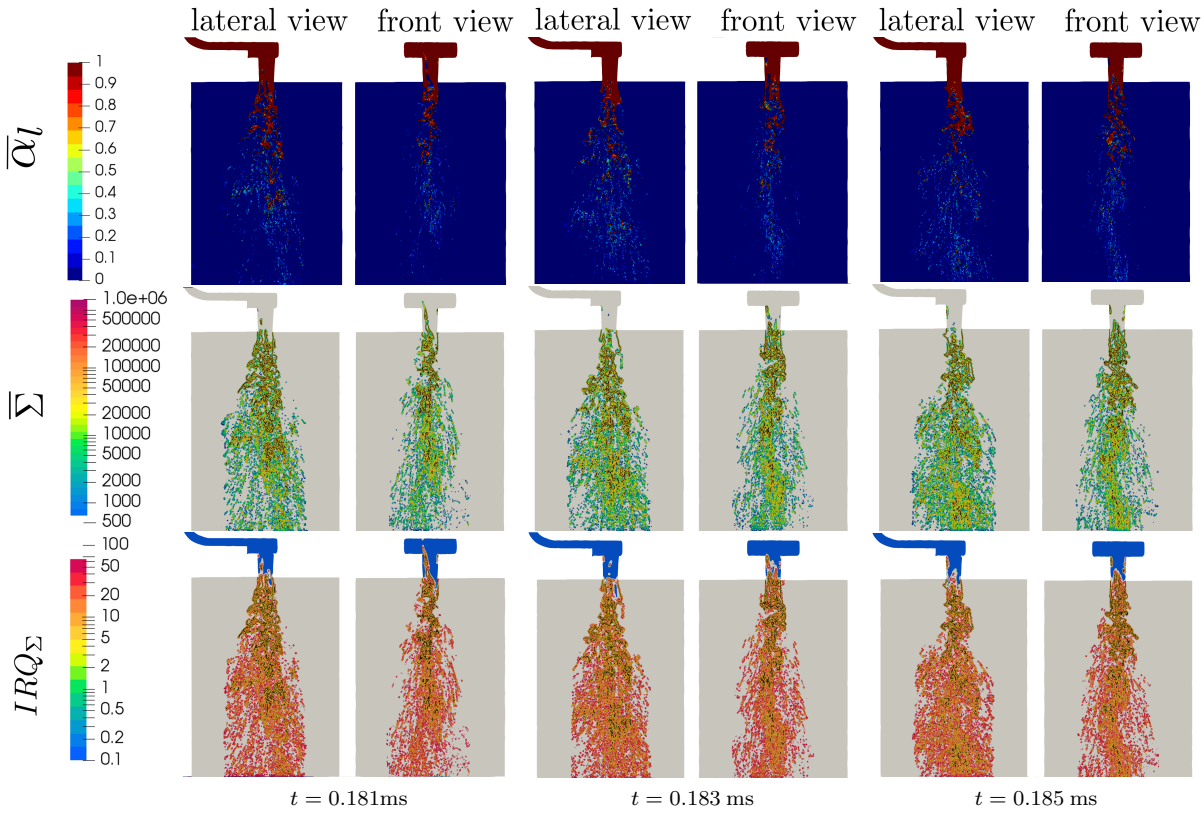

Figure 6.7: *config. ID-10, temporal evolution of liquid volume fraction (first row), liquid/gas surface density (second row), IRQ_Σ (third row) on D_1 and D_2. $\overline{\Sigma}$ and IRQ_Σ are shown with log scale color bar to enhance visualization. Black line identifies the liquid/NC interface for $\alpha_l = 0.5$.*

Looking at the evolution of the resolved volume fraction field on D_1 and D_2, it is clear that a denser jet region is situated between nozzle outlet and $0.5\,mm$ far from it. In config. ID-10, atomization efficiency is higher, as confirmed by the higher values of TKE_{tot} and E_k (see Sec. 5.1.5). As soon as the fuel leaves the nozzle, the cavitating vortices expands and liquid is atomized: an intact liquid core is not visible, rather long ligaments and droplets can

be appreciated. The central zone is occupied by vapor, which disappears at almost $0.75\,mm$ from nozzle outlet, where the jet is almost disrupt. Nevertheless, the fine discretization used in the region extending from nozzle outlet up to $2\,mm$ far from it, this is not enough to capture these droplets originated during the breakup process. The AVOF employed in the present work is not able to capture interface accurately for the dilute region since nor geometric reconstruction of interface (geometric-VOF) or specific sub-grid interface models are used. On the other hand higher mesh resolution would have been unaffordable and demanding from a computational point of view. Thus, $\overline{\Sigma}$ and IRQ_Σ can be computed to understand which are the limit of validity of the approach employed. Focusing on the zones of spray where the black contour of liquid/NC gases interface is visible, one can notice that $\overline{\Sigma}$ is the highest. This means that in the cells crossed by the interface, the resolved area per control volume is high. This value must be compared with the Σ_{min} as suggest the IRQ_Σ sensor. The sensor must be considered in the zones where only interface is visible. The value of the sensor in these cells is between 10 and 20. Higher values of IRQ are reached in zones where $\overline{\alpha_l} << 0.5$, thus, these values cannot gives a reliable index for a proper interface capture. In general it is possible to say that the AVOF gives reliable results till $1\,mm$ from nozzle outlet. Plane A_1 has been chosen for the visualization on the cross-sectional area of the jet (Fig. 6.8) since at $0.25\,mm$ from nozzle outlet, the vapor generation reaches its peak.

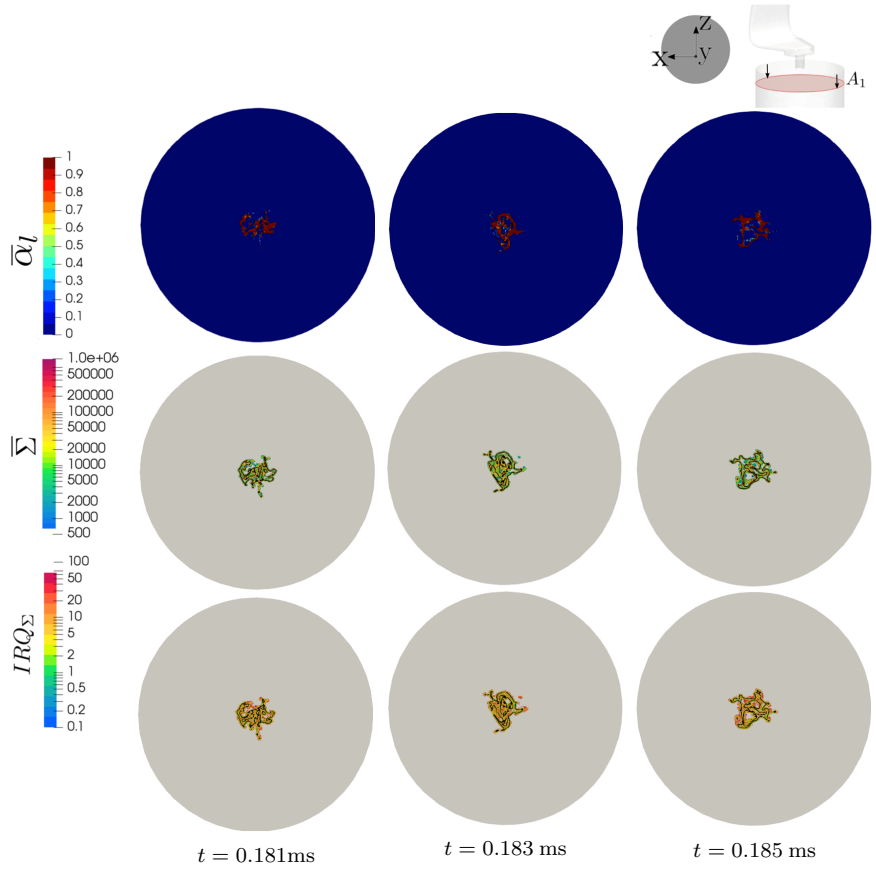

Figure 6.8: *config. ID-10, temporal evolution of liquid volume fraction (first row), liquid/gas surface density (second row), IRQ_Σ (third row) on plane at $0.25\,mm$ from nozzle outlet.$\overline{\Sigma}$ and IRQ_Σ are shown with log scale color bar to enhance visualization. Black line identifies the liquid/NC interface for $\alpha_l = 0.5$.*

In this way it is possible to see from time to time, the non-axial expansion of the jet on the same plane. At time $0.181\,ms$ the jet seems to be split into two regions: the upper region is more compact, with some ligaments on the external part, the lower region is a kind of hollow circle, whose center is filled with vapor. Conversely, at time $0.183\,ms$ and $0.185\,ms$, smaller structures and thinner ligaments are visible. The core is always occupied by vapor. This different spray pattern is mostly due to different vapor content that is time to time injected in the ambient domain through the cavitating string developing inside the nozzle orifice. $\overline{\Sigma}$ is still the highest at liquid/NC gases interface. IRQ_Σ is about 5-20, which is index of reliable interface capturing. Higher values of IRQ are reached in zones where $\overline{\alpha_l} << 0.5$, thus, these values cannot gives a reliable index for a proper interface capture.

The same visualization has been performed for the config. ID-3: Fig. 6.9 shows the evolution from $t = 0.181\text{ms}$ to $t = 0.185$ ms for the resolved liquid volume fraction, the estimate of $\overline{\Sigma}$, and the $IRQ_{\overline{\Sigma}}$ on D_1 and D_2, while in Fig. 6.10 the fields are visualized on a plane perpendicular to the nozzle axis, which is far 0.25 mm from the nozzle outlet.

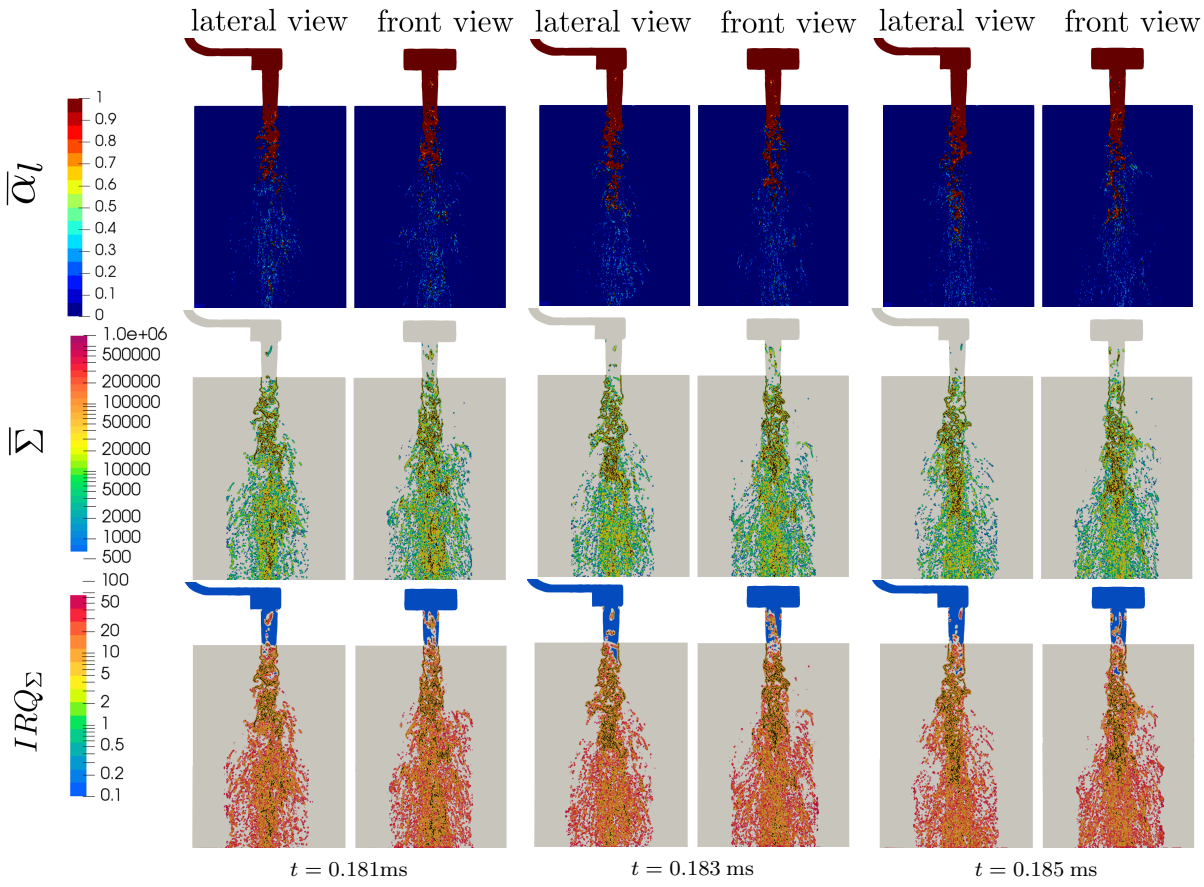

Figure 6.9: *config. ID-3, temporal evolution of liquid volume fraction (first row), liquid/gas surface density (second row), IRQ_Σ (third row) on D_1 and D_2.$\overline{\Sigma}$ and IRQ_Σ are shown with log scale color bar to enhance visualization. Black line identifies the liquid/NC interface for $\alpha_l = 0.5$.*

In config. ID-3 the denser jet region is situated between nozzle outlet and $0.75\,mm$ from nozzle outlet. In config. ID-3, atomization efficiency is lower, as confirmed by the smaller values of TKE_{tot} and E_k (see Sec. 5.1.5). The cavitating vortices are less intense. For this reason an intact liquid core is now visible, and disintegration of the jet is mainly operated by instabilities on the liquid surface. At time $t = 0.183\text{ms}$ and time $t = 0.185$ ms the dense

region can also reach $1\,mm$ from nozzle outlet. $\overline{\Sigma}$ and IRQ_Σ have been computed as well. As previously mentioned, the sensor must be considered in the zones where only interface is visible. The value of the sensor in these cells is between 10 and 20. Higher values of IRQ are reached in zones where $\overline{\alpha_l} << 0.5$, thus, these values cannot give a reliable index for a proper interface capture. In general it is possible to conclude that the AVOF gives reliable results up to $1\,mm$ far from nozzle outlet as evinced for ID-10.

Fig. 6.10 shows the cross-sectional area of the jet on plane A_1. Compared to ID-10, the jet is always narrower from time to time and just a few ligaments are produced externally due to surface instabilities. The core does not show a vapor content as high as the one observed in ID-10 and therefore, the jet appears not spread in the non-axial direction. $\overline{\Sigma}$ is still the highest at liquid/NC gases interface. IRQ_Σ is about 5-20, which is index of reliable interface capturing. Higher values of IRQ are reached in zones where $\overline{\alpha_l} << 0.5$, thus, these values cannot gives a reliable index for a proper interface capture.

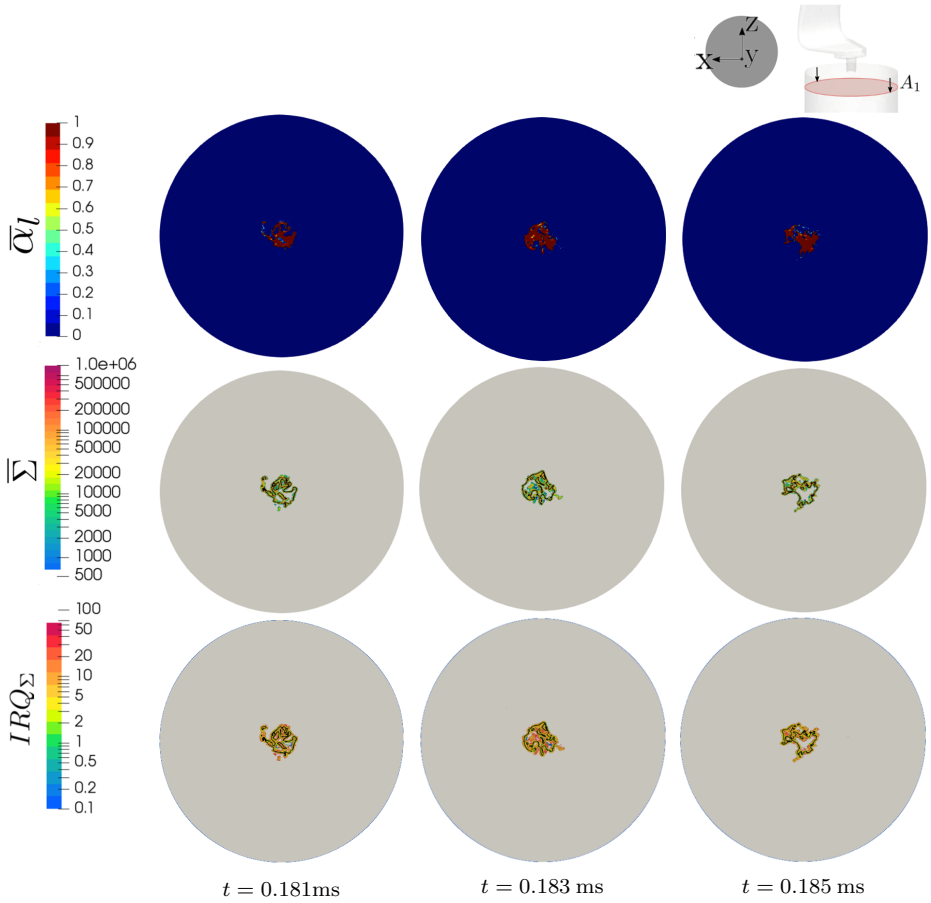

Figure 6.10: *config. ID-3, temporal evolution of liquid volume fraction (first row), liquid/gas surface density (second row), IRQ_Σ (third row) on plane at $0.25\,mm$ from nozzle outlet. $\overline{\Sigma}$ and IRQ_Σ are shown with log scale color bar to enhance visualization. Black line identifies the liquid/NC interface for $\alpha_l = 0.5$.*

6.3 Vortex Dynamic and Primary Breakup

Vortex dynamic concepts can help to understand the mechanism behind the liquid/air surface deformation in a jet in the primary atomization process. In particular, the generation of the streamwise vortices and their interaction with spanwise vortices, produces different instabil-

ities at the liquid surface. However, the link between the vortex dynamics and the surface dynamics in primary atomization is poorly understood. In the past, there have been several studies of the jet instabilities from the vortex dynamic perspective but most of them did not consider any density and viscosity discontinuities. In [98], [244], the authors investigate the vortex dynamics for a two phase problem using a single-fluid model (VOF-LEVEL SET). As expected, the vortex dynamic analysis helped explaining the three major atomization cascades at different flow conditions. Although, interesting findings of that research did not involve any phase change phenomena. In injectors, one of the primary atomization mechanism is cavitation (and bubble collapse as well). Vortices generation have effect not only on three-dimensional instabilities at the surface but it is also responsible for the vapor generation, which influences the jet angle as well. In [8], the effect of the vorticity dynamics has been investigated taking into account the cavitation, but the analysis mainly focused on the internal nozzle flow rather than on the primary breakup.

Recalling the momentum equation in the convective form (Cauchy formulation):

$$\rho\frac{D\mathbf{U}}{Dt} = -\nabla\hat{p} + \nabla\cdot\boldsymbol{\tau} + \mathbf{f}_\sigma + S_U - \mathbf{g}\cdot\mathbf{x}\nabla\rho \tag{6.19}$$

and applying the operator $\nabla\times$, it follows that:

$$\underbrace{\nabla\times\left(\frac{D\mathbf{U}}{Dt}\right)}_{\text{I}} = \underbrace{\nabla\times\left(\frac{-\nabla\hat{p}}{\rho}\right)}_{\text{II}} + \underbrace{\nabla\times\left(\frac{\nabla\cdot\boldsymbol{\tau}}{\rho}\right)}_{\text{III}} + \underbrace{\nabla\times\left(\frac{\mathbf{f}_\sigma}{\rho}\right)}_{\text{IV}} + \underbrace{\nabla\times\left(\frac{-\mathbf{g}\cdot\mathbf{x}\nabla\rho}{\rho}\right)}_{V} \tag{6.20}$$

Where the source S_u is not considered in the following treatise.

The term I can be rewritten as:

$$\nabla\times\left(\frac{D\mathbf{U}}{Dt}\right) = \frac{\partial\omega}{\partial t} + (\mathbf{U}\cdot\nabla)\omega + \omega(\nabla\cdot\mathbf{U}) - (\omega\cdot\nabla)\mathbf{U} = \frac{D\omega}{Dt} + \omega(\nabla\cdot\mathbf{U}) - (\omega\cdot\nabla)\mathbf{U} \tag{6.21}$$

The term II can be rewritten as:

$$\nabla\times\left(\frac{-\nabla\hat{p}}{\rho}\right) = \frac{1}{\rho^2}\nabla\rho\times\nabla\hat{p} - \underbrace{\frac{1}{\rho}(\nabla\times\nabla\hat{p})}_{\text{zero}} \tag{6.22}$$

where the second term on RHS is zero for curl applied to a gradient.

The term III is not developed for sake of simplicity but it would include both momentum diffusion and turbulent momentum diffusion.

The term IV appears only when multiphase approach is used, and its related to the surface tension forces. It can be rearranged as follows, using Eq. 2.23:

$$\nabla\times\left(\frac{\mathbf{f}_\sigma}{\rho}\right) = \nabla\times\left(\frac{\sigma\kappa\nabla\alpha_l}{\rho}\right) = \nabla\left(\frac{\sigma\kappa}{\rho}\right)\times\nabla\alpha_l + \underbrace{\frac{\sigma\kappa}{\rho}(\nabla\times\nabla\alpha_l)}_{\text{zero}} \tag{6.23}$$

The term V is related to the body forces. If buoyancy is negligible, as in the present work, this term is also negligible, but in general it reads:

$$\nabla\times\left(\frac{-\mathbf{g}\cdot\mathbf{x}\nabla\rho}{\rho}\right) = \nabla\times\left(\frac{-\mathbf{g}\cdot\mathbf{x}}{\rho}\right)\times\nabla\rho + \left(\frac{-\mathbf{g}\cdot\mathbf{x}}{\rho}\right)\nabla\times\rho \tag{6.24}$$

For the present study,the resulting vorticity dynamic equation reads:

$$\frac{D\omega}{Dt} = \underbrace{-\omega(\nabla\cdot\mathbf{U})}_{\text{stretching due to compressibility}} + \underbrace{(\omega\cdot\nabla)\mathbf{U}}_{\text{stretching or tilting due to velocity gradient}} + \underbrace{\frac{1}{\rho^2}\nabla\rho\times\nabla\hat{p}}_{\text{baroclinicity}} + \underbrace{\nabla\times\left(\frac{\nabla\cdot\boldsymbol{\tau}}{\rho}\right)}_{\text{vorticity diffusion+turb diffusion}} + \underbrace{\nabla\left(\frac{\sigma\kappa}{\rho}\right)\times\nabla\alpha_l}_{\text{vorticity generation at the surface}} \tag{6.25}$$

In the work of Jarrabashi et al. [98], vorticity diffusion and vorticity generation due to the surface tension are said to be two orders of magnitude smaller than other terms and the authors had decided to neglect them. However, depending on the Re and the We numbers, these term could become relevant. For this reason, in the present work also these terms have been analyzed. In [98] the stretching due to the compressibility effect has been neglected as well, being $\nabla\cdot\mathbf{U}=0$ for a non phase-changing jet. This is not true in the present study where continuity equation is used in the non-conservative form to build the cavitation model and ensures volume fluxes consistency (Eq. 2.13). Additionally, it must be underlined that the baroclinity effect can be caught only using a cavitation model based on a bubble model. As already mentioned in [8] and [244], using a barotropic model, the misalignment of pressure and density field cannot be represented.

Denoting with y the streamwise direction (nozzle-axis), with z the spanwise direction and with x the crosswise direction, it is now possible to project the Eq. 6.25 on each direction and identify, for each term, what is the contribution to the generation of stretching or tilting, especially along streamwise direction. This helps to identify which are the terms responsible for the streamwise vorticity generation.

$$\frac{D\omega_x}{Dt} = -\omega_x(\nabla\cdot\mathbf{U}) + \left(\omega_x\frac{\partial U_x}{\partial x}+\omega_y\frac{\partial U_x}{\partial y}+\omega_z\frac{\partial U_x}{\partial z}\right) + \left(\frac{1}{\rho^2}\left(\frac{\partial\rho}{\partial y}\frac{\partial\hat{p}}{\partial z}-\frac{\partial\hat{p}}{\partial y}\frac{\partial\rho}{\partial z}\right)\right) + \left(\frac{\partial\left(\left(\frac{\nabla\cdot\tau}{\rho}\right)\cdot\mathbf{k}\right)}{\partial y}-\frac{\partial\left(\left(\frac{\nabla\cdot\tau}{\rho}\right)\cdot\mathbf{j}\right)}{\partial z}\right) + \left(\frac{\partial\frac{\sigma\kappa}{\rho}}{\partial y}\frac{\partial\alpha_l}{\partial z}-\frac{\partial\frac{\sigma\kappa}{\rho}}{\partial z}\frac{\partial\alpha_l}{\partial y}\right) \tag{6.26}$$

$$\frac{D\omega_y}{Dt} = \underbrace{-\omega_y(\nabla\cdot\mathbf{U})}_{\text{I}} + \underbrace{\left(\omega_x\frac{\partial U_y}{\partial x}+\omega_y\frac{\partial U_y}{\partial y}+\omega_z\frac{\partial U_y}{\partial z}\right)}_{\text{II}} - \underbrace{\left(\frac{1}{\rho^2}\left(\frac{\partial\rho}{\partial x}\frac{\partial\hat{p}}{\partial z}-\frac{\partial\hat{p}}{\partial x}\frac{\partial\rho}{\partial z}\right)\right)}_{\text{III}} - \underbrace{\left(\frac{\partial\left(\left(\frac{\nabla\cdot\tau}{\rho}\right)\cdot\mathbf{k}\right)}{\partial x}-\frac{\partial\left(\left(\frac{\nabla\cdot\tau}{\rho}\right)\cdot\mathbf{i}\right)}{\partial z}\right)}_{\text{IV}} - \underbrace{\left(\frac{\partial\frac{\sigma\kappa}{\rho}}{\partial x}\frac{\partial\alpha_l}{\partial z}-\frac{\partial\frac{\sigma\kappa}{\rho}}{\partial z}\frac{\partial\alpha_l}{\partial x}\right)}_{\text{V}} \tag{6.27}$$

$$\frac{D\omega_z}{Dt} = -\omega_z(\nabla\cdot\mathbf{U}) + \left(\omega_x\frac{\partial U_z}{\partial x}+\omega_y\frac{\partial U_z}{\partial y}+\omega_z\frac{\partial U_z}{\partial z}\right) + \left(\frac{1}{\rho^2}\left(\frac{\partial\rho}{\partial x}\frac{\partial\hat{p}}{\partial y}-\frac{\partial\hat{p}}{\partial x}\frac{\partial\rho}{\partial y}\right)\right) + \left(\frac{\partial\left(\left(\frac{\nabla\cdot\tau}{\rho}\right)\cdot\mathbf{j}\right)}{\partial x}-\frac{\partial\left(\left(\frac{\nabla\cdot\tau}{\rho}\right)\cdot\mathbf{i}\right)}{\partial y}\right) + \left(\frac{\partial\frac{\sigma\kappa}{\rho}}{\partial x}\frac{\partial\alpha_l}{\partial y}-\frac{\partial\frac{\sigma\kappa}{\rho}}{\partial y}\frac{\partial\alpha_l}{\partial x}\right) \tag{6.28}$$

where $\omega_x, \omega_y, \omega_z$ denote respectively the crosswise, the streamwise and the spanwise vorticity components.

The Eq. 6.27 is the one that describes the variation of streamwise vorticity, which could be associated either to production or to destruction. The term I of Eq. 6.27 (compressibility effect) can be expanded as follows:

$$-\omega_y(\nabla\cdot\mathbf{U}) = -\omega_y\frac{\partial U_x}{\partial x} - \omega_y\frac{\partial U_y}{\partial y} - \omega_y\frac{\partial U_z}{\partial z} \tag{6.29}$$

The three terms on the RHS of 6.29 are respectively:

- $-\omega_y\frac{\partial U_x}{\partial x}$ crosswise vortex stretching
- $-\omega_y\frac{\partial U_y}{\partial y}$ streamwise vortex stretching
- $-\omega_y\frac{\partial U_z}{\partial z}$ spanwise vortex stretching

The term II on the RHS of Eq. 6.27 denotes respectively:

- $\omega_x \frac{\partial U_y}{\partial x}$ crosswise vortex tilting

- $\omega_y \frac{\partial U_y}{\partial y}$ streamwise vortex stretching

- $\omega_z \frac{\partial U_y}{\partial z}$ spanwise vortex tilting

It can be noticed that, in the zones where phase-change is active, the streamwise vortex stretching is canceled out, due to different signs in the two previous terms.

The term III on the RHS of Eq. 6.27 denotes respectively:

- $\frac{1}{\rho^2} \frac{\partial \hat{p}}{\partial x} \frac{\partial \rho}{\partial z}$ baroclinic effect due to normal pressure gradient

- $-\frac{1}{\rho^2} \frac{\partial \hat{p}}{\partial z} \frac{\partial \rho}{\partial x}$ baroclinic effect due to spanwise pressure gradient

The term IV on the RHS of Eq. 6.27 denotes respectively:

- $\frac{\partial\left(\left(\frac{\nabla \cdot \tau}{\rho}\right) \cdot \mathbf{k}\right)}{\partial x}$ vortex diffusion in crosswise direction

- $-\frac{\partial\left(\left(\frac{\nabla \cdot \tau}{\rho}\right) \cdot \mathbf{i}\right)}{\partial z}$ vortex diffusion in spanwise direction

The term V on he RHS of Eq. 6.27 represents respectively:

- $\frac{\partial \frac{\sigma \kappa}{\rho}}{\partial x} \frac{\partial \alpha_l}{\partial z}$ Marangoni effect in crosswise direction

- $-\frac{\partial \frac{\sigma \kappa}{\rho}}{\partial z} \frac{\partial \alpha_l}{\partial x}$ Marangoni effect in spanwise direction

Fig. 6.11 shows the contribution of each term in the generation of ω_y for config. ID-3 (black line) and config. ID-10 (gray line). As suggested in the work of Zandian et al. [244], for low density ratio (ρ_{nc}/ρ_l), like the case studied here, baroclinicity is the most important factor (see Fig. 6.11c), since the density gradient normal to the interface is high. Baroclinicity is only slightly larger than stretching and tilting (II). These terms are more important near the nozzle tip rather than far from it. The compressibility effect, shown in Fig. 6.11a, produces as a final effect a vortex stretching in the spanwise and crosswise direction (being streamwise vortex stretching canceled out by the opposite term in (II)). This term is only active in the region where phase-change is still occurring: the term rapidly increases in the zone where the average vapor fraction is increasing (from $0\,mm$ to $0.4\,mm$), it decreases when bubbles collapse occur, and progressively tends to zero. Vorticity generation in the streamwise direction (Fig, 6.11d) due to vorticity diffusion and surface tension (Fig. 6.11e) shows a similar profile: near the nozzle tip both the terms have a negative effect. As soon as the jet is expanding by the effect of the other terms, also vorticity diffusion and surface tension have a positive effect.

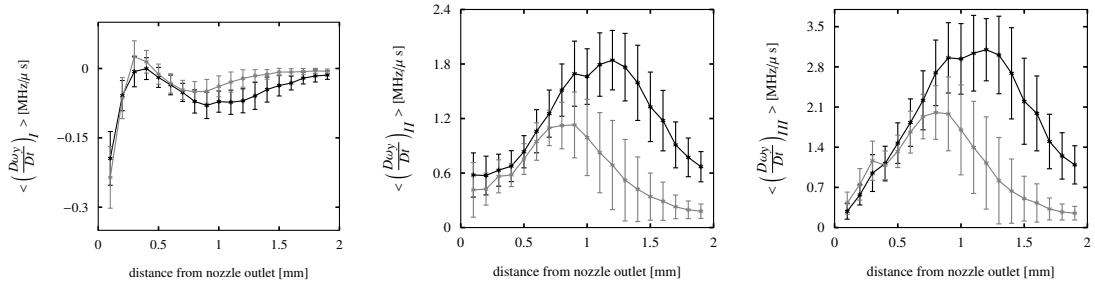

(a) *compressibility (I)* **(b)** *stretching and tilting (II)* **(c)** *baroclinity (III)*

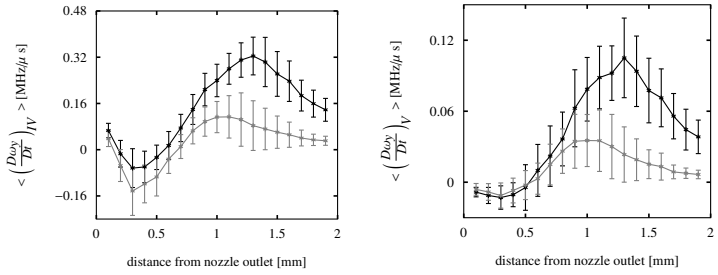

(d) *viscous term (IV)* **(e)** *surface tension term (V)*

Figure 6.11: *Time average of the Streamwise vorticity dynamic terms (see Eq. 6.27) MFR-weighted average. Planes position corresponds to the planes* $0.1\,mm$ *spaced in the refined region of ambient domain: — config-10,* **—** *config-3.*

All these terms are higher for the config. ID-3 for the streamwise vorticity generation, because a MFR weight has been applied, but in both cases it is possible to conclude that compressibility term (I), viscous term (IV) and surface tension term (V) are 1-2 order of magnitude smaller than stretching and tilting term (II) and baroclinicity term(III), as shown in Fig. 6.12.

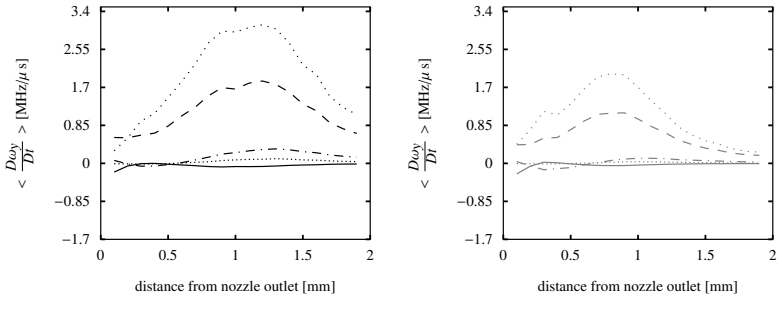

(a) *id-3 streamwise vorticity* **(b)** *id-10 streamwise vorticity*

Figure 6.12: *Analysis of the order of magnitude for streamwise vorticity generation equation (Eq. 6.27) in the refined region of the ambient domain: (a)* **—** *config-3;(b) — config-10; — (I); – – – (II); . . .(III); - - - (IV); ...(V)*

However, a similar analysis performed on the spanwise vorticity generation and crosswise

vorticity generation has revealed an opposite behavior:

- baroclinity term is 1 order of magnitude smaller, cause now the density gradient is evaluated parallel to the nozzle direction. It is true that mixture density is progressively diminishing far from nozzle, but the highest density variation still remains perpendicular to the nozzle direction.
- vortex stretching and tilting have now an opposite trend respect to baroclinity.

For both the configurations, viscous term (IV) and surface tension term (V) can be neglected also for the spanwise (Fig. 6.13) and the crosswise (Fig. 6.14) vorticity generation.

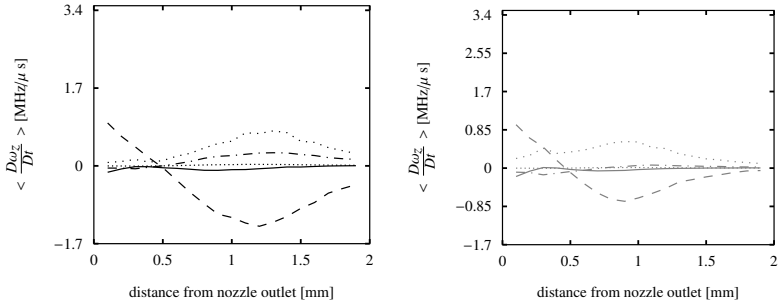

(a) *id-3 spanwise vorticity* **(b)** *id-10 spanwise vorticity*

Figure 6.13: *Analysis of the order of magnitude for spanwise vorticity generation equation (Eq. 6.28) in the refined region of the ambient domain: (a) — config-3;(b) — config-10; — (I); – – – (II); . . .(III); – - – (IV); ...(V)*

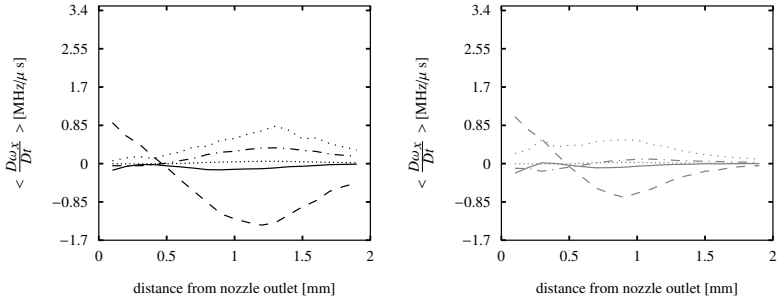

(a) *id-3 crosswise vorticity* **(b)** *id-10 crosswise vorticity*

Figure 6.14: *Analysis of the order of magnitude for crosswise vorticity generation equation (Eq. 6.26) in the refined region of the ambient domain: (a) — ID-3;(b) — ID-10; — (I); – – – (II); . . .(III); – - – (IV); ...(V)*

Generally, comparing the outcome of the analysis on the streamwise vorticity generation in Fig. 6.12, on the spanwise vorticity generation in Fig. 6.13 and on the crosswise vorticity generation in Fig. 6.14, it is possible to conclude that baroclinicity is the most important factor in the generation of the streamwise vortices and in the manifestation of 3D instabilities at low density ratio. This result is also shown in Fig. 6.15, where the dynamics of vorticity are analyzed in a temporal interval of $4\,\mu s$. The baroclinic term is the most important factor in the wrinkling of the interface. A minor contribution is given by the stretching and the tilting terms. Compressibility term is relevant only at the interface among vapor and liquid where phase-change is occurring. Finally, the viscous term (vorticity diffusion) acts mostly in the

zones where surface strain is high. However, it is almost two order of magnitude smaller, as the surface tension term, than baroclinc term and stretching/tilting term.

Baroclinic and stretching/tilting terms are the most relevant within the nozzle orifice: the former is localized in the vapor zones, the latter is intense also in the sac where vortical structures are present, as mentioned before in the nozzle flow analysis (Chapter 5).

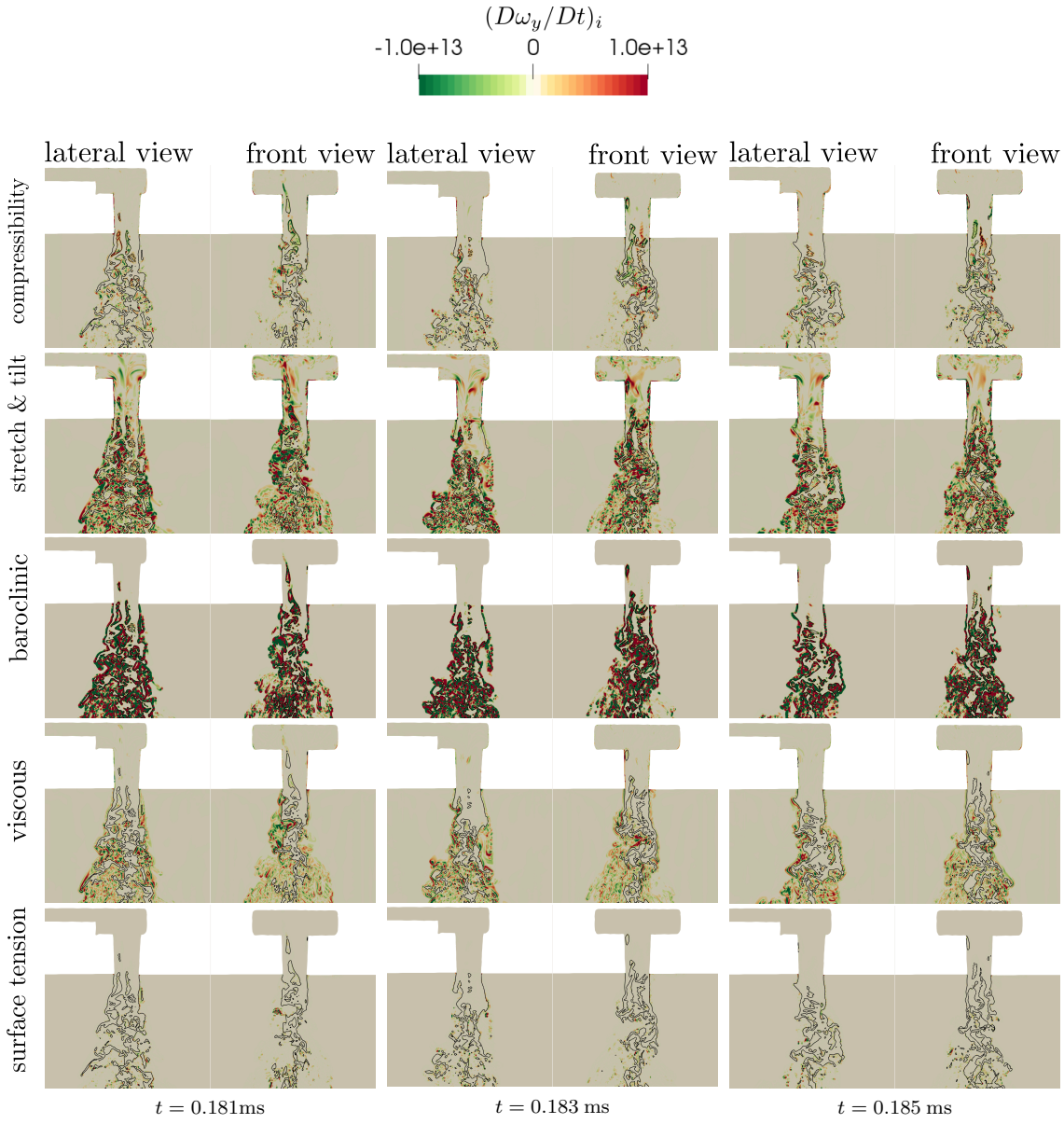

Figure 6.15: *config. ID-10, temporal evolution of streamwise vorticity dynamics terms on D_1 and D_2. Black line identifies the liquid interface for $\alpha_l = 0.5$.*

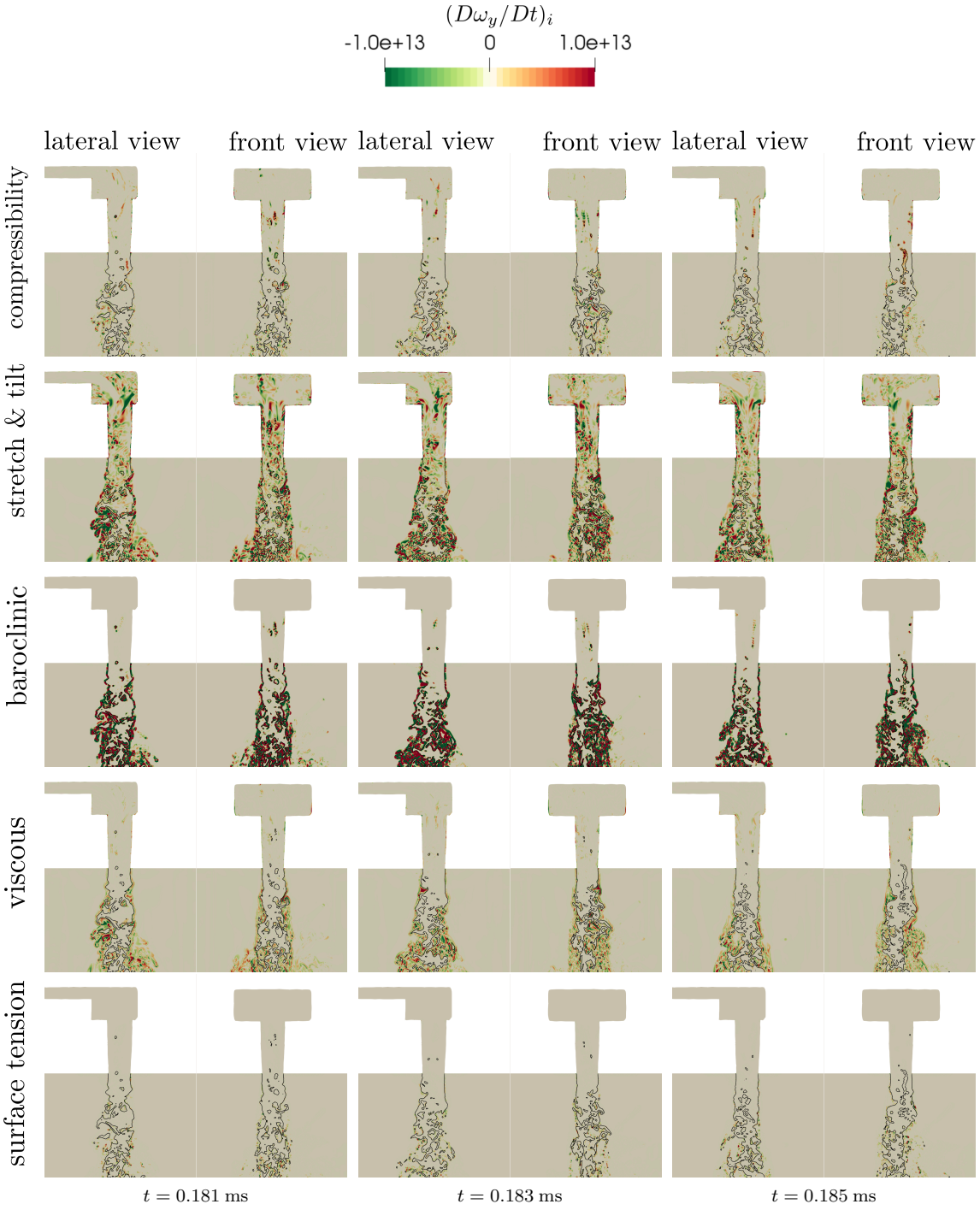

Figure 6.16: *config. ID-3, temporal evolution of streamwise vorticity dynamics terms on D_1 and D_2. Black line identifies the liquid interface for $\alpha_l = 0.5$.*

The same conclusions are valid also for the config. ID-3 (Fig. 6.16). Performing a comparison among them, one can notice that the higher the baroclinicity is, the more the surface instabilities we have.

6.4 Comparison with experiments

In Fig. 6.17a and Fig. 6.17b are respectively shown the instantaneous views (lateral and front view) for ID-10 and ID-3, of an ambient region length of $2\,mm$. This zone corresponds to the refined region of the mesh employed for the numerical simulations.

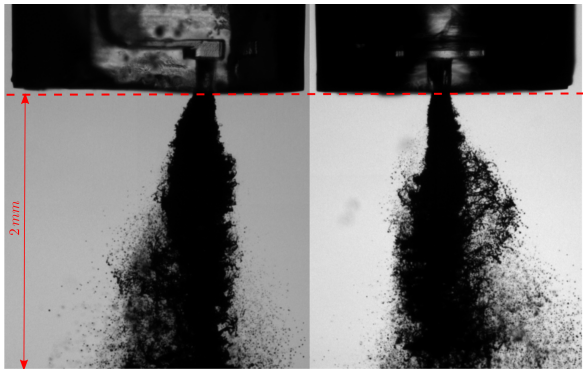

(a) *id-10*

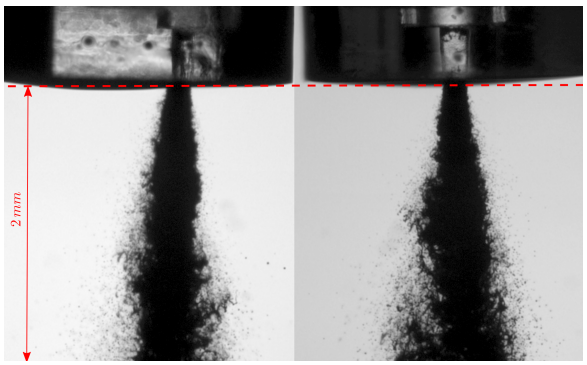

(b) *id-3*

Figure 6.17: *Experimental instantaneous views of the primary breakup for the $\theta = 0°$ (front view) and $\theta = 90°$ (side view): (a) config. ID-10; (b) config. ID-3;*

As it has been already pointed out in the instantaneous views of the numerical results, config. ID-10 is characterized by a wider jet than config. ID-3. Even if both the jets could have some flapping behavior, config. ID-10 seems to be more subjected to a surface flapping due to higher cavitation. In addition, an asymmetric structure of the jet is clearly visible comparing the lateral view (left top picture in Fig. 6.17a) and the front view (right top picture in Fig. 6.17a). On the former view, the jet is wider and more developed on the left side; it is wider close to the nozzle tip as well. On the latter view, the jet is narrower near the nozzle tip and presents a more symmetric structure along the nozzle axis. Conversely, config. ID-3 does not present any particular asymmetry. Till $1\,mm$ from nozzle tip, the jet has the same width; After that length, the jet is almost 25% wider in the front view (right bottom picture in Fig. 6.17b).

A qualitative comparison of the experimental spray structure and of the numerical one is shown for the config. ID-10 in Fig 6.18. The same comparison is proposed for the config. ID-3 in Fig. 6.19. Spray width and angle have been described in a reliable way for both the configurations.

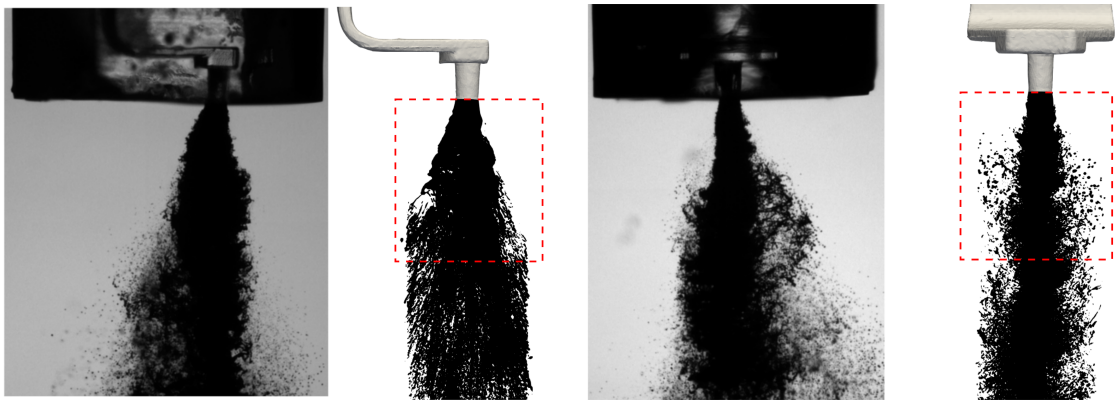

(a) *id-10* $\theta = 90°$ *view* **(b)** *id-10* $\theta = 0°$ *view*

Figure 6.18: *Qualitative comparison of the instantaneous views of the primary breakup for config. ID-10: (a)* $\theta = 90°$ *(front view) ;(b)* $\theta = 0°$ *(side view). On the left experimental view on the right Numerical view. Red-dashed box represents the region where AVOF is accurately capturing the interface.*

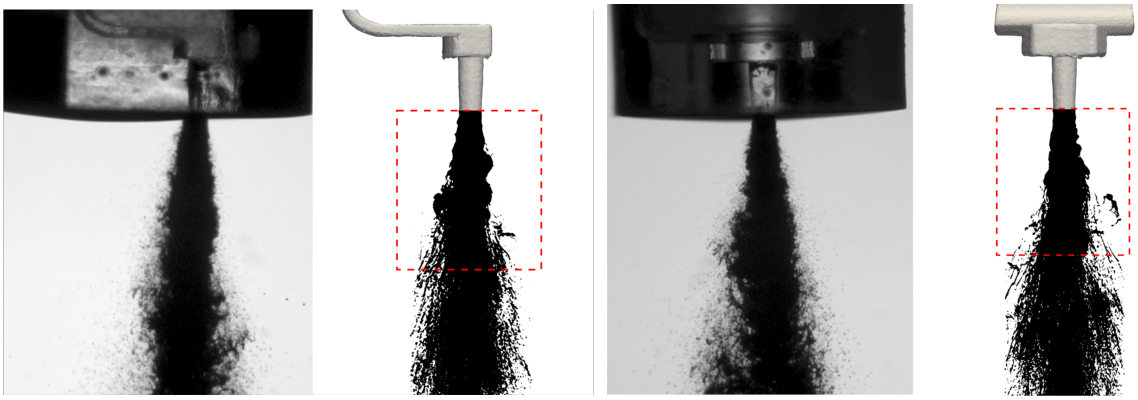

(a) *id-3* $\theta = 90°$ *view* **(b)** *id-3* $\theta = 0°$ *view*

Figure 6.19: *Qualitative comparison of the instantaneous views of the primary breakup for config. ID-3: (a)* $\theta = 90°$ *(front view) ;(b)* $\theta = 0°$ *(side view). On the left experimental view on the right Numerical view. Red-dashed box represents the region where AVOF is accurately capturing the interface.*

Finally, shadowgraphies of the close up views are used to evaluate the time-average spray angles (right angle and left angle for each view) and spray width. Then, the outcome of this analysis has been compared with the same analysis performed on the numerical results. In the present work the liquid iso-surfaces are represented by a contour value of $\alpha_l = 0.5$. This choice has the drawback of loosing part of the information of the liquid fraction below that chosen threshold, which could impair the evaluation of the angle.

The identification of the interface between gaseous phase and liquid is not straightforward due to the space discretization of the image and due to non-white background. Even if the background has been removed from the original picture, the interfaces in the images are still biased. The average experimental angles are computed using as a reference value the mean value of the interface for the 16-bit level of gray image. In addition, the experimental pictures represent a 3D projection of a spray in a 2D plane. Therefore, continuous values of the liquid volume fraction are considered. The interface should denote progressive value of liquid volume fraction but it is not easy to correlate a specific gray value to a specific liquid

volume fraction threshold.

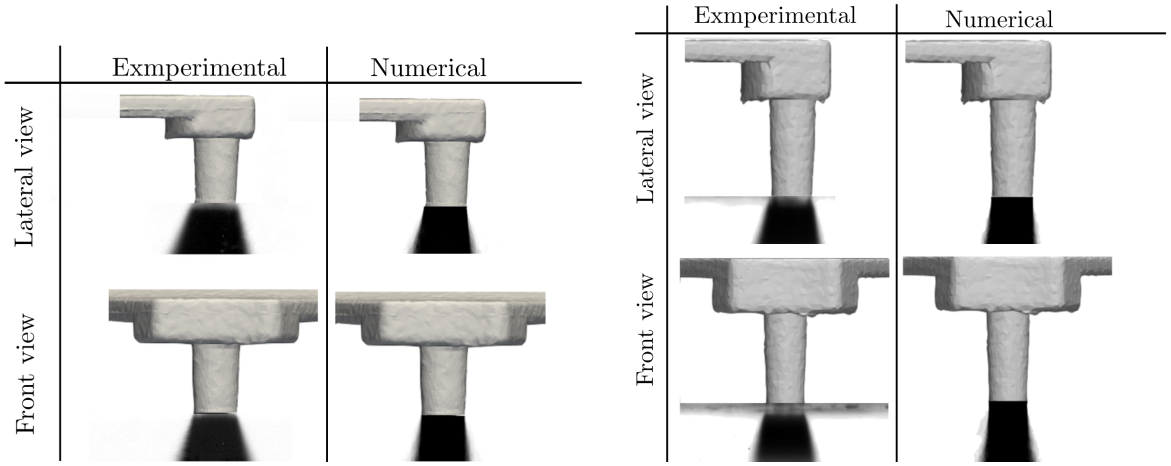

(a) *id-10* **(b)** *id-3*

Figure 6.20: *Experimental vs. Numerical: close-up view of average spray width for config. ID-10 (a), and config. ID-3. For each configuration are shown lateral and front views.*

Vice-versa, from the numerical side, in order to obtain the same picture, iso-surfaces of liquid volume fraction should have been computed during the simulation for several instants of time and for several liquid volume fraction values. However, this procedure becomes time consuming and computationally unaffordable when very fine meshes are used. In the present work the iso-surfaces have been only computed for $\overline{\alpha_l} = 0.25$ and $\overline{\alpha_l} = 0.5$ but it is not enough to have an accurate computation of average spray angles: lower values of alpha liquid should have been used to have a wider range of liquid fractions for the jet interface representation. This can be easily noticed looking at Fig. 6.20. To support angles computation, average liquid fraction on plane D_1(see Fig. 6.21a and Fig. 6.22a) and D_2 (see Fig. 6.21b and Fig. 6.22b) are used.

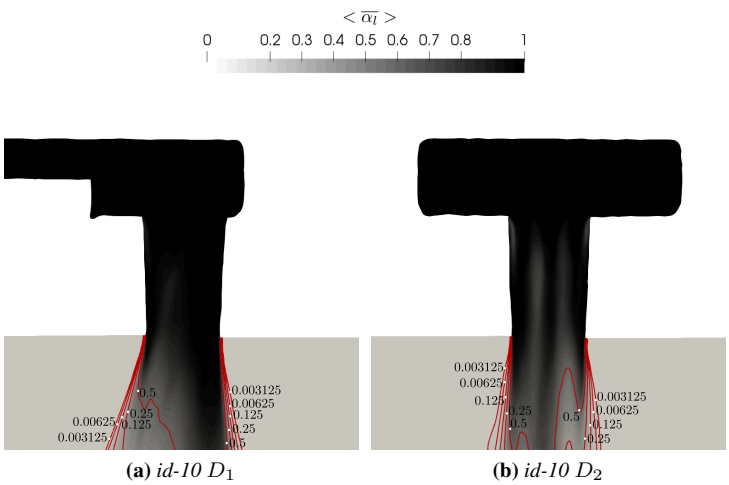

(a) *id-10* D_1 **(b)** *id-10* D_2

Figure 6.21: *config. ID-10: average alpha liquid fraction with red iso contour lines at 0.003125, 0.0625, 0.0125, 0.25, 0.5.*

config. ID-10, $\theta = 90\,^\circ$ (plane D_1), **LSA**, Fig. 6.21a					
Experimental	Numerical				
Mean 16 bit value	$\overline{\alpha_l} = 0.5$	$\overline{\alpha_l} = 0.25$	$\overline{\alpha_l} = 0.125$	$\overline{\alpha_l} = 0.00625$	$\overline{\alpha_l} = 0.003125$
23.19 °	9.87 °	13.10 °	15.3 °	17.067°	18.285 °

Table 6.1: *comparison of Experimental average LSA and numerical average LSA on plane D_2*

config. ID-10, $\theta = 90\,^\circ$ (plane D_1), **RSA**, Fig. 6.21a					
Experimental	Numerical				
Mean 16 bit value	$\overline{\alpha_l} = 0.5$	$\overline{\alpha_l} = 0.25$	$\overline{\alpha_l} = 0.125$	$\overline{\alpha_l} = 0.00625$	$\overline{\alpha_l} = 0.003125$
14.29 °	4.22 °	6.25 °	7.54 °	9.5 °	11.31 °

Table 6.2: *comparison of Experimental average RSA and numerical average RSA on plane D_2*

config. ID-10, $\theta = 0\,^\circ$ (plane D_2), **LSA**, Fig. 6.21b					
Experimental	Numerical				
Mean 16 bit value	$\overline{\alpha_l} = 0.5$	$\overline{\alpha_l} = 0.25$	$\overline{\alpha_l} = 0.125$	$\overline{\alpha_l} = 0.00625$	$\overline{\alpha_l} = 0.003125$
14.74 °	2.11 °	4.21 °	6.036 °	8.298 °	11.983 °

Table 6.3: *comparison of Experimental average LSA and numerical average LSA on plane D_1*

config. ID-10, $\theta = 0\,^\circ$ (plane D_2), **RSA**, Fig. 6.21b					
Experimental	Numerical				
Mean 16 bit value	$\overline{\alpha_l} = 0.5$	$\overline{\alpha_l} = 0.25$	$\overline{\alpha_l} = 0.125$	$\overline{\alpha_l} = 0.00625$	$\overline{\alpha_l} = 0.003125$
14.797 °	0.74 °	3.28 °	5.48 °	8.18°	10.71°

Table 6.4: *comparison of Experimental average RSA and numerical average RSA on plane D_1*

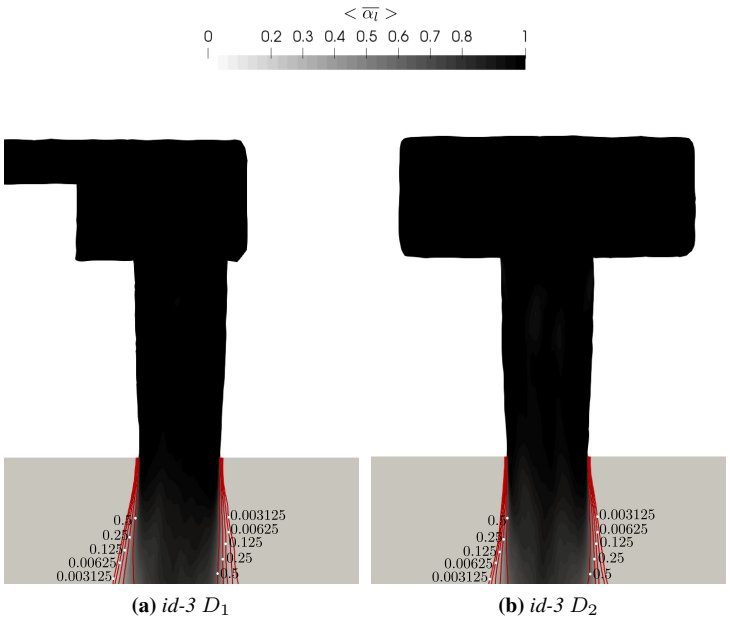

(a) *id-3 D_1* **(b)** *id-3 D_2*

Figure 6.22: *config. ID-3: average alpha liquid fraction with red iso-contour lines at 0.003125, 0.0625, 0.0125. 0.25, 0.5.*

The red lines denote the contour values of the average liquid volume fraction on the 2D planes for $< \overline{\alpha_l} >= [0.003125, 0.0625, 0.0125.0.25, 0.5]$. The average Left Spray Angles

(LSAs) and average Right Spray Angles (RSAs) are computed for each contour value and the outcomes of the measurements procedure are reported for the config. ID-10 in Tabs. 6.1,6.2,6.3, 6.4.

For the config. ID-3 the measurement are reported in Tabs. 6.5.6.6,6.7,6.8.

config. ID-3, $\theta = 90\,^\circ$ (plane D_1), **LSA**, Fig. 6.22a					
Experimental	Numerical				
Mean 16 bit value	$\overline{\alpha_l} = 0.5$	$\overline{\alpha_l} = 0.25$	$\overline{\alpha_l} = 0.125$	$\overline{\alpha_l} = 0.00625$	$\overline{\alpha_l} = 0.003125$
15.74 °	4.9°	7.51°	9.43°	11.27°	12.32°

Table 6.5: *comparison of Experimental average LSA and numerical average LSA on plane D_2*

config. ID-3, $\theta = 90\,^\circ$ (plane D_1), **RSA**, Fig. 6.22a					
Experimental	Numerical				
Mean 16 bit value	$\overline{\alpha_l} = 0.5$	$\overline{\alpha_l} = 0.25$	$\overline{\alpha_l} = 0.125$	$\overline{\alpha_l} = 0.00625$	$\overline{\alpha_l} = 0.003125$
10.389°	-1.18 °	1.66 °	3.75°	6.08°	8.82°

Table 6.6: *comparison of Experimental average RSA and numerical average RSA on plane D_2*

config. ID-3, $\theta = 0\,^\circ$ (plane D_2), **LSA**, Fig. 6.22b					
Experimental	Numerical				
Mean 16 bit value	$\overline{\alpha_l} = 0.5$	$\overline{\alpha_l} = 0.25$	$\overline{\alpha_l} = 0.125$	$\overline{\alpha_l} = 0.00625$	$\overline{\alpha_l} = 0.003125$
12.68 °	0°	3.05°	5.24°	6.83°	7.77°

Table 6.7: *comparison of Experimental average LSA and numerical average LSA on plane D_1*

config. ID-3, $\theta = 0\,^\circ$ (plane D_2), **RSA**, Fig. 6.22b					
Experimental	Numerical				
Mean 16 bit value	$\overline{\alpha_l} = 0.5$	$\overline{\alpha_l} = 0.25$	$\overline{\alpha_l} = 0.125$	$\overline{\alpha_l} = 0.00625$	$\overline{\alpha_l} = 0.003125$
12.28°	3.05°	5.48°	5.9°	7.611°	9.72°

Table 6.8: *comparison of Experimental average RSA and numerical average RSA on plane D_1*

Decreasing the liquid fraction iso-value it is clear that the numerical angle estimate increases and it is much more coherent with the estimate of the angle from experimental pictures. $\overline{\alpha_l} = 0.00625$ seems to be a good level for spray comparison. In general, for both the configurations, for the smallest iso-value, the relative error is about the 20%. However, also the estimate of the angle from shadowgraphies is not straightforward, thus the relative error computed is purely indicative.

6.5 Droplet size

As introduced in Sec. 6.2, Σ can be used to estimate the droplet size distribution and the mean droplet diameter. This said, a length scale can be defined as ratio $\overline{\alpha_l}/\overline{\Sigma}$, which is linked to the Sauter Mean Diameter (SMD). On the other hand, for mono-dispersed spray of spherical droplets, the SMD will have the following form [3] :

$$\frac{6\overline{\alpha_l}}{\Sigma} \tag{6.30}$$

However, for very small volume fraction leading to bubbly flow, Eq. 6.30 becomes:

$$\frac{6\overline{\alpha_l}(1-\overline{\alpha_l})}{\Sigma} \tag{6.31}$$

In the end, in order to consider all the structures, the final SMD is derived multiplying Eq. 6.31 by $\overline{\alpha_l}$ [11]:

$$SMD = \frac{6\overline{\alpha_l}(1-\overline{\alpha_l})}{\Sigma} \tag{6.32}$$

The value of SMD is shown respectively in Fig. 6.23 and Fig. 6.24 for ID-10 and ID-3: lateral and front view are proposed for three instants of time. In Fig, 6.25 the SMD is extrapolated for both the configurations on the center-line in the y-direction. The red dashed box denotes the region where AVOF provides accurate results: in this zone SMD estimate is giving reasonable information of the diameter of the droplets. Close to the liquid/NC gases interface (outer zone of the jet) and close to the liquid/vapor interface (inner part of the jet), SMD it is about $1-2\,\mu m$. Its value progressively increases to tens of microns in the zones where ligaments and big droplets are present.

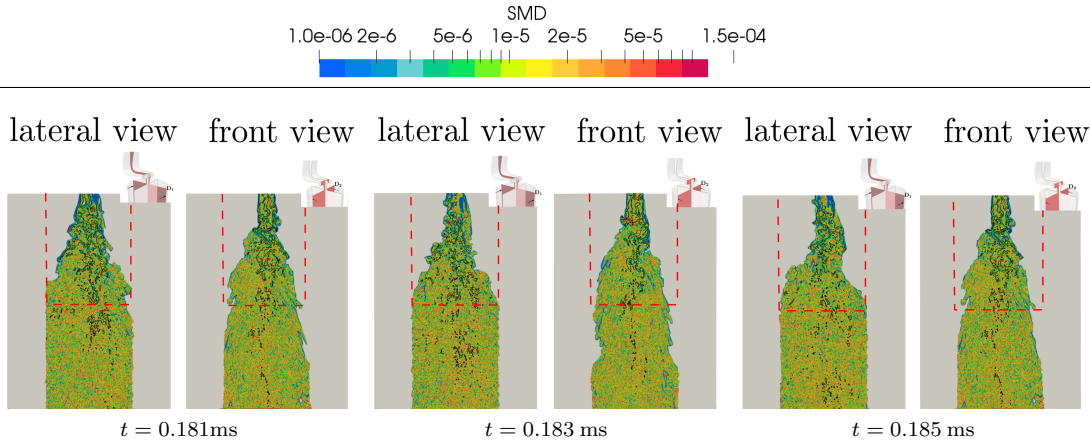

Figure 6.23: *config. ID-10: temporal evolution of SMD. Log scale color bar is used to enhance visualization. Black line identifies the liquid/NC interface for* $\overline{\alpha_l} = 0.5$. *Red-dashed box represents the region where AVOF is accurately capturing the interface.*

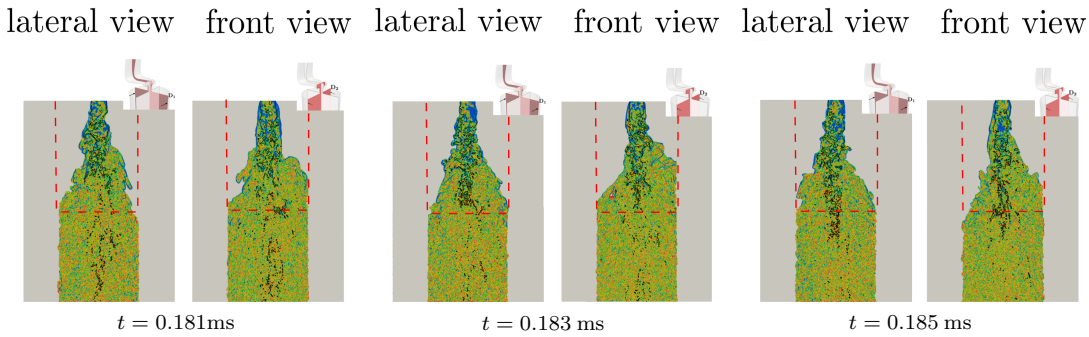

Figure 6.24: *config. ID-3: temporal evolution of SMD. Log scale color bar is used to enhance visualization. Black line identifies the liquid/NC interface for* $\overline{\alpha_l} = 0.5$. *Red-dashed box represents the region where AVOF is accurately capturing the interface.*

The values of SMD extrapolated on the center-line (Fig. 6.25) shows that SMD is almost smaller than $D_{out}/4$. For some structures $D/4 \leq SMD \leq D/2$, and barely $D/2 \leq SMD \leq 3D/4$. These SMD values are in accordance with the injection pressure ($100\,bar$) and the nozzle outlet diameter of about $150\,\mu m$.

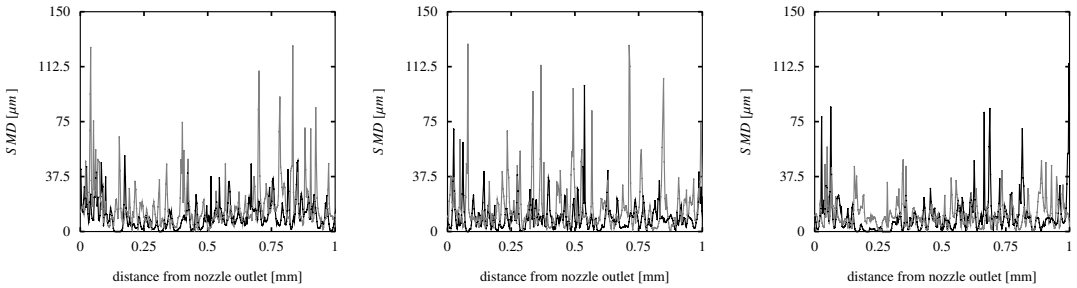

$t = 0.181$ms $t = 0.183$ ms $t = 0.185$ ms

Figure 6.25: *Estimate of SMD along the center-line in y-direction for a maximum distance of* $1\ mm$ *from nozzle outlet: — ID-3; — ID-10.*

A better insight of SMD at different cross sectional area in the ambient domain is given by Fig. 6.26 and Fig. 6.27, where SMD values are respectively shown for ID-10 and ID-3.

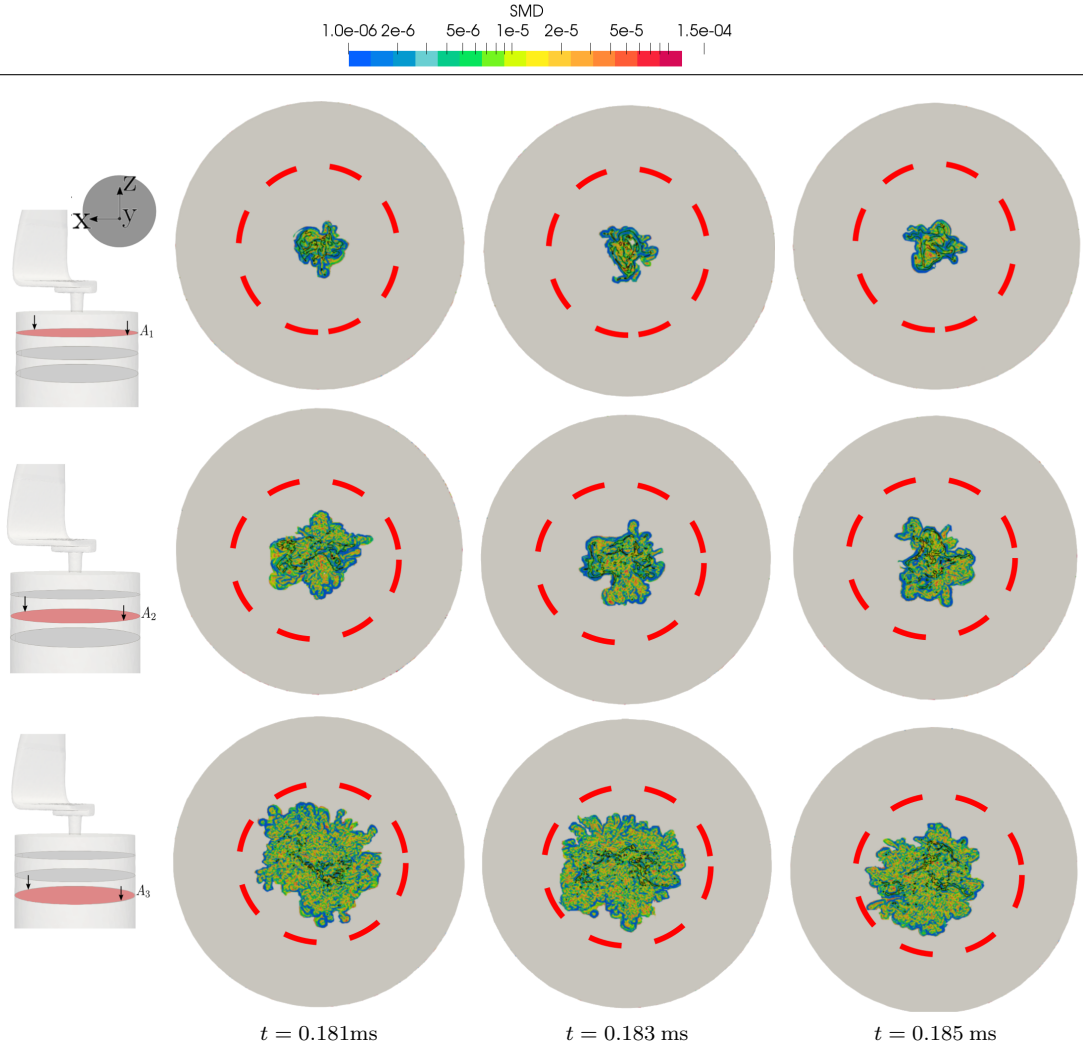

$t = 0.181$ms $t = 0.183$ ms $t = 0.185$ ms

Figure 6.26: *config. ID-10, temporal evolution of SMD on* A_1, A_2 *and* A_3. *Log scale color bar is used to enhance visualization. Black line identifies the liquid/NC interface for* $\overline{\alpha_l} = 0.5$. *Red-dashed box represents the region where AVOF is accurately capturing the interface.*

On plane A_1, as mentioned above, close to the interfaces the values of SMD are the smallest, while in the zone of ligaments and big droplets, SMD is about tens of microns. On plane A_2 and especially on plane A_3, the jet is already enough atomized (see sec. 6.1). Thus, excluding some thin ligaments, that are identified by high SMD values and high $\overline{\alpha_l}$ within the black iso-value, the other zones are the ones characterized by a very low value of $\overline{\alpha_l}$. For this reason the value of SMD is mostly governed by the interface density (gradient of liquid fraction).

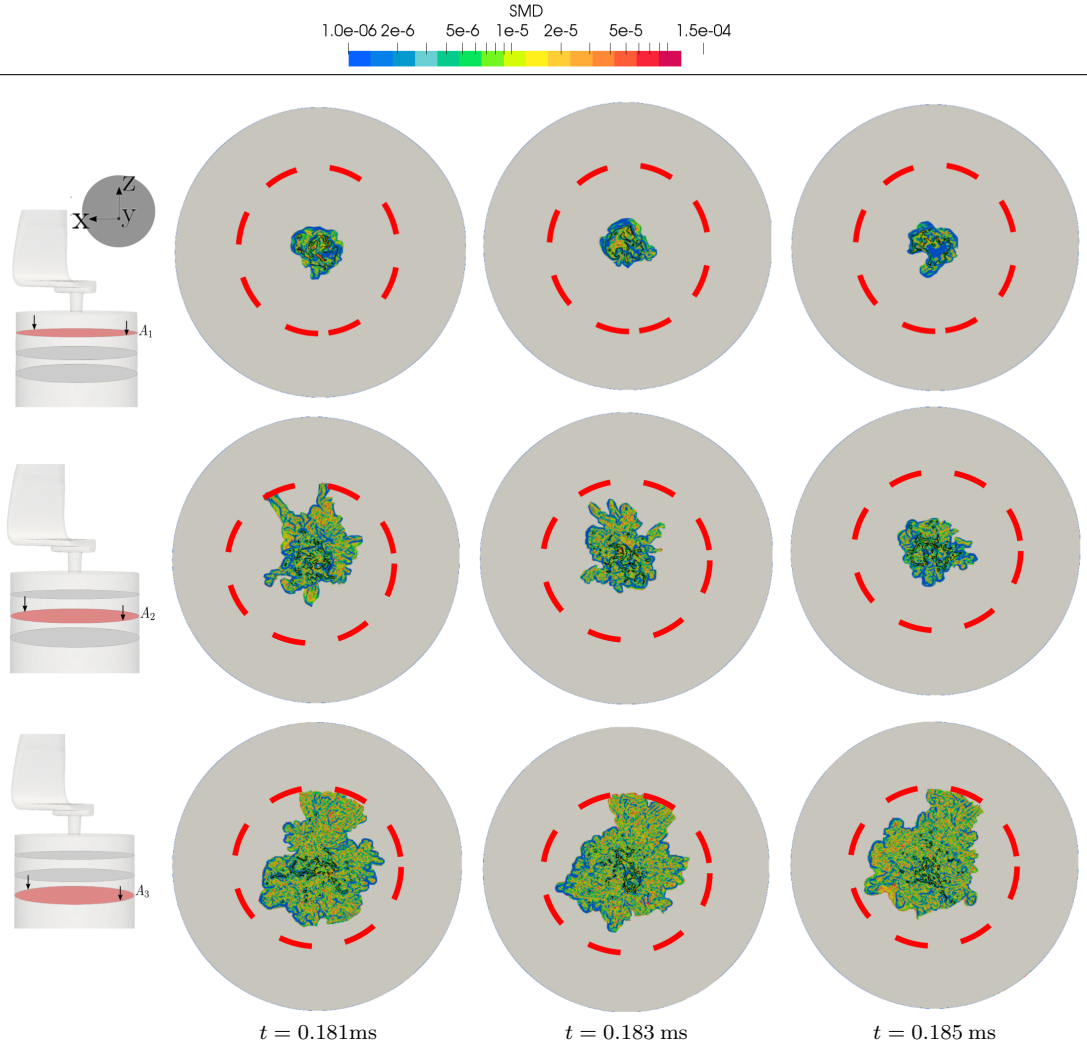

Figure 6.27: *config. ID-3, temporal evolution of SMD on A_1, A_2 and A_3. Log scale color bar is used to enhance visualization. Black line identifies the liquid/NC interface for $\overline{\alpha_l} = 0.5$. Red-dashed box represents the region where AVOF is accurately capturing the interface.*

6.6 Conclusion

From a first analysis on the sequence of internal nozzle flow and primary breakup is not possible to define a clear cavitation regime, since cavitating structures evolve and change in time. This unsteadiness was firstly noticed looking at the time signal of C_d in Sec.5.1.4. In addition, the outcomes of the analysis of average void fractions on planes D_1 and D_2 have confirmed what was outlined in Sec.5: the configuration ID-10 is more asymmetric than ID-3 due to higher vapor content in the inner core. Although the vapor content of

ID-3 in the jet is very low, in both the configurations the vapor generation reaches a peak at almost $0.25\,mm$ from nozzle outlet. The vapor bubbles are all collapsed at $1\,mm$. The different vapor content has a consequence on the different jet width and in the end on the atomization efficiency: as predicted by TKE_{tot} and E_k, this is higher in ID-10. Conversely, jet of config. ID-3 is characterized by a narrower jet, whose core is denser. In the end, this opposite behavior must be addressed to the different geometrical features of the BFS. Nevertheless both the configurations have shown that mean flow direction was not aligned with the nozzle axis, the mean jet flow direction is almost parallel to the nozzle one. Vorticity dynamics applied to the jet has shown the pivotal role of streamwise vortices in the surface deformation and thus on atomization. These vortices are really high in denser spray, as the jet of ID-3, and they can be considered as the main promoters of interface deformation. The latter is mainly operated by baroclinity effect acting on liquid/NC gases interface, where the density gradient is the highest. Also stretching/tilting term is of the same order of magnitude as baroclinity one, and therefore plays an important role as well. Conversely, surface tension effect, viscous effect and compressibility effect can be neglected in this analysis. The analysis on the interface resolution has also confirmed that the AVOF employed in the present work provides reliable results at maximum $1\,mm$ from nozzle outlet. Then, the comparison with experimental shadowgraphies has confirmed the reliability of the solver and of the AVOF approach used in the aforementioned region. However, the validation performed comparing the numerical and experimental LSA and RSA has shown to be too much sensitive to the void fraction threshold used to compute the angles. A reasonable value of the angle can be obtained for $\overline{\alpha_l} \leq 0.003125$. In the end SMD has been estimated using a model proposed in literature ([3], [11]). As confirmed by the interface resolution analysis, the estimate of SMD is reliable till $1\,mm$ from nozzle outlet and gives reasonable results for the operative pressure used and the geometry of the nozzle under analysis.

CHAPTER 7

Conclusions and Future perspective

In the present work, internal nozzle flow and primary atomization in the context of injectors for GDI engines have been presented. The purpose of any injector is to provide the right amount of fuel during the injection time, with some specific features which are not easy to control such as the jet angle, the JWP, the droplets diameters. These are essential for a proper fuel-air mixing and consequently for a good combustion process. In the context of GDI engines, in the last decades the tendency was to increase the operative pressure condition of the injectors, to increase the overall ICE efficiency. Due to the complex geometries of the injectors, higher pressure often determines higher velocities and thus, bigger local pressure drops at nozzle inlet and along the nozzle itself. These conditions lead to the so called cavitation: this influences the most the primary atomization. Therefore, the modeling of atomization is mostly related to the phenomena occurring inside the nozzle, in particular cavitation and turbulence. As a matter of fact, in the jet flows characterized by high Reynolds numbers, atomization process is strictly linked to the right prediction of turbulence within the nozzle orifices. However, at the present state of computational resources and time, DNS of internal nozzle flow and primary atomization is not feasible or it is too much demanding from the computational point of view. On the other hand, nowadays the progress in the computational power has made more affordable a LES simulation for this kind of industrial applications. The CFD is in fact widely employed by the injector industry and designers to improve their efficiency and clarify some phenomena which are difficult to investigate by mean of only experimental measurements. In order to do this, *ad-hoc* CFD-tool are needed. In this context the aim of the present research was to illustrate the developed three-phase VOF pressure based solver, with the ability to capture the air/vapor interface and model phase-change phenomena as well. Two numerical test cases and one injector geometry (available form literature) have been used for verification and validation. In the first case, the modified rising bubble problem, proved the ability of the implemented three-phase solver to capture the interface with very limited diffusion, providing similar results of high-order solvers. The second numerical problem, proposed for the first time by the authors [77], was thought to verify mass conservation properties of the VOF solver with phase-change. Both with cavitation and condensation, the

solver proved to be able to limit the mass relative error to a very small value with some minor, almost negligible, error peaks of the order of 0.001% when bubbles collapse. Among all the available approach for cavitation description, cavitation model based on simplified RP equation has been implemented within the VOF approach. Although its simplicity in describing the cavitation dynamics, it has the great advantage to be able to take into account the baroclinity effect, since the model does not rely on a barotropic equation of state. Additionally, the simplified equation can be directly manipulated to obtain the linearized source term for the void fraction equations and the pressure equation. Conversely, when equations of state are used, additional mass fraction equations must be resolved to finally compute the vapor quality at the equilibrium. A first validation has been performed on an injector test case from literature [199], [23]. Although the case dealt with water injection in air at $2-3\,bar$, this test case has been widely used in literature due to the good experimental measurements of velocity field and rms velocity available inside the nozzle. The aim of this simulation was to prove the predictive capability on real internal nozzle-flow conditions. The agreement between experiments and predicted average velocity, also when both liquid and vapor are present, has shown to be satisfying. Also rms values of the velocity has been captured fairly well. The small over-prediction of the fluctuating velocity at the left-hand corner of the channel has shown that the amount of predicted turbulent kinetic energy is too large in that region and probably is due to an overestimation of vapor production along the shear layer which causes enhancement of the velocity gradients and thus of the turbulence production. Comparisons with high-speed camera visualizations have shown that the cavitation developing regime has been well-captured as well.

The solver has been finally used to simulate two real glass-nozzle injectors for which high-speed camera visualizations were available. The aim of the simulation was to prove the predictive capability on the real internal nozzle-flow conditions and the extent primary break-up description. These two configurations have been chosen among ten glass-nozzle injectors which can be easily mounted on the same feeding system. Configurations ID-3 and ID-10 have been chosen because they have shown respectively best JWP and worst JWP. These are characterized by different geometrical features, which have shown to be the main responsible for different cavitation and consequently jet atomization. The most relevant are the nozzle length, the conicity factor and the BFS shape. The latter has been here identified with the BFS ratio of Eq.5.1. Respect to the simulations performed on the nominal geometries [76], here the geometries have been reconstructed by micro-XCT measurements performed on the real injectors. The purpose was to simulate the internal nozzle flow when also surface imperfections are taken into account. The in-nozzle flow analysis has pointed out the pivotal role of the BFS shape in the sac flow determination. This acts as a vortex generator and in the end it is the responsible for higher or lower string cavitation in the nozzle. Although both the configurations have shown a similar behavior in terms of direct, side and reverse flows, it has been noticed that the higher the BFS ratio is, the higher the direct-MFR and the smaller the side-MFR will be. In particular this ratio has more influence on the side flow. It is also possible to conclude that the higher the ratio is, the smaller the counter rotating vortices produced at the nozzle inlet will be. In both cases, reverse flow has a minor importance than side and direct flow, which are almost the double. This means the dead space is not big enough to promote any kind of additional rotation to the flow at the nozzle inlet, and detachment as well. The vortex formation is therefore due to a different combination of direct and side flow due to BFS shape, which in some cases can lead to a mixed shear-string behavior. For this, also shear cavitation is influenced by BFS features, but in a minor way. The opposite flow behavior of ID-10 and ID-3 is also proven by the different values of computed discharge coefficient: ID-10 shows a bigger oscillation in time of C_d and a smaller average value since

characterized by higher cavitation. Conversely ID-3, shows smaller oscillation in time of C_d and higher average value due to lower cavitation. From the analysis of total turbulent kinetic energy and non-axial kinetic energy it can be also evinced that ID-10 is the configuration with the higher deflection of the jet and higher primary atomization. For both the cases the ratio TKE_{sgs}/TKE_{tot} at nozzle outlet has shown that LES simulation is providing accurate results, since at least the 80% of the turbulent kinetic energy is resolved by the simulation [166]. Only ID-3 is out of 1.3% for this requirement, but it is still considered acceptable. Comparisons with high-speed camera visualization have shown that either shear cavitation and string cavitation regimes have been quite well-captured. However, during the validation process, it has been noticed that the geometry coming through the micro XCT measurements has too much influence on the fluid vena detachment at the nozzle inlet. Micro-XCT is not able to perfectly reproduce a curvature of the edges under sub-micrometer voxel resolution and had to be manually corrected with some hypothesis on the sharpness. The quality of the curvature of the edges obtained by the measurements is one of the main shortcomings of this procedure and it could impair the results. As a matter of fact, even after having recovered sharp edges at the nozzle inlet, shear cavitation seems to be a bit underestimated, especially in config. ID-3. However, this small underestimation could also come from the approximation introduced by the RP equation used to built the cavitation model.

For what concerns the primary atomizaion, the solver has shown to be reliable in the denser spray region: the interface resolution has been verified computing an estimate of interface density and using the IRQ_{Σ} sensor. The values prove that the AVOF approach is reliable till $1\,mm$ from nozzle outlet. This limit is due to the lack of additional subgrid models at the interface.

For the first time a vorticity dynamic analysis has been used for the internal nozzle flow and the primary break-up. This has helped to identify the baroclinity effect as the most important one for the generation of surface instabilities in the primary break-up. Vortex stretching and tilting result as the second promoters of the streamwise vorticity generation outside the nozzle but are as relevant as the baroclinty within the sac and the nozzle. Compressibility effect is important only when phase-change occurs but in general is 1-2 order of magnitude smaller than baroclinic and stretching/tilting term. The viscous term and the surface tension terms can be neglected as well. Additionally, the same analysis performed in the spanwise and the crosswise direction have shown clearly that streamwise vorticity is two order of magnitude bigger.

About the primary break-up, the comparison with high-speed camera visualization have shown a very good agreement for both the configurations and it confirms the outcomes of the in-nozzle flow analysis. Average LSA and RSA are measured both for the numerical and experimental images. The method has shown to be a bit sensitive to the liquid volume fraction value used for the comparison. In the end, the SMD has given a good estimate of droplet diameters in the first millimeter of primary breakup.

This said, the solver and the AVOF approach used have proven to predict the in-nozzle flow and primary atomization for the two glass nozzle injectors proposed. The results have outlined that the different behavior among config. ID-10 and ID-3 are significantly due to the geometry differences and due to the inlet flow conditions developing from the small details in the sac. For this reason, a simulation on real injectors is essential, even if XCT cannot represent properly the curvature of the edges. “Sac height”, “off h” and “dead space” geometrical features determine how the fuel will enter the nozzle: these geometrical features influences particularly the flow at the nozzle inlet. Even if similarities have been shown in terms of direct, side and reverse flow, the bigger the BFS the smaller the effect of side flow and counter vortices formation: ID-3 has shown to be characterized by less cavitation occurrence, while

ID-10 (lower BFS) has higher cavitation. Additionally, the BFS provides a pressure drop among S_1 and N_1, reducing the available Δp to discharge the fuel. This produces a different effect according to the nozzle length and the conicity. If the outlet pressure is considered as almost imposed by the ambient domain, the acceleration induced on the shorter nozzle (ID-10) will be higher, and consequently the counter rotating vortices will expand more, producing a higher vapor content at the nozzle outlet section. Conversely, for longer nozzle (ID-3), which is also characterized by higher conicity factor, the acceleration induced will be smaller. Considering that side flow in ID-3 has shown to be smaller, the fact that the flow finds a longer and narrower nozzle does not help in the expansion and creation of counter rotating vortices along the nozzle. As a consequence, string cavitation is less intense in ID-3. Although the vapor content of ID-3 in the jet is lower than ID-10, in both the configurations the vapor generation reaches a peak at almost $0.25\,mm$ from nozzle outlet. The vapor bubbles are all collapsed at $1\,mm$. The different vapor content has a consequence on the different jet width and in the end on the atomization efficiency: as predicted by TKE_{tot} and E_k, this is higher in ID-10. Conversely, config. ID-3 is characterized by a narrower jet, whose core is denser. According to the outcomes of the numerics, experimental measurements and their comparisons, it is possible to confirm the dominant role of the BFS in determining the opposite in-nozzle flow behavior and primary atomization as well.

Even if the solver has proven to be capable to model primary breakup and resolve the main in-nozzle flow structure, further improvement could be made to overcome some approximations in the description of the phenomena. The most important improvement would deal with the possibility to take into account the compressibility effect of vapor and NC gases. As a matter of fact, this becomes higher increasing the operative pressure condition of the injector. This feature of the solver, would require either a modification of the structures of the equations and in particular of the source terms coming from cavitation model. Following this path, probably a different approach relying on non-linear barotropic equation of state would be more accurate than RP-equation in the computation of the vapor quality.

Thermal effects should be taken into account to get a real understanding of the real conditions of the engine. Also the vapor collapse term (condensation), coming from RP-equation should be studied in details, as in the current simulations, no local detailed validations of the vapor collapse has been made. More accuracy could be achieved computing the real fluid properties from a tabulated database, using as input static pressure and temperature or enthalpy. From the point of view of multiphase flow and turbulence, in the present work the interface subgrid terms have been neglected. AVOF is able to capture the interface only where the mesh resolution is fine enough. A lot of work should be performed for the analysis of this subgrid terms and it would firstly require an *a-priori* analysis on a liquid jet. Phase change must be treated in this analysis as well. After this, a model should be proposed for those subgrid terms whose presence is mandatory to describe the interface with LES approach. This kind of work has been widely investigated by other researcher. Nevertheless, in literature this analysis is performed only on simple test cases such as rising bubble [114, 115] or separation of phase [221], whose flow condition are really far from the ones occurring in atomization and jet flow. Chesnel, in the past, has proposed an *a-priori* test on jet flow using LS and GFM but without considering phase change phenomena due to cavitation [3].

In general, the solver could capture accurately the interface depending on the mesh resolution and length at which occurs the primary atomization: with the mesh employed, the AVOF cannot accurately capture the interface further than $1\,mm$ from the nozzle tip, when operative pressure is $100\,bar$. To be able to resolve also far away from the nozzle, the mesh should be more refined or alternative method such as AMR or different numerical approaches and interface sub-grid models must be introduced. Of course, when the operative pressure is

$0.22\,MPa$, as the one used in the water injection test case, the AVOF can resolve interface further than $1\,mm$.

However, the present work has the aim to develop a tool for the modelization of GDI injectors, whose operates at higher pressure ($100 - 500\,bar$). In that case, mesh should be refined. To resolve the atomization on longer distances, an alternative could be to couple the solver with other approaches based on interface density equation [3], [11], or on interface-parcel numerical generation [124] or on weak coupling [82]. However, these coupling will introduce additional equations and further numerical models that need validation when applied to internal nozzle flow, characterized by mixed shear-string cavitation, and high speed jet with large liquid/gas density ratio.

A final remark must be done also on the approximation involved in the study of the injector system. In the present work, the simulations on the real glass nozzle injectors have been performed on simplified geometries, supposed to be at maximum injector lift, with MFR almost constant. Although they provide interesting outcomes for the design purpose, it would be more accurate to consider the effect of the needle motion, as performed in previous works [156], [157], [158], [75]. The moving mesh strategy adopted to handle the displacement of the cell vertices in the computational mesh was based on topological changes [160]. In these works, the VOF-dynamic solver adopted considered a liquid phase and a gaseous one. The latter was considered as composed of vapor and air. Therefore, was not possible to capture any interface among vapor and air within the gaseous phase. Additionally, to avoid the spurious condensation at the liquid-gaseous jet interface, condensation source term was deactivated outside the nozzle. Neglecting condensation in the ambient region was justified for the problem considered in that work, largely because the nozzle geometry and the operating conditions studied have been specifically designed to study cavitation and limit condensation of the cavitating bubbles in the nozzle. For this reason, the simulations had shown good agreement with experimental results during the early stage of injection. Conversely, the solver shown in the present work, can capture separately liquid, air and vapor. Moreover, the implemented cavitation model only acts among liquid and vapor of the same component. This allows to consider also the bubble collapse nearby the nozzle tip, in the ambient domain, which has shown to be relevant for the jet atomization and cone angle determination. Hence, future developments would deal with the application of the new solver for the analysis of the needle dynamics within injector as well.

APPENDIX $\mathcal{A}$

Derivation of the source terms in a three-phase VOF solver with phase change

In this section, the derivation of the formulation of the term S_α of Eq. (2.6) is shown. From the definition of total derivative:

$$\frac{D\alpha_i}{Dt} = \frac{\partial \alpha_i}{\partial t} + \mathbf{U} \cdot \nabla \alpha_i \tag{A.1}$$

it follows:

$$\frac{\partial \alpha_i}{\partial t} + \nabla \cdot (\mathbf{U}\alpha_i) = \frac{D\alpha_i}{Dt} + \alpha_i \nabla \cdot \mathbf{U} \tag{A.2}$$

so that system of equations (2.5) can be written in the equivalent form:

$$\begin{cases} \dfrac{D\alpha_l}{Dt} = -\alpha_l \nabla \cdot \mathbf{U} - \dfrac{S_\alpha}{\rho_l} \\ \dfrac{D\alpha_v}{Dt} = -\alpha_v \nabla \cdot \mathbf{U} + \dfrac{S_\alpha}{\rho_v} \\ \dfrac{D\alpha_{nc}}{Dt} = -\alpha_{nc} \nabla \cdot \mathbf{U} \end{cases} \tag{A.3}$$

where the subscripts *l*, *v* and *nc* are used for liquid, vapor and non-condensable gases respectively. To ensure the boundedness of the solution of (A.3), the derived form of the compatibility condition $\alpha_l + \alpha_v + \alpha_{nc} = 1$ is used for closure:

$$\frac{D\alpha_l}{Dt} + \frac{D\alpha_v}{Dt} + \frac{D\alpha_{nc}}{Dt} = 0 \tag{A.4}$$

Substituting the expressions for $\frac{D\alpha_l}{Dt}$ and $\frac{D\alpha_{nc}}{Dt}$ from (A.3) into Eq. (A.4), the cavitation source term S_α is written as a function of $\frac{D\alpha_v}{Dt}$:

$$S_\alpha = \rho_l(\alpha_l + \alpha_{nc})\ \nabla \cdot \mathbf{U} - \rho_l \frac{D\alpha_v}{Dt} \tag{A.5}$$

Similarly, starting from Eq. (2.13) and considering each phase as incompressible, it holds:

$$\begin{aligned}
\nabla \cdot \mathbf{U} = & -\frac{1}{\rho}\frac{D\rho}{Dt} \\
= & -\frac{1}{\rho}\left[\frac{D(\rho_l\alpha_l)}{Dt} + \frac{D(\rho_{nc}\alpha_{nc})}{Dt} + \frac{D(\rho_v\alpha_v)}{Dt}\right] \\
= & -\frac{1}{\rho}\left(\rho_l\frac{D\alpha_l}{Dt} + \rho_{nc}\frac{D\alpha_{nc}}{Dt} + \rho_v\frac{D\alpha_v}{Dt}\right) \\
= & -\frac{1}{\rho}\left(-\rho_l\alpha_l\nabla\cdot\mathbf{U} - S_\alpha - \rho_{nc}\alpha_{nc}\nabla\cdot\mathbf{U} + \rho_v\frac{D\alpha_v}{Dt}\right)
\end{aligned} \tag{A.6}$$

so

$$S_\alpha = \rho_v\frac{D\alpha_v}{Dt} - (\rho_l\alpha_l + \rho_{nc}\alpha_{nc} - \rho)\ \nabla\cdot\mathbf{U} \tag{A.7}$$

From the combination of Eq. (A.5) and Eq. (A.7), the final form of the mass conservation for an incompressible flow, Eq. (2.13), takes the form:

$$\nabla\cdot\mathbf{U} = \frac{\rho_l - \rho_v}{\rho + \alpha_{nc}(\rho_l - \rho_{nc})}\frac{D\alpha_v}{Dt} \tag{A.8}$$

The formulation of the term S_α is obtained from the transport equation of α_v of (A.3):

$$\frac{D\alpha_v}{Dt} = -\alpha_v\nabla\cdot\mathbf{U} + \frac{S_\alpha}{\rho_v} \tag{A.9}$$

which is rewritten as:

$$S_\alpha = \rho_v\frac{D\alpha_v}{Dt} + \rho_v\alpha_v\nabla\cdot\mathbf{U} \tag{A.10}$$

and:

$$\begin{aligned}
S_\alpha &= \rho_v\frac{D\alpha_v}{Dt} + \rho_v\alpha_v\frac{\rho_l - \rho_v}{\rho + \alpha_{nc}(\rho_l - \rho_{nc})}\frac{D\alpha_v}{Dt} \\
&= \rho_v\frac{D\alpha_v}{Dt}\left[1 + \frac{\alpha_v(\rho_l - \rho_v)}{\rho + \alpha_{nc}(\rho_l - \rho_{nc})}\right] \\
&= \rho_v\frac{D\alpha_v}{Dt}\left[\frac{\rho + \alpha_{nc}\rho_l - \alpha_{nc}\rho_{nc} + \alpha_v\rho_l - \alpha_v\rho_v}{\rho + \alpha_{nc}(\rho_l - \rho_{nc})}\right] \\
&= \rho_v\frac{D\alpha_v}{Dt}\left[\frac{(\rho - \alpha_{nc}\rho_{nc} - \alpha_v\rho_v) + \alpha_{nc}\rho_l + \alpha_v\rho_l}{\rho + \alpha_{nc}(\rho_l - \rho_{nc})}\right] \\
&= \rho_v\frac{D\alpha_v}{Dt}\left[\frac{\alpha_l\rho_l + \alpha_{nc}\rho_l + \alpha_v\rho_l}{\rho + \alpha_{nc}(\rho_l - \rho_{nc})}\right] \\
&= \rho_v\frac{D\alpha_v}{Dt}\left[\frac{\rho_l\left(\alpha_l + \alpha_v + \alpha_{nc}\right)}{\rho + \alpha_{nc}(\rho_l - \rho_{nc})}\right]
\end{aligned} \tag{A.11}$$

leading to:

$$S_\alpha = \rho_v \frac{D\alpha_v}{Dt}\left[\frac{\rho_l}{\rho + \alpha_{nc}(\rho_l - \rho_{nc})}\right] \tag{A.12}$$

and to the final form of the system (2.5)

$$\begin{cases} \dfrac{\partial \alpha_l}{\partial t} + \nabla \cdot (\mathbf{U}\alpha_l) = & -\dfrac{\rho_v}{\rho + \alpha_{nc}(\rho_l - \rho_{nc})} \dfrac{D\alpha_v}{Dt} \\ \dfrac{\partial \alpha_v}{\partial t} + \nabla \cdot (\mathbf{U}\alpha_v) = \dfrac{\rho_l}{\rho + \alpha_{nc}(\rho_l - \rho_{nc})} \dfrac{D\alpha_v}{Dt} \\ \dfrac{\partial \alpha_{nc}}{\partial t} + \nabla \cdot (\mathbf{U}\alpha_{nc}) = 0 \end{cases} \tag{A.13}$$

APPENDIX $\mathcal{B}$

Derivation of the cavitation term for a three-phase VOF solver

The rates of fuel vaporization and condensation are determined by a simplification of the Rayleigh-Plesset equation which assumes spherical bubbles of radius R subject to uniform pressure variations. Spherical bubbles are then represented by a fraction of the vapor phase in the computational cell; from [187] and considering that a in a cell liquid, vapor and air may coexist, it follows:

$$V_v = N_b \frac{4}{3}\pi R^3 = n_0 V_l \frac{4}{3}\pi R^3 \tag{B.1}$$

where V_v and V_l are respectively the volume of the vapor and the liquid in the computational cell of volume V, N_b is the number of spherical bubbles of radius R in the computational cell and n_0 is defined as the bubble concentration per unit volume of pure liquid. From Eq. (B.1), it follows:

$$\frac{V_v}{V_l + V_v} = \frac{n_0 V_l \frac{4}{3}\pi R^3}{V_l + n_0 V_l \frac{4}{3}\pi R^3} = \frac{n_0 \frac{4}{3}\pi R^3}{1 + n_0 \frac{4}{3}\pi R^3} \tag{B.2}$$

From the definition of volume fraction, being $V_l + V_v + V_{nc} = V$ and dividing the LHS of the previous equation by V, it follows:

$$\frac{V_v}{V_l + V_v} = \frac{V_v/V}{(V_l + V_v)/V} = \frac{\alpha_v}{\alpha_v + \alpha_l} \tag{B.3}$$

so:

$$\frac{\alpha_v}{\alpha_v + \alpha_l} = \frac{n_0 \frac{4}{3}\pi R^3}{1 + n_0 \frac{4}{3}\pi R^3} \tag{B.4}$$

Rearranging Eq. (B.4), the vapor volume fraction reads:

$$\alpha_v = \alpha_l \, n_0 \frac{4}{3}\pi R^3 \tag{B.5}$$

From Eq. (B.5) the rate of fuel vaporization is calculated as:

$$\frac{D\alpha_v}{Dt} = \frac{D\left(\alpha_l n_0 \frac{4}{3}\pi R^3\right)}{Dt} = n_0 \, \frac{4}{3}\pi R^3 \frac{D\alpha_l}{Dt} + \alpha_l \, n_0 4\pi R^2 \frac{DR}{Dt} \tag{B.6}$$

From system (A.3) and Eq. (2.6):

$$\frac{D\alpha_l}{Dt} = -\alpha_l \nabla \cdot \mathbf{U} - \frac{\rho_v}{\rho + \alpha_{nc}(\rho_l - \rho_{nc})} \, \frac{D\alpha_v}{Dt} \tag{B.7}$$

The substitution of Eq. (B.7) in Eq. (B.6) leads to:

$$\frac{D\alpha_v}{Dt} = \frac{\alpha_l n_0 4\pi R^2 \frac{DR}{Dt}}{1 + n_0 \frac{4}{3}\pi R^3 \left(\frac{\rho + \alpha_{nc}(\rho_v - \rho_{nc})}{\rho + \alpha_{nc}(\rho_l - \rho_{nc})} \right)} \tag{B.8}$$

The formulation of the bubble growth rate $\frac{DR}{Dt}$, has been the main topic of several studies in the past [129, 162, 164]; in this work, the formulation from Rayleigh [129] is used:

$$\frac{DR}{Dt} = \text{sign}\big(p(R) - p_\infty\big) \sqrt{\frac{2}{3} \frac{p(R) - p_\infty}{\rho_l}} \tag{B.9}$$

where $p(R)$ is the pressure in the liquid at the bubble boundary and p_∞ is the pressure at a large distance from the bubble. To model either the bubble growth and its collapse in a single equation, $p(R)$ is set in Eq. (B.9) to the vapor saturation pressure p_{sat} and p_∞ to the pressure inside the computational cell, so it follows:

$$\frac{DR}{Dt} = -(p - p_{sat}) \sqrt{\frac{2}{3} \frac{1}{\rho_l |p - p_{sat}|}} = \begin{cases} -min(p - p_{sat}, 0) \sqrt{\frac{2}{3} \frac{1}{\rho_l |p - p_{sat}|}} & if \; p < p_{sat} \\ -max(p - p_{sat}, 0) \sqrt{\frac{2}{3} \frac{1}{\rho_l |p - p_{sat}|}} & if \; p > p_{sat} \end{cases} \tag{B.10}$$

which describes both the bubble grow and its collapse; as a consequence:

$$\frac{D\alpha_v}{Dt} = \begin{cases} \frac{3\alpha_v \frac{DR}{Dt}}{R + R^4 \frac{4}{3}\pi n_0 \left[\frac{\rho + \alpha_{nc}(\rho_v - \rho_{nc})}{\rho + \alpha_{nc}(\rho_l - \rho_{nc})} \right]} = -\frac{3\alpha_v max(p - p_{sat}, 0) \sqrt{\frac{2}{3} \frac{1}{\rho_l |p - p_{sat}|}}}{R + R^4 \frac{4}{3}\pi n_0 \left[\frac{\rho + \alpha_{nc}(\rho_v - \rho_{nc})}{\rho + \alpha_{nc}(\rho_l - \rho_{nc})} \right]} = \alpha_v \left(\frac{D\alpha_v}{Dt} \right)^+ & if \; p > p_{sat} \\ \frac{\alpha_l 4\pi n_0 R^2 \frac{DR}{Dt}}{1 + R^3 \frac{4}{3}\pi n_0 \left[\frac{\rho + \alpha_{nc}(\rho_v - \rho_{nc})}{\rho + \alpha_{nc}(\rho_l - \rho_{nc})} \right]} = -\frac{\alpha_l 4\pi n_0 R^2 min(p - p_{sat}, 0) \sqrt{\frac{2}{3} \frac{1}{\rho_l |p - p_{sat}|}}}{1 + R^3 \frac{4}{3}\pi n_0 \left[\frac{\rho + \alpha_{nc}(\rho_v - \rho_{nc})}{\rho + \alpha_{nc}(\rho_l - \rho_{nc})} \right]} = \alpha_l \left(\frac{D\alpha_v}{Dt} \right)^- & if \; p < p_{sat} \end{cases} \tag{B.11}$$

APPENDIX C

Two-dimensional simulation of the evolution of the free-surface in a partially cavitating/condensating liquid column

The same numerical problem presented in Sec. 3.2 and described in Fig. 3.7 is simulated here in two dimensions. The aspect ratio of the two-dimensional domain was width/height=0.5: the height of the domain is Δy and the width along the transverse direction is $\Delta y/2$. Similarly to Sec. 3.2, simulations on two different grids have been performed, namely grid A (now 320x640 cells) and grid B (now 640x1280 cells); the two grids have the same cell aspect ratio equal to unity. The same benchmark quantities reported for the one-dimensional simulations has been selected to monitor the numerical properties of the solver: the position, sharpness and modeled velocity of the interface, the overall mass conservation and the instantaneous mass balance between the liquid fuel and the fuel vapor. The same boundary and initial conditions of the one-dimensional tests has been applied; for a fair comparison, also the results of this section are presented as in Sec. 3.2.

C.0.1 Cavitation test: results

Starting from an hydrostatic distribution of the pressure in the domain, the liquid starts cavitating. Being the vapor lighter than the liquid, it moves upwards and pushes the non-condensable gas (air) out of the domain. Results of Fig. C.1 and Fig. C.2 show similar trends to those reported in Fig. 3.8; for the two-dimensional case, absolute values of the mass are larger if compared to the one-dimensional case, because now the domain is extended over the x-direction and the amount of mass in the domain is larger.

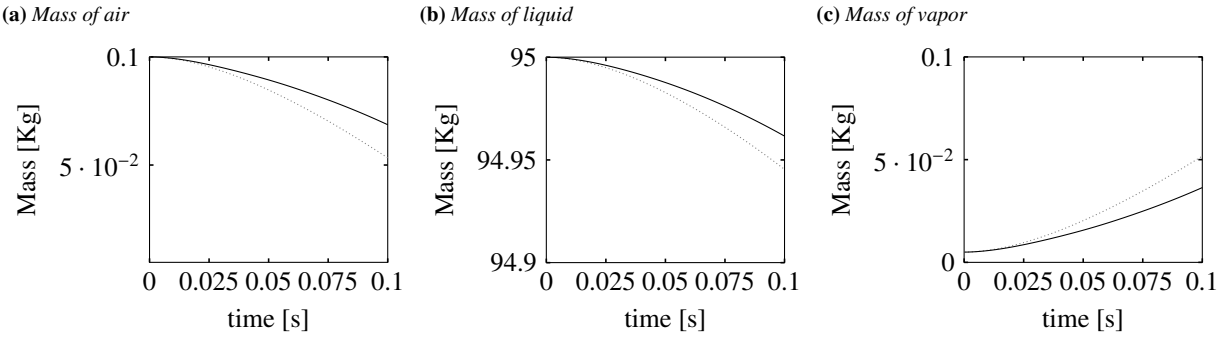

Figure C.1: *Two-dimensional cavitation problem, validation test case. Evolution in time of: (a) air mass (b) liquid mass; (c) vapor mass for two different grids: .... grid A (320X640 cells); — grid B (640x1280 cells).*

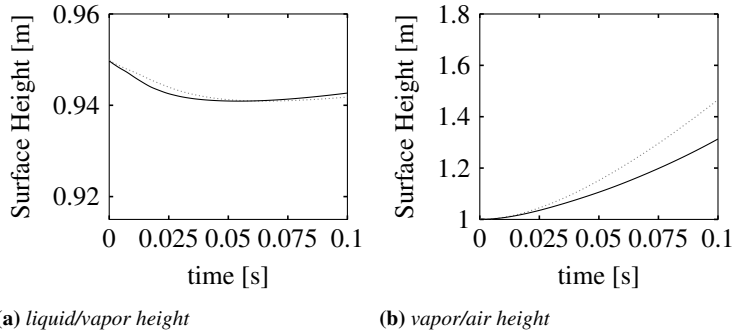

Figure C.2: *Two-dimensional cavitation problem. Evolution in time of the surface heights: (a) liquid/vapor (b) air/vapor for two different grids: .... grid A (320x640 cells); — grid B (640x1280 cells).*

The evolution of the two surface fronts is shown in Fig. C.3. The black solid line is the contour line of α_v=0.5, that bounds the region of the vapor: the upper line in Fig. C.3 is then the vapor-air interface, while the lower line is the vapor-liquid interface.

The liquid/vapor and the air/vapor interface velocities, calculated by Eq. (3.13), are reported in Fig. C.4 for the two-dimensional simulations. Again, they are very similar to the values achieved in Fig. 3.11; this is not surprising, because the free-surface in this specific test-case evolves mostly over a main direction.

Finally, the mass of each phase fraction has been monitored to compute the time step continuity error and the mass conservation error in the domain (Fig. C.5 and Tab. C.1). They are still very limited, in accordance to what it has been shown for the one-dimensional test case. This proves that the numerical accuracy of the solver is maintained also in presence of cavitation and multi-dimensional domains.

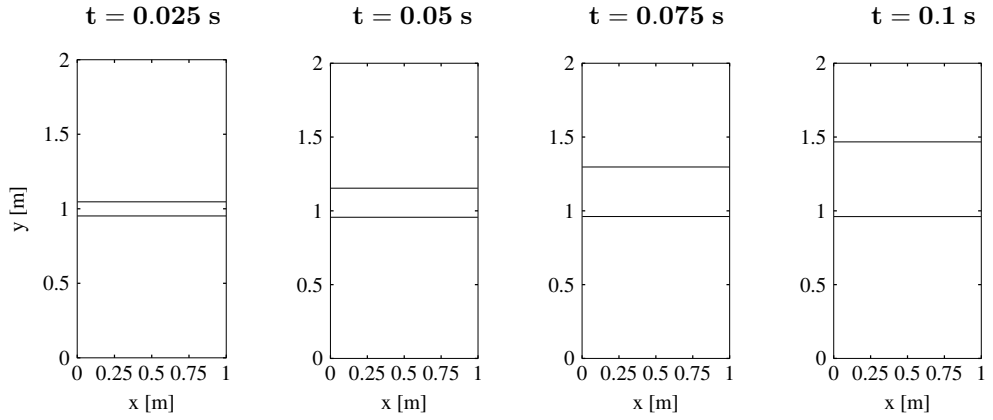

Grid A

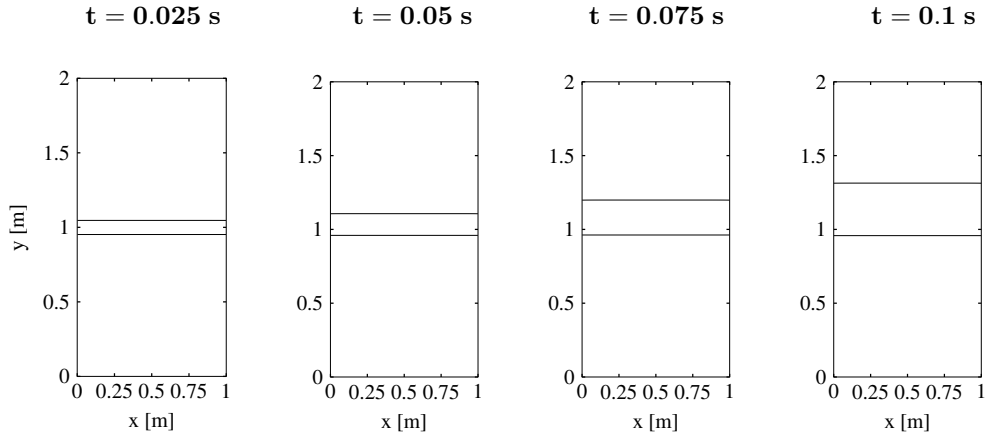

Grid B

Figure C.3: *Two-dimensional cavitation problem. Evolution in time of the void fraction profiles of the fuel-vapor, that bound the vapor region, from 0.025 to 0.1 s. Top) grid A, 320x640 cells; bottom) grid B, 640X1280 cells. Legend:* α_v **—**.

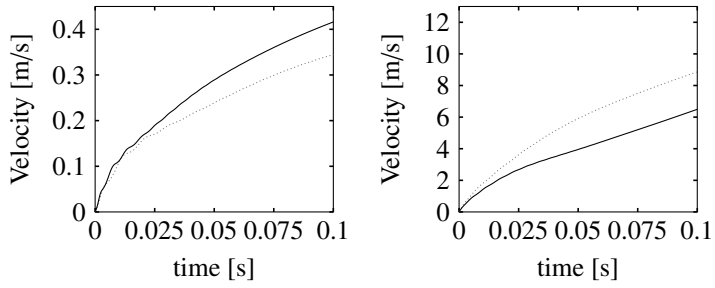

(a) *modeled liquid/vapor surface velocity* **(b)** *modeled vapor/air surface velocity*

Figure C.4: *Two-dimensional cavitation problem, validation test case. Evolution in time of the modeled surface velocity: (a) liquid/vapor; (b) air/vapor on two different grids: .... grid A (320x640 cells);* **—** *grid B (640x1280 cells)*

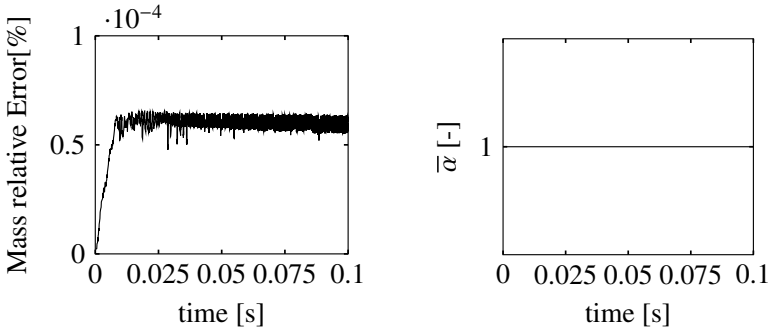

Grid A

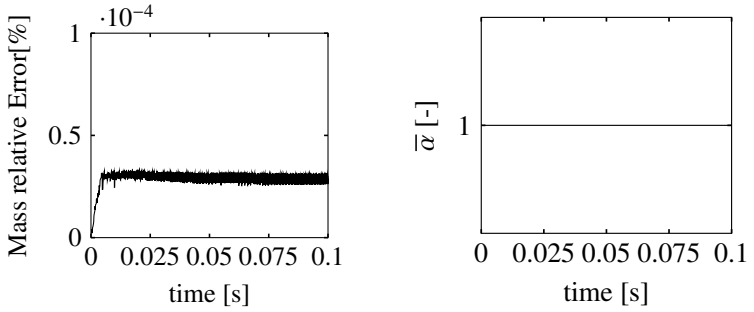

Grid B

Figure C.5: *Two-dimensional cavitation test case, evolution in time of: left) mass relative error; right) sum of the volume-weighted void fractions (see Eq. 3.17). Grid A: 320x640 cells. Grid B: 640x1280 cells.*

Table C.1: *Relative error in the global mass conservation for the cavitation test case.*

No. cells	320x640	640x1280
$E_{global}\%$	0.106	0.026

C.0.2 Condensation test: results

Similarly to what has been done in Sec. 3.2, the distribution of the phase-fractions derived from the calculation of the two-dimensional liquid column problem with cavitation is set as initial condition. Vapor condensation is artificially triggered by changing the threshold value of the liquid saturation pressure; as a result, the vapor changes direction of its motion and a suction of non-condensable gas (air) from the upper boundary is observed. Fig. C.6a shows the evolution of the global mass of the separate phases in the domain in time.

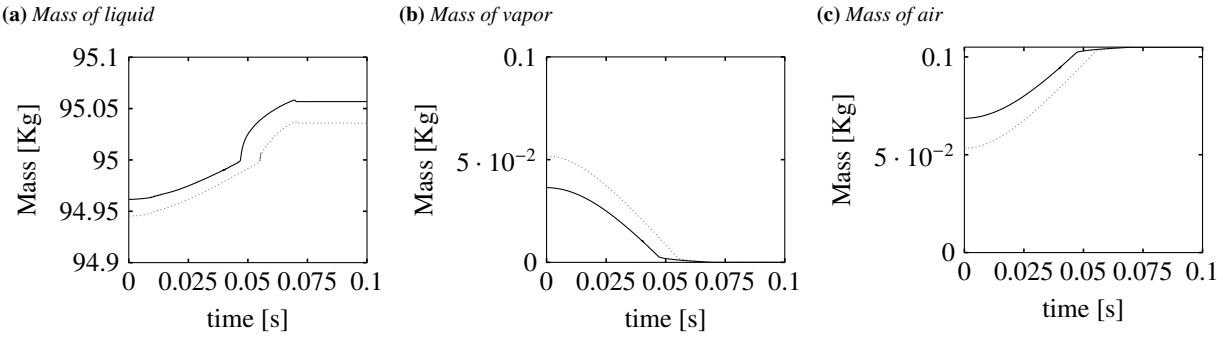

Figure C.6: *Two-dimensional condensation problem, validation test case. Evolution in time of: (a) liquid mass; (b) vapor mass; (c) air mass on two different grids: .... grid A (320x640 cells); — grid B (640x1280 cells).*

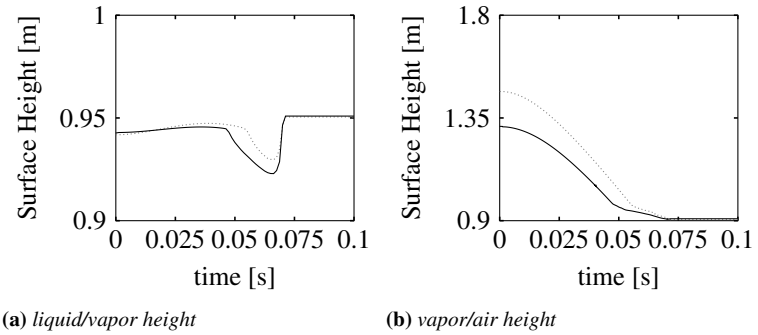

Figure C.7: *Two-dimensional condensation problem. Evolution in time of the surface heights: (a) liquid/vapor (b) air/vapor for two different grids: .... grid A (320x640 cells); — grid B (640x1280 cells).*

The evolution of the two surfaces fronts (liquid/vapor and air/vapor) is shown in Fig. C.8 for a duration of 0.5 s. The black solid line is the iso-contour line of the phase fraction of the vapor at 0.5. The upper-line locates the vapor-air interface, while the lower line is the vapor-liquid interface; the region of the fuel-vapor is therefore bounded by these two lines. Approximately at t=$0.6\ s$, the fuel-vapor is fully condensed and the visualization of two interfaces is not possible anymore; for clarity, a black dotted line for the liquid-air interface is used at $0.75\ s$ and $0.1\ s$.

The liquid/vapor and the air/vapor interface velocities, calculated by Eq. (3.13), are plotted in Fig. C.9. Again, they are very similar to the values achieved in Fig. 3.16 for the one-dimensional case; this is not surprising, because the free-surface in this specific test-case evolves mostly in one-direction and also the one-dimensional domain is sufficient to describe the evolution of the experiment.

Finally, Fig. C.10 shows that also for the two-dimensional simulations, the global errors for the two grid resolutions tested are still very limited and that the solver is very accurate in the handling of the phase change with multi-dimensional domains. It is important to remark that the error peak presents at $0.075\ s$ is smaller than the one observed in the one-dimensional case (Fig. 3.17): in multi-dimensional problems, the influence of the boundary conditions on the solution is smaller, so the errors in the solution of the linear systems can be spread over the multiple directions. This is not possible in a one-dimensional test case.

Appendix C. Two-dimensional simulation of the evolution of the free-surface in a partially cavitating/condensating liquid column

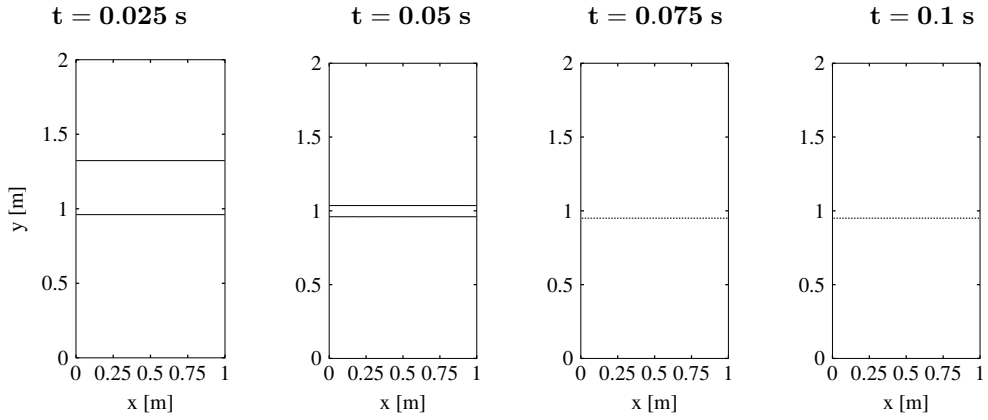

Grid A

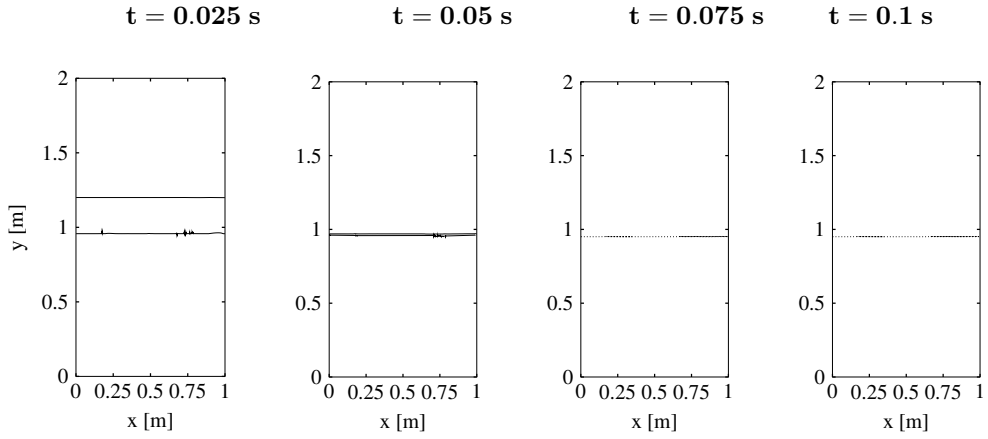

Grid B

Figure C.8: *Two-dimensional condensation problem. Evolution in time of the iso-contour line of the fuel-vapor $\alpha_v = 0.5$, that bounds the vapor region, from 0.025 to 0.1 s. Top) grid A, 320x640 cells; bottom) grid B, 640X1280 cells. Legend: α_v —.*

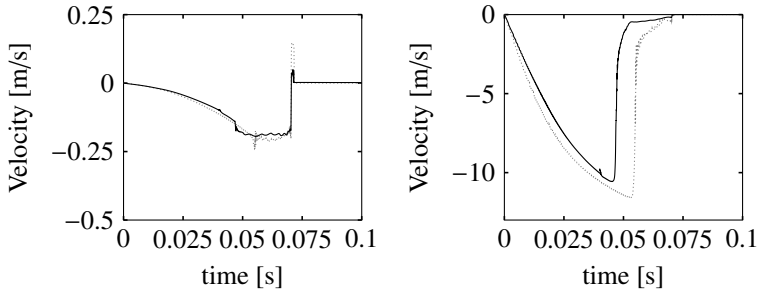

(a) *liquid/vapor surface velocity* **(b)** *vapor/air surface velocity*

Figure C.9: *Two-dimensional condensation problem, validation test case. Evolution in time of the mean interface velocity: (a) liquid/vapor surface velocity and (b) air/vapor surface velocity.* `interPhaseChangeMixingFoam` *behavior using two different discretizations: .... 320X640 cells; — 640X1280 cells*

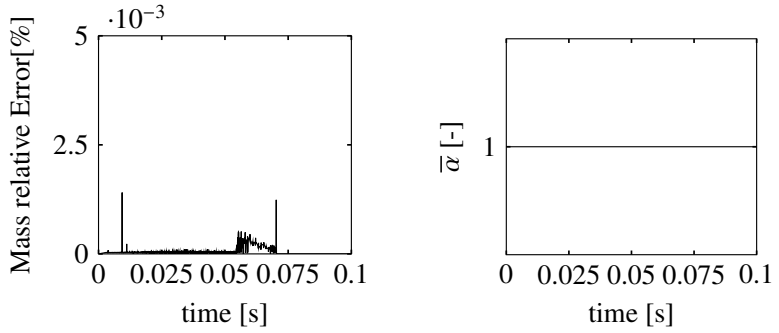

Grid B

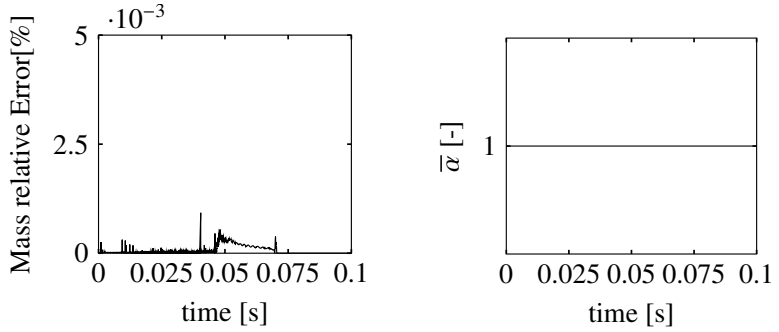

Grid B

Figure C.10: *Two-dimensional condensation test case, evolution in time of: left) mass relative error; right) sum of the volume-weighted void fractions (see Eq. 3.17). Grid A: 320x640 cells. Grid B: 640x1280 cells.*

Table C.2: *Relative (percentage) error on global mass conservation for condensation test case*

No. cells	320x640	640x1280
$E_{global}\%$	0.1496	0.1385

Bibliography

[1] *Large Eddy Simulation for Incompressible Flows*. Springer-Verlag, 2006.

[2] *Computational Methods for Multiphase Flow*. Cambridge University Press, 2007.

[3] *Large Eddy Simulation for atomization : application to automotive engines injection.* PhD thesis, Université de Rouen, June 2010.

[4] Moataz O. Abu-Al-Saud, Stéphane Popinet, and Hamdi A. Tchelepi. A conservative and well-balanced surface tension model. *Journal of Computational Physics*, 371:896 – 913, 2018.

[5] A. Agresta, J. Hélie, E. Kull, N. Lamarque, A. Lyubar, and S. Schuster. Real-size real-shape real-pressure transparent nozzles to contribute to nozzle design and cavitation control for gdi. In *29th Conference on Liquid Atomization and Spray Systems, ILASS-Europe, 2-4 September 2019, Paris, France*.

[6] P.G. Aleiferis, Y. Hardalupas, D. Kolokotronis, A.M.K.P. Taylor, A. Arioka, and M. Saito. Experimental investigation of the internal flow field of a model gasoline injector using micro-particle image velocimetry. In *Powertrain & Fluid Systems Conference and Exhibition*. SAE International, oct 2006.

[7] P.G. Aleiferis, Y. Hardalupas, D. Kolokotronis, A.M.K.P. Taylor, and T. Kimura. Investigation of the internal flow field of a diesel model injector using particle image velocimetry and cfd. In *JSAE/SAE International Fuels & Lubricants Meeting*. SAE International, jul 2007.

[8] Mireia Altimira and Laszlo Fuchs. Numerical investigation of throttle flow under cavitating conditions. *International Journal of Multiphase Flow*, 75:124 – 136, 2015.

[9] Antonio Andreini, Cosimo Bianchini, Stefano Puggelli, and F.X. Demoulin. Development of a turbulent liquid flux model for eulerian-eulerian multiphase flow simulations. *International Journal of Multiphase Flow*, 81:88 – 103, 2016.

[10] A. Andriotis and Manolis Gavaises. Influence of vortex flow and cavitation on near-nozzle diesel spray dispersion angle. *Atomization and Sprays*, 19(3):247–261, 2009.

[11] J. Anez, A. Ahmed, N. Hecht, B. Duret, J. Reveillon, and F.X. Demoulin. Eulerian-lagrangian spray atomization model coupled with interface capturing method for diesel injectors. *International Journal of Multiphase Flow*, 113:325 – 342, 2019.

[12] W. Aniszewski, A. Bogusławski, M. Marek, and A. Tyliszczak. A new approach to sub-grid surface tension for les of two-phase flows. *Journal of Computational Physics*, 231(21):7368 – 7397, 2012.

[13] Wojciech Aniszewski. Improvements, testing and development of the adm-τ sub-grid surface tension model for two-phase les. *Journal of Computational Physics*, 327:389 – 415, 2016.

[14] Roger E.A. Arndt. Cavitation in vortical flows. *Annual Review of Fluid Mechanics*, 34(1):143–175, 2002.

[15] J.A. Astolfi, P. Dorange, J.Y. Billard, and I. Cid Tomas. An Experimental Investigation of Cavitation Inception and Development on a Two-Dimensional Eppler Hydrofoil . *Journal of Fluids Engineering*, 122(1):164–173, 10 1999.

[16] A. Baraldi, M.S. Dodd, and A. Ferrante. A mass-conserving volume-of-fluid method: Volume tracking and droplet surface-tension in incompressible isotropic turbulence. *Computers & Fluids*, 96:322 – 337, 2014.

[17] S. Barre, J. Rolland, G. Boitel, E. Goncalves, and R. Fortes Patella. Experiments and modeling of cavitating flows in venturi: attached sheet cavitation. *European Journal of Mechanics - B/Fluids*, 28(3):444 – 464, 2009.

[18] C. Baumgarten. *Mixture Formation in Internal Combustion Engines*. Heat and Mass Transfer. Springer Berlin Heidelberg, 2006.

[19] P.-A. Beau, M. Funk, R. Lebas, and F.-X. Demoulin. Applying quasi-multiphase model to simulate atomization processes in diesel engines: Modeling of the slip velocity. apr 2005.

[20] M. Behzad, N. Ashgriz, and B.W. Karney. Surface breakup of a non-turbulent liquid jet injected into a high pressure gaseous crossflow. *International Journal of Multiphase Flow*, 80:100 – 117, 2016.

[21] Rickard E. Bensow and Göran Bark. Implicit LES predictions of the cavitating flow on a propeller. *Journal of Fluids Engineering*, 132(4):041302, 2010.

[22] W. Bergwerk. Flow pattern in diesel nozzle spray holes. *Proceedings of the Institution of Mechanical Engineers*, 173(1):655–660, 1959.

[23] Bariş Biçer and Akira Sou. Application of the improved cavitation model to turbulent cavitating flow in fuel injector nozzle. *Applied Mathematical Modelling*, 40(7):4712 – 4726, 2016.

[24] Z. Bilicki and J. Kestin. Physical aspects of the relaxation model in two-phase flow. *Proceedings of the Royal Society of London A: Mathematical, Physical and Engineering Sciences*, 428(1875):379–397, 1990.

[25] G. A. Bird. *Molecular Gas Dynamics and the Direct Simulation of Gas Flows (Oxford Engineering Science Series)*. Clarendon Press, jun 1994.

[26] Marc Boivin, Olivier Simonin, and Kyle D. Squires. On the prediction of gas-solid flows with two-way coupling using large eddy simulation. *Physics of Fluids*, 12(8):2080–2090, 2000.

[27] J.P. Boris and D.L. Book. Solution of continuity equations by the method of flux-corrected transport. In JOHN KILLEEN, editor, *Controlled Fusion*, volume 16 of *Methods in Computational Physics: Advances in Research and Applications*, pages 85 – 129. Elsevier, 1976.

[28] Dieter Bothe and Stefan Fleckenstein. A volume-of-fluid-based method for mass transfer processes at fluid particles. *Chemical Engineering Science*, 101:283 – 302, 2013.

[29] J.U Brackbill, D.B Kothe, and C Zemach. A continuum method for modeling surface tension. *Journal of Computational Physics*, 100(2):335 – 354, 1992.

[30] C.E. Brennen. *Cavitation and Bubble Dynamics*. Cavitation and Bubble Dynamics. Cambridge University Press, 2013.

[31] Elie Bretin, Alexandre Danescu, José Penuelas, and Simon Masnou. Multiphase mean curvature flows with high mobility contrasts: A phase-field approach, with applications to nanowires. *Journal of Computational Physics*, 365:324 – 349, 2018.

[32] Federico Brusiani, Sergio Negro, Gian Marco Bianchi, Maryam Moulai, Kshitij Neroorkar, and David Schmidt. Comparison of the homogeneous relaxation model and a rayleigh plesset cavitation model in predicting the cavitating flow through various injector hole shapes. In *SAE 2013 World Congress & Exhibition*. SAE International, apr 2013.

[33] M. Cailloux, J. Hèlie, J. Reveillon, and F. X. Demoulin. Large eddy simulation of a cavitating multiphase flow for liquid injection. *Journal of Physics: Conference Series*, 656(1):012081, 2015.

[34] M. Cailloux, J. Helie, J. Reveillon, and F. X. Demoulin. Large eddy simulation of a cavitating multiphase flow for liquid injection. *Journal of Physics: Conference Series*, 656:012081, dec 2015.

[35] ISABELLE CALMET and JACQUES MAGNAUDET. Statistical structure of high-reynolds-number turbulence close to the free surface of an open-channel flow. *Journal of Fluid Mechanics*, 474:355–378, 2003.

[36] SEBASTIEN M. CANDEL and THIERRY J. POINSOT. Flame stretch and the balance equation for the flame area. *Combustion Science and Technology*, 70(1-3):1–15, 1990.

[37] Jesse Capecelatro and Olivier Desjardins. An euler-lagrange strategy for simulating particle-laden flows. *Journal of Computational Physics*, 238:1 – 31, 2013.

[38] Georges L. Chahine. *Bubble Interactions with Vortices*, pages 783–828. Springer Netherlands, Dordrecht, 1995.

[39] H. Chaves, M. Knapp, A. Kubitzek, F. Obermeier, et al. Experimental study of cavitation in the nozzle hole of diesel injectors using transparent nozzles. *SAE Technical Paper 950290*, 1995.

[40] Humberto Chaves, Robert Knake, and Ricard Miranda. Particle image velocimetry measurements of the cavitating flow in a real size transparent vco nozzle. In *ICMF-2007 - 6th Int. Conference on Multiphase Flow, Leipzig, Germany*, 2007.

[41] Xinfu Chen. Generation and propagation of interfaces for reaction-diffusion equations. *Journal of Differential Equations*, 96(1):116 – 141, 1992.

[42] Ying Chen, Xin Chen, Jie Li, Zhaoxin Gong, and Chuanjing Lu. Large eddy simulation and investigation on the flow structure of the cascading cavitation shedding regime around 3d twisted hydrofoil. *Ocean Engineering*, 129:1 – 19, 2017.

[43] Zhou Chen, Zhixia He, Weiwei Shang, Lian Duan, Han Zhou, Genmiao Guo, and Wei Guan. Experimental study on the effect of nozzle geometry on string cavitation in real-size optical diesel nozzles and spray characteristics. *Fuel*, 232:562 – 571, 2018.

[44] J. Chesnel, J. Reveillon, T. Ménard, and F.X. Demoulin. Large eddy simulation of liquid jet atomization. *Atomization and Sprays*, 21(9):711–736, 2011. cited By 26.

[45] R. Clift, J.R. Grace, and M.E. Weber. *Bubbles, Drops, and Particles*. Dover Civil and Mechanical Engineering Series. Dover Publications, 2005.

[46] O. Coutier-Delgosha, R. Fortes-Patella, and J. L. Reboud. Evaluation of the turbulence model influence on the numerical simulations of unsteady cavitation. *Journal of Fluids Engineering*, 125(1):38, 2003.

[47] Jiwen Cui, Houhu Lai, Kunpeng Feng, and Yarui Ma. Quantitative analysis of the minor deviations in nozzle internal geometry effect on the cavitating flow. *Experimental Thermal and Fluid Science*, 94:89 – 98, 2018.

[48] Lakehal D, Brian L Smith, and Massimo Milelli. Large-eddy simulation of bubbly turbulent shear flows. *Journal of Turbulence*, 3:N25, January 2002.

[49] D'Agostino, L. and Green, S.I. Simultaneous cavitation susceptibility meter and holographic measurements of nuclei in liquids. *Journal of Fluids Engineering*, 114(2):261–267, 1992.

[50] N.G. Deen, T. Solberg, and B.H. Hjertager. Large eddy simulation of the gas-liquid flow in a square cross-sectioned bubble column. *Chemical engineering science*, 56(21-22):6341–6349, 2001.

[51] Filippo Maria Denaro. What does finite volume-based implicit filtering really resolve in large-eddy simulations? *Journal of Computational Physics*, 230(10):3849 – 3883, 2011.

[52] Olivier Desjardins, Vincent Moureau, and Heinz Pitsch. An accurate conservative level set/ghost fluid method for simulating turbulent atomization. *Journal of Computational Physics*, 227(18):8395 – 8416, 2008.

[53] M. Dianat, M. Skarysz, and A. Garmory. A coupled level set and volume of fluid method for automotive exterior water management applications. *International Journal of Multiphase Flow*, 91:19 – 38, 2017.

[54] P. Downar-Zapolski, Z. Bilicki, L. Bolle, and J. Franco. The non-equilibrium relaxation model for one-dimensional flashing liquid flow. *International Journal of Multiphase Flow*, 22(3):473 – 483, 1996.

[55] D A Drew. Mathematical modeling of two-phase flow. *Annual Review of Fluid Mechanics*, 15(1):261–291, 1983.

[56] J Du, B. Fix, J. Glimm, X. Jia, X. Li, Y. Li, and L. Wu. A simple package for front tracking. *J. Comput. Phys.*, 213:613–628, 2006.

[57] C. Dumouchel, J. Cousin, and K. Triballier. On the role of the liquid flow characteristics on low-Weber-number atomization processes. *Experiments in Fluids*, 38:637–647, May 2005.

[58] B. Duret, R. Canu, J. Reveillon, and F.X. Demoulin. A pressure based method for vaporizing compressible two-phase flows with interface capturing approach. *International Journal of Multiphase Flow*, 108:42 – 50, 2018.

[59] B. Duret, J. Reveillon, T. Menard, and F.X. Demoulin. Improving primary atomization modeling through dns of two-phase flows. *International Journal of Multiphase Flow*, 55:130 – 137, 2013.

[60] J.K. Eaton and J.R. Fessler. Preferential concentration of particles by turbulence. *International Journal of Multiphase Flow*, 20:169 – 209, 1994.

[61] W. Edelbauer. Numerical simulation of cavitating injector flow and liquid spray break-up by combination of eulerian—eulerian and volume—of—fluid methods. *Computers & Fluids*, 144:19 – 33, 2017.

[62] David Edwards. *Interfacial Transport Processes and Rheology (Butterworth-Heinemann Series in Chemical Engineering)*. Butterworth-Heinemann, oct 2013.

[63] Christian P. Egerer, Steffen J. Schmidt, Stefan Hickel, and Nikolaus A. Adams. Efficient implicit les method for the simulation of turbulent cavitating flows. *Journal of Computational Physics*, 316:453 – 469, 2016.

[64] S. Elghobashi, T. Abou-Arab, M. Rizk, and A. Mostafa. Prediction of the particle-laden jet with a two-equation turbulence model. *International Journal of Multiphase Flow*, 10(6):697 – 710, 1984.

[65] Ronald P Fedkiw, Tariq Aslam, Barry Merriman, and Stanley Osher. A non-oscillatory eulerian approach to interfaces in multimaterial flows (the ghost fluid method). *Journal of Computational Physics*, 152(2):457 – 492, 1999.

[66] J.H. Ferziger and M. Peric. *Computational Methods for Fluid Dynamics*. Springer Berlin Heidelberg, 2001.

[67] Stefan Fleckenstein and Dieter Bothe. A volume-of-fluid-based numerical method for multi-component mass transfer with local volume changes. *Journal of Computational Physics*, 301:35 – 58, 2015.

[68] Michel J.-M. Franc J.P. *Fundamentals of Cavitation*. Kluwer Academic Publishers, 2005.

[69] Daniel Fuster, Anne Bagué, Thomas Boeck, Luis Le Moyne, Anthony Leboissetier, Stéphane Popinet, Pascal Ray, Ruben Scardovelli, and Stéphane Zaleski. Simulation of primary atomization with an octree adaptive mesh refinement and vof method. *International Journal of Multiphase Flow*, 35(6):550 – 565, 2009.

[70] L. C. Ganippa, G. Bark, S. Andersson, and J. Chomiak. Cavitation: a contributory factor in the transition from symmetric to asymmetric jets in cross-flow nozzles. *Experiments in Fluids*, 36(4):627–634, Apr 2004.

[71] Harald Garcke, Britta Nestler, and Barbara Stoth. On anisotropic order parameter models for multi-phase systems and their sharp interface limits. *Physica D: Nonlinear Phenomena*, 115(1):87 – 108, 1998.

[72] M. Gavaises, A. Andriotis, D. Papoulias, N. Mitroglou, and A. Theodorakakos. Characterization of string cavitation in large-scale diesel nozzles with tapered holes. *Physics of Fluids*, 21(5):052107, 2009.

[73] M. Gavaises, A. Andriotis, D. Papoulias, N. Mitroglou, and A. Theodorakakos. Characterization of string cavitation in large-scale diesel nozzles with tapered holes. *Physics of Fluids*, 21(5), 2009.

[74] Manolis Gavaises, Fabio Villa, Phoevos Koukouvinis, Marco Marengo, and Jean-Pierre Franc. Visualisation and les simulation of cavitation cloud formation and collapse in an axisymmetric geometry. *International Journal of Multiphase Flow*, 68:14 – 26, 2015.

[75] F. Giussani, A. Montorfano, F. Piscaglia, A. Onorati, J. Hélie, and S.M. Aithal. Dynamic vof modelling of the internal flow in gdi fuel injectors. *Energy Procedia*, 101(Supplement C):574 – 581, 2016. ATI 2016 - 71st Conference of the Italian Thermal Machines Engineering Association.

[76] F. Giussani, F. Piscaglia, J. Hélie, and S.M. Aithal. A 3-phase solver for the simulation of internal nozzle cavitating flows in fuel-injectors using openfoam. In *29th Conference on Liquid Atomization and Spray Systems, ILASS-Europe, 2-4 September 2019, Paris, France*.

[77] F. Giussani, F. Piscaglia, G. Saez-Mischlich, and J. Hélie. A three-phase vof solver for the simulation of in-nozzle cavitation effects on liquid atomization. *Journal of Computational Physics*, page 109068, 2019.

[78] Denis Gueyffier, Jie Li, Ali Nadim, Ruben Scardovelli, and Stéphane Zaleski. Volume-of-fluid interface tracking with smoothed surface stress methods for three-dimensional flows. *Journal of Computational Physics*, 152(2):423 – 456, 1999.

[79] Hanratty, T.J. and Theofanous, T. and Delhaye, J.M. and Eaton, J. and McLaughlin, J. and Prosperetti, A. and Sundaresan, S. and Tryggvason, G. Workshop Findings. *International Journal of Multiphase Flow*, 29(7):1147–1059, 2003.

[80] Ami Harten. High resolution schemes for hyperbolic conservation laws. *Journal of Computational Physics*, 135(2):260 – 278, 1997.

[81] Zhi Xia He, Zhuang Shao, Zhi Wei Zhou, and Xi Cheng Tao. Experimental study of hydraulic flip phenomenon inside diesel nozzles using diesel and biodiesel. In *Advances in Manufacturing Science and Engineering V*, volume 945 of *Advanced Materials Research*, pages 940–943. Trans Tech Publications, 7 2014.

[82] J. Helie, Mahabat M. K., and M. Gorokhovski. Large eddy simulation of a turbulent spray jet generated by high-pressure injection: impact of the in-nozzle flow. *Journal of Turbulence*, 17(9):823–846, 2016.

[83] J. Hèlie, M. M. Khan, and M. Gorokhovski. Large eddy simulation of a turbulent spray jet generated by high pressure injection: impact of the in-nozzle flow. *Journal of Turbulence*, 17(9), 2016.

[84] M. Herrmann. A sub-grid surface dynamics model for sub-filter surface tension induced interface dynamics. *Computers & Fluids*, 87:92 – 101, 2013. USNCCM Moving Boundaries.

[85] Jörg Heyse, Frank Schatz, Beate Ader, Jörg Schlerfer, and Sven Haubold. Electroformed multilayer orifice plate for improved fuel injection characteristics. *SAE Transactions*, 106:2051–2062, 1997.

[86] C.W Hirt and B.D Nichols. Volume of fluid (vof) method for the dynamics of free boundaries. *Journal of Computational Physics*, 39(1):201 – 225, 1981.

[87] C.W Hirt and B.D Nichols. Volume of fluid (vof) method for the dynamics of free boundaries. *Journal of Computational Physics*, 39(1):201 – 225, 1981.

[88] Ryan W. Houim and Kenneth K. Kuo. A ghost fluid method for compressible reacting flows with phase change. *Journal of Computational Physics*, 235:865 – 900, 2013.

[89] X.Y. Hu and N.A. Adams. Scale separation for implicit large eddy simulation. *Journal of Computational Physics*, 230(19):7240 – 7249, 2011.

[90] Biao Huang, Antoine Ducoin, and Yin Lu Young. Physical and numerical investigation of cavitating flows around a pitching hydrofoil. *Physics of Fluids*, 25(10):102109, 2013.

[91] Biao Huang, Yin L. Young, Guoyu Wang, and Wei Shyy. Combined experimental and computational investigation of unsteady structure of sheet/cloud cavitation. *Journal of Fluids Engineering*, 135(7):071301, may 2013.

[92] Biao Huang, Yu Zhao, and Guoyu Wang. Large eddy simulation of turbulent vortex-cavitation interactions in transient sheet/cloud cavitating flows. *Computers & Fluids*, 92:113 – 124, 2014.

[93] R. Husson, L.C. Ganippa, and H. Zhao. Flow and cavitation structure in a scaled-up multi hole optical diesel nozzle. In *22nd European Conference on Liquid Atomization and Spray Systems (ILASS), 8-10 September 2008, Como (Italy)*, 2008.

[94] S. Hysing, S. Turek, D. Kuzmin, N. Parolini, E. Burman, S. Ganesan, and L. Tobiska. Quantitative benchmark computations of two-dimensional bubble dynamics. *Int. Journal for Numerical Methods in Fluids*, 60(11):1259–1288, 2009.

[95] U. Iben, A. Morozov, E. Winklhofer, and F. Wolf. Laser-pulse interferometry applied to high-pressure fluid flow in micro channels. *Experiments in Fluids*, 50(3):597–611, 2011.

[96] R.I Issa. Solution of the implicitly discretised fluid flow equations by operator-splitting. *Journal of Computational Physics*, 62(1):40 – 65, 1986.

[97] R.I Issa. Solution of the implicitly discretised fluid flow equations by operator-splitting. *Journal of Computational Physics*, 62(1):40 – 65, 1986.

[98] D. Jarrahbashi, W. A. Sirignano, P. P. Popov, and F. Hussain. Early spray development at high gas density: hole, ligament and bridge formations. *Journal of Fluid Mechanics*, 792:186–231, 2016.

[99] D. Jarrahbashi and W.A. Sirignano. Vorticity dynamics for transient high-pressure liquid injection a. *Phys. Fluids*, 26(10):73, 2014. cited By 1.

[100] B. Ji, X.W. Luo, Roger E.A. Arndt, Xiaoxing Peng, and Yulin Wu. Large eddy simulation and theoretical investigations of the transient cavitating vortical flow structure around a naca66 hydrofoil. *International Journal of Multiphase Flow*, 68:121 – 134, 2015.

[101] Bin Ji, Xianwu Luo, Roger E.A. Arndt, and Yulin Wu. Numerical simulation of three dimensional cavitation shedding dynamics with special emphasis on cavitation-vortex interaction. *Ocean Engineering*, 87:64 – 77, 2014.

[102] V. John and G. Matthies. MooNMD – a program package based on mapped finite element methods. *Computeing and visualization in science*, (9):1179–1195, 2004.

[103] S. Jollet, H. Hansen, K. Bitner, D. Niemeyer, and F. Dinkelacker. Experimental and numerical investigations of 90 μm real-size transparent nozzles with high pressure conditions. In *ILASS Europe, 26th Annual Conference on Liquid Atomization and Spray Systems, 8-10 Sep. 2014, Bremen, Germany*, 2014.

[104] I. Kataoka. Local instant formulation of two-phase flow. *International Journal of Multiphase Flow*, 12(5):745 – 758, 1986.

[105] E.E. Kawakami and R.A. Arndt. Investigation of the behavior of ventilated supercavities. *ASME. J. Fluids Eng.*, 133(9), 2011.

[106] J. H. Kim, K. Nishida, and H. Hiroyasu. Characteristics of the internal flow in a diesel injection nozzle. *Int. Journal of Fluid Mechanics Research*, 24(1-3):34–44, 1997.

[107] Markus Klein, S. Ketterl, and J. Hasslberger. Large eddy simulation of multiphase flows using the volume of fluid method: Part 1—governing equations and a priori analysis. *Experimental and Computational Multiphase Flow*, 1(2):130–144, May 2019.

[108] J. Klostermann, K. Schaake, and R. Schwarze. Numerical simulation of a single rising bubble by vof with surface compression. *Int. Journal for Numerical Methods in Fluids*, 71(8):960–982, 2013.

[109] Bernard Knaepen, Olivier Debliquy, and Daniele Carati. Large-eddy simulation without filter. *Journal of Computational Physics*, 205(1):98 – 107, 2005.

[110] Phoevos Koukouvinis, Homa Naseri, and Manolis Gavaises. Performance of turbulence and cavitation models in prediction of incipient and developed cavitation. *International Journal of Engine Research*, 18(4):333–350, 2017.

[111] Robert F. Kunz, David A. Boger, David R. Stinebring, Thomas S. Chyczewski, Jules W. Lindau, Howard J. Gibeling, Sankaran Venkateswaran, and T.R. Govindan. A preconditioned navier—stokes method for two-phase flows with application to cavitation prediction. *Computers & Fluids*, 29(8):849 – 875, 2000.

[112] E. Labourasse, D. Lacanette, A. Toutant, P. Lubin, S. Vincent, O. Lebaigue, J.-P. Caltagirone, and P. Sagaut. Towards large eddy simulation of isothermal two-phase flows: Governing equations and a priori tests. *International Journal of Multiphase Flow*, 33(1):1–39, jan 2007.

[113] S. Lain, D. Br´oder, M. Sommerfeld, and M.F. G´oz. Modelling hydrodynamics and turbulence in a bubble column using the euler-lagrange procedure. *International Journal of Multiphase Flow*, 28(8):1381 – 1407, 2002.

[114] Djamel Lakehal. Leis for the prediction of turbulent multifluid flows applied to thermal-hydraulics applications. *Nuclear Engineering and Design*, 240:2096–2106, 09 2010.

[115] Djamel Lakehal. Status and future developments of large-eddy simulation of turbulent multi-fluid flows (leis and less). *International Journal of Multiphase Flow*, 104:322 – 337, 2018.

[116] Djamel Lakehal and Daniel Caviezel. Large-eddy simulation of convective wall-boiling flow along an idealized pwr rod bundle. *Nuclear Engineering and Design*, 321:104 – 117, 2017. Multi-scale multi-physics analysis of reactor transients in the NURESAFE project.

[117] DJAMEL LAKEHAL and PETAR LIOVIC. Turbulence structure and interaction with steep breaking waves. *Journal of Fluid Mechanics*, 674:522–577, 2011.

[118] E. Lauer, X.Y. Hu, S. Hickel, and N.A. Adams. Numerical modelling and investigation of symmetric and asymmetric cavitation bubble dynamics. *Computers & Fluids*, 69:1 – 19, 2012.

[119] R. Lebas, T. Menard, P.A. Beau, A. Berlemont, and F.X. Demoulin. Numerical simulation of primary break-up and atomization: Dns and modelling study. *International Journal of Multiphase Flow*, 35(3):247 – 260, 2009.

[120] Sang Bong Lee. A study on temporal accuracy of openfoam. *International Journal of Naval Architecture and Ocean Engineering*, 9(4):429 – 438, 2017.

[121] M. Lesieur, O. Metais, and P. Comte. *Large-Eddy Simulations of Turbulence*. Cambridge University Press, 2005.

[122] Randall J. LeVeque. *Numerical Methods for Conservation Laws*. Lectures in Mathematics, ETH Zurich, 2007.

[123] Shan Qing Li, Pengdong Wang, and Tianai Lu. Numerical simulation of direct contact condensation of subsonic steam injected in a water pool using vof method and les turbulence model. 2015.

[124] Xiaoyi Li, Marios C. Soteriou, Wookyung Kim, and Jeffrey M. Cohen. High Fidelity Simulation of the Spray Generated by a Realistic Swirling Flow Injector. *Journal of Engineering for Gas Turbines and Power*, 136(7), 02 2014.

[125] Petar Liovic and Djamel Lakehal. Multi-physics treatment in the vicinity of arbitrarily deformable gas-liquid interfaces. *Journal of Computational Physics*, 222(2):504 – 535, 2007.

[126] Petar Liovic and Djamel Lakehal. Subgrid-scale modelling of surface tension within interface tracking-based large eddy and interface simulation of 3d interfacial flows. *Computers & Fluids*, 63:27 – 46, 2012.

[127] Hong Liu, Weilong Zhang, Ming Jia, Yan'an Yan, and Yang He. An improved method for coupling the in-nozzle cavitation with multi-fluid-quasi-vof model for diesel spray. *Computers & Fluids*, 177:20 – 32, 2018.

[128] Yun Long, Xin ping Long, Bin Ji, Wen xin Huai, and Zhong dong Qian. Verification and validation of urans simulations of the turbulent cavitating flow around the hydrofoil. *Journal of Hydrodynamics, Ser. B*, 29(4):610 – 620, 2017.

[129] O.M. F.R.S. Lord Rayleigh. Viii. on the pressure developed in a liquid during the collapse of a spherical cavity. *The London, Edinburgh, and Dublin Philosophical Magazine and Journal of Science*, 34(200):94–98, 1917.

[130] Xianwu Luo, Bin Ji, Xiaoxing Peng, Hongyuan Xu, and Michihiro Nishi. Numerical simulation of cavity shedding from a three-dimensional twisted hydrofoil and induced pressure fluctuation by large-eddy simulation. *Journal of Fluids Engineering*, 134(4):041202, 2012.

[131] T. Ma, T. Ziegenhein, D. Lucas, and J. Fröhlich. Large eddy simulations of the gas-liquid flow in a rectangular bubble column. *Nuclear Engineering and Design*, 299:146 – 153, 2016. CFD4NRS-5.

[132] S. Makhlouf, J. Hélie, G. Grimoux, J. Cousin, L. Gestri, A. Wood, and G. Wigley. Large eddy simulation of cavitation and atomization in injector flows using openfoam. In *ICLASS 2012, 12th Triennial Int. Conference on Liquid Atomization and Spray Systems, Heidelberg, Germany*, 2012.

[133] Frank Earl Marble and James E. Broadwell. The coherent flame model for turbulent chemical reactions. final report 1 mar 75–31 jan 77. 1977.

[134] J. Martínez, F. Piscaglia, A. Montorfano, A. Onorati, and S.M. Aithal. Influence of spatial discretization schemes on accuracy of explicit LES: Canonical problems to engine-like geometries. *Computers & Fluids*, 117:62 – 78, 2015. `http://dx.doi.org/10.1016/j.compfluid.2015.05.007`.

[135] Cyril Mauger, Loïc Méès, Marc Michard, Alexandre Azouzi, and Stéphane Valette. Shadowgraph, Schlieren and interferometry in a 2D cavitating channel flow. *Experiments in Fluids*, 53(6):1895–1913, 2012.

[136] T. Ménard, S. Tanguy, and A. Berlemont. Coupling level set/vof/ghost fluid methods: Validation and application to 3d simulation of the primary break-up of a liquid jet. *International Journal of Multiphase Flow*, 33(5):510 – 524, 2007.

[137] S. Menon, P.-K. Yeung, and W.-W. Kim. Effect of subgrid models on the computed interscale energy transfer in isotropic turbulence. *Computers & Fluids*, 25(2):165 – 180, 1996.

[138] C. L. Merkle, J. Z. Feng, and Buelow P. E. O. Computational modeling of the dynamics of sheet cavitation. In *Proceedings of the 3rd International Symposium on Cavitation,vol. 2, Grenoble, France, 1998.*, 1998.

[139] M. Milelli, B. L. Smith, and D. Lakehal. *Large-Eddy Simulation of Turbulent Shear Flows Laden with Bubbles*, pages 461–470. Springer Netherlands, Dordrecht, 2001.

[140] A Mirjalili, S.S Jain, and Dodd M.S. Interface-capturing methods for two-phase flows: an overview and recent developments. *Ann Res Briefs Center Turbul Res*, pages 117–135, 2017.

[141] Murali-Girija Mithun, Phoevos Koukouvinis, and Manolis Gavaises. Numerical simulation of cavitation and atomization using a fully compressible three-phase model. *Phys. Rev. Fluids*, 3:064304, Jun 2018.

[142] Murali-Girija Mithun, Phoevos Koukouvinis, and Manolis Gavaises. Numerical simulation of cavitation and atomization using a fully compressible three-phase model. *Phys. Rev. Fluids*, 3:064304, Jun 2018.

[143] K Nagasaka. The development of fine atomization injector. *JSAE Review*, 21(3):309–313, July 2000.

[144] S. Navarro-Martinez. Large eddy simulation of spray atomization with a probability density function method. *International Journal of Multiphase Flow*, 63:11 – 22, 2014.

[145] Kshitij Neroorkar, Bradley Shields, Ronald O. Grover, Jr., Alejandro Plazas Torres, and David Schmidt. Application of the homogeneous relaxation model to simulating cavitating flow of a diesel fuel. In *SAE 2012 World Congress & Exhibition*. SAE International, apr 2012.

[146] Kshitij Deepak Neroorkar. *Modeling of Flash Boiling Flows in Injectors with Gasoline-Ethanol Fuel Blends*. PhD thesis, University of Massachusetts - Amherst, 2011.

[147] B. Niçeno, M.T. Dhotre, and N.G. Deen. One-equation sub-grid scale (sgs) modelling for euler-euler large eddy simulation (eeles) of dispersed bubbly flow. *Chemical Engineering Science*, 63(15):3923 – 3931, 2008.

[148] F. Nicoud and F. Ducros. Subgrid-Scale Stress Modelling Based on the Square of the Velocity Gradient Tensor. *Flow, Turbulence and Combustion*, 62:pp. 183–200, 1999.

[149] W. H. Nurick. Orifice cavitation and its effect on spray mixing. *Journal of Fluids Engineering*, 98(4):681, 1976.

[150] Elin Olsson and Gunilla Kreiss. A conservative level set method for two phase flow. *Journal of Computational Physics*, 210(1):225 – 246, 2005.

[151] F. Orley, T. Trummler, S. Hickel, M. S. Mihatsch, S. J. Schmidt, and N. A. Adams. Large-eddy simulation of cavitating nozzle flow and primary jet break-up. *Physics of Fluids*, 27(8):086101, 2015.

[152] S. Osher and J.A. Sethian. Fronts propagating with curvature-dependent speed: algorithms based on Hamilton-Jacobi formulations. *J. Comput. Phys.*, (79):12–49, 1988.

[153] A. Papoutsakis, A. Theodorakakos, E. Giannadakis, and D. Papoulias. Les predictions of the vortical flow structures in diesel injector nozzles. *SAE Technical Paper 2009-01-0833*, 2009.

[154] Blaine Raphael Parkin. *Scale effects in cavitating flow*. PhD thesis, California Institute of Technology, 1952.

[155] N. Parolini and E. Burman. A finite element level set method cor viscout free-surface flows. In *Applied and Industrial Mathematics in Italy, Proceedings of SIMAI 2004*, pages 417–427. World Scientific, Singapore, 2005.

[156] F. Piscaglia, F. Giussani, A. Montorfano, J. Hélie, and S.M. Aithal. A multiphase dynamic-vof solver to model primary jet atomization and cavitation inside high-pressure fuel injectors in openfoam. *Acta Astronautica*, 2018.

[157] F. Piscaglia, A. Montorfano, F. Giussani, J. Hélie, and Aithal S.M. Multiphase VOF Simulation of Gasoline Injectors with Topologically Changing Grids. In *11th OpenFOAM Workshop, Guimarães, Portugal*, June 2016.

[158] F. Piscaglia, A. Montorfano, J. Hélie, and F. X. Demoulin. Development of a Multi-Phase VOF Dynamic Solver in OpenFOAM: an Application to the Simulation of the Opening and Closure Events in High Pressure GDI Injectors. In *ICMF-2016 - 9th Int. Conference on Multiphase Flow, Firenze, Italy*, 2016.

[159] F. Piscaglia, A. Montorfano, and A. Onorati. Development of a Non-Reflecting Boundary Condition for Multidimensional Nonlinear Duct Acoustic Computation. *Journal of Sound and Vibration*, 332(4):922–935, 2013. `http://dx.doi.org/10.1016/j.jsv.2012.09.030`.

[160] F. Piscaglia, A. Montorfano, and A. Onorati. Towards the LES Simulation of IC Engines with Parallel Topologically Changing Meshes. *SAE Int. J. Engines*, 6(2):926–940, 2013. `http://dx.doi.org/10.4271/2013-01-1096`.

[161] H. Pitsch and Olivier Desjardins. Detailed numerical investigation of turbulent atomization of liquid jets. *Atomization and Sprays*, 20(4):311–336, 2010.

[162] M. S. Plesset. The dynamics of cavitation bubbles. *Journal of Applied Mechanincs*, 16:277–282, 1949.

[163] M. S. Plesset. Cavitating flows. Technical report, Division of Engineering and Applied Science, California Institute of Technology, 1969.

[164] M S Plesset and A Prosperetti. Bubble dynamics and cavitation. *Annual Review of Fluid Mechanics*, 9(1):145–185, 1977.

[165] S.B. Pope. The evolution of surfaces in turbulence. *International Journal of Engineering Science*, 26(5):445 – 469, 1988.

[166] S.B. Pope. *Turbulent Flows*. Cambridge University Press, 2000.

[167] Stéphane Popinet. An accurate adaptive solver for surface-tension-driven interfacial flows. *Journal of Computational Physics*, 228(16):5838 – 5866, 2009.

[168] Stéphane Popinet and Stéphane Zaleski. A front-tracking algorithm for accurate representation of surface tension. *International Journal for Numerical Methods in Fluids*, 30(6):775–793.

[169] S. Quan, J. Lou, and D.P. Schmidt. Modeling Merging and Breakup in the Moving Mesh Interface Tracking Method for Multiphase Flow Simulations. *Journal of Computational Physics*, 228, 2009.

[170] J. Reboud, B. Stutz, and O. Coutier. Two-phase flow structure of cavitation:experiments and modelling of unsteady effects. In *3rd International Symposium on Cavitation, april 1998, Grenoble, France*, 1998.

[171] B A Reid, M Gavaises, N Mitroglou, G K Hargrave, C P Garner, and R M McDavid. String cavitation formation inside fuel injectors. *Journal of Physics: Conference Series*, 656(1):012099, 2015.

[172] B. A. Reid, G. K. Hargrave, C. P. Garner, and G. Wigley. An investigation of string cavitation in a true-scale fuel injector flow geometry at high pressure. *Physics of Fluids*, 22(3):031703, 2010.

[173] B.A. Reid, M. Gavaises, N. Mitroglou, G.K. Hargrave, C.P. Garner, E.J. Long, and R.M. McDavid. On the formation of string cavitation inside fuel injectors. *Experiments in Fluids*, 55(1), 2014.

[174] R. D. Reitz. *Atomization and other breakup regimes of a liquid jet*. PhD thesis, Princeton Univ., NJ., 1978.

[175] Wei-Min Ren and Hamid Sayar. Influence of nozzle geometry on spray atomization and shape for port fuel injector. March 2001.

[176] A. J. Reynolds. Thermo-fluid dynamic theory of two-phase flow. by m. i SHIL . eyrolles 1975. 248 pp. 83f or $21.60. *Journal of Fluid Mechanics*, 78(03):638, dec 1976.

[177] C.M. Rhie and W. L. Chow. A numerical study of the turbulent flow past an isolated airfoil with trailing edge separation. *AIAA J.*, 21:1525–1532, 1983.

[178] Johan Roenby, Henrik Bredmose, and Hrvoje Jasak. A computational method for sharp interface advection. *Royal Society Open Science*, 3(11):160405, Nov 2016.

[179] Ehsan Roohi, Amir Pouyan Zahiri, and Mahmood Passandideh-Fard. Numerical simulation of cavitation around a two-dimensional hydrofoil using vof method and les turbulence model. *Applied Mathematical Modelling*, 37(9):6469 – 6488, 2013.

[180] P. Sagaut. *Large-Eddy Simulation for Incompressible Flows: an Introduction*. Scientific computation. Springer-Verlag, 2006.

[181] Kaushik Saha, Sibendu Som, and Michele Battistoni. Investigation of homogeneous relaxation model parameters and their implications for gasoline injectors. *Atomization and Sprays*, 27(4), 1 2017.

[182] J. Sauer and G. H. Schnerr. Unsteady cavitating flow: A new cavitation model based on modified front capturing method and bubble dynamics, 2000 2000.

[183] R. Saurel, F. Petitpas, and R. Abgrall. Modelling phase transition in metastable liquids: application to cavitating and flashing flows. *Journal of Fluid Mechanics*, 607:313–350, 2008.

[184] Ruben Scardovelli and Stephane Zaleski. Analytical relations connecting linear interfaces and volume fractions in rectangular grids. *Journal of Computational Physics*, 164(1):228 – 237, 2000.

[185] Johannes Schindelin, Ignacio Arganda-Carreras, Erwin Frise, Verena Kaynig, Mark Longair, Tobias Pietzsch, Stephan Preibisch, Curtis Rueden, Stephan Saalfeld, Benjamin Schmid, Jean-Yves Tinevez, Daniel James White, Volker Hartenstein, Kevin Eliceiri, Pavel Tomancak, and Albert Cardona. Fiji: an open-source platform for biological-image analysis. *Nature Methods*, 9(7):676–682, June 2012.

[186] D. P. Schmidt and M. L. Corradini. The internal flow of diesel fuel injector nozzles: A review. *Int. Journal of Engine Research*, 2(1):1–22, 2001.

[187] Günter H. Schnerr and Jürgen Sauer. Physical and Numerical Modeling of Unsteady Cavitation Dynamics. In *ICMF-2001, 4th International Conference on Multiphase Flow*, May 2001.

[188] Weller Thermo-Fluids Section and H. G. Weller. The development of a new flame area combustion model using conditional averaging, 1993.

[189] J. Serras-Pereira, Z. van Romunde, P.G. Aleiferis, D. Richardson, S. Wallace, and R.F. Cracknell. Cavitation, primary break-up and flash boiling of gasoline, iso-octane and n-pentane with a real-size optical direct-injection nozzle. *Fuel*, 89(9):2592 – 2607, 2010.

[190] J. A. Sethian and Peter Smereka. Level set methods for fluid interfaces. *Annual Review of Fluid Mechanics*, 35(1):341–372, 2003.

[191] LIAN SHEN and DICK K. P. YUE. Large-eddy simulation of free-surface turbulence. *Journal of Fluid Mechanics*, 440:75–116, 2001.

[192] J. M. Shi, K. Wenzlawski, J. Helie, H. Nuglish, and J. Cousin. Urans ans sas analysis of flow dynamics in a gdi nozzle. In *ILASS - Europe 2010, 23rd Annual Conference on Liquid Atomization and Spray Systems, Brno, Czech Republic, September 2010*, 2010.

[193] J. Shinjo and A. Umemura. Simulation of liquid jet primary breakup: Dynamics of ligament and droplet formation. *International Journal of Multiphase Flow*, 36(7):513 – 532, 2010.

[194] Ashok K. Singhal, Mahesh M. Athavale, Huiying Li, and Yu Jiang. Mathematical basis and validation of the full cavitation model. *Journal of Fluids Engineering*, 124(3):617, 2002.

[195] William A. Sirignano. Volume averaging for the analysis of turbulent spray flows. *International Journal of Multiphase Flow*, 31(6):675–705, June 2005.

[196] Oscar J. Soriano-Palao, Martin Sommerfeld, and Axel Burkhardt. Modelling the influence of the nozzle geometry on the primary breakup of diesel jets. *International Journal of Spray and Combustion Dynamics*, 6(2):113–146, 2014.

[197] Celia Soteriou, Richard Andrews, and Mark Smith. Direct injection diesel sprays and the effect of cavitation and hydraulic flip on atomization. In *SAE Technical Paper*. SAE Int., 02 1995.

[198] Celia Soteriou, Richard Andrews, and Mark Smith. Further studies of cavitation and atomization in diesel injection. In *International Fuels & Lubricants Meeting & Exposition*. SAE International, may 1999.

[199] Akira Sou, Bariş Biçer, and Akio Tomiyama. Numerical simulation of incipient cavitation flow in a nozzle of fuel injector. *Computers & Fluids*, 103:42–48, 2014.

[200] Akira Sou, Shigeo Hosokawa, and Akio Tomiyama. Effects of cavitation in a nozzle on liquid jet atomization. *International Journal of Heat and Mass Transfer*, 50(17):3575 – 3582, 2007.

[201] Akira SOU, MAULANA Muhammad Ilham, Kenji ISOZAKI, Shigeo HOSOKAWA, and Akio TOMIYAMA. Effects of nozzle geometry on cavitation in nozzles of pressure atomizers. *Journal of Fluid Science and Technology*, 3(5):622–632, 2008.

[202] D.B. Spalding. A method for computing steady and unsteady flows possessing discontinuities of density. Cham report 910/2, 1974.

[203] Kyle D. Squires and Hidekatsu Yamazaki. Preferential concentration of marine particles in isotropic turbulence. *Deep Sea Research Part I: Oceanographic Research Papers*, 42(11):1989 – 2004, 1995.

[204] B. Stutz and J. L. Reboud. Experiments on unsteady cavitation. *Experiments in Fluids*, 22(3):191–198, Jan 1997.

[205] B. Stutz and J.-L. Reboud. Two-phase flow structure of sheet cavitation. *Physics of Fluids*, 9(12):3678–3686, 1997.

[206] M. Sussman, K.M. Smith, M.Y. Hussaini, M. Ohta, and R. Zhi-Wei. A sharp interface method for incompressible two-phase flows. *Journal of Computational Physics*, 221(2):469 – 505, 2007.

[207] Mark Sussman and Elbridge Gerry Puckett. A coupled level set and volume-of-fluid method for computing 3d and axisymmetric incompressible two-phase flows. *Journal of Computational Physics*, 162(2):301 – 337, 2000.

[208] H Takewaki, A Nishiguchi, and T Yabe. Cubic interpolated pseudo-particle method (cip) for solving hyperbolic-type equations. *Journal of Computational Physics*, 61(2):261 – 268, 1985.

[209] Hideaki Takewaki and Takashi Yabe. The cubic-interpolated pseudo particle (cip) method: application to nonlinear and multi-dimensional hyperbolic equations. *Journal of Computational Physics*, 70(2):355 – 372, 1987.

[210] A. L. Tassin, C. Y. Li, S. L. Ceccio, and L. P. Bernal. Velocity field measurements of cavitating flows. *Experiments in Fluids*, 20(2):125–130, Dec 1995.

[211] Tayfun E. Tezduyar. Interface-Tracking and Interface-Capturing Techniques forComputation of Moving Boundaries and Interfaces. In *Proceedings of the 6th World Congress on Computational Mechanis, ept. 5-10, 2004, Beijing, China*, 2019.

[212] The OpenFOAM Foundation. OpenFOAM User Guide.

[213] A. Toutant, M. Chandesris, D. Jamet, and O. Lebaigue. Jump conditions for filtered quantities at an under-resolved discontinuous interface. part 1: Theoretical development. *International Journal of Multiphase Flow*, 35(12):1100 – 1118, 2009.

[214] A. Toutant, E. Labourasse, O. Lebaigue, and O. Simonin. Interaction between a deformable buoyant bubble and a homogeneous isotropic turbulence. In *Conference on Turbulence and Interactions TI2006,May 29 - June 2,2006, Porquerolles,France*, 2006.

[215] A. Toutant, E. Labourasse, O. Lebaigue, and O. Simonin. Dns of the interaction between a deformable buoyant bubble and a spatially decaying turbulence: A priori tests for les two-phase flow modelling. *Computers & Fluids*, 37(7):877 – 886, 2008. Special Issue of the Turbulence and Interaction-TI2006 Conference.

[216] Arnaud Trouvé and Thierry Poinsot. The evolution equation for the flame surface density in turbulent premixed combustion. *Journal of Fluid Mechanics*, 278:1–31, 1994.

[217] G. Tryggvason, B. Bunner, A. Esmaeeli, D. Juric, N. Al-Rawahi, B. Tauber, J. Han, S. Nas, and Y.J. Jan. A Front-Tracking Method for the Computations of Multiphase Flow. *Journal of Computational Physics*, 169:708–759, 2001.

[218] S. Turek. Efficient solvers for incompressible flow problems, an algorithmic and computational approach. In *Lecture notes in computational science and engineering*, volume 6. Springer, Berlin, 1999.

[219] Ariane Vallet. *Contribution a la modelisation de l'atomisation d'un jet liquide haute pression*. PhD thesis, 1997. Thése de doctorat dirigée par Borghi, Roland Physique Rouen 1997.

[220] Ariane Vallet and Roland Borghi. Modélisation eulerienne de l'atomisation d'un jet liquide. *Comptes Rendus de l'Académie des Sciences - Series IIB - Mechanics-Physics-Astronomy*, 327(10):1015 – 1020, 1999.

[221] S. Vincent, J. Larocque, D. Lacanette, A. Toutant, P. Lubin, and P. Sagaut. Numerical simulation of phase separation and a priori two-phase les filtering. *Computers & Fluids*, 37(7):898 – 906, 2008. Special Issue of the Turbulence and Interaction-TI2006 Conference.

[222] H. Wadell. Sphericity and roundness of rock particles. *The Journal of Geology*, 41(3):310–331, 1933.

[223] Y. Wang and R. D. Reitz. Eulerian two-phase flow cfd simulation using a compressible and equilibrium eight-equation model. In *ILASS 2015, 27th Annual Conference on Liquid Atomization and Spray Systems, Raleigh,NC*, 2015.

[224] Zhaoyuan Wang, Jianming Yang, Bonguk Koo, and Frederick Stern. A coupled level set and volume-of-fluid method for sharp interface simulation of plunging breaking waves. *International Journal of Multiphase Flow*, 35(3):227 – 246, 2009.

[225] Kent E. Wardle and Henry G. Weller. Hybrid Multiphase CFD Solver for Coupled Dispersed/Segregated Flows in Liquid-Liquid Extraction. *International Journal of Chemical Engineering*, article ID 128936, vol. 2013:1–13, 2013.

[226] Seiichi Washio. 1 - review of cavitation nuclei. In Seiichi Washio, editor, *Recent Developments in Cavitation Mechanisms*, pages 1 – 44. Woodhead Publishing, 2014.

[227] H. Watanabe, M. Nishikori, T. Hayashi, M. Suzuki, N. Kakehashi, and M. Ikemoto. Visualization analysis of relationship between vortex flow and cavitation behavior in diesel nozzle. *Int. Journal of Engine Research*, (1):5–12, 2014.

[228] Andre Weiner and Dieter Bothe. Advanced subgrid-scale modeling for convection-dominated species transport at fluid interfaces with application to mass transfer from rising bubbles. *Journal of Computational Physics*, 347:261 – 289, 2017.

[229] H. G. Weller. A new approach to vof-based interface capturing methods for incompressible and compressible flow. Technical report, 01 2008.

[230] H.G. Weller. A new approach to VOF-based interface capturing methods for incompressible and compressible flow. Technical report TR/HGW/04, OpenCFD Ltd., 2008.

[231] F. A. Williams. Spray combustion and atomization. *The Physics of Fluids*, 1(6):541–545, 1958.

[232] E. Winklhofer, E. Kull, E. Kelz, and A. Morozov. Comprehensive hydraulic and flow field documentation in model throttle experiments under cavitation conditions. In *ILASS 2001, 17th European Conference on Liquid Atomization and Spray Systems, Zurich, Switzerland*, 2001.

[233] Y. Wu, A. Montorfano, F. Piscaglia, and A. Onorati. A Study of the Organized in-Cylinder Motion by a Dynamic Adaptive Scale-Resolving Turbulence Model. *Flow, Turbulence and Combustion*, Dec 2017.

[234] T. Yabe and T. Aoki. A universal solver for hyperbolic equations by cubic-polynomial interpolation i. one-dimensional solver. *Computer Physics Communications*, 66(2):219 – 232, 1991.

[235] T. Yabe, T. Ishikawa, P.Y. Wang, T. Aoki, Y. Kadota, and F. Ikeda. A universal solver for hyperbolic equations by cubic-polynomial interpolation ii. two- and three-dimensional solvers. *Computer Physics Communications*, 66(2):233 – 242, 1991.

[236] Di Yang, Bicheng Chen, Scott A. Socolofsky, Marcelo Chamecki, and Charles Meneveau. Large-eddy simulation and parameterization of buoyant plume dynamics in stratified flow. *Journal of Fluid Mechanics*, 794:798–833, 2016.

[237] Xiaofeng Yang and Ashley J. James. Analytic relations for reconstructing piecewise linear interfaces in triangular and tetrahedral grids. *J. Comput. Physics*, 214:41–54, 2006.

[238] B. Yin, S. Yu, H. Jia, and J. Yu. Numerical research of diesel spray and atomization coupled cavitation by large eddy simulation (les) under high injection pressure. *International Journal of Heat and Fluid Flow*, 59:1 – 9, 2016.

[239] H. Yu, L. Goldsworthy, P.A. Brandner, and V. Garaniya. Development of a compressible multiphase cavitation approach for diesel spray modelling. *Applied Mathematical Modelling*, 45:705 – 727, 2017.

[240] W. Yuan and G. H. Schnerr. Numerical simulation of two-phase flow in injection nozzles: Interaction of cavitation and external jet formation. *Journal of Fluids Engineering*, 125(6):963–969, 2004.

[241] Weixing Yuan, Jürgen Sauer, and Günter H. Schnerr. Modeling and computation of unsteady cavitation flows in injection nozzles. *Mécanique & Industries*, 2(5):383 – 394, 2001.

[242] Weixing Yuan and Gunnter H. Schnerr. Numerical simulation of two-phase flow in injection nozzles: Interaction of cavitation and external jet formation. *Journal of Fluids Engineering*, 125:963–969, 2004.

[243] Steven T. Zalesak. Fully multidimensional flux-corrected transport algorithms for fluids. *Journal of Computational Physics*, 31(3):335 – 362, 1979.

[244] A. Zandian, W. A. Sirignano, and F. Hussain. Understanding liquid-jet atomization cascades via vortex dynamics. *Journal of Fluid Mechanics*, 843:293–354, 2018.

[245] P. Zwart, A. Gerber, and T. Belamri. A two-phase flow model for predicting cavitation dynamics. In *ICMF-2004 - 5th Int. Conference on Multiphase Flow, Yokohama, Japan*, 2004.